

Carbon and Metal Oxide Based Electrode Materials for Sodium Ion Batteries and
Sodium Ion Capacitors

by

Jia Ding

A thesis submitted in partial fulfillment of the requirements for the degree of

Doctor of Philosophy

In

Materials Engineering

Department of Chemical and Materials Engineering
University of Alberta

© Jia Ding, 2015

Abstract

This thesis is focused on the design and fabrication of carbon-based electrode materials for sodium-ion batteries (NIBs) and sodium-ion capacitors (NICs), as well as metal oxide (SnO_2) based anode material for NIBs and lithium-ion batteries (LIBs).

Na ion based energy storage systems are attracting significant interest as a potential lower cost alternative to Li ion based systems due to the geographically democratic reserves of the sodium metal. In its infancy, there is a strong demand for suitable electrode materials. In our first attempt, we created carbon materials (CPM-A) as NIB anodes, which exhibited many attractive electrochemical properties, similar to graphite as a LIB anode. An abundant wild plant, peat moss was chosen as the carbon precursor. The highly cross-linked polymer tissue of peat moss suppressed the nucleation of equilibrium graphite phase at high temperatures, instead transforming into highly ordered pseudographitic domains with substantially larger interlayer spacing (0.388nm) than that of graphite (0.335nm). These domains can provide Na intercalation sites analogous to the Li storage sites in graphite. By inheriting the unique cellular structure of peat moss leaves, CPM-A were composed of 3D macroporous frameworks of carbon nanosheets, which not only provided facile electrolyte access pathways but also greatly reduced the Na bulk diffusion distances. Benefiting from all these superiorities, the best CPM-A anode exhibited many highly desirable features, including low capacity voltage, negligible voltage hysteresis, high Coulombic efficiency, good cycling retention and high rate capacity. Based on this set of CPM-A specimens with tunable graphitic order, surface area and heteroatoms level, we also discovered the inner correlation between the physical/chemical properties of carbon and the galvanostatic voltage profile of the corresponding NIB anode, which provided important guidance for future carbon NIB anode design and preparation.

In our second attempt, we built a Na-ion based hybrid capacitor device (NIC) which has spanned the energy-power divide between the traditional batteries and supercapacitors. Both the anode carbon and cathode carbon were entirely derived from a highly economical biowaste: peanut shell. By skillfully utilizing the heterogeneous tissue of peanut shell, an adsorption cathode carbon (PSNC) and an intercalation anode carbon (PSOC) were prepared using the outer and inner skin of peanut shell, respectively. The cathode carbon has a high surface area, a high level of oxygen doping and a unique hierarchically porous architecture, which all positively contribute to the excellent capacitive performance. On the contrary, the anode carbon is highly ordered with low surface area and low heteroatom doping, and thus provides large intercalation capacity in the low voltage region. By pre-sodiating the anode, the working voltage windows of both the cathode and anode in the full NIC cell were optimized. In more detail, the cathode swung within a wide voltage window from 1.5 to 4.2V hence the high adsorption capacity of PSNC was fully utilized. The anode was restricted within the low voltage region (below 0.1V), in order to achieve the largest possible working voltage window for the full device. Benefiting from the excellent electrochemical properties of electrode materials and the optimized working style of the electrodes, the resultant NIC devices can offer a state-of-the-art cyclically stable combination of energy and power densities, even comparable to the performances of previously reported Li-ion capacitors (LICs).

In the third attempt, we tried to develop anode materials with high volumetric capacity for NIBs. SnO₂ was chosen as the active material. A glucose mediated self-assembling method was employed to prepare a novel SnO₂-carbon nanocomposite, which exhibited very promising cyclability and rate behavior as both a NIB and LIB anode. In addition to the advanced material synthesis, we also made systemic investigation on the fundamental energy storage mechanism of SnO₂ anodes. Combining characterization methods of TEM, XRD and XPS, the phase

transformations of SnO_2 during the sodiation/desodiation, lithiation/delithiation processes have been studied in detail. These analyses have revealed the inner cause of the capacity discrepancy for SnO_2 anode between Li and Na systems, which although frequently observed has never been explained. The much lower capacity of SnO_2 anode against Na is due to the kinetic difficulty of Na-Sn alloying reaction to reach the terminal $\text{Na}_{15}\text{Sn}_4$ intermetallic. Therefore, a large portion of the active material only shuffles between SnO_2 and $\text{Sn}+\text{NaO}_2$. The characterization data also revealed a critical difference in the conversion reactions between the two systems. LiO_2 is reduced directly to SnO_2 and Li, whereas the NaO_2 to SnO_2 reaction proceeds through an intermediate SnO phase. These fundamental findings have great significance for future SnO_2 anode development.

Preface

This thesis is organized into 5 chapters:

Chapter 1 of this thesis is an introduction of the research background, fundamental principles, as well as a description of the motivation and research scope of this thesis.

Chapter 2 of this thesis has been published as **Jia Ding**, Huanlei Wang, Zhi Li, Alireza Kohandehghan, Kai Cui, Zhanwei Xu, Benjamin Zahiri, Xuehai Tan, Elmira Memarzadeh Lotfabad, Brian C. Olsen, and David Mitlin, “Carbon Nanosheet Frameworks Derived from Peat Moss as High Performance Sodium Ion Battery Anodes”, *ACS Nano*, 2013, 7(12), 11004-11015.

Chapter 3 of this thesis has been published as **Jia Ding**, Huanlei Wang, Zhi Li, Kai Cui, Dimitre Karpuzov, Xuehai Tan, Alireza Kohandehghan, and David Mitlin, “Peanut Shell Hybrid Sodium Ion Capacitor with Extreme Energy - Power Rivals Lithium Ion Capacitors”, *Energy & Environmental Science*, 2015, 8, 941-955.

Chapter 4 of this thesis has been published as **Jia Ding**, Zhi Li, Huanlei Wang, Kai Cui, Alireza Kohandehghan, Xuehai Tan, Dimitre Karpuzov, and David Mitlin, “Sodiation *vs.* Lithiation Phase Transformations in a High Rate - High Stability SnO₂ in Carbon Nanocomposite”, *Journal of Materials Chemistry A*, 2015, 3(13), 7100-7111.

Chapter 5 of this thesis presents the conclusion remarks of the projects included in this thesis.

For each work presented in this thesis, I was responsible for the primary thinking, concept formation, experiments design and operation, data collection and analysis, as well as the manuscript composition/submission/revision. Dr. David Mitlin was the supervisory author and was involved with idea, concept formation and manuscript composition/revision. In the first paper (*ACS Nano*, 2013, 7(12), 11004-11015), Huanlei Wang and Zhi Li gave me the training and assistance on the carbon porosity

characterization. Zhanwei Xu provided me assistance on the Raman data analysis. Xuehai Tan, Elmira Memarzadeh Lotfabad and Beniamin Zahiri provided me the training and assistance on the transmission electron microscopy (TEM) operation. Alireza Kohandehghan provided me assistance on the electron energy loss spectroscopy (EELS) data analysis. Kai Cui was responsible for EELS data collection. Brian C. Olsen was responsible for the scheme drawing. In the second paper (*Energy & Environmental Science*, 2015, 8, 941-955), Huanlei Wang and Zhi Li gave me training on the hybrid device assembling and tests. Kai Cui was responsible for EELS data collection. Dimitre Karpuzov was responsible for X-ray photoelectron spectroscopy (XPS) data collection. Xuehai Tan gave me assistance on the transmission electron microscopy (TEM) operation. Alireza Kohandehghan gave me assistance on the EELS data analysis. In the third paper (*Journal of Materials Chemistry A*, 2015, 3(13), 7100-7111), Huanlei Wang gave me assistance on the porosity characterization. Zhi Li gave me assistance on the electrochemical kinetics data analysis. Xuehai Tan gave me assistance on the transmission electron microscopy (TEM) operation. Alireza Kohandehghan provided me assistance on the EELS data (element maps) and XRD data analysis. Kai Cui was responsible for EELS data collection. Dimitre Karpuzov was responsible for XPS data collection.

Acknowledgements

Here I would like to acknowledge everyone who has contributed to the coming together of this thesis. First and foremost, I would like to express my sincere gratitude and appreciation to my supervisor, Dr. David Mitlin, who has supported me throughout this research with his knowledge and patience, and also for giving me the resources I needed. It was such a great honor and fortune for me to be guided by him.

My gratitude also goes to Dr. Thomas Thundat for his considerate co-supervision and wonderful inspiration. I am also very grateful to my colleagues in Mitlin group for their invaluable and unconditional help. Many thanks go to Huanlei Wang, Zhi Li, Xuehai Tan, Zhanwei Xu, Alireza Kohandehghan, Tyler Stephenson, Chris Holt, Brian Olsen, Elmira Memarzadeh, and Behdokht Farbod. My sincere thanks also go to Kai Cui for TEM assistance and Dimitre Karpuzov for XPS assistance. Finally, thanks to all the technicians and staff members of the Chemical and Materials Engineering (CME) Department, National Institute for Nanotechnology (NINT), Alberta Centre for Surface Engineering and Science (ACSES), and Cross-Cancer Institute at University of Alberta.

I also thank to all my other friends for their unequivocal supports. Last but not least, my heartfelt gratitude goes to my family for all the support and encouragement given to me during my graduate career. This thesis is dedicated to them.

Table of Contents

1	Introduction	1
1.1	Li/Na ion batteries	2
1.1.1	The principle of electrochemical process	2
1.1.2	Thermodynamics	3
1.1.3	Kinetics	5
1.2	Carbonaceous materials as Na ion battery anodes	6
1.3	Sn/SnO ₂ based materials as Na ion battery anodes	14
1.3.1	Sn-based NIB anodes	14
1.3.2	SnO ₂ -based NIB anodes	20
1.4	Li/Na ion capacitors	22
1.4.1	Concepts	22
1.4.2	Configuration of Li/Na ion capacitors	24
1.5	Carbonaceous materials synthesis	26
1.5.1	Lignocellulosic biomass precursors	26
1.5.2	Pyrolysis, hydrothermal carbonization	28
1.6	Motivation and scope of this thesis	31
1.7	References	33
2	Carbon Nanosheet Frameworks Derived from Peat Moss as High Performance Sodium Ion Battery Anodes	42
2.1	Introduction	42
2.2	Experimental procedures	44
2.2.1	Material synthesis	44
2.2.2	Material characterization	45
2.2.3	Electrochemical test	45
2.3	Results and discussion	46
2.4	Conclusion	71

2.5 References	72
3 Peanut Shell Hybrid Sodium Ion Capacitor with Extreme Energy - Power Rivals	
Lithium Ion Capacitors	77
3.1 Introduction	77
3.2 Experimental procedures	79
3.2.1 Materials	79
3.2.2 Material characterization	80
3.2.3 Electrochemical testing	81
3.3 Results and discussion	82
3.4 Conclusion	115
3.5 References	115
4 Sodiation vs. Lithiation Phase Transformations in a High Rate - High Stability	
SnO ₂ in Carbon Nanocomposite	124
4.1 Introduction	124
4.2 Experimental procedure	126
4.2.1 Materials preparation	126
4.2.2 Material characterization	126
4.2.3 Electrochemical measurements	127
4.3 Result and discussion	127
4.3.1 As-synthesized microstructure	127
4.3.2 Electrochemical performance and phase transformations vs. Li	131
4.3.3 Electrochemical performance and phase transformations vs. Na	144
4.4 Conclusion	157
4.5 References	157
5 Concluding remarks	164

List of Tables

Table 1-1: Comparison of properties of various LIB and NIB anodes.	14
Table 1-2: Characteristics of lithium and sodium.	18
Table 2-1: Physical parameters and electrochemical properties for CPM, CPM-A and CAC.....	52
Table 2-2: Elemental composition information for CPM, CPM-A and CAC.	56
Table 2-3: Performance comparison of CPM-1100-A <i>versus</i> state of the art NIB carbons reported in literature.	65
Table 2-4: Resistance values simulated from modeling the experimental impedance (Figure 2-16) using the equivalent circuits shown in Figure 2-17.	70
Table 3-1: Carbon structure, electrical conductivity and textural properties of Peanut Shell Nanosheet Carbon (PSNC) and Peanut Shell Ordered Carbon (PSOC), with baseline commercial activated carbon CAC also shown.	91
Table 3-2: Surface chemistry of PSNC and PSOC, with baseline CAC also shown. .	93
Table 3-3: Capacity retention comparison with literature reported hybrid devices. .	114

List of Figures

- Figure 1-1:** Schematic diagram demonstrating the electrons and Li^+ ions transfer during charge and discharge processes. Adapted from ref 7 with permission from the Royal Society of Chemistry, Copyright 2011.3
- Figure 1-2:** (A) Cyclic voltammograms (CV) of LiFePO_4 electrode. Adapted from ref 10 with permission from the Royal Society of Chemistry, Copyright 2011. (B) Galvanostatic discharge/charge profiles of graphite electrode. Adapted from ref 11 with permission from Wiley-VCH, Copyright 1998.....5
- Figure 1-3:** (A) Potential profiles of Na/graphite cell showing the lack of electrochemical activity of graphite against Na. Adapted from ref 12 with permission from Wiley-VCH, Copyright 2013. (B) Potential profiles of the first charge/discharge cycle for saccharose-coke derived carbon in EC/ NaClO_4 electrolyte at 7mA g^{-1} . Adapted from ref 15 with permission from the Elsevier, Copyright 2002. (C) Sodium potential profiles of glucose pyrolyzed to 1150°C . Adapted from ref 16 with permission from the Electrochemical Society, Copyright 2000. (D) Voltage/capacity plots of carbon aerogel microspheres in sodium cells, 1 M NaClO_4 dissolved in DME, THF, and EC:THF as electrolytes. Adapted from ref 18 with permission from the Electrochemical Society, Copyright 2005.7
- Figure 1-4:** (A) SEM image of the interconnected macroporous structure of the templated carbon. (B) Rate capability of the templated carbon. Adapted from ref 19 with permission from the Royal Society of Chemistry, Copyright 2011. (C) TEM image of the hollow carbon nanospheres (HCS). (D) Rate performance of HCS and carbon spheres (CS). Adapted from ref 20 with permission from Wiley-VCH, Copyright 2012.8
- Figure 1-5:** (A) Charge/discharge profiles of the templated carbon and commercial Timrex 300. Adapted from ref 19 with permission from the Royal Society of

Chemistry, Copyright 2011. (B) Galvanostatic charge/discharge profiles of hollow carbon nanospheres at $50\text{mA}\text{g}^{-1}$. Adapted from ref 20 with permission from Wiley-VCH, Copyright 2012. (C) Charge/discharge profiles of the chemically activated polypyrrole–functionalized graphene sheets at a current density of $50\text{mA}\text{g}^{-1}$. Adapted from ref 21 with permission from Wiley-VCH, Copyright 2013....9

Figure 1-6: (A) SEM image of the hollow polyaniline nanowires (PANI-HNWs). (B) Capacities of PANI-HNWs derived carbon (HCNW) electrode as a function of cycle number at different current densities. (C) Charge/discharge profiles of HCNW electrode between 0 and 1.2V at a current density of $50\text{mA}\text{g}^{-1}$. Adapted from ref 22 with permission from the American Chemical Society, Copyright 2012. (D) FESEM image of the cellulose nanofiber derived carbons (CNFs). (E) Rate performance of CNFs. (F) Charge/discharge profiles of CNFs at $40\text{mA}\text{g}^{-1}$. Adapted from ref 23 with permission from the Royal Society of Chemistry, Copyright 2014. (G) FESEM image of electrospun PAN-F127 derived carbon nanofibers (P-CNFs). (H) Discharge capacity of P-CNFs electrode at various current densities. (I) Voltage profiles of P-CNFs electrode at a current density of $50\text{mA}\text{g}^{-1}$. Adapted from ref 24 with permission from the Royal Society of Chemistry, Copyright 2013. 10

Figure 1-7: Voltage profiles and dQ/dV plots (inserts) of (a) Na/sphere carbon cell and (b) Na/hard carbon cell cycled between 0.001-2V at $15\text{mA}\text{g}^{-1}$. Adapted from ref 25 with permission from the Elsevier, Copyright 2014. 12

Figure 1-8: (A) Charge/discharge profiles of a chemically activated carbon with a surface area of $1477\text{m}^2\text{g}^{-1}$. Adapted from ref 21 with permission from Wiley-VCH, Copyright 2013. (B) Charge/discharge profiles of an unactivated carbon with a surface area of $3\text{m}^2\text{g}^{-1}$. Adapted from ref 18 with permission from the Electrochemical Society, Copyright 2005. 12

Figure 1-9: (A) Linear and natural logarithm transformed models plotting the reversible capacity in the 1st cycle as a function of DFT specific pore volume of

carbon specimen. (B) Reversible capacity vs. logit transform of the percentage of the unexposed carbon atoms. Adapted from ref 26 with permission from the Elsevier, Copyright 2014. 13

Figure 1-10: (A) Voltage profiles of the first desodiation and second sodiation of a sputtered Sn film superimposed on the Na-Sn binary phase diagram. (B) Voltage profiles of the first desodiation and second sodiation of sputtered Sn film superimposed on the predicted DFT voltage profile. Adapted from ref 34 with permission from the Electrochemical Society, Copyright 2012. 16

Figure 1-11: (A) Differential capacity vs. cell potential curves of pure microcrystalline Sn obtained after 1st cycle at $\sim 50\text{mA g}^{-1}$ in the potential window of 0.01-1.2V. Adapted from ref 35 with permission from the Elsevier, Copyright 2013. (B) Cyclic voltammograms of mesoporous C/Sn composite anodes in Sn-Na batteries at a scan rate of 0.05 mVs^{-1} . Adapted from ref 36 with permission from Wiley-VCH, Copyright 2013. 17

Figure 1-12: (A) Electron diffraction pattern evolution as sodiation proceeds. Adapted from ref 37 with permission from the American Chemical Society, Copyright 2013. (B) Schematic illustration of the structure evolution of Sn nano particles (NPs) during the sodiation. Adapted from ref 39 with permission from the American Chemical Society, Copyright 2012. 17

Figure 1-13: (A) SEM image of the Sn thin film deposited on wood fibers (Sn@WF). (B) Cycling performance of Sn@WF, the Al_2O_3 coated fiber and the Cu current collector baseline. Adapted from ref 41 with permission from the American Chemical Society, Copyright 2013. (C) SEM image of cathodic electrodeposition synthesized Sn nanofibers. (D) Cycle performance and Coulombic efficiency of the Sn nanofibers over a voltage range of 0.001 to 0.65 V vs. Na/Na^+ . Adapted from ref 42 with permission from the American Chemical Society, Copyright 2014. 19

Figure 1-14: (A) TEM image of SnO_2 /reduced graphene oxide nanocomposite

(SnO₂-RGO). (B) Cycling performance of SnO₂-RGO in 1M NaClO₄ in EC-PC with and without FEC additive. Adapted from ref 50 with permission from the Royal Society of Chemistry, Copyright 2014. (C) Low magnification TEM image of SnO₂ on multiwall carbon nanotube composite (SnO₂@MWCNT). (D) Cycling performances of SnO₂@MWCNT, bare MWCNT and SnO₂. Adapted from ref 51 with permission from the Elsevier, Copyright 2013. (E) Low magnification TEM image of SnO₂ anchored graphene nanocomposites (SnO₂@graphene). (F) Cycling performance of SnO₂@graphene, bare SnO₂ and graphene. Adapted from ref 49 with permission from the Royal Society of Chemistry, Copyright 2013.21

Figure 1-15: (A) Cyclic voltammograms (CV) of a supercapacitor material, where the response to a linear change in potential is a constant current. (B) Cyclic voltammograms (CV) of a battery material which exhibits faradaic redox peaks. Adapted from ref 52 with permission of Science AAAS.23

Figure 1-16: (A) Schematic voltage profile of a conventional EDLC supercapacitor, utilizing active carbon as electrodes. (C) Schematic voltage profiles of a Li-ion capacitor cell. (B)(D) Comparison of the characteristics of Li-ion batteries, EDLCs and Lithium-ion capacitors over six important criteria for electrochemical energy storage device. Adapted from ref 74 with permission from the Royal Society of Chemistry, Copyright 2012.26

Figure 1-17: (A) Chemical structure of lignin. (B) 3 types of building blocks of lignin.27

Figure 1-18: (A) SEM image of monodispersed carbon spheres obtained by hydrothermal carbonization with sugar as precursor. Adapted from ref 127 with permission from the Elsevier, Copyright 2001. (B) SEM image of “hard” biomass (oak leaf) after hydrothermal carbonization. Adapted from ref 96 with permission from American Chemical Society, Copyright 2007.30

Figure 2-1: The preparation route of CPM-1100-A carbons derived from peat moss

as anode.....	46
Figure 2-2: (A) Photograph of the fully dehydrated peat moss precursor. (B) Environmental SEM image of the fully dehydrated peat moss precursor.....	47
Figure 2-3: (A) Low magnification SEM micrograph of peat moss derived carbon (CPM-1100-A). (B) SEM micrograph of CPM-1400-A.....	48
Figure 2-4: (A) Higher magnification SEM micrograph highlighting the hollow macroporous architecture of the carbon particles (CPM-1100-A). (B) SEM micrograph of CPM-1100-A, highlighting the macroporous architecture. (C) SEM micrograph of a commercial activated carbon (CAC) particle.....	48
Figure 2-5: HAADF TEM micrograph and EELS thickness profile (inset) of the arrowed carbon strand in CPM-A.....	49
Figure 2-6: HRTEM micrographs of CPM-600-A (A), CPM-900-A (B), CPM-1100-A (C) and CPM-1400-A (D), respectively.....	49
Figure 2-7: (A) XRD patterns of the activated specimens (CPM-A) and of commercial activated carbon (CAC). (B) XRD patterns of the un-activated specimens (CPM).....	50
Figure 2-8: Raman spectra of CPM-A, CAC (A) and fitted Raman spectra of CPM-A and CAC specimens.....	53
Figure 2-9: (A,C,E) Nitrogen adsorption-desorption isotherms of CPM-A, CPM and CAC specimens. (B,D,F) Pore size distribution calculated from the adsorption isotherms of CPM-A, CPM and CAC specimens, using DFT method.....	55
Figure 2-10: Cyclic Voltammogram of CPM-A electrodes between 0.001 and 2.8 V at a scanning rate of 0.1 mVs ⁻¹ (Left panels). Galvanostatic discharge/charge curves of CPM-A electrodes at current density of 50mAhg ⁻¹ (Right panels).....	57
Figure 2-11: Galvanostatic discharge/charge profiles of un-activated CPM electrodes.....	58

Figure 2-12: (A-C) Potential profiles of CPM, CPM-A and commercial active carbon electrodes. (B, D) Summary of capacity potential distribution of CPM, CPM-A and commercial active carbon electrodes. (10th cycle at current density of 50mAhg⁻¹ in all the figures).....60

Figure 2-13: (A) XRD spectra for CPM-1400 and CAC electrodes, demonstrating Na intercalation-induced dilation of the interlayer spacing in the majority pseudographitic phase of CPM-1400. The peaks at $2\theta = 26.4^\circ$ are for the secondary (~ 20 wt.%) equilibrium graphite phase also present in CPM-1400, which is inactive and hence remains invariant with voltage. The electrodes were galvanostatically discharged to a) 0.2V, b) 0.1 V, c) 0.05 V, d) 0.001V vs. Na/Na⁺. (B) Dependence of the mean interlayer spacing on discharge voltage, values derived from (A).62

Figure 2-14: Extended cycling performance of the CPM, CPM-A and CAC electrodes, with coulombic efficiency of CPM-1100-A electrode being displayed.....63

Figure 2-15: (A) Volumetric capacity of CPM-1100-A. (B) Cross section SEM image of the CPM-1100-A electrode.66

Figure 2-16: (A) Electrochemical impedance spectra of CPM, CPM-A and CAC electrodes before cycling. (B) Electrochemical impedance spectra of CPM, CPM-A and CAC electrodes after cycling for 210 cycles.....67

Figure 2-17: Equivalent electronic circuits used to simulate the EIS data. For the spectra of all the as prepared specimens, equivalent circuit (A) was used. R_{el} is the sum of resistances of electrical connections in the experiment setup including ionic diffusion resistance in the electrolyte. R_{ct} reflects the charge transfer resistance and Z_w (Warburg-type element) represents Na diffusion impedance within carbon materials.....67

Figure 2-18: (A-B) The total charge transfer resistance within all the interfaces ($R_{ct}+R_f$) and sum of resistance of electrical connections in the experimental setup (R_{el}) changes as functions of the cycle number. (C-D) Electrochemical impedance

spectra of CPM-1100-A (C) and CPM-1400-A (D) (As-prepared, 30th cycle, 100th cycle, 150th cycle and 210th cycle)..... 69

Figure 2-19: Rate performance of CPM-A (A) and CPM (B) electrodes. 70

Figure 3-1: Material synthesis process employed for each of the electrodes and the relevant cathode/anode charge storage mechanisms in the sodium ion capacitor (NIC). 82

Figure 3-2: (A) Low magnification SEM micrograph illustrating the macroscopic morphology of PSNC-3-800. (B) TEM micrograph of PSNC-3-800 highlighting the morphology of the carbon nanosheets. (C) HAADF image (holey carbon support also visible) and insert of a thickness profile of PSNC-3-800, measured with low loss EELS along the white arrow. (D) HRTEM micrograph of PSNC-3-800. (E) Low magnification SEM micrograph highlighting the morphology of PSOC-A with an insert highlighting the thickness of the carbon sheet. (F) HRTEM micrograph of PSOC-A. 84

Figure 3-3: SEM micrographs of (A) PSNC-3-850 and (B) PSNC-2-800, (C) PSOC, (D) the baseline commercial activated carbon (CAC). 85

Figure 3-4: HAADF TEM micrographs and thickness profiles (insert) of (A) PSNC-3-850 and (B) PSNC-2-800, measured from low-loss EELS along the white arrows. HRTEM micrographs of (C) PSNC-3-850, (D) PSNC-2-800, and (E) PSOC. 87

Figure 3-5: SEM micrographs of cathode and anode carbons achieved when employing the entire peanut shell as a single precursor for either synthesis process. (A) cathode carbon. (B) anode carbon. 88

Figure 3-6: (A) XRD patterns of the PSNC and PSOC specimens. (B) Raman spectra of PSNC-3-800 and PSOC-A. (C) O 1s and C 1s core level XPS spectra fits for PSNC-3-800. (D) Nitrogen adsorption-desorption isotherms of PSNC and PSOC. (E) Pore size distribution of PSNCs. (F) Pore size distribution of PSOCs, calculated

from the adsorption isotherms using DFT method.	88
Figure 3-7: Scheme illustrating the <i>R</i> values calculation based on XRD patterns for PSNCs (A) and PSOCs (B).	89
Figure 3-8: (A) Raman spectra of PSNC-2-800, PSNC-3-850 and PSOC specimens. (B-G) Fitted Raman spectra of PSOC, PSNC and CAC.	92
Figure 3-9: (A)-(B) Nitrogen adsorption-desorption isotherms and pore size distributions of CAC.	93
Figure 3-10: (A) XPS survey spectra of PSNC, PSOC and hydrothermal biochar. Magnified views of the C 1s, N 1s and O 1s core level XPS spectra with fits for (B) PSNC-3-850, (C) PSNC-2-800, (D) PSOC, (E) PSOC-A, (F) hydrothermal obtained biochar.	94
Figure 3-11: Half – cell performance of PSNC and CAC, tested between 1.5 - 4.2 V vs. Na metal. (A) Cyclic voltammograms (CVs) of PSNC-3-800. (B) Dependence of anodic and cathodic current (at 2.75 V) on scan rate, indicating the deviation from linear behavior. (C) Galvanostatic discharge/charge profiles of PSNC-3-800, at current densities from 0.8 to 25.6 Ag ⁻¹ . (D) Specific capacitance of PSNC versus current density. (E) Cycling stability of PSNC (tested at 3.2 Ag ⁻¹ for 10,000 cycles), with an insert comparison to state-of-the-art Na and Li cathodes in hybrid devices. (F) Specific capacity vs. current density for PSNC-3-800, comparing with best literature reports for both Na (tested at same voltage window) and Li (tested at the wider 1.5-4.5 V vs. Li/Li ⁺) hybrid cathodes.	96
Figure 3-12: (A-C) Cyclic voltammograms (CVs) of PSNC-3-850, PSNC-2-800, and CAC, respectively. (D) <i>IR</i> drops of PSNC specimens and CAC in half cells.	97
Figure 3-13: Galvanostatic discharge/charge profiles of (A) PSNC-3-800, (B) PSNC-3-850, (C) PSNC-2-800 and (D) CAC, (E) PSNC-3-800 within voltage region of 2.7-4.2 V vs. Na/Na ⁺	98

Figure 3-14: The electrochemical performance of cathode carbon (A) and anode carbon (B) that were derived from the entire peanut shell without separation. 99

Figure 3-15: The electrochemical performance of PSNC-3-800 (A) and PSOC-A (B) with two different electrode mass loadings..... 102

Figure 3-16: The volumetric capacity of PSNC-3-800 (A) and PSOC-A (B). 102

Figure 3-17: Cross section SEM images of (A) PSNC-3-800 (B) CAC, (C) PSOC-A and (D) commercial graphite thin film electrodes with commercial mass loadings.. 103

Figure 3-18: Half - cell performance of PSOC and PSOC-A. (A) CVs of PSOC-A, tested at 0.1 mVs^{-1} . (B) Galvanostatic discharge/charge profiles of PSOC-A, tested at 0.1 Ag^{-1} . (C) (left) XRD spectra for PSOC discharged at 50 mAhg^{-1} to 0.2, 0.1 and 0.001 V. (right) The mean interlayer spacing at several cut-off voltages. (D) Rate performance and CE of PSOC and PSOC-A. (E) Rate capability comparison of PSOC-A with the literature published carbonaceous materials employed as Na anodes. (F) Cycling capacity retention and CE of PSOC and PSOC-A, tested at 3.2 Ag^{-1} for 10,000 cycles..... 104

Figure 3-19: (A) CVs of PSOC specimen at a scan rate of 0.1 mVs^{-1} . (B) Galvanostatic discharge/charge profiles of PSOC at density of 0.1 Ag^{-1} . (C-D) Galvanostatic discharge/charge profiles of PSOC-A (C) and PSOC (D) at current densities of 0.1, 0.2, 0.4 and 0.8 Ag^{-1} . (E) Dependence of anodic and cathodic peak currents on scan rate for PSOC and PSOC-A. (F) Galvanostatic discharge/charge profiles of PSNC-3-800//PSOC-A hybrid Na-ion capacitor at low current densities. 105

Figure 3-20: Electrochemical performance of the hybrid Na-ion capacitors (NICs). (A) Galvanostatic profiles of PSNC-3-800//PSOC-A, the low current density results being shown in **Figure 3-21A**. (B) Ragone plot of PSNC-3-800//PSOC-A at 0°C , 25°C and 65°C . The calculated energy and power densities are based on the total mass (solid) or volume (hollow) of the active electrodes. (C) Ragone plot (active mass normalized) comparing a device based on PSNC//PSOC to CAC//PSOC and to

symmetric PSNC//PSNC and CAC//CAC systems. The PSNC//PSNC and CAC//CAC store charge based on EDLC only. (D) Energy - power density performance comparison (all active mass normalized) of PSNC-3-800//PSOC-A *versus* state-of-the-art reported energy storage systems in literature. (○:Na-ion capacitor, △:Li-ion capacitor, ☆:Aqueous asymmetric EDCL + faradaic capacitor, □: Ionic liquid EDLC capacitor). (E) Cycling stability and coulombic efficiency of PSNC-3-800//PSOC-A, tested at 6.4 Ag^{-1} for 10,000 cycles. (F) PSNC-3-800//PSOC-A devices were tested at 25°C and at 65°C , in both cases undergoing 100,000 cycles at 51.2 Ag^{-1} within a voltage window of 1.5-3.5V. 108

Figure 3-21: (A) Galvanostatic discharge/charge profiles of PSNC-3-800//PSOC-A hybrid Na-ion capacitor at low current densities. (B) Nyquist plots of PSNC-3-800//PSOC-A and CAC//PSOC-A after rate tests. (C) Cycling stability of PSNC-3-800//PSOC-A hybrid ion capacitor at a current density of 100 Ag^{-1} and voltage window of 2.2-3.8V. (D) The cyclability of Na-Na cell..... 109

Figure 3-22: Equivalent electronic circuits used to simulate the EIS data. R_{es} is the sum of resistances of electrical connections in the experiment setup including ionic diffusion resistance in the electrolyte. R_{ct} reflects the charge transfer resistance and Z_{w} (Warburg-type element) represents Na diffusion impedance within carbon materials..... 111

Figure 4-1: As-synthesized microstructures. (A) Indexed XRD pattern of C-SnO₂ and SnO₂ specimens, showing SnO₂ being present as the rutile phase. (B) Nitrogen adsorption-desorption isotherms of C-SnO₂ and SnO₂, and pore size distribution of both specimens (insert). 128

Figure 4-2: (A) Thermogravimetric curves of C-SnO₂ and SnO₂ specimens. (B) XPS survey spectrum of C-SnO₂ and high resolution spectrum of Sn 3d level (insert). 129

Figure 4-3: (A) SEM micrograph revealing the continuous macroscopic

morphology of the nanocomposite. (B) Conventional bright field TEM micrograph and indexed SAD further highlighting the highly interconnected architecture with rutile SnO₂ phase embedded in the carbon. (C) HRTEM micrograph of one such cluster of SnO₂ nanocrystallites within the carbon. (D) HAADF TEM micrograph and EELS elemental maps of Sn, O and C. 130

Figure 4-4: (A) Conventional TEM micrograph of the baseline SnO₂ specimen. (B) HRTEM micrograph of two overlapping SnO₂ particles. 131

Figure 4-5: Electrochemical performance of C-SnO₂ *versus* Li, tested between 0.01 and 3V. (A) Cyclic voltammograms (CVs) at 0.1 mVs⁻¹ for the first 10 cycles, also showing the 2nd CV of the baseline pure carbon. (B) Galvanostatic discharge/charge profiles at 0.5 Ag⁻¹ for cycles 1 – 400. 132

Figure 4-6: Electrochemical performance of SnO₂ *vs.* Li. (A) CVs of SnO₂, tested at 0.1 mVs⁻¹. (B) Galvanostatic discharge/charge profiles of SnO₂, tested at 0.5Ag⁻¹. . 133

Figure 4-7: Derivate curves dQ/dV *vs.* V for C-SnO₂ electrode against Li. 133

Figure 4-8: Electrochemical performance of pure carbon in a half-cell *vs.* Na, Li. (A) CVs of pure carbon electrode for the cycle 1 – 10 *vs.* Na, tested at 0.1 mVs⁻¹. (C) Galvanostatic discharge/charge profiles of pure carbon electrode, tested at 0.08 Ag⁻¹. (B) CVs of pure carbon electrode for the cycle 1 – 10 *vs.* Li, tested at 0.1 mVs⁻¹. (D) Galvanostatic discharge/charge profiles of pure carbon electrode, tested at 0.5 Ag⁻¹ *vs.* Li. 134

Figure 4-9: (A) Rate performance of the baseline pure amorphous carbon electrodes *vs.* Na and *vs.* Li, tested 0.01-3V. (B) Cycling performance of pure carbon electrodes, tested 0.01-3V. (C) Rate performance of the baseline pure amorphous carbon electrodes *vs.* Na and *vs.* Li, tested 0.01-1.5V. (D) Cycling performance of pure carbon electrodes, tested 0.01-1.5V. 135

Figure 4-10: Cycling performance of C-SnO₂ and SnO₂ (0.5 Ag⁻¹), with

corresponding coulombic efficiency (CE) displayed on the right axis.	136
Figure 4-11: Rate performance of C-SnO ₂ and SnO ₂	137
Figure 4-12: Rate capability comparison of C-SnO ₂ with state-of-the-art SnO ₂ (■), Sn (●) based LIBs anodes from literature. All plotted literature capacities were obtained from tests also performed with a 0.01-3V voltage window.	137
Figure 4-13: Electrochemical performance of C-SnO ₂ <i>versus</i> Li, tested between 0.01 and 1.5 V. (A) Cycling performance of C-SnO ₂ (0.5 Ag ⁻¹), with corresponding coulombic efficiency (CE) displayed on the right axis. (B) Rate performance of C-SnO ₂	138
Figure 4-14: The raw galvanostatic discharge/charge profiles	139
Figure 4-15: XRD pattern for the plastic tape on the stainless steel current collector.	140
Figure 4-16: XRD patterns of C-SnO ₂ at various cut-off voltages: first lithiation to 0.5V, first lithiation to 0.01 V, first delithiation to 1V, first delithiation to 1.5V, first delithiation to 3V.	141
Figure 4-17: XPS spectra for Sn 3d levels of C-SnO ₂ at open circuit voltage (prior to testing, used as a baseline), first lithiation to 0.01V, first delithiation to 1V, first delithiation to 1.5V, first delithiation to 3V.	142
Figure 4-18: XPS spectra for C 1s (left) and O 1s (right) of C-SnO ₂ electrodes at the same cut-off voltages.	143
Figure 4-19: Electrochemical performance of C-SnO ₂ and SnO ₂ <i>vs.</i> Na, tested between 0.01 and 3V. (A) CVs of C-SnO ₂ for the cycle 1 - 10, tested at 0.1 mVs ⁻¹ . (B) CVs of electrode at various scan rates from 0.1 to 5 mVs ⁻¹ . The shift of the conversion/dealloying peaks as function of scan rate (inset).	144
Figure 4-20: Electrochemical performance of SnO ₂ <i>versus</i> Na. (A) Cyclic voltammograms (CVs) of SnO ₂ electrode. (B) Galvanostatic discharge/charge profiles of SnO ₂ electrode at current density of 0.08Ag ⁻¹	145

Figure 4-21: Galvanostatic discharge/charge profiles of C-SnO ₂ , tested at 80 mA g ⁻¹ .	146
Figure 4-22: (A) Cycling performance of C-SnO ₂ and SnO ₂ (0.08 Ag ⁻¹), with corresponding CE displayed on the right axis. (B) Cycling capacity retention comparison of C-SnO ₂ with state-of-the-art SnO ₂ based NIBs anodes from literature.	147
Figure 4-23: (A-C) TEM micrographs of C-SnO ₂ with corresponding histograms for the size of the active SnO ₂ nanocrystal assemblies (not individual crystallites). (A) Open circuit potential. (B) Sodiated to 0.01V. (C) Desodiated to 3V.	148
Figure 4-24: (A) Rate performance of C-SnO ₂ and SnO ₂ electrodes. (B) Rate capability comparison of C-SnO ₂ with state-of-the-art SnO ₂ based NIBs anodes from literature.	150
Figure 4-25: Electrochemical performance of C-SnO ₂ versus Na, tested between 0.01 and 1.5 V. (A) Cycling performance (0.08 Ag ⁻¹), with corresponding CE displayed on the right axis. (B) Rate performance.	151
Figure 4-26: (A) XRD patterns of C-SnO ₂ at various cut-off voltages: first sodiation to 0.5V, first sodiation to 0.01 V, first desodiation to 1.5V, first desodiation to 3V.	152
Figure 4-27: (A) XRD patterns of SnO ₂ electrodes at various cut-off voltages: first sodiation to 0.5V, first sodiation to 0.01 V, first desodiation to 1.5V, first desodiation to 3V.	152
Figure 4-28: XPS spectra for Sn 3d levels of C-SnO ₂ at open circuit voltage, first sodiation to 0.01 V, first desodiation to 1.5V, first desodiation to 3V.	154
Figure 4-29: XPS spectra for C 1s (left panel) and O 1s (right panel) levels of C-SnO ₂ electrodes at various cut-off voltages (open circuit voltage, first sodiated to 0.01 V, first desodiated to 1.5V, first desodiated to 3V vs. Na/Na ⁺).	154
Figure 4-30: XPS depth profiling for Sn 3d levels of C-SnO ₂ upon sodiation to 0.01V with Ar etching rate of 5 nm/min.	155
Figure 4-31: HRTEM micrographs of C-SnO ₂ electrodes with corresponding	

indexed FFT patterns corresponding to regions in white squares. (A) first sodiation to 0.5 V. (B,C,D) first sodiation to 0.01 V. The regions indicated by double arrows in (B) (C) are the same region with different magnification. (E) first desodiation to 1.5V, (F) first desodiation to 3V..... 156

1

Introduction

Limited availability of fossil fuels and climate change have greatly threaten the world economy and ecology. Environmentally friendly energy resources with high energy/power densities are under urgent demand. Among various energy resources, electrical energy storage (EES) systems play a crucial role as a successfully commercialized green energy technology. As one of the most important member of EES systems, Li-ion based system, *e.g.* lithium ion battery (LIB), has been tremendously investigated and widely applied in the past several decades.^{1,2,3} Recently, the application of Li ion based energy storage system has expanded from portable electronics to large scale ones, such as electric vehicles, grid storage batteries and even stationary facilities. The rapid expansion of the relevant markets results in an increasing concern about the insufficient Li resource on earth to satisfy the demand.⁴ The shortage of Li supply is expected to largely raise the cost of the final energy storage products.

Sodium is attracting significant attention as a potential alternative to lithium recently. Sodium shares similar chemical characteristics in many respects as lithium, and the basic electrochemical principles of the Na ion and Li ion based energy storage systems are almost identical. However, sodium has obvious cost advantage due to its inexhaustible resource on earth, especially for large scale applications where large amounts of alkali are needed. In addition to the economic factor for industries, for academia there will be significant unexplored opportunities in research, because both the host materials and the relevant charge storage mechanism

for Na have been explored considerably less than that of for Li.

However, there are also substantial new challenges of developing Na ion based systems. Firstly, Na ion is 39.5% larger (106 vs. 76 pm) and 231% heavier (22.98 vs. 6.94 gmol⁻¹) than that of Li ion. Since most battery reactions involve ion diffusion processes (*e.g.* ion interaction, phase transformation, etc.) within electrode material bulk, the reaction kinetics in Na ion based systems are expected to be much slower. Therefore, the Na ion based devices are expected to be inferior to Li ones in terms of reversible capacity, cycling retention and rate capability, etc. Moreover, the standard potential difference between Na/Na⁺ and Li/Li⁺ is 0.3V, which may result in a narrower voltage window and lower energy densities for the final devices. These are the main obstacles in developing Na ion based energy storage systems at present, which are also the critical issues to be overcome in our works.

1.1 Li/Na ion batteries

1.1.1 The principle of electrochemical process

Since Na ion batteries (NIBs) share the same electrochemical principles as Li ion batteries, we use LIBs as an example elaborating the principles of electrochemical process.

A rechargeable Li ion battery acts as a galvanic cell and an electrolytic cell during discharge and charge processes, respectively. Oxidation and reduction reactions occur in the cathode and anode respectively during charging process, and vice versa upon discharge. During discharging process, the anode oxidizes and gives off electrons. The cathode is reduced by accepting the electrons. In case of charging process, electrons are pumped from the cathode to the anode by the external power supply, making a potential difference between the two for further discharge. Electrons travel through the external circuit, to balance the battery electronically, cations (Li⁺/Na⁺) transfer between electrodes in the internal circuit.^{5,6}

Figure 1-1 illustrates the schematic charging/discharging processes of a typical Li ion battery with graphite and LiCoO₂ as anode and cathode, respectively.⁷ The electrolyte applied was EC organic solvent with LiPF₆ lithium salt. Li⁺ ions can reversibly intercalate between the parallel graphene layers of graphite (LiC₆), which occurs around 0.1V vs. Li/Li⁺. The cathode reaction is $\text{LiCoO}_2 = 1/2 \text{Li}^+ + 1/2\text{e}^- + \text{Li}_{0.5}\text{CoO}_2$, with a standard electrode potential of 4.35V vs. Li/Li⁺.⁸ Upon charging, Li⁺ ions remove from the cathode into the electrolyte and then intercalate into graphite. Upon discharging, Li⁺ ions extract from graphite, dissolve into electrolyte and further intercalate into LiCoO₂ cathode.⁹

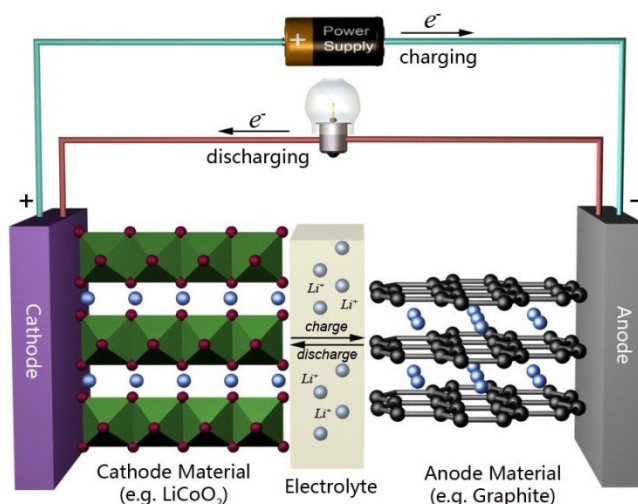


Figure 1-1: Schematic diagram demonstrating the electrons and Li⁺ ions transfer during charge and discharge processes. Adapted from ref 7 with permission from the Royal Society of Chemistry, Copyright 2011.

1.1.2 Thermodynamics

The discharging process is thermodynamically spontaneous based on the voltage difference between the cathode and anode. The driving force for each electrode reaction is the formation Gibbs free energy (ΔG_f°) difference between the products and the reactants which follows as:

$$\Delta G_{\text{rxn}}^0 = \sum \Delta G_f^0 (\text{products}) - \sum \Delta G_f^0 (\text{reactants}) \quad (1)$$

According to the Nernst equation, this chemical driving force is equivalent to an

electrostatic driving force ($-nEF$) where, E is the standard potential of the electrode, n is the stoichiometric number of electrons involved in the reaction and F is the Faraday's constant. Therefore, the standard potential of the electrode equals to:

$$E^0 = \frac{-\Delta G_{\text{rxn}}^0}{nF} \quad (2)$$

The standard open circuit voltage of a lithium ion battery equals to the standard potential difference between anode and cathode:

$$E_{\text{Cell}}^0 = E_{\text{cathode}}^0 - E_{\text{anode}}^0 \quad (3)$$

From another point of view, based on the reversible Li^+ ions transport between the cathode and anode, a lithium ion battery can also be considered as a concentration cell, with a full cell voltage proportional to the difference in chemical potential of Li^+ ions between each electrode. Therefore, the voltage of an open circuit battery equals to:

$$V_{\text{oc}} = \frac{-[\mu_{\text{Li}}^{\text{cathode}} - \mu_{\text{Li}}^{\text{anode}}]}{nF} \quad (4)$$

Where, $\mu_{\text{Li}}^{(\text{cathode})}$ and $\mu_{\text{Li}}^{(\text{anode})}$ are the chemical potentials of Li^+ ions in the cathode and anode, respectively. When the battery is fully charged, $\mu_{\text{Li}}^{(\text{cathode})} < \mu_{\text{Li}}^{(\text{anode})}$ and V_{oc} is positive. Upon discharge, Li^+ ions transfer from the higher chemical potential region in the anode to the lower chemical potential region in the cathode. The chemical potential change of Li^+ ions in each electrode can be expressed by the Nernst equation:

$$\mu_i = \mu_i^0 + RT \ln a_i \quad (5)$$

Where, μ_i^0 is the chemical potential of species i (*i.e.* Li^+ ions) in its standard state, a_i is the activity of species, T is the temperature and R is the ideal gas constant. Because the activity of a species is its effective concentration, the Nernst equation indicates that both the chemical potential and the voltage change as a function of the amount of Li^+ ions in each electrode. Typically the potential change is monitored over time.

These are the thermodynamic principles of lithium ion battery. However, for batteries in a closed circuit, they will exhibit voltage loss resulting from certain kinetic factors. Therefore, there is always overpotential between the measured voltage

and the equilibrium voltage of a battery decided by thermodynamic principles.

1.1.3 Kinetics

If there is a net current allowed to flow in a closed circuit battery, the potentials (V) of both anode and cathode will shift away from their equilibrium (open circuit) values (V_{oc}). This potential change is named overpotential/polarization (η) given by: $\eta = V_{oc} - V$.

The overpotential resulting from circuit resistance, activation energy barrier and ion concentration all exist in Li ion batteries. Moreover, it should be noted that the electrode reactions in batteries are always bulk reactions (*e.g.* phase transformation, intercalation/extraction etc.) combining with charge transfer processes. Therefore, the kinetics of Li ion diffusion within the material bulks is also a significant deciding factor for the total voltage loss of the battery.

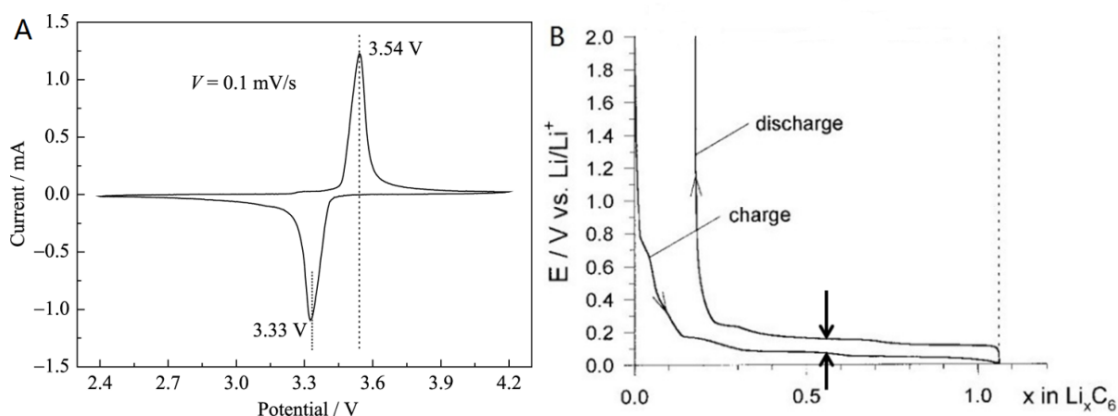


Figure 1-2: (A) Cyclic voltammograms (CV) of LiFePO₄ electrode. Adapted from ref 10 with permission from the Royal Society of Chemistry, Copyright 2011. (B) Galvanostatic discharge/charge profiles of graphite electrode. Adapted from ref 11 with permission from Wiley-VCH, Copyright 1998.

Figure 1-2 displayed the overpotential of two classic LIB electrodes (*i.e.* LiFePO₄ and graphite). The standard potential of LiFePO₄ electrode is located at 3.45 V. In the cathodic scan, the redox peak is located at 3.33V, resulting in an overpotential (η) equaling to -0.12V. In the anodic scan, the redox peak is located at 3.54V, resulting in an overpotential (η) equaling to 0.09V.¹⁰ These values agree

with the principle that the cathodic/anodic overpotential should be positive/negative, respectively. As shown in **Figure 1-2B**, there is also a voltage difference between the discharging and charging processes for graphite electrode as a result of kinetic overpotential.¹¹

The overpotential is a significant issue for the practical application of lithium ion batteries, because the voltage loss can largely reduce the energy densities of the batteries. People have done tremendous works on developing advanced electrode materials in order to improve the kinetics of electrode reaction and diminish the voltage loss.

1.2 Carbonaceous materials as Na ion battery anodes

Currently, the lack of appropriate electrode material has seriously impeded the progress of Na ion batteries. As a successfully applied electrode material for LIBs, carbonaceous material has been studied for Na storage with a top priority.

Unfortunately, graphite, the most successfully commercialized anode material for LIBs, displays negligible capacity against Na due to the much larger ion diameter of Na⁺ (**Figure 1-3A**).^{12,13} Hard carbon with imperfect graphitic structure and large graphene interlayers instead, turns out to be a usable anode. In the earlier studies, some hard carbons have exhibited measurable capacity for Na storage.¹⁴ As shown in **Figure 1-3B**, the D. Billaud's group reported a 209mAhg⁻¹ capacity of carbon fibers (with Brunauer-Emmett-Teller (BET) surface area of ~1 m²g⁻¹, density of ~2 g/cm³).¹⁵ Dahn *et al.* reported that hard carbon derived from pyrolyzed glucose (density of ~1.5 g/cm³) could achieve an initial reversible capacity 300mAhg⁻¹,^{16,17} as shown in **Figure 1-3C**. In L. Tirado *et al.*'s study, the carbon microspheres (with BET surface area of 3 m²g⁻¹) derived from resorcinol-formaldehyde displayed a 285mAhg⁻¹ reversible capacity.¹⁸ In these studies, the majority Na storage capacity concentrated at the low voltage region (*i.e.*

0-0.2V vs. Na/Na⁺), as shown in **Figure 1-3 (C-D)**. Analogous to graphite for LIBs, this feature is highly desirable for achieving wide voltage windows and high energy densities of the final batteries.

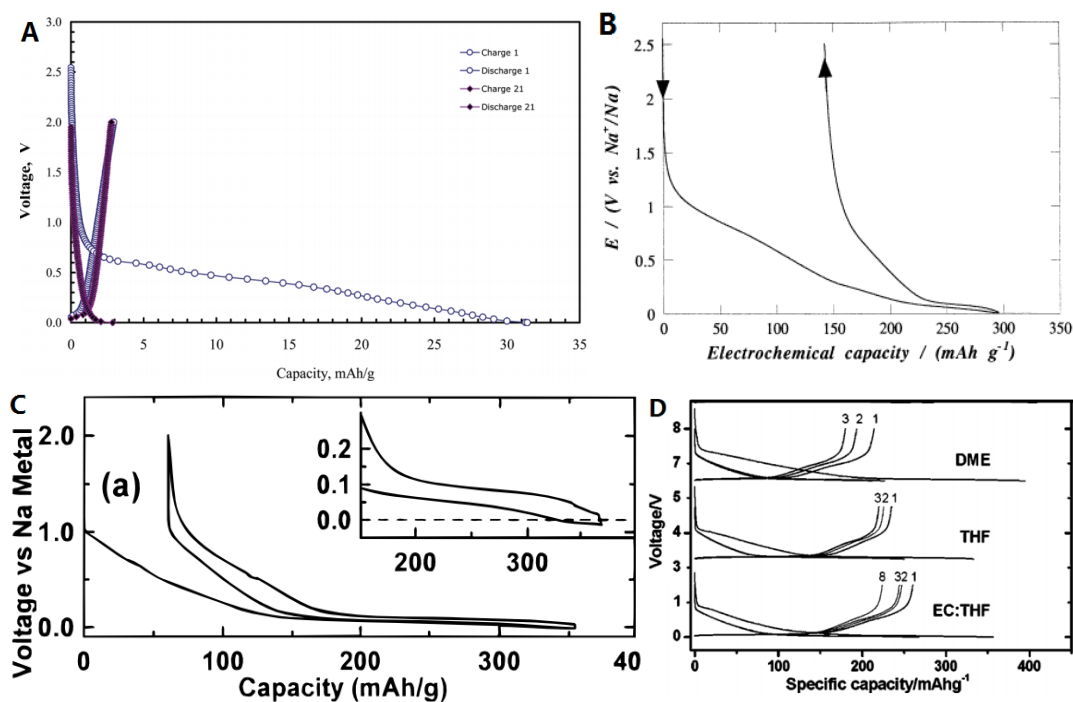


Figure 1-3: (A) Potential profiles of Na/graphite cell showing the lack of electrochemical activity of graphite against Na. Adapted from ref 12 with permission from Wiley-VCH, Copyright 2013. (B) Potential profiles of the first charge/discharge cycle for saccharose-coke derived carbon in EC/NaClO₄ electrolyte at 7mA g⁻¹. Adapted from ref 15 with permission from the Elsevier, Copyright 2002. (C) Sodium potential profiles of glucose pyrolyzed to 1150°C. Adapted from ref 16 with permission from the Electrochemical Society, Copyright 2000. (D) Voltage/capacity plots of carbon aerogel microspheres in sodium cells, 1 M NaClO₄ dissolved in DME, THF, and EC:THF as electrolytes. Adapted from ref 18 with permission from the Electrochemical Society, Copyright 2005.

However, these carbons still have significant issues for practical utilization. Firstly, the cycling lives (*i.e.* cyclability) were limited below 50 cycles, which were too short for practical use. Secondly, the capacities severely decayed under relatively high current densities (>1C) due to the extremely slow kinetics of Na ion diffusion.

In later studies, people tried to improve the cyclability and rate performance of the carbon anodes by introducing porous structures in carbons. As shown in **Figure**

1-4 (A-B), Wenzel *et al.* firstly generated macro-porosity in carbon through a nanocasting process using silica monolith as a hard template (with BET surface area of $346 \text{ m}^2\text{g}^{-1}$ and pore volume of $0.79\text{cm}^3\text{g}^{-1}$). The large surface area and pore volume have greatly improved the rate performance of the carbon anode (*ca.* 150mAhg^{-1} at current density of 0.2C).¹⁹ As shown in **Figure 1-4C**, J. Maier's group prepared hollow carbon nanospheres (with BET surface area of $410\text{m}^2\text{g}^{-1}$) from D-Glucose using poly(styrene) as a sacrificing template. Considerable specific capacities were maintained under high current densities (*i.e.* $75, 50 \text{mAhg}^{-1}$ at $5, 10 \text{Ag}^{-1}$), as shown in **Figure 1-4D**.²⁰ In the following studies, people tried to generate porosity in carbons by the activation methods in place of the high cost sacrificial template methods. Various pore-generating reagents were used during the synthesis in order to substantially increase the surface area and pore volume of the carbons. For instance, in H. Wang *et al.*'s study, nitrogen-doped carbon sheets with BET surface area of $1477 \text{ m}^2\text{g}^{-1}$ and pore volume of $2.02 \text{ cm}^3\text{g}^{-1}$ were prepared using KOH as the activation reagent.²¹

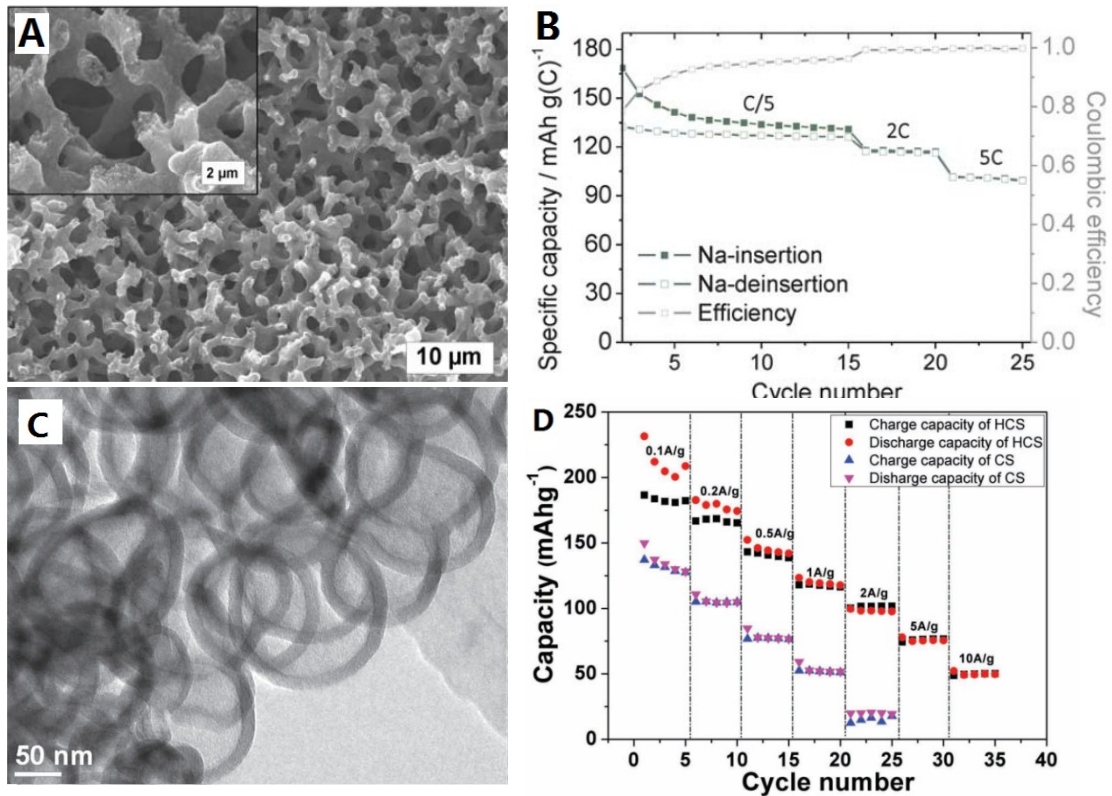


Figure 1-4: (A) SEM image of the interconnected macroporous structure of the

templated carbon. (B) Rate capability of the templated carbon. Adapted from ref 19 with permission from the Royal Society of Chemistry, Copyright 2011. (C) TEM image of the hollow carbon nanospheres (HCS). (D) Rate performance of HCS and carbon spheres (CS). Adapted from ref 20 with permission from Wiley-VCH, Copyright 2012.

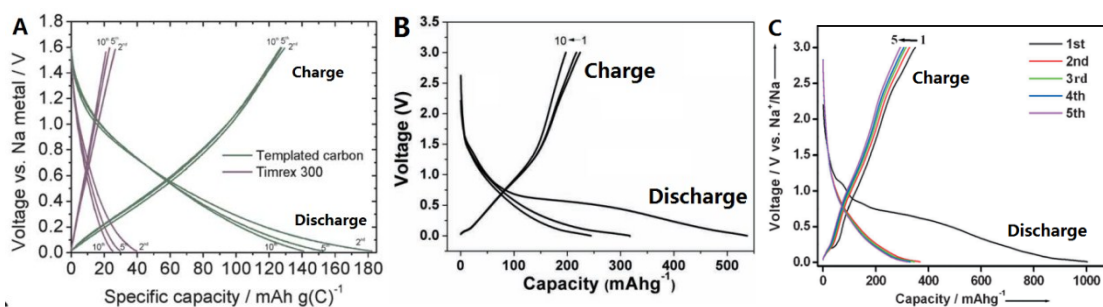


Figure 1-5: (A) Charge/discharge profiles of the templated carbon and commercial Timrex 300. Adapted from ref 19 with permission from the Royal Society of Chemistry, Copyright 2011. (B) Galvanostatic charge/discharge profiles of hollow carbon nanospheres at 50 mA g⁻¹. Adapted from ref 20 with permission from Wiley-VCH, Copyright 2012. (C) Charge/discharge profiles of the chemically activated polypyrrole-functionalized graphene sheets at a current density of 50 mA g⁻¹. Adapted from ref 21 with permission from Wiley-VCH, Copyright 2013.

Based on these studies, it can be concluded that the introduced porosities in carbon indeed have positive effects on the rate capabilities. However, they also created some other issues. Firstly, the capacity voltages of these anodes were substantially shifted to the high voltage regions (as shown in **Figure 1-5**). This is highly undesirable, because it could largely narrow the voltage window of a full battery. Secondly, these anodes always exhibited severe hysteresis between the discharging and charging processes. For instance, the voltages of desodiation were always over 1 V higher than that of sodiation, resulting in a large proportion of charge capacity above 2.5 V vs. Na/Na⁺. These issues greatly declined the potential of these carbons for practical application as anodes.

Basically the causes of the high capacity voltage and hysteresis were unclear by far. The uniform distribution of capacity as function of voltage in the galvanostatic profile indicates that the carbon has Na storage sites with a distribution of energies. This energy distribution should mainly result from the graphitic structures of the

carbons, which are dominantly decided by the precursor tissue, synthesis procedure and activation process.

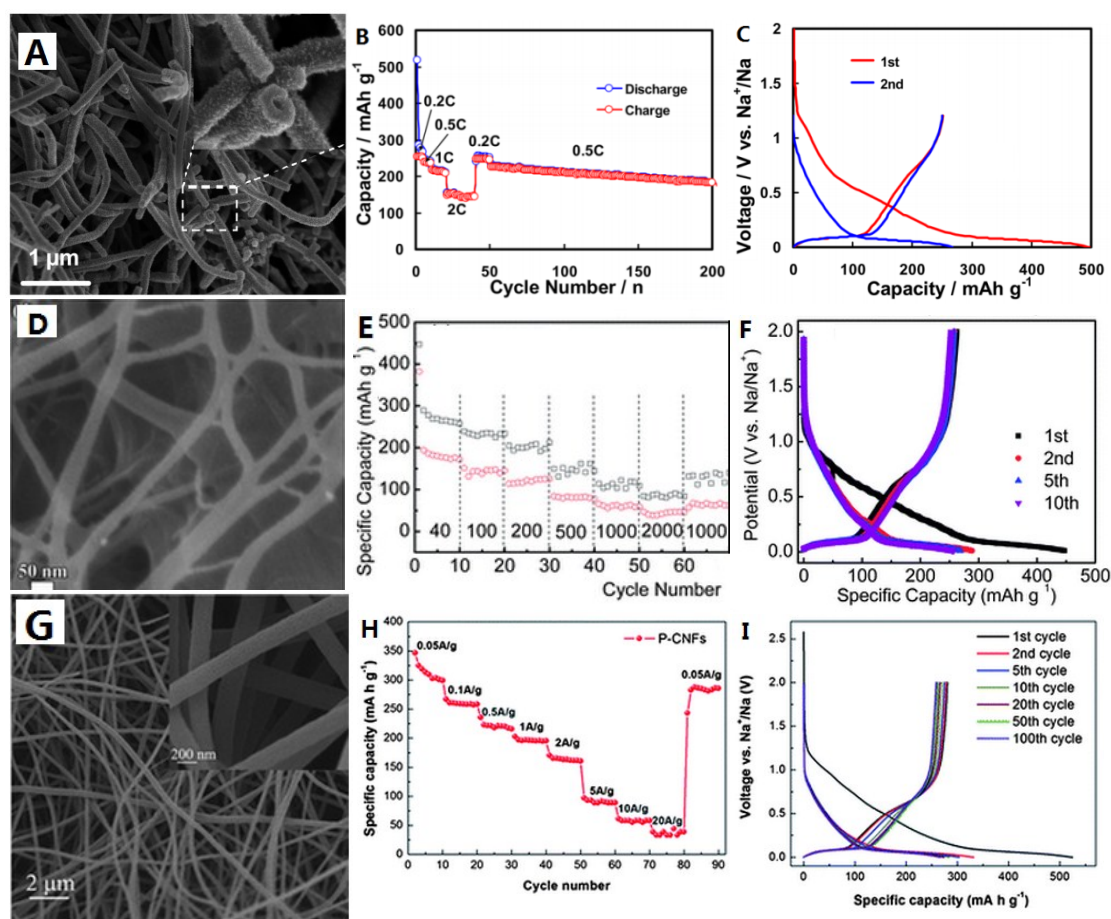


Figure 1-6: (A) SEM image of the hollow polyaniline nanowires (PANI-HNWs). (B) Capacities of PANI-HNWs derived carbon (HCNW) electrode as a function of cycle number at different current densities. (C) Charge/discharge profiles of HCNW electrode between 0 and 1.2V at a current density of 50 mA g^{-1} . Adapted from ref 22 with permission from the American Chemical Society, Copyright 2012. (D) FESEM image of the cellulose nanofiber derived carbons (CNFs). (E) Rate performance of CNFs. (F) Charge/discharge profiles of CNFs at 40 mA g^{-1} . Adapted from ref 23 with permission from the Royal Society of Chemistry, Copyright 2014. (G) FESEM image of electrospun PAN-F127 derived carbon nanofibers (P-CNFs). (H) Discharge capacity of P-CNFs electrode at various current densities. (I) Voltage profiles of P-CNFs electrode at a current density of 50 mA g^{-1} . Adapted from ref 24 with permission from the Royal Society of Chemistry, Copyright 2013.

Afterwards, researchers started to try new carbon synthesis strategies in order to achieve a combination of practical discharge/charge properties and improved rate capabilities. For instance, people prepared carbons with various nano-scale

architectures (*e.g.* hollow nanowires, nanofibers, nanosheets, *etc*) without any extra activation process. The nano-scale architectures can largely reduce the Na bulk diffusion distance necessary for sodiation/desodiation, thus have obvious positive effects on the rate performances of these carbon anodes. As shown in **Figure 1-6(A-B)**, Cao *et al.* prepared hollow carbon nanowires by directly carbonizing the polyaniline precursor.²² The carbon anode displayed a considerable capacity at 2C. Li *et al.* prepared carbon nanofibers through an electrospinning plus carbonize procedure (**Figure 1-6D**).²³ Benefiting from the nano-scale diameter ($\sim 200\text{nm}$) of the fibers, the anode displayed a combination of high specific capacity and excellent rate performance (**Figure 1-6E**). As shown in **Figure 1-6(G-H)**, Luo *et al.* prepared carbon nanofibers $\sim 50\text{nm}$ in diameter by directly carbonizing the cellulose nanofibers,²⁴ which exhibited excellent capacity maintenance at current density as high as 20A/g. In addition to the competitive rate performances, it should also be noted that the galvanostatic discharge/charge profiles of these carbon anodes are highly practical. As shown in **Figure 1-6(C,F,I)**, the majorities of Na storage capacities were obtained at low voltage regions (below 0.2V *vs.* Na/Na⁺), and the hysteresis between discharge/charge processes were negligible. One common ground in synthesis strategy among these carbons is the absence of extra porosity generation process. Both the surface area and pore volume of these carbons were much lower than that of the highly porous carbons abovementioned. So the comparable rate performances should benefit from the special nano-scale architectures of the carbons.

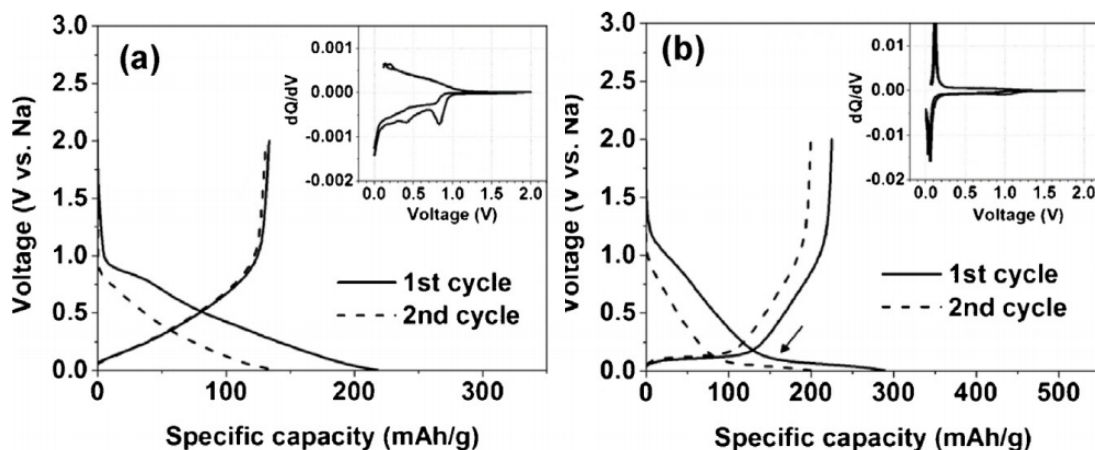


Figure 1-7: Voltage profiles and dQ/dV plots (inserts) of (a) Na/sphere carbon cell and (b) Na/hard carbon cell cycled between 0.001-2V at 15mA g^{-1} . Adapted from ref 25 with permission from the Elsevier, Copyright 2014.

Unlike other anodes (*e.g.* alloying, conversion based ones) having standard galvanostatic voltage profiles, the galvanostatic discharge/charge profiles of carbon anodes can always be substantially different in shapes. **Figure 1-7** shows a typical example of this phenomenon.²⁵ Although the two carbons were derived from the same precursor, they still exhibited largely different voltage profiles.

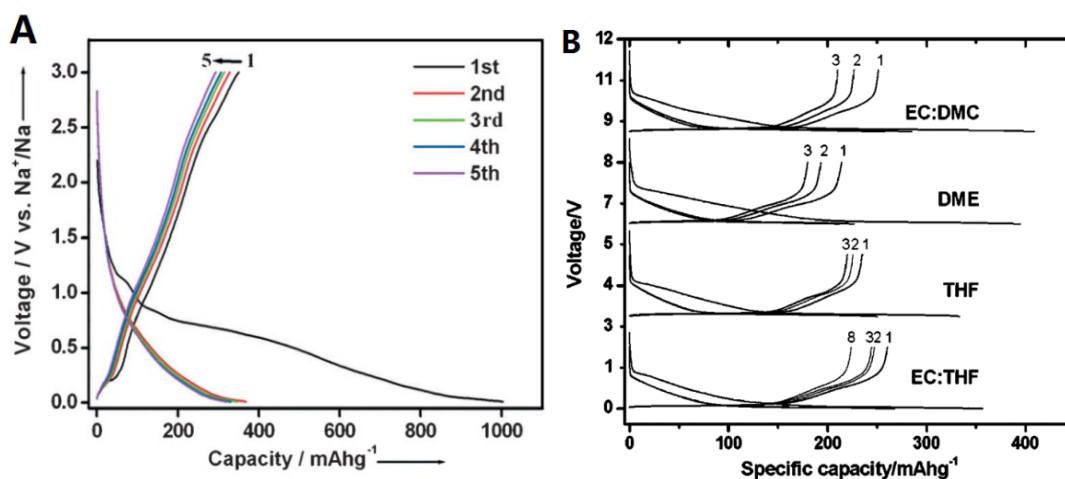


Figure 1-8: (A) Charge/discharge profiles of a chemically activated carbon with a surface area of $1477\text{ m}^2\text{g}^{-1}$. Adapted from ref 21 with permission from Wiley-VCH, Copyright 2013. (B) Charge/discharge profiles of an unactivated carbon with a surface area of $3\text{ m}^2\text{g}^{-1}$. Adapted from ref 18 with permission from the Electrochemical Society, Copyright 2005.

In the early 20th, Dahn *et al.* have proposed the first hypothesis elaborating the

correlation between the voltage profile of carbon anode and the microstructure of carbon.¹⁶ They claimed that the sloping part of the potential profile results from the Na insertion between parallel or nearly parallel graphene layers, and the low-voltage plateau part results from the insertion of the Na ions into nanopores (named “pore-filling”). This hypothesis has perfectly explained their experimental results. However, many following results went beyond this hypothesis. Firstly, it was always observed that some highly porous carbons displayed negligible “pore-filling” plateau capacities. As an example shown in **Figure 1-8A**, a carbon anode with pore volume of $2.02\text{cm}^3\text{g}^{-1}$ obtained only $\sim 70\text{mAhg}^{-1}$ plateau capacity. On the contrary, some carbons almost free of pores have shown large plateau capacities. As an example shown in **Figure 1-8B**, the plateau capacity of the carbon anode is as high as 200mAhg^{-1} , but the total pore volume of the carbon is negligible.

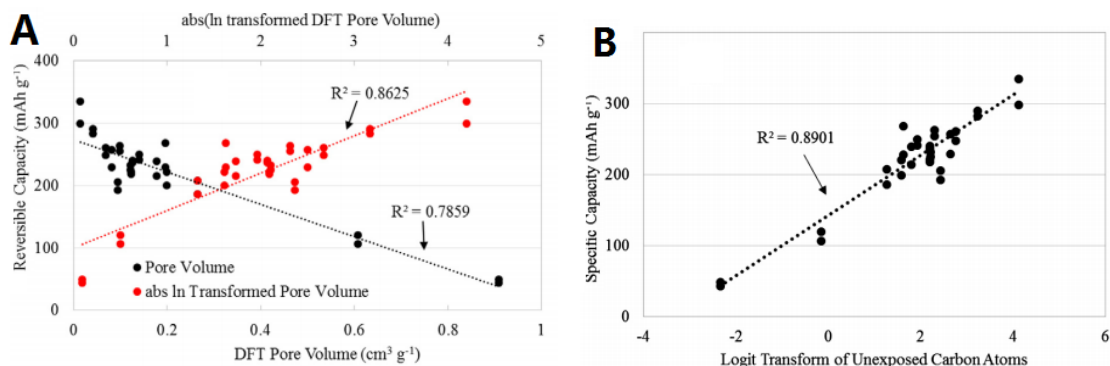


Figure 1-9: (A) Linear and natural logarithm transformed models plotting the reversible capacity in the 1st cycle as a function of DFT specific pore volume of carbon specimen. (B) Reversible capacity vs. logit transform of the percentage of the unexposed carbon atoms. Adapted from ref 26 with permission from the Elsevier, Copyright 2014.

With the increasing accumulation of experimental data, people discovered that the plateau capacity always has a close connection with some graphitic structure parameters of the carbon instead of the pore volume. Bommier *et al.* have proposed a negative correlation between the measurable pore volume and the reversible capacities of carbons, based on a vast amount of data points shown in **Figure 1-9**.²⁶ Meanwhile, they also proposed a positive correlation between the reversible

capacity and the percentage of the unexposed atoms in carbon.

In sum, due to the complexity of carbon materials, there is still controversy over Na storage mechanism in carbon by far. Nevertheless, all these ongoing studies can provide important guidance for developing better carbons for Na storage.

1.3 Sn/SnO₂ based materials as Na ion battery anodes

1.3.1 Sn-based NIB anodes

Along with the development of energy storage devices, there is an increasing demand of small volume devices. In certain conditions, the volumetric property is the only factor that really matters for the real devices. Therefore, it is highly desirable for electrode materials having high volumetric capacities for Li/Na storage.

Table 1-1: Comparison of properties of various LIB and NIB anodes.

Material	Density (gcm ⁻³)	Theoretical gravimetric capacity (mAhg ⁻¹)	Theoretical volumetric capacity (mAhcm ⁻³)	Volume change (%)	Lithiation/Sodiation Potential vs. Li/Li ⁺ /Na/Na ⁺ (V)
Lithiation					
Graphite	2.25	372	837	10	0.05
Li	0.53	3862	2062	100	0
Si	2.33	3590	8365	280	0.37
Sn	7.29	994	7246	260	0.03,0.3,0.6
Sb	6.7	660	4422	200	~0.8
Sodiation					
Hard carbons	~1.5	~200-300	~300-450	-- ^a	-- ^a
Na	0.97	1165	1130	100	0
Sn	7.29	847	6174	420	0.03,0.08,0.13
Sb	6.7	660	4422	290	0.5
Ge	5.35	369	1974	126	0.15
P	2.7	2596	7009	491	~0.2

^a There were different values for various carbons.

As shown in **Table 1-1**, graphite has theoretical volumetric capacity of 837 mAhcm⁻³ as a LIBs anode. For most carbons as NIBs anodes, the volumetric capacities are lower than 450 mAhcm⁻³. These values are apparently not large enough to meet the increasing demand of high volumetric capacities nowadays. Element materials such as Si, Sn, Sb, Ge, Pb, etc. could also be Li/Na ions host materials because they can electrochemically alloy with Li and Na metals. Due to the large densities, these anodes have theoretical volumetric capacities much higher than that of graphite and hard carbons.^{27,28,29,30,31,32,33} Therefore, they could be highly competitive anode candidates for small volume devices.

Among these alloying based anodes, Sn is the most promising one both for Li and Na based systems. Especially for Na, the theoretical volumetric capacity of Sn is as high as 6174 mAhcm⁻³. This is very attractive for NIBs, which are significantly inferior to LIBs in volumetric density. Actually Sn should be even more important for NIBs if we consider the very limited choices of NIBs anodes available.

The Na storage mechanism of Sn anode was firstly investigated by applying Sn thin film as working electrode in a half-cell configuration.³⁴ **Figure 1-10A** shows the voltage profiles of the first sodiation/desodiation processes overlaying on a Sn-Na phase diagram. Basically, during the sodiation process, there are four distinct plateaus at 0.46 V, 0.2V, 0.08V and 0.03V. These four plateaus correspond to the formation of intermetallic phases of NaSn₅, NaSn, Na₉Sn₄, Na₁₅Sn₄, respectively. **Figure 1-10B** displays the calculated voltage profile (red dashed line) by density functional theory (DFT). Resulting from certain kinetic factors, the sodiation (cathodic) profile locates below the calculated one, indicating a negative overpotential. On the contrary, the desodiation (anodic) profile locates above the calculated one, which indicates a positive overpotential.

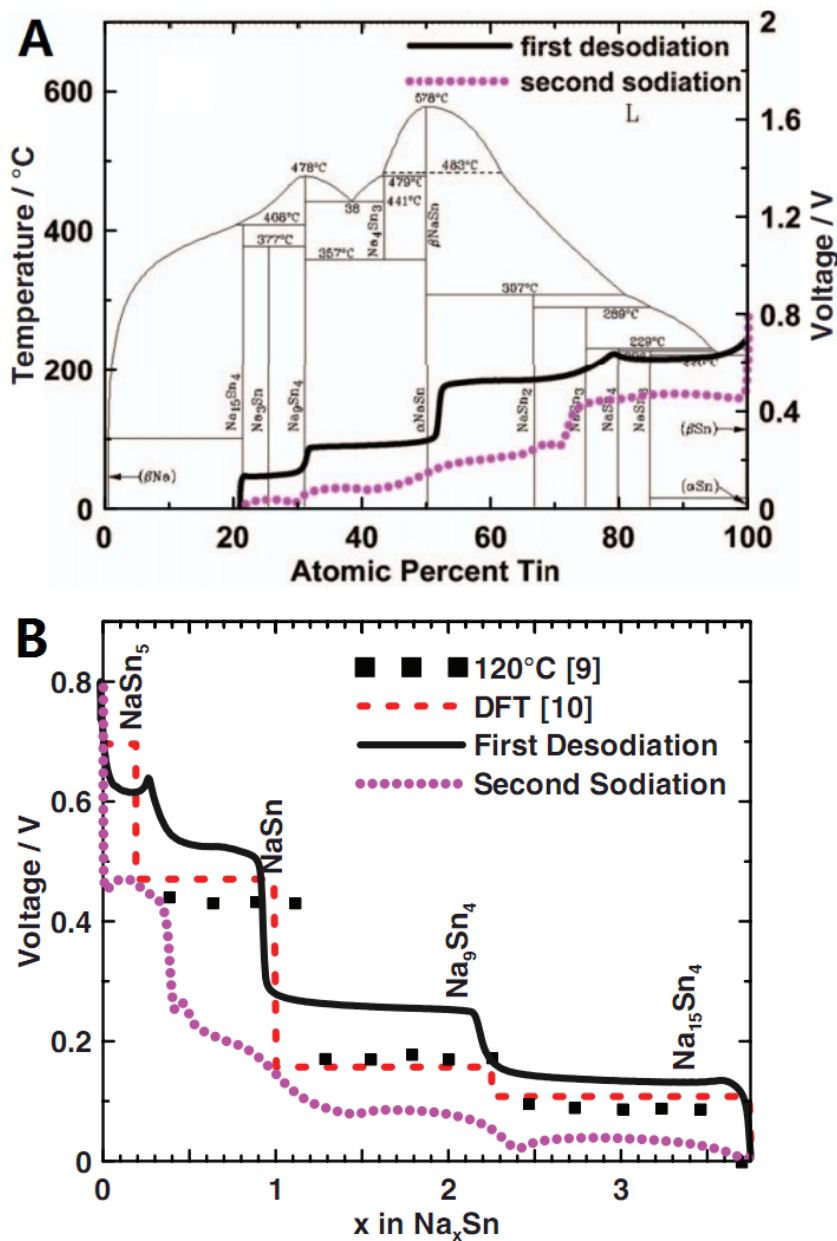


Figure 1-10: (A) Voltage profiles of the first desodiation and second sodiation of a sputtered Sn film superimposed on the Na-Sn binary phase diagram. (B) Voltage profiles of the first desodiation and second sodiation of sputtered Sn film superimposed on the predicted DFT voltage profile. Adapted from ref 34 with permission from the Electrochemical Society, Copyright 2012.

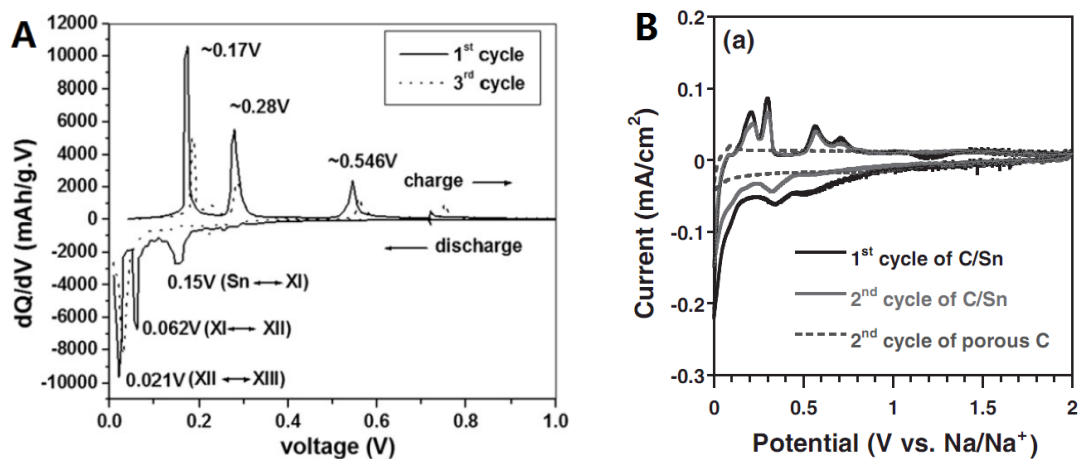


Figure 1-11: (A) Differential capacity vs. cell potential curves of pure microcrystalline Sn obtained after 1st cycle at $\sim 50\text{mA g}^{-1}$ in the potential window of 0.01-1.2V. Adapted from ref 35 with permission from the Elsevier, Copyright 2013. (B) Cyclic voltammograms of mesoporous C/Sn composite anodes in Sn-Na batteries at a scan rate of 0.05 mVs^{-1} . Adapted from ref 36 with permission from Wiley-VCH, Copyright 2013.

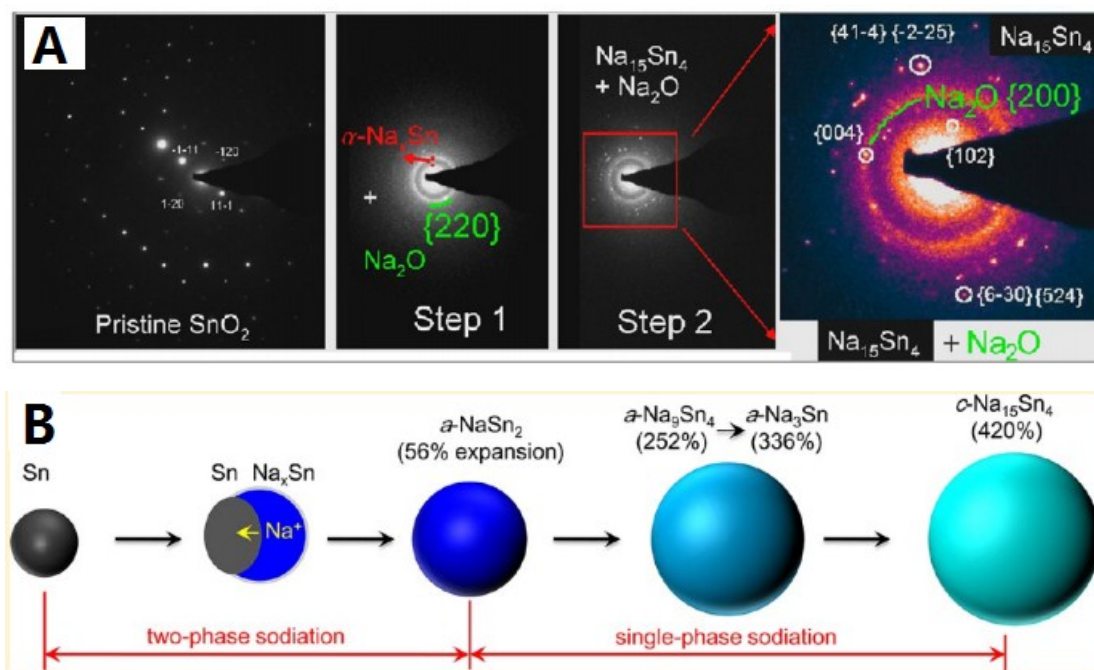


Figure 1-12: (A) Electron diffraction pattern evolution as sodiation proceeds. Adapted from ref 37 with permission from the American Chemical Society, Copyright 2013. (B) Schematic illustration of the structure evolution of Sn nano particles (NPs) during the sodiation. Adapted from ref 39 with permission from the American Chemical Society, Copyright 2012.

Besides galvanostatic profiles, derivative curves (*i.e.* dQ/dV vs. V) and cyclic voltammograms (CV) curves can also indicate the voltages at which the

intermetallic phases form. **Figure 1-11A** shows a typical derivative curve of the Sn thin film anode,³⁵ and **Figure 1-11B** shows a CV curve of Sn/C composite anode against Na³⁶. The positions of the redox peaks on both the derivative and CV curves agree well with the plateau voltages in the galvanostatic profiles shown in **Figure 1-10**.

People have also utilized more advanced characterization methods (*e.g. in situ* transmission electron microscopy (TEM), etc.) to investigate the phase transformation and microstructure evolution of Sn anode during sodiation/desodiation processes.³⁷ As shown in **Figure 1-12A**, it was observed that all the intermediate phases (NaSn₅, NaSn, Na₉Sn₄) were amorphous, which could be named α -Na_xSn. After full sodiation, the final Na₁₅Sn₄ phase displayed a crystalline texture interspersing among an amorphous Na₂O matrix. Based on the stoichiometric ratio of the equilibrium Na₁₅Sn₄ phase, the theoretical capacity of Sn anode could be calculated as 847 mAhg⁻¹.

Table 1-2: Characteristics of lithium and sodium.

Parameter	Lithium	Sodium
Ion radius (Å)	0.76	1.06
Atomic weight (g/mol)	6.9	23
E° (V vs. Li/Li ⁺)	0	0.3

In fact, people are greatly challenged when they develop practical Sn anodes for batteries, especially for NIBs. The most dominant challenge should be the huge volume change of Sn anode during the alloying reaction. This repeated volume change can easily result in mechanical and structural disintegration of the active material in the forms of cracking and fracturing. For NIBs, this issue is expected to be even more severe due to the much larger Na ion (as shown in **Table 1-2**).³⁸ As shown in **Figure 1-12B**, a Sn nano particle will display ~ 420% volume expansion

after sodiating to the final $\text{Na}_{15}\text{Sn}_4$ phase.³⁹ The capacity of Sn anode decays rapidly as a result of this huge volume change. Another challenge is the slow kinetics of ion diffusion within Sn bulk, especially for Na with much larger mass/size. Based on either DFT calculation³⁷ or experimental observation^{36,40}, the propagation of Na ions within Sn bulk could be more than one magnitude slower than that of Li ions.

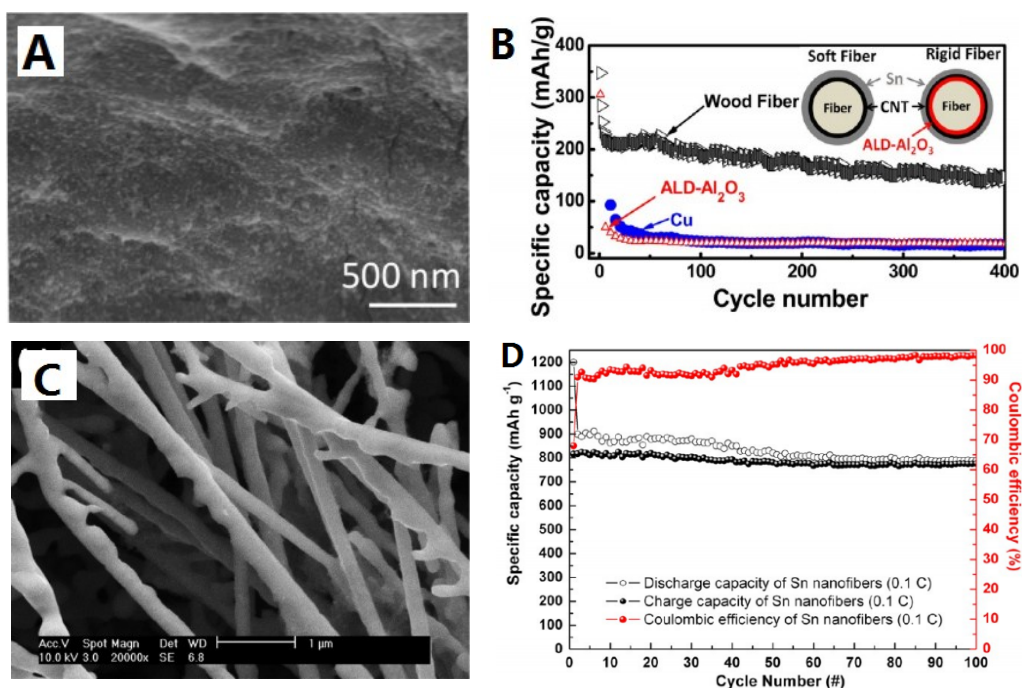


Figure 1-13: (A) SEM image of the Sn thin film deposited on wood fibers (Sn@WF). (B) Cycling performance of Sn@WF, the Al₂O₃ coated fiber and the Cu current collector baseline. Adapted from ref 41 with permission from the American Chemical Society, Copyright 2013. (C) SEM image of cathodic electrodeposition synthesized Sn nanofibers. (D) Cycle performance and Coulombic efficiency of the Sn nanofibers over a voltage range of 0.001 to 0.65 V vs. Na/Na⁺. Adapted from ref 42 with permission from the American Chemical Society, Copyright 2014.

Researchers therefore tried to prepare advanced Sn-based composites to solve these two issues. For instance, as shown in **Figure 1-13A**, H. Zhu *et al.* used a soft substrate (*i.e.* natural wood fiber) to release the mechanical stress of Sn film.⁴¹ The thin Sn@WF composite anode displayed good cycling stability upon 400 repeated cycles (**Figure 1-13B**). D. Nam *et al.* prepared Sn nanofibers with ~370 nm in diameter as NIBs anode (**Figure 1-13C**).⁴² Benefiting from the 1D nano architecture which was better at accommodating large strain and stress, this Sn

nanofibers anode displayed largely improved cyclability than bulk Sn anode.

1.3.2 SnO₂-based NIB anodes

In addition to Sn metal, the oxides of Sn (*e.g.* SnO₂, SnO^{43,44}) can also be Li/Na ion host materials. Researchers discovered that the oxides could be reduced by Li/Na into Sn metal, which can further alloy with Li/Na analogous to Sn anode.^{37,45}

Due to the advantages of SnO₂ including low cost, environmental compatibility and safe work voltage, SnO₂-based materials have been tremendously studied as anodes for LIBs.^{46,47,48} It is commonly accepted that the reversible conversion reaction between Li and SnO₂ also contribute to the overall capacity of the SnO₂ based anode. Combining the alloying reaction ($\text{Sn} + 4.4\text{Li}^+ + 4.4\text{e}^- \leftrightarrow \text{Li}_{4.4}\text{Sn}$) and conversion reaction ($\text{SnO}_2 + 4\text{Li} + 4\text{e}^- \leftrightarrow \text{Sn} + \text{Li}_2\text{O}$), SnO₂ anode can exhibit a theoretical capacity of 1494 mAhg⁻¹ (*i.e.* 8.4 equivalent of lithium per SnO₂). Unfortunately, the poor electronic conductivity of SnO₂ can greatly decrease the activity of conversion reaction. The reversibility of the conversion reaction therefore largely depends on the structures of SnO₂-based materials.

For the new Na system, the Na storage mechanism of SnO₂ anode remains unclear by far. Some studies proposed that SnO₂ would behave identically to that in Li system, resulting in a theoretical capacity of 1378 mAhg⁻¹.⁴⁹ However some other studies claimed that the conversion reaction is irreversible from the very first cycle, and only the alloying reaction can contribute to the final theoretical capacity (*i.e.* 667 mAhg⁻¹).⁵⁰ Although there is controversy over the charge storage mechanism, it is commonly agreed that the much larger/heavier Na ions have posed significant challenge on achieving good electrochemical performance for SnO₂-based NIB anodes.^{36,41}

In the current studies, people prefer to introduce inactive soft matrices for accommodating the volume change of Sn. For instance in LIBs studies, the most commonly used soft matrix were various carbons, such as graphene, CNT and

amorphous carbons.

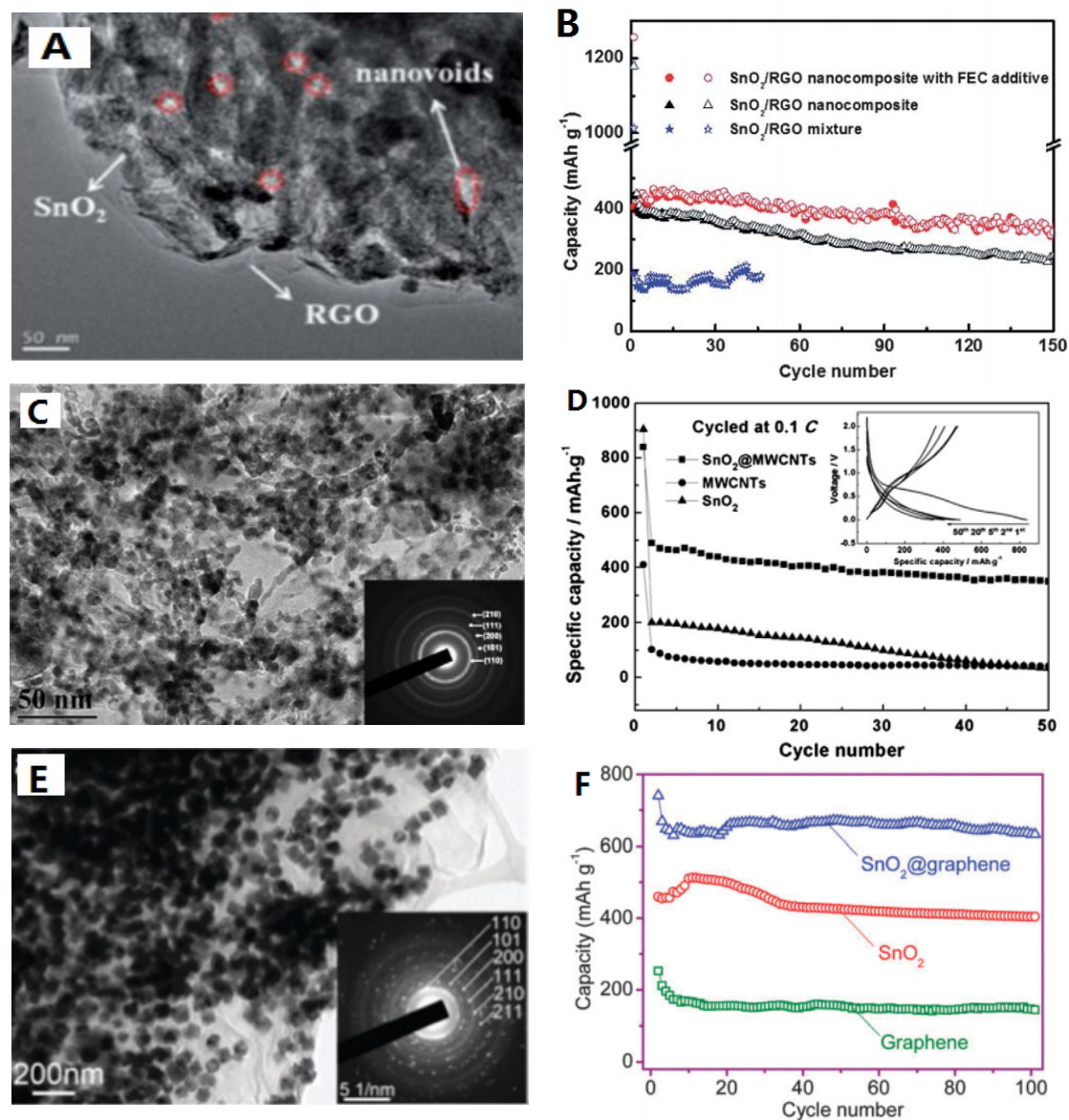


Figure 1-14: (A) TEM image of SnO₂/reduced graphene oxide nanocomposite (SnO₂-RGO). (B) Cycling performance of SnO₂-RGO in 1M NaClO₄ in EC-PC with and without FEC additive. Adapted from ref 50 with permission from the Royal Society of Chemistry, Copyright 2014. (C) Low magnification TEM image of SnO₂ on multiwall carbon nanotube composite (SnO₂@MWCNT). (D) Cycling performances of SnO₂@MWCNT, bare MWCNT and SnO₂. Adapted from ref 51 with permission from the Elsevier, Copyright 2013. (E) Low magnification TEM image of SnO₂ anchored graphene nanocomposites (SnO₂@graphene). (F) Cycling performance of SnO₂@graphene, bare SnO₂ and graphene. Adapted from ref 49 with permission from the Royal Society of Chemistry, Copyright 2013.

Figure 1-14 displayed the morphologies of some SnO₂-based NIBs anodes

recently reported, as well as the corresponding electrochemical performances. **Figure 1-14A, E** shows the morphologies of two SnO₂-graphene nanocomposites.^{49,50} Although the material in **Figure 1-14E** has much larger SnO₂ particle size (~100nm vs. ~5nm), the overall specific capacity instead is higher. These two composites displayed similar cyclability. **Figure 1-14E** shows the morphology of a SnO₂@CNT composite.⁵¹ The performance indicated that the CNT can both increase the overall specific capacity and the cyclability of the anodes (**Figure 1-14F**). It should be specially noted that the solid electrolyte interface (SEI) stabilizing additive (*e.g.* fluoroethylene carbonate, FEC) can greatly improve the cyclability of SnO₂-based anode.

Although these studies indeed provided some useful information, the most important knowledge about the Na storage mechanism of SnO₂ still remains unclear. Moreover, according to the experimental capacities reported (*i.e.* below 600 mAhg⁻¹), there is a huge discrepancy between these values and the theoretical capacity due to certain unknown reason. Therefore for the future researches, it is highly desired to investigate the Na storage mechanism of SnO₂ based anode.

1.4 Li/Na ion capacitors

1.4.1 Concepts

Basically, there are two dominant rechargeable energy storage systems, *i.e.* secondary ion batteries and supercapacitors.^{52, 53} Batteries have high energy densities which can keep our devices working all day, but they always take hours to recharge.^{54,55,56,57,58} Supercapacitors are able to exhibit rapid power delivery, but they always have very low energy densities.^{59,60,61,62,63,64}

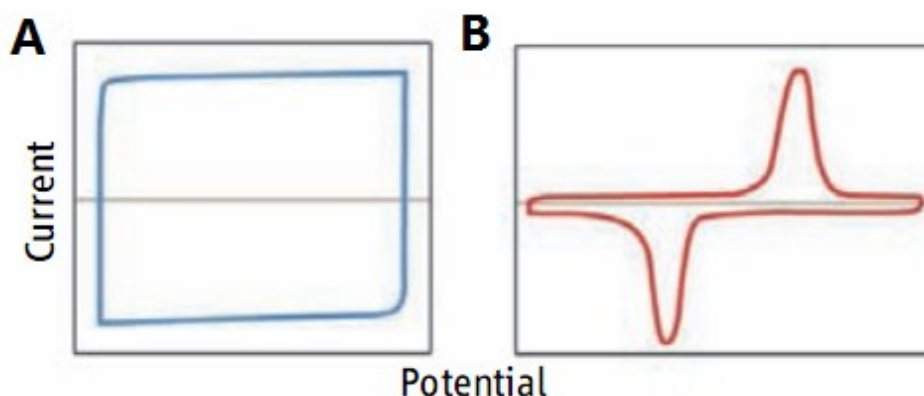


Figure 1-15: (A) Cyclic voltammograms (CV) of a supercapacitor material, where the response to a linear change in potential is a constant current. (B) Cyclic voltammograms (CV) of a battery material which exhibits faradaic redox peaks. Adapted from ref 52 with permission of Science AAAS.

The difference in energy storage property between batteries and supercapacitors results from the intrinsically different electrochemical processes taking place within the devices. For batteries, the electrodes will involve redox reactions within bulk electrode materials, thus provide large charge storage capability.⁵² As shown in **Figure 1-15B**, these redox reactions could be clearly characterized as redox peaks by cyclic voltammogram (CV) tests. The kinetics of the electrochemical reaction in battery is largely controlled by the slow ion diffusion process, which dominantly limits the power density of batteries. For example, commercial lithium ion batteries can deliver a specific energy density of 200 Whkg^{-1} , but only a maximum specific power density of 350 Wkg^{-1} . For electrical double-layer capacitors (EDLCs), charge is stored by ion adsorption on the surface of electrode materials. The absence of bulk redox reaction for supercapacitors results in a rectangle shaped CV (as shown in **Figure 1-15A**). The response to change in voltage for supercapacitors is rapid, thus leads to high power density.^{65,66,67} However because the charge is confined on the electrode surface, the energy densities of supercapacitors are much lower than that of batteries. For instance, most electrochemical supercapacitors can deliver specific power densities as high as 10 kW kg^{-1} , but deliver specific energy densities around 5 Whkg^{-1} only.

Tremendous works are performed to push the performance limitations of both batteries and supercapacitors. The performance distinction between the two systems has been greatly blurred. For batteries, their power performances are greatly improved by applying nano-scale electrode materials. For supercapacitors, their energy densities are increased by adding extra pseudo-capacitance through surface redox reactions.^{68,69,70,71,72,73} It should be noted that the high pseudo-capacitance could be obtained without satisfying the excellent cycling life and power density of the supercapacitor.

However, these progresses are still far distant from the target of truly bridging the gap between batteries and supercapacitors. In order to meet the energy and power density demand for applications ranging from microelectronic devices to electrical vehicles, people started to develop a new hybrid ion capacitor system which could truly combine the advantages of batteries and supercapacitors.^{74,75,76} This hybrid system is named lithium ion capacitor (LIC) as Li ions are the charge carriers. When employing Na^+ and $\text{ClO}_4^-/\text{PF}_6^-$ as charge carriers, the device is named sodium ion capacitor, *i.e.* NIC.^{77,78,79}

1.4.2 Configuration of Li/Na ion capacitors

Basically, the configuration of Li/Na ion capacitors is a combination of battery and supercapacitor. It couples a bulk intercalation-based battery-style negative electrode (anode, faradaic process) and a surface adsorption-based capacitor-style positive electrode (cathode, non-faradaic process) together. Based on this configuration, the working voltage window of the device could be largely expanded on the basis of the conventional supercapacitors.

Figure 1-16A displays the voltage profile of a conventional organic EDLC utilizing active carbon (AC) as both negative and positive electrodes.⁷⁴ The voltage applied should be limited to 2.7V in order to avoid any fatal degradation of the device caused by various considerable side reactions. The maximum energy density

is limited to 10 Whkg^{-1} . **Figure 1-16C** shows the voltage profile of a lithium ion capacitor using graphite as the anode and active carbon as the cathode in an organic system. The graphite anode is the battery-type electrode involving Li^+ intercalation/extraction, and the active carbon cathode is the capacitor-type electrode involving surface adsorption/desorption.^{80,81} As shown in the figure, the adsorption cathode sweeps within the voltage window equivalent to that in the supercapacitors, however the working voltage of the graphite anode can be very close to 0V vs. Li/Li^+ . As a result, the hybrid Li ion capacitors have large overall working voltage windows over 4 V , and energy densities over 30 Whkg^{-1} . It should be noted that there are cation and anion consuming processes for Li/Na ion capacitors during discharge/charge, which are substantially different from those happened in batteries. For instance, during charging process, cations (Li^+ , Na^+) intercalate into the anode bulk and anions (e.g. PF_6^- , ClO_4^-) adsorb on the cathode surface, respectively, resulting in ions consuming in the electrolyte.

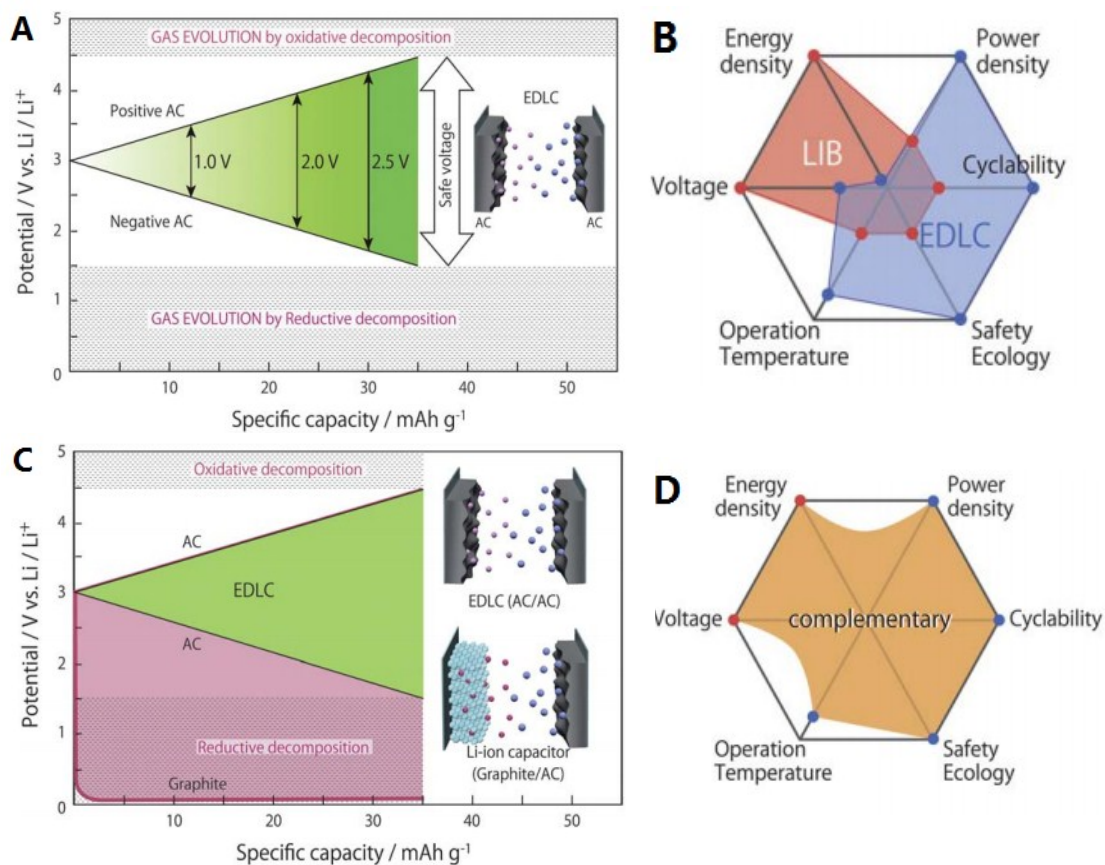


Figure 1-16: (A) Schematic voltage profile of a conventional EDLC supercapacitor, utilizing active carbon as electrodes. (C) Schematic voltage profiles of a Li-ion capacitor cell. (B)(D) Comparison of the characteristics of Li-ion batteries, EDLCs and Lithium-ion capacitors over six important criteria for electrochemical energy storage device. Adapted from ref 74 with permission from the Royal Society of Chemistry, Copyright 2012.

As shown in **Figure 1-16 (B-D)**, hybrid Li/Na ion capacitors are expected to expand the performance of six important criteria for both batteries and supercapacitors. In theory, they will integrate the high working voltage, energy density of batteries, together with the excellent power density, cyclability, working temperature range and safety ecology of supercapacitors. This ultimate goal of Li/Na ion capacitors has posed very high challenges for preparing the electrode materials. Firstly, there is a high requirement for the power behavior of the anode material. The kinetics of anode reaction should be fast enough to catch up with the cathode reaction. In order to achieve this, various nanostructured materials have been utilized as anodes.^{82,83,84,85} Secondly, the specific capacities of the cathode materials need be largely increased. Due to the typically low capacity of the cathode, there is always a necessity to use excess cathode materials in order to achieve the charge balance between two electrodes.^{86,87,88} Therefore a larger specific capacity of the cathode can reduce the total mass of the electrode material applied, thus increases the energy and power densities of the device.

1.5 Carbonaceous materials synthesis

1.5.1 Lignocellulosic biomass precursors

As a renewable natural resource, lignocellulosic material is an important inexhaustible supply of carbon precursors. Comparing to coal or petroleum, lignocellulosic materials are more evenly distributed on earth. With regards to the increasing prices of oil and other fossil resources in the long term, there is obvious

economic advantage exploring these much cheaper carbon sources.^{89,90} Therefore in the last decade, tremendous studies have been performed producing various carbon materials from these lignocellulosic materials.^{91,92,93,94}

It is known that the precursor tissue and the synthesis procedure are the dominant decisive factors for the resultant carbon properties.^{95,96} Therefore in order to obtain controllable carbon properties, firstly we should get familiar with the polymer tissues of the lignocellulosic materials. Basically, most of the lignocellulosic materials are mainly composed by carbohydrate polymers (*e.g.* cellulose, hemicellulose, etc.) and aromatic polymers such as lignin. The carbohydrate polymers are typically assembled by various sugar monomers. For example, cellulose is a polysaccharide consisted of a linear chain of several hundreds to over ten thousands β (1 \rightarrow 4) linked D-glucose unit ((C₆H₁₀O₅)), which should be strong, crystalline and resistant to hydrolysis.^{97,98} Hemicellulose could be considered as shorter cellulose (0.500-3K units *vs.* 7-15K units) with plenty of branches.⁹⁹ Different from cellulose which is mainly composed by anhydrous glucose, hemicellulose may include xylose, mannose, arabinose and galactose. Typically, hemicellulose has random, amorphous structure, which is much easier to be hydrolyzed by dilute acid or base.

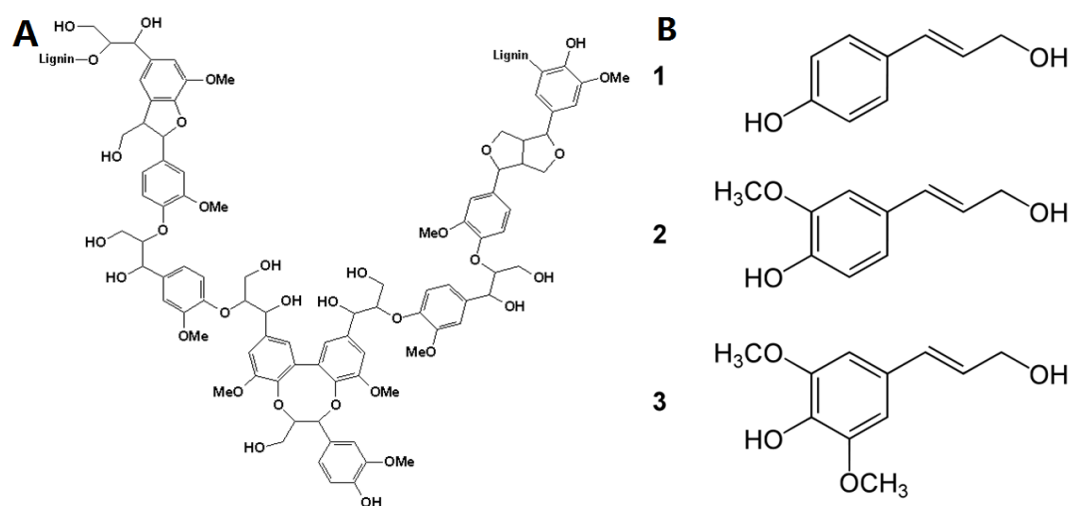


Figure 1-17: (A) Chemical structure of lignin. (B) 3 types of building blocks of lignin.

Totally different from the 2D fiber-like cellulose and hemicellulose, lignin is a 3D cross-linked aromatic polymer assembled by phenyl propane units.¹⁰⁰ **Figure 1-17A** displayed a small piece of lignin, where the cross-linking structure of lignin could be roughly observed. **Figure 1-16B** shows 3 types of building blocks of lignin (1. Paracoumaryl alcohol; 2. Coniferyl alcohol; 3. Sinapyl alcohol).

In addition to the main components, lignocellulosic materials also include some other impurities, such as pectin, free-sugars, proteins and various inorganic compounds. All these minorities could be selectively removed by certain pre-treatments.

Due to the substantially different polymer structures, the components in lignocellulosic materials will behave very differently during the carbon synthesis processes (*e.g.* pyrolysis, hydrothermal carbonization, etc.).^{95,96, 101, 102, 103} Furthermore, there is a significant variation on the mass ratios between these components among different lignocellulosic precursors. Therefore in theory people can prepare carbons with different properties by changing the specific synthesis procedures. As mentioned above, people need to take consideration of both the precursor tissue and the synthesis strategy in order to prepare carbons with desired attributes.

1.5.2 Pyrolysis, hydrothermal carbonization

People are always motivated to search facile, low cost, environmentally friendly and nontoxic routes to produce novel materials potential for future commercialization. The topic of advanced carbon materials preparation is under enormously study because carbons have been widely applied in the fields of catalyst,¹⁰⁴ adsorbents,^{105,106} energy storage/conversion,^{107,108} gas storage,¹⁰⁹ water treatment,¹¹⁰ etc.¹¹¹ Especially after the discoveries of low dimensional carbon materials (*e.g.* fullerenes, carbon nanotube, graphene, etc.), the carbon related material science has become a hot field.

Carbon synthesis is defined as a process of transforming the starting carbon sources (*e.g.* coal, fuel, petroleum pitch, biomass, carbohydrates, etc.) to carbonaceous solids. Methods like pyrolysis, high voltage arc electricity treatment, hydrothermal carbonization, laser ablation, etc. have been utilized for carbon synthesis. For the biomass precursors which are of our particular interest in this thesis, the most commonly used methods are pyrolysis^{112,113,114} and hydrothermal carbonization.^{95,96}

Pyrolysis is defined as the thermal decomposition process of materials in the absence of oxygen or when significantly less oxygen is present than required for complete combustion. The general reactions that occur during typical pyrolysis include: (1) Primary pyrolysis reactions at high temperature which releases volatiles and forms char; (2) condensation of certain volatiles in the cooler parts of the fuel, followed by secondary reactions which produce tar; (3) autocatalytic secondary pyrolysis reactions and simultaneously occurred primary pyrolytic reactions; (4) further thermal decomposition, reforming, water gas shift reactions, radicals recombination and dehydrations. After the pyrolysis, nonmetallic elements including P, N, S, H, etc. are locked into the final carbonaceous solids as heteroatoms.

Hydrothermal treatment is a classic technique for inorganic materials synthesis for half a century. Various solid state compounds (oxides, sulfides, microporous phases)^{115,116,117,118} have been prepared through hydrothermal synthesis. Basically, it is a facile, efficient and environmentally benign synthesis method.

In the last several decades, hydrothermal treatment for preparing carbonaceous materials (*i.e.* hydrothermal carbonization) has attracted considerable attention. By far, carbon materials with different morphology, chemical composition, graphitic microstructure, degree of crystalline, surface functionality, etc. have been successfully synthesized through hydrothermal carbonization methods.^{119,120,121}

Basically, the commonly applied hydrothermal conditions could be classified as high-temperature and low-temperature ones. For high-temperature hydrothermal

treatment (300-800°C), the temperature will be far above the thermal stable region of most organics. Therefore the high-temperature hydrothermal treatment is also considered as a “thermolysis” process. Carbons with high degree of crystalline can be prepared through the high-temperature hydrothermal treatment. Low temperature hydrothermal treatment always performs below 300°C, which is presumably considered as a greatly accelerated “coalification” process. Various nanostructured carbons with low degree of crystalline were successfully prepared through the low-temperature hydrothermal treatment.

The starting carbon sources (*i.e.* precursors) utilized for the hydrothermal carbonization include various carbohydrates,^{122,123} organic molecules,^{124,125} and lignocellulosic biomasses.¹²⁶ The chemical reactions happened are very complicated, and it is impossible to provide a clear picture of them. However, it is for sure that a series of reactions including dehydration, condensation, polymerization and aromatization will happen during the hydrothermal carbonization.

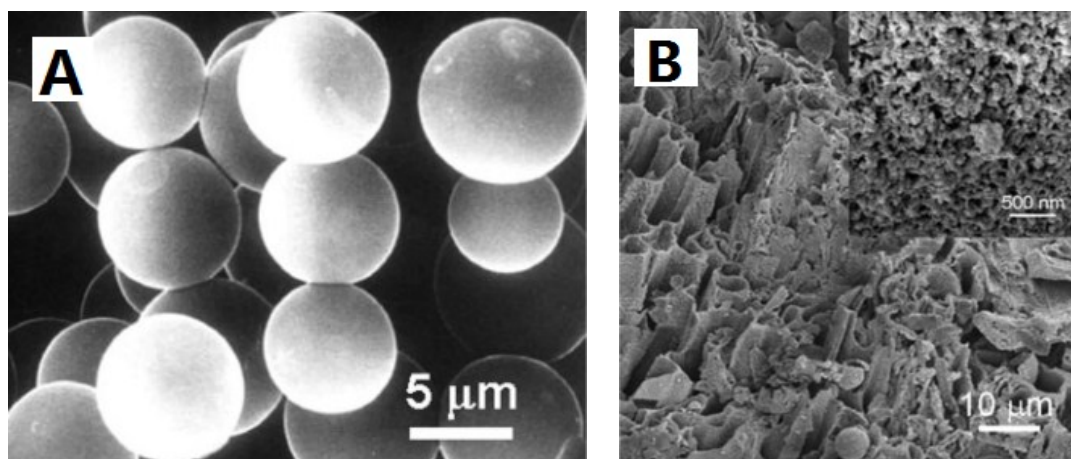


Figure 1-18: (A) SEM image of monodispersed carbon spheres obtained by hydrothermal carbonization with sugar as precursor. Adapted from ref 127 with permission from the Elsevier, Copyright 2001. (B) SEM image of “hard” biomass (oak leaf) after hydrothermal carbonization. Adapted from ref 96 with permission from American Chemical Society, Copyright 2007.

When applying lignocellulosic biomass as the precursor, the morphology of the final product is essentially influenced by the intrinsic composition of the biomass.^{95,96} Basically, the “soft” components (*e.g.* glucose, starch, lignin, etc.) in

the biomass will lose their original morphology and form globular carbonaceous nanoparticles. For instance, **Figure 1-18A** displayed the carbon spheres derived from the glucose precursor.¹²⁷ However, the “hard” components with extended crystalline cellulose scaffold would maintain their outer shape in the macro- and micro-scale. For example, for most cellulose-rich biomass precursors, the well-defined cellular shapes could be largely preserved after hydrothermal carbonization (as shown in **Figure 1-18B**).⁹⁶

Specific to the three dominant polymers in lignocellulosic precursors (*i.e.* cellulose, hemicellulose and lignin), most lignin and a large portion of hemicellulose will be hydrolyzed into soluble organic compounds. The cellulose will lose part of its crystallinity, but its main scaffold will still remain.

The resultant carbons could be substantially different in size, shape, yield, graphitic structure, surface chemistry, etc. These properties are all essentially influenced by the temperature, pressure and reaction time of the hydrothermal carbonization.

Finally, it should be noted that the carbons prepared by hydrothermal carbonization could be heavily functionalized by oxygen groups. The presence of these polar groups will make the carbons highly hydrophilic.¹²⁸

1.6 Motivation and scope of this thesis

Due to the increasing concern about the global scarcity and cost disadvantage of lithium, the development of sodium ion based energy storage systems becomes highly desired. However this new system poses great challenges for preparing suitable electrode materials due to the much larger and heavier Na ions than that of Li ions. Most of the present electrode materials are unqualified for practical use due to their inferior rate capability, poor cycling stability and low specific capacity for Na storage.

My doctoral researches are firstly aiming at exploring advanced materials with

promising electrochemical performance for Na based energy storage systems. In addition, they also include fundamental investigations on the Na ion intercalation chemistry, Na storage mechanisms, as well as the inner correlation between synthesis, structure and performance of the electrode materials. The insights and conclusions of this thesis are expected to offer solid scientific guidance for the future researches in this area.

Chapter 2 will present my studies on developing carbonaceous materials as anodes for Na ion batteries. I have skillfully chosen an abundant wild plant, peat moss as the carbon precursor, which has a very unique highly cross-linked polymer tissue and an intrinsic macroporous cellular architecture. Based on these special attributes, I've designed a novel synthesis procedure combining a high temperature carbonization step and a follow-up mild air activation treatment. Firstly, the high temperature carbonization transformed the cross-linked polymer into highly ordered pseudo graphitic arrays with substantially dilated interlayer spacing, which allows for significant Na ion intercalation. Secondly, the following air activation introduced hierarchical micro-/meso- porosity, which can greatly improve the electrolyte access and reduced the Na bulk diffusion distances. The resultant carbon anodes exhibited outstanding Na storage performance in terms of considerable specific capacity, negligible voltage hysteresis, high Coulombic efficiency and superb cycling retention.

Chapter 3 will present my works on developing the carbon-based sodium ion capacitor devices. A couple of adsorption and intercalation carbons was prepared from the biowaste peanut shell, and served as the cathode and anode of the hybrid device, respectively. The cathode and anode carbons were substantially different in surface area, graphitic order, heteroatoms doping and porous structure, which resulted in totally different Na storage behaviors. In addition to the performance optimization for each electrode material, I also optimized the properties of the full hybrid device by skillfully controlling the working voltage windows of both

electrodes. Benefiting from the excellent electrode material and the advanced working mode, the final NIC devices exhibited superb electrochemical performances rivaling that of most Li counterparts in terms of energy, power densities and cyclability.

Chapter 4 will present my studies on preparing SnO₂-based anodes for NIBs. A hierarchically nanostructured SnO₂-carbon composite was prepared through a glucose mediated self-assembling process. The material has delivered very promising electrochemical performances as both NIB and LIs anodes, being among the best in terms of cyclability and rate capability. In addition to the materials synthesis, I have also performed side-by-side study on the phase transformations of nano SnO₂-based anodes during sodiation and lithiation processes. The systemic investigation has not only clearly revealed the Na storage mechanism, but also perfectly explained the large discrepancy between experimental and theoretical capacities in NIBs. Furthermore, I also discovered the kinetic difficulty of Na bulk diffusion, plus the resultant incompleteness of the Na-Sn alloying reaction.

1.7 References

- 1 M. Armand, J. M. Tarascon, *Nature*, 2008, **451**, 652-657.
- 2 P. Simon, Y. Gogotsi, *Nat. Mater.*, 2008, **7**, 845-854.
- 3 Y. -M. Chiang, *Science*, 2010, **330**, 1485-1486.
- 4 H. L. Pan, Y. S. Hu, L. Q. Chen, *Energy Environ. Sci.*, 2013, **6**, 2338-2360.
- 5 H. K. Liu, G. X. Wang, Z. P. Guo, J. Z. Wang, K. Konstantinov, *J. Nanosci. Nanotechnol.*, 2006, **6**, 1-15.
- 6 M. Wakihara, O. Yamamoto, *Lithium Ion Batteries, Fundamentals and Performance*, Wiley-VCH, Japan, 1998.
- 7 R. Liu, J. Duay, S. B. Lee, *Chem. Commun.*, 2011, **47**, 1384-1404.
- 8 X. Zuo, C. Fan, X. Xiao, J. Liu, J. Nan, *J. Power Sources*, 2012, **219**, 94-99.
- 9 S. Flandrois, B. Simon, *Carbon*, 1999, **37**, 165-180.

- 10 L. Yuan, Z. Huang, W. Zhang, X. Hu, J. Chen, Y. Huang, J. B. Goodenough, *Energy Environ. Sci.*, 2011, **4**, 269-284.
- 11 M. Winter, J. O. Besenhard, M. E. Spahr, P. Novak, *Adv. Mater.*, 1998, **10**, 725-763.
- 12 M. D. Slater, D. Kim, E. Lee, C. S. Johnson, *Adv. Funct. Mater.*, 2013, **23**, 947-958.
- 13 G. E. Pascal and M. Fouletier, *Solid State Ionics*, 1988, **28**, 1172-1175.
- 14 M. M. Doeff, Y. P. Ma, S. J. Visco and L. C. Dejonghe, *J. Electrochem. Soc.*, 1993, **140**, L169-L170.
- 15 P. Thomas and D. Billaud, *Electrochim. Acta*, 2002, **47**, 3303-3307.
- 16 D. A. Stevens and J. R. Dahn, *J. Electrochem. Soc.*, 2000, **147**, A1271-A1273.
- 17 D. A. Stevens and J. R. Dahn, *J. Electrochem. Soc.*, 2001, **148**, A803-A811.
- 18 R. Alcántara, P. Lavela, G. F. Ortiz and J. L. Tirado, *Electrochem. Solid-State Lett.*, 2005, **8**, A222-A225.
- 19 S. Wenzel, T. Hara, J. Janek and P. Adelhelm, *Energy Environ. Sci.*, 2011, **4**, 3342-3345.
- 20 K. Tang, L. Fu, R. J. White, L. Yu, M.-M. Titirici, M. Antonietti and J. Maier, *Adv. Energy Mater.*, 2012, **2**, 873-877.
- 21 H. G. Wang, Z. Wu, F. L. Meng, D. L. Ma, X. L. Huang, L. M. Wang and X. B. Zhang, *ChemSusChem*, 2013, **6**, 56-60.
- 22 Y. Cao, L. Xiao, M. L. Sushko, W. Wang, B. Schwenzer, J. Xiao, Z. Nie, L. V. Saraf, Z. Yang and J. Liu, *Nano Lett.*, 2012, **12**, 3783-3787.
- 23 Li, W.; Zeng, L.; Yang, Z.; Gu, L.; Wang, J.; Liu, X.; Cheng, J.; Yu, Y. *Nanoscale*, 2014, **6**, 693-698.
- 24 Luo, W.; Schardt, J.; Bommier, C.; Wang, B.; Razink, J.; Simonsen, J.; Ji, X. C. *J. Mater. Chem. A*, 2013, **1**, 10662-10666.
- 25 V. G. Pol, E. Lee, D. Zhou, F. Dogan, J. M. Calderon-Moreno, C. S. Johnson, *Electrochim. Acta*, 2014, **127**, 61-67.

- 26 C. Bommier, W. Luo, W. Gao, A. Greaney, S. Ma, X. Ji, *Carbon*, 2014, **76**, 165-174.
- 27 W. -J. Zhang, *J. Power Sources*, 2011, **196**, 13-24.
- 28 L. Baggetto, H. Y. Hah, J. C. Jumas, C. E. Johnson, J. A. Johnson, J. K. Keum, C. A. Bridges, G. M. Veith, *J. Power Sources*, 2014, **267**, 329-336.
- 29 L. Baggetto, J. K. Keum, J. F. Browning, G. M. Veith, *Electrochem. Commun.*, 2013, **34**, 41-44.
- 30 J. Qian, X. Wu, Y. Cao, X. Ai, H. Yang, *Angew. Chem.*, 2013, **125**, 4731-4734.
- 31 Y. Kim, Y. Park, A. Choi, N. S. Choi, J. Kim, J. Lee, J. H. Ryu, S. M. Oh, K. T. Lee, *Adv. Mater.*, 2013, **25**, 3045-3049.
- 32 M. He, K. Kravchyk, M. Walter, M. V. Kovalenko, *Nano Lett.*, 2014, **14**, 1255-1262.
- 33 K. J. Rhodes, R. Meisner, M. Kirkham, N. Dudney, C. Daniel, *J. Electrochem. Soc.*, 2012, **159**, 294-299.
- 34 L. D. Ellis, T. D. Hatchard, M. N. Obrovac, *J. Electrochem. Soc.*, 2012, **159**, 1801-1805.
- 35 M. K. Datta, R. Epur, Partha Saha, Karan Kadakia, S. K. Park, P. N. Kumta, *J. Power Sources*, 2013, **225**, 316-322.
- 36 Y. Xu, Y. Zhu, Y. Liu, C. S. Wang, *Adv. Energy Mater.*, 2013, **3**, 128-133.
- 37 M. Gu, A. Kushima, Y. Shao, J. Zhang, J. Liu, N. D. Browning, J. Li, C. Wang, *Nano Lett.*, 2013, **13**, 5203-5211.
- 38 D. Buchholz, A. Moretti, R. Kloepsch, S. Nowak, V. Siozios, M. Winter, and S. Passerini, *Chem. Mater.*, 2013, **25**, 142-148.
- 39 J. W. Wang, X. H. Liu, S. X. Mao, J. Y. Huang, *Nano Lett.*, 2012, **12**, 5897-5902.
- 40 J. Y. Huang, L. Zhong, C. M. Wang, J. P. Sullivan, W. Xu, L. Q. Zhang, S. X. Mao, N. S. Hudak, X. H. Liu, A. Subramanian, H. Fan, L. Qi, A. Kushima, J. Li, *Science*, 2010, **330**, 1515-1520.

- 41 H. Zhu, Z. Jia, Y. Chen, N. Weadock, J. Wan, O. Vaaland, X. Han, T. Li, L. Hu, *Nano Lett.*, 2013, **13**, 3093-3100.
- 42 D. Nam, T. Kim, K. S. Hong, H. S. Kwon, *ACS Nano*, 2014, **8**, 11824-11835.
- 43 M. Shimizu, H. Usui, H. Sakaguchi, *J. Power Sources*, 2014, **248**, 378-382.
- 44 D. W. Su, X. Q. Xie, G. X. Wang, *Chem-Eur. J.*, 2014, **20**, 3192-3197.
- 45 Z. Chen, M. Zhou, Y. Cao, X. Ai, H. Yang, J. Liu, *Adv. Energy Mater.*, 2012, **2**, 95-102.
- 46 C. Guan, X. H. Wang, Q. Zhang, Z. X. Fan, H. Zhang, H. J. Fan, *Nano Lett.*, 2014, **14**, 4852-4858.
- 47 X. S. Zhou, L. J. Wan, Y. G. Guo, *Adv. Mater.*, 2013, **25**, 2152-2157.
- 48 X. Fan, J. Shao, X. Xiao, X. Wang, S. Li, H. Ge, L. Chen, C. S. Wang, *J. Mater. Chem. A*, 2014, **2**, 18367-18374.
- 49 D. Su, H. Ahn, G. Wang, *Chem. Commun.*, 2013, **49**, 3131-3133.
- 50 Y. Wang, Y. Lim, M. Park, S. Chou, J. H. Kim, H. K. Liu, S. X. Dou, Y. J. Kim, *J. Mater. Chem. A*, 2014, **2**, 529-534.
- 51 Y. Wang, D. Su, C. Wang, G. Wang, *Electrochem. Commun.*, 2013, **29**, 8-11.
- 52 Patrice Simon, Yury Gogotsi, Bruce Dunn, *Science*, 2014, **343**, 1210-1211.
- 53 N. Choi, Z. Chen, S. A. Freunberger, X. Ji, Y. Sun, K. Amine, G. Yushin, L. F. Nazar, J. Cho, and P. G. Bruce. *Angew. Chem. Int. Ed.*, 2012, **51**, 9994-10024.
- 54 B. R. Liu, P. Soares, C. Checkles, Y. Zhao and G. H. Yu, *Nano Lett.*, 2013, **13**, 3414-3419.
- 55 Y. J. Gong, S. B. Yang, L. Zhan, L. L. Ma, R. Vajtai and P. M. Ajayan, *Adv. Funct. Mater.*, 2014, **24**, 125-130.
- 56 S. M. Oh, S. T. Myung, C. S. Yoon, J. Liu, J. Hassoun, B. Scrosati, K. Amine, Y. K. Sun. *Nano Lett.*, 2014, **14**, 1620-1626.
- 57 R. Mukherjee, R. Krishnan, T. M. Lu and N. Koratkar, *Nano Energy*, 2012, **1**, 518-533.

- 58 C. B. Zhu, K. P. Song, P. A. van Aken, J. Maier and Y. Yu, *Nano Lett.*, 2014, **14**, 2175-2180.
- 59 J. X. Zhu, L. J. Cao, Y. S. Wu, Y. J. Gong, Z. Liu, H. E. Hoster, Y. H. Zhang, S. T. Zhang, S. B. Yang, Q. Y. Yan, P. M. Ajayan, R. Vajtai, *Nano Lett.*, 2013, **13**, 5408-5413.
- 60 J. Han, L. L. Zhang, S. Lee, J. Oh, K. S. Lee, J. R. Potts, J. Y. Ji, X. Zhao, R. S. Ruoff and S. Park, *ACS Nano*, 2013, **7**, 19-26.
- 61 L. Qie, W. M. Chen, H. H. Xu, X. Q. Xiong, Y. Jiang, F. Zou, X. L. Hu, Y. Xin, Z. L. Zhang and Y. H. Huang, *Energy Environ. Sci.*, 2013, **6**, 2497-2504.
- 62 M. R. Lukatskaya, O. Mashtalir, C. E. Ren, Y. Dall'Agnese, P. Rozier, P. L. Taberna, M. Naguib, P. Simon, M. W. Barsoum and Y. Gogotsi, *Science*, 2013, **341**, 1502-1505.
- 63 W. J. Qian, F. X. Sun, Y. H. Xu, L. H. Qiu, C. H. Liu, S. D. Wang and F. Yan, *Energy Environ. Sci.*, 2014, **7**, 379-386.
- 64 Z. Li, L. Zhang, B. S. Amirkhiz, X. H. Tan, Z. W. Xu, H. L. Wang, B. C. Olsen, C. M. B. Holt and D. Mitlin, *Adv. Energy Mater.*, 2012, **2**, 431-437.
- 65 F. Beguin, E. Frackowiak, Ed., *Supercapacitors: Materials, Systems and Applications*, Wiley-VCH, Weinheim, Germany, 2013.
- 66 J. R. Miller, P. Simon, *Science*, 2008, **321**, 651-652.
- 67 P. Simon, Y. Gogotsi, *Acc. Chem. Res.*, 2013, **46**, 1094-1103.
- 68 K. Brezesinski, J. Wang, J. Haetge, C. Reitz, S. O. Steinmueller, S. H. Tolbert, B. M. Smarsly, B. Dunn, T. Brezesinski, *J. Am. Chem. Soc.*, 2012, **132**, 6982-6990.
- 69 C. Hu, K. Chang, M. Lin, Y. Wu, *Nano Lett.*, 2006, **6**, 2690-2695.
- 70 G. Yu, L. Hu, M. Vosgueritchian, H. Wang, X. Xie, J. R. McDonough, X. Cui, Y. Cui, Z. Bao, *Nano Lett.*, 2011, **11**, 2905-2911.
- 71 Y. He, W. Chen, X. Li, Z. Zhang, J. Fu, C. Zhao, E. Xie, *ACS Nano*, 2013, **7**, 174-182.

- 72 J. W. Kim, V. Augustyn, B. Dunn, *Adv. Energy Mater.*, 2012, **2**, 141-148.
- 73 V. Augustyn, J. Come, M. A. Lowe, J. W. Kim, P. L. Taberna, S. H. Tolbert, H. D. Abruna, P. Simon and B. Dunn, *Nat. Mater.*, 2013, **12**, 518-522.
- 74 K. Naoi, S. Ishimoto, J. Miyamoto and W. Naoi, *Energy Environ. Sci.*, 2012, **5**, 9363-9373.
- 75 Z. Chen, Y. Yuan, H. H. Zhou, X. L. Wang, Z. H. Gan, F. S. Wang and Y. F. Lu, *Adv. Mater.*, 2014, **26**, 339-345.
- 76 A. Jain, V. Aravindan, S. Jayaraman, P. S. Kumar, R. Balasubramanian, S. Ramakrishna, S. Madhavi and M. P. Srinivasan, *Sci. Rep.*, 2013, **3**, 3002.
- 77 Z. Chen, V. Augustyn, X. L. Jia, Q. F. Xiao, B. Dunn and Y. F. Lu, *ACS Nano*, 2012, **6**, 4319-4327.
- 78 J. Yin, L. Qi and H. Y. Wang, *ACS Appl. Mater. Inter.*, 2012, **4**, 2762-2768.
- 79 R. Ding, L. Qi and H. Wang, *Electrochim. Acta*, 2013, **114**, 726-735.
- 80 V. Khomenko, E. Raymundo-Pinero and F. Beguin, *J. Power Sources*, 2008, **177**, 643-651.
- 81 A. Yoshino, T. Tsubata, M. Shimoyamada, H. Satake, Y. Okana, S. Mori and S. Yata, *J. Electrochem. Soc.*, 2004, **151**, 2180-2182.
- 82 H. L. Wang, Z. W. Xu, Z. Li, K. Cui, J. Ding, A. Kohandehghan, X. H. Tan, B. Zahiri, B. C. Olsen, C. M. B. Holt and D. Mitlin, *Nano Lett.*, 2014, **14**, 1987-1994.
- 83 K. Leng, F. Zhang, L. Zhang, T. F. Zhang, Y. P. Wu, Y. H. Lu, Y. Huang and Y. S. Chen, *Nano Res.*, 2013, **6**, 581-592.
- 84 S. Shi, C. J. Xu, C. Yang, Y. Y. Chen, J. J. Liu and F. Y. Kang, *Sci. Rep.*, 2013, **3**, 2598.
- 85 X. Zhao, L. L. Zhang, S. Murali, M. D. Stoller, Q. H. Zhang, Y. W. Zhu and R. S. Ruoff, *ACS Nano*, 2012, **6**, 5404-5412.
- 86 H. Kim, M. Y. Cho, M. H. Kim, K. Y. Park, H. Gwon, Y. Lee, K. C. Roh and K. Kang, *Adv. Energy Mater.*, 2013, **3**, 1500-1506.

- 87 F. Zhang, T. F. Zhang, X. Yang, L. Zhang, K. Leng, Y. Huang and Y. S. Chen, *Energy Environ. Sci.*, 2013, **6**, 1623-1632.
- 88 S. R. Sivakkumar, A. G. Pandolfo, *J. Appl. Electrochem.*, 2014, **44**, 105-113.
- 89 N. Mosier, C. Wyman, B. Dale, R. Elander, Y. Lee, M. Holtzapple, M. Ladisch, *Bioresour. Technol.*, 2005, **96**, 673-688.
- 90 J. B. Binder, R. T. Raines, *J. Am. Chem. Soc.*, 2009, **131**, 1979-1985.
- 91 Y. Zhai, Y. Dou, D. Zhao, P. F. Fulvio, R. T. Mayes, S. Dai, *Adv. Mater.*, 2011, **23**, 4828-4850.
- 92 E. Raymundo-Pinero, M. Cadek, F. Beguin, *Adv. Funct. Mater.*, 2009, **19**, 1032-1039.
- 93 H. Wang, Z. Li, D. Mitlin, *ChemElectroChem*, 2014, **1**, 332-337.
- 94 M. Sevilla, A. B. Fuertes, R. Mokaya, *Energy Environ. Sci.*, 2011, **4**, 1400-1410.
- 95 B. Hu, K. Wang, L. Wu, S. Yu, M. Antonietti, M. M. Titirici, *Adv. Mater.*, 2010, **22**, 813-828.
- 96 M. M. Titirici, A. Thomas, S. H. Yu, J. O. Muller, M. Antonietti, *Chem. Mater.*, 2007, **19**, 4205-4212.
- 97 D. Klemm, B. Heublein, H. P. Fink, A. Bohn, *Angew. Chem., Int. Ed.*, 2005, **44**, 3358-3393.
- 98 D. Y. Kim, Y. Nishiyama, M. Wada, S. Kuga, *Carbon*, 2001, **39**, 1051-1056.
- 99 N. Shibuya, A. Misaki, *Agric. Bio. Chem.*, 1978, **42**, 2267-2274.
- 100 R. K. Sharma, J. B. Wooten, V. L. Baliga, X. H. Lin, W. G. Chan, M. R. Hajaligol, *Fuel*, 2004, **83**, 1469-1482.
- 101 H. Yang, R. Yan, H. Chen, D. H. Lee, C. Zheng, *Fuel*, 2007, **86**, 1781-1788.
- 102 M. V. Ramiah, *J. Appl. Polym. Sci.*, 1970, **14**, 1323-1337.
- 103 T. Hosoya, H. Kawamoto, S. Saka, *J. Anal. Appl. Pyrolysis*, 2007, **80**, 118-125.
- 104 G. Liu, X. Li, J. Lee, B. N. Popov, *Catal. Sci. Technol.*, 2011, **1**, 207-217.
- 105 Z. Yong, V. G. Mata, A. E. Rodrigues, *Adsorption*, 2001, **7**, 41-50.

- 106 Z. Yong, V. Mata, A. E. Rodrigues, *Sep. Purif. Technol.*, 2002, **26**, 195-205.
- 107 E. Frackowiak, F. Beguin, *Carbon*, 2001, **39**, 937-950.
- 108 L. L. Zhang, X. S. Zhao, *Chem. Soc. Rev.*, 2009, **38**, 2520-2531.
- 109 V. C. Menon, *J. Porous Mater.*, 1998, **5**, 43-58.
- 110 P. Hadi, M. Xu, C. Ning, C. S. K. Lin, G. McKay, *Chem. Eng. J.*, 2015, **260**, 895-906.
- 111 S. H. Yu, X. J. Cui, L. L. Li, K. Li, B. Yu, M. Antonietti, H. Colfen, *Adv. Mater.*, 2004, **16**, 1636-1640.
- 112 F. Shafizadeh, *J. Anal. Appl. Pyrolysis*, 1982, **3**, 283-305.
- 113 D. Mohan, C. U. Pittman, P. H. Steele, *Energy Fuel*, 2006, **20**, 848-889.
- 114 K. Raveendran, A. Ganesh, K. C. Khilar, *Fuel*, 1996, **75**, 987-998.
- 115 A. Rabenau, *Angew. Chem. Int. Ed.*, 1985, **24**, 1026-1040.
- 116 S. Somiya, R. Roy, *Bull. Mater. Sci.*, 2000, **23**, 453-460.
- 117 H. Schafer, *Annu. Rev. Mater. Sci.*, 1985, **15**, 1-41.
- 118 S. Feng, R. Xu, *Acc. Chem. Res.*, 2001, **34**, 239-247.
- 119 T. Fujino, J. M. Calderon-Moreno, S. Swamy, T. Hirose, M. Yoshimura, *Solid State Ionics*, 2002, **151**, 197-203.
- 120 Y. Yang, J. Cui, M. Zheng, C. Hu, S. Tan, Y. Xiao, Q. Yang, Y. Liu, *Chem. Commun.*, 2012, **48**, 380-382.
- 121 M. M. Titirici, M. Antonietti, *Chem. Soc. Rev.*, 2010, **39**, 103-116.
- 122 N. Baccile, G. Laurent, F. Babonneau, F. Fayon, M. M. Titirici, M. Antonietti, *J. Phys. Chem. C*, 2009, **113**, 9644-9654.
- 123 M. M. Titirici, M. Antonietti, N. Baccile, *Green Chem.*, 2008, **10**, 1204-1212.
- 124 X. C. Ma, F. Xu, Y. Du, L. Y. Chen, J. M. Shen, L. C. Wang, Y. T. Qian, *Carbon*, 2006, **44**, 2861-2864.
- 125 T. Luo, L. S. Gao, J. W. Liu, L. Y. Chen, J. M. Shen, L. C. Wang, Y. T. Qian, *J. Phys. Chem. B*, 2005, **109**, 15272-15277.

- 126 H. Wang, Z. W. Xu, A. Kohandehghan, Z. Li, K. Cui, X. H. Tan, T. J. Stephenson, C. K. King'onde, C. M. B. Holt, B. C. Olsen, J. K. Tak, D. Harfield, A. O. Anyia and D. Mitlin, *ACS Nano*, 2013, **7**, 5131-5141.
- 127 Q. Wang, H. Li, Q. Chen, X. J. Huang, *Carbon*, 2001, **39**, 2211-2214.
- 128 R. Demir-Cakan, N. Baccile, M. Antonietti, M. M. Titirici, *Chem. Mater.*, 2009, **21**, 484-490.

2

Carbon Nanosheet Frameworks Derived from Peat Moss as High Performance Sodium Ion Battery Anodes*

2.1 Introduction

Advanced portable and automotive electrical energy storage (EES) systems are primarily based on lithium ion battery (LIB) technologies. However, there is increasing concern about the use of lithium due to its cost disadvantage and overall global scarcity. Sodium is an attractive alternative to lithium due to its markedly lower cost and much wider global abundance. Sodium ion batteries (NIBs) are therefore attracting increasing scientific attention, particularly with regard to large-scale stationary applications where their lower gravimetric energy density is less of an issue.^{1,2}

Substantial success has been recently achieved in developing NIB cathode materials,^{3,4,5} with less obvious choices being available for the anode. Researchers have developed inorganic intercalation compounds,⁶ organic compounds,⁷ or alloying metal/metal oxides^{8,9,10} as potential anode materials. However, each class of such materials displays certain intrinsic limitations, such as a high overpotential

* Material in this chapter has been published in:

Jia Ding, Huanlei Wang, Zhi Li, Alireza Kohandehghan, Zhanwei Xu, Benjamin Zahiri, Kai Cui, Xuehai Tan, Elmira Memarzadeh Lotfabad, Brian C. Olsen, and David Mitlin, *ACS Nano*, 7, (2013), 11004-11015.

associated with conversion reaction or alloying reaction electrodes. Carbonaceous material is a dominant candidate as electrode material for EES devices.^{11,12,13,14,15} Due to its desirable electrochemical attributes, graphite remains the dominant anode material for commercial LIBs.^{16,17} These attributes include a closely spaced (*i.e.* low voltage hysteresis on charge *vs.* discharge) voltage plateau close to Li/Li^+ ,^{18,19} which for a given cathode material leads to the widest possible voltage window. Due to the minor and highly reversible dilation of the graphite lattice during lithiation/delithiation ($c/2$ changes from 3.35 to 3.6Å), the electrodes are stable upon extensive cycling. Moreover, graphite achieves superior coulombic efficiency due to relatively low levels of cycling-induced solid electrolyte interface (SEI) growth. A NIB anode that displays these characteristics would be very useful.²⁰

However reports of LIB-graphite analogues for NIBs are scarce. Traditional "soft" carbons with substantial turbostratic disorder display as much as 50% of the total capacity in the less useful > 0.5 V range.²¹ Early work on non-graphitizable "hard" carbons demonstrated considerable capacity (200-300mAhg⁻¹), but have unqualified cyclability and rate performance.^{22,23,24,25} templated carbons,²⁶ hollow carbon spheres,²⁷ and carbon nanosheets²⁸ have demonstrated improved rate performance because of their porosity. A recent study on hollow carbon nanowires derived from polyaniline reported attractive potential *versus* capacity profiles in addition to improved rate capability, the former being attributed to a combination of pore filling and a dilated graphene layer spacing.²⁹

A survey of the existing literature on carbons with optimum energy storage attributes shows that it is essential to couple the intrinsic structure of the precursor with tailored carbonization/activation treatment.^{30,31} Since no two precursors are identical, neither should be the synthesis routes designed to extract the maximum electrochemical performance. Moreover both the precursor and the synthesis process should be "green" in terms of minimal use of harmful chemicals and ideally a negative or a net zero CO₂ footprint.³² It also has to be economically viable. Peat

moss is one of the most abundant plant species, with peatland (land with a naturally accumulated layer of peat moss), covering around 4 million km² of land (3% of the earth!).³³ Peat moss is also well known for its astonishing water-holding ability due to the open macroscopic cellular structure in the leaves. As will be demonstrated, such macroscopic structure leads to very favorable electrode architectures in the post pyrolysis - post activation specimens. Unlike the various woods that are cellulose-rich, peat moss has a high content of cross-linked polymers including hemicellulose and lignin (*ca.* 80 wt% total).³⁴ This would make it difficult to graphitize the majority of the material even at high carbonization temperatures.³⁵ In this work, we take full advantage of both the cellular structure and the high degree of crosslinking. Through a facile tailored synthesis process of carbonization and activation, this virtually inexhaustible biomass is converted into NIB anodes with the electrochemical characteristics approaching that of graphite when employed in lithium ion batteries.

2.2 Experimental procedures

2.2.1 Material synthesis

The compressed peat moss biomass was purchased from Premier Horticulture Company, Canada (20 kg in pack). Before the synthesis process, impurities (including small wood sticks, coarse stalks of peat moss, *etc.*) in the peat moss were thoroughly picked out, leaving only the fine peat moss leaves. For the pyrolysis carbonization process, typically 10 g peat moss precursor is loaded in a tubular furnace and carbonized at a range of temperature (600-1400°C) with argon flow of 100 sccm min⁻¹. The heating rate is 5 min⁻¹. The yield is from 2.5-4.5 g. The obtained hard carbon is carefully washed in 20% KOH at 70°C for 2h and 2M HCl at 60°C for 15 h to remove the impurities. The purified samples are further rinsed by MQ-water and then collected by filtration. After dried at 120°C for 12 h in vacuum oven, carbonized peat moss (CPM) is achieved. Some of the CPM specimens are further activated at 300°C

for 3h (at a heating rate of 5 min^{-1} in the tubular furnace) in a dry air flow of 50 sccm min^{-1} . The obtained activated peat moss (designated CPM-A) is firstly ground and then washed with 2M HCl and MQ-water again before use.

2.2.2 Material characterization

To investigate the morphology of peat moss precursor, S-3000N SEM with variable working pressure is used. For the morphologies of carbon, a Hitachi S-4800 SEM equipped with field emission gun is used. TEM analysis is performed using a JEOL JEM-2010 TEM, with an accelerating voltage of 200 kV. The surface area and porous structure are characterized by nitrogen adsorption at 77 K with a Quantachrome Autosorb¹. The samples were outgassed at 250°C for 4h under vacuum prior to the gas sorption measurements. The pore size distributions were evaluated by a non-local DFT method using nitrogen adsorption data and assuming slit-pore geometry. XRD analysis was performed using a Bruker AXS D8 Discover diffractometer with the Cu $K\alpha$ radiation. XPS was obtained on an Axis Ultra spectrometer. All the samples were dried at 120°C in vacuum oven overnight to remove the absorbed water before XPS analysis.

2.2.3 Electrochemical test

Electrochemical tests were carried out using coin cells CR2032. The slurry of 80% active materials, 10% carbon black (Super-P) and 10% poly(vinylidenedifluoride) in N-methylpyrrolidone (the weight ratio is 95% active materials and 5% poly(vinylidenedifluoride) for the *ex situ* XRD tests electrodes) was coated on copper foil using a doctor blade and then dried at 110°C overnight in vacuum oven, resulting in electrodes with a mass loading of $\sim 1 \text{ mg cm}^{-2}$. Na metal was used as counter electrode and separated from the working electrode with polyethene separator. The electrolyte was 1 M NaClO_4 dissolved in a mixture of ethylene carbonate (EC) and diethyl carbonate (DEC) with a volume ratio of 1:1. Cyclic voltammetry

measurements were conducted on a Solartron 1470 Multistat system. The charge-discharge measurements were performed using an Arbin BT2000 Potentiostat. Electrochemical impedance spectroscopy measurements were also performed using a Solartron 1470E Multichannel Potentiostat/Cell Test System. All electrochemical tests were conducted at room temperature.

2.3 Results and discussion

The peat moss precursor is firstly carbonized at a range of temperatures ($T_{carb} = 600^{\circ}\text{C}$, 900°C , 1100°C , 1400°C) under an inert atmosphere. Some of the samples were then activated under air flow at 300°C for 3 hours. The entire synthesis process, along with the initial precursor structure, the post carbonization and activation microstructures, and the possible sodiation mechanisms is illustrated in **Figure 2-1**. The key linkages between all of these aspects will be discussed in the subsequent text. The as prepared Carbonized Peat Moss is named CPM- x , and the further Activated carbon is named CPM- x -A, where x refers to the carbonization temperature. For comparison, a Commercial Activated Carbon (NORIT® A SUPRA) labeled as CAC was also analyzed.

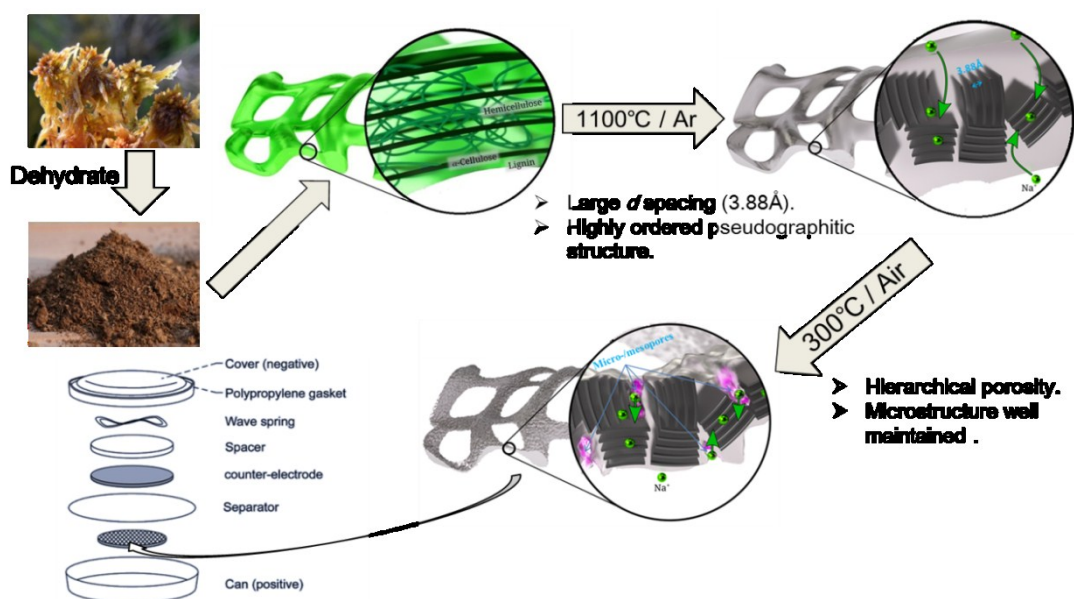


Figure 2-1: The preparation route of CPM-1100-A carbons derived from peat moss as anode.

Figure 2-2A shows a macroscopic photograph of the as-received peat moss employed as the carbon precursor. The material consists of relatively coarse (mm and cm-scale) agglomerates that could be handled by hand without disintegrating. The peat moss consists of "wound" macroscopic assemblies of leaves (termed "stem leaves") along the main stem. The stem leaves are primarily composed of clear cells, termed hyaline cells. Because of the large volume of hyaline cells and the thin yet flexible cell walls, the peat moss delivers astonishing absorbent and water-holding capacity (can hold 16-26 times as much water as the dry weight),³⁶ like a sponge. The commercial products of peat moss biomass are fully dried plants that were harvested on the peatland. Water and cytoplasm in the hyaline cell were forced out, leaving only the cell wall. In the scanning electron microscopy (SEM) images of peat moss precursor (**Figure 2-2B**), the shape of the hyaline cell can be observed (arrowed). The removal of the cytoplasm leaves numerous macroscopic voids, while the cell walls build up an interconnected framework. The cell walls contain *ca.* 20% in weight of α -cellulose, which is a long straight 1,4 glycosidic linkage polymer.³⁷ The α -cellulose acts as a hard scaffold, conferring the mechanical strength of the whole carbon framework.³⁸ This scaffolding remains in place during pyrolysis, with the α -cellulose rich portions of the material being expected to preferentially graphitize at lower temperatures.

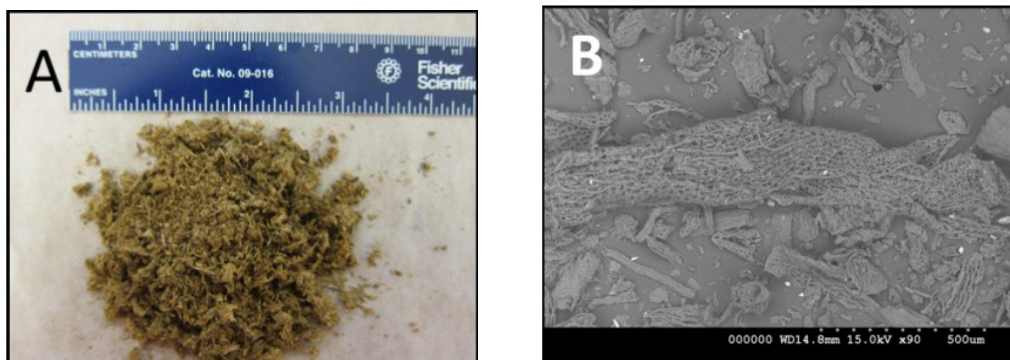


Figure 2-2: (A) Photograph of the fully dehydrated peat moss precursor. (B) Environmental SEM image of the fully dehydrated peat moss precursor.

Figure 2-3A shows a low magnification SEM micrograph of a peat moss leaf

carbonized at 1100°C. The final product had this type of morphology regardless of the carbonization temperature. Even when the carbonization temperature is increased to 1400°C (**Figure 2-3B**), the macroscopic carbon frameworks do not collapse.

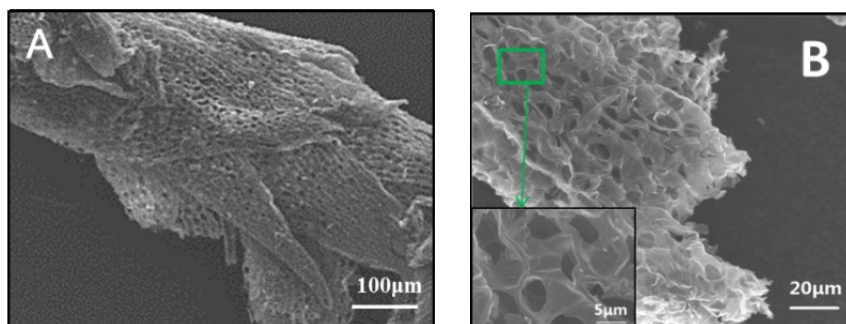


Figure 2-3: (A) Low magnification SEM micrograph of peat moss derived carbon (CPM-1100-A). (B) SEM micrograph of CPM-1400-A.

After mechanical grinding, the larger carbon framework breaks up into irregularly shaped carbon particles that are 20-300 µm in dimensions. According to the SEM images **Figure 2-4 (A-B)**, each carbon particle displays a hollow three-dimensional architecture with linked macropores. The unique open morphologies of the CPM specimens are fundamentally different from those of commercial activated carbons, such as the highly popular NORIT SUPRA. **Figure 2-4C** shows the SEM micrographs of CAC particulates that are effectively 3D micron-scale clumps without any open structure to facilitate electrolyte penetration and ion diffusion. As will be demonstrated, the intrinsic macroscopic openness of CPM specimens is one essential feature for optimum material utilization during sodium insertion/extraction.

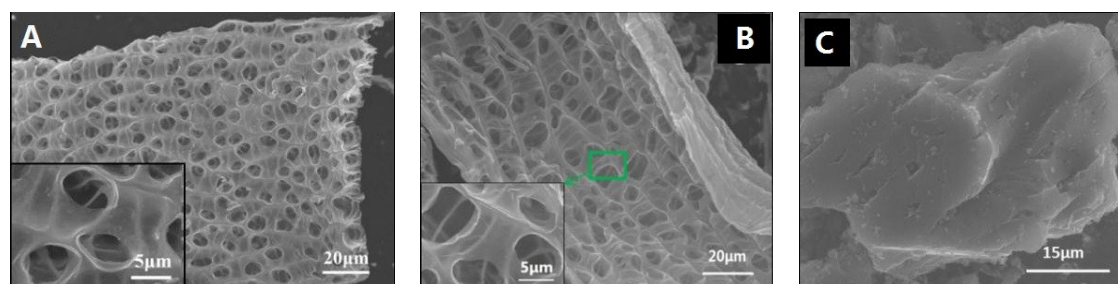


Figure 2-4: (A) Higher magnification SEM micrograph highlighting the hollow macroporous architecture of the carbon particles (CPM-1100-A). (B) SEM micrograph of CPM-1100-A, highlighting the macroporous architecture. (C) SEM micrograph of a commercial activated carbon (CAC) particle.

Figure 2-5 show high angle annual dark field (HAADF) transmission electron microscopy (TEM) micrographs and electron energy loss spectroscopy (EELS) thickness profiles of the CPM-A specimen. The carbon walls derived from the hyaline display thicknesses between 60-180 nm, with such location-to-location thickness variations being encountered in all the CPM specimens. The resultant Na diffusion distances are at the maximum of 1/2 of those thicknesses (there is electrolyte contact on both sides of the macropores). Moreover these air-activated specimens contain micro and mesopores that actually further reduce the diffusion distances due to electrolyte penetration.

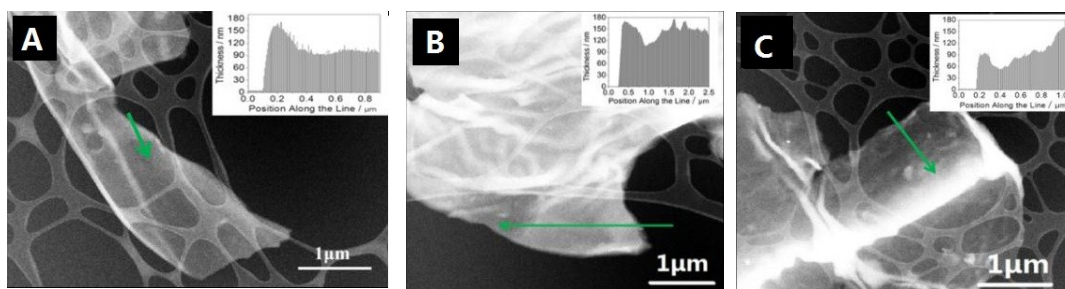


Figure 2-5: HAADF TEM micrograph and EELS thickness profile (inset) of the arrowed carbon strand in CPM-A.

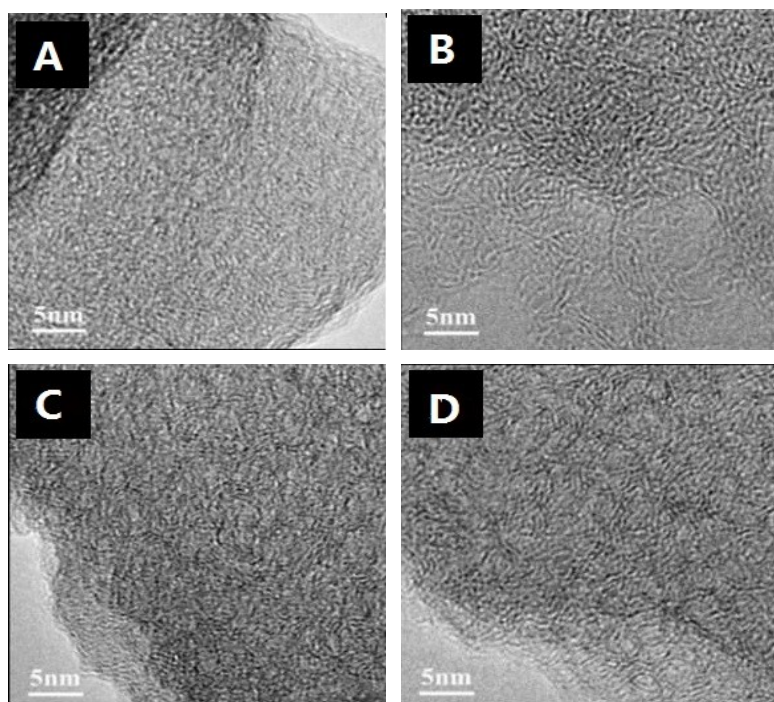


Figure 2-6: HRTEM micrographs of CPM-600-A (A), CPM-900-A (B), CPM-1100-A (C) and CPM-1400-A (D), respectively.

The low carbonization temperature specimen (CPM-600-A) displays highly disordered structure, with limited evidence of any graphitic nanocrystallites. The contrast displayed in the HRTEM micrograph of this material, shown in **Figure 2-6A**, agrees with the interpretation that such structure is primarily amorphous with any "graphitic" domains being sub-2nm in scale.³⁹ With increasing carbonization temperature, the material becomes progressively more ordered. **Figure 2-6B** shows the HRTEM micrograph of the CPM-900-A specimen, while **Figure 2-6C** shows the CPM-1100-A sample, which will be demonstrated to possess optimum electrochemical properties. The CPM-1100-A specimen shows evidence of substantial local order, though without the presence of equilibrium graphite phase. The CPM-1400-A specimen (**Figure 2-6D**) is highly ordered. As Raman and XRD will demonstrate the material is now actually partially graphitic, with the domains containing graphite of equilibrium interplanar spacing. All the specimens show HRTEM contrast consistent with what is typically reported for microporous and mesoporous carbons. However we believe that due to ambiguities created by the inevitable pore and material overlap in the TEM specimens, nitrogen sorption analysis, discussed next, is more effective in identifying the porosity.

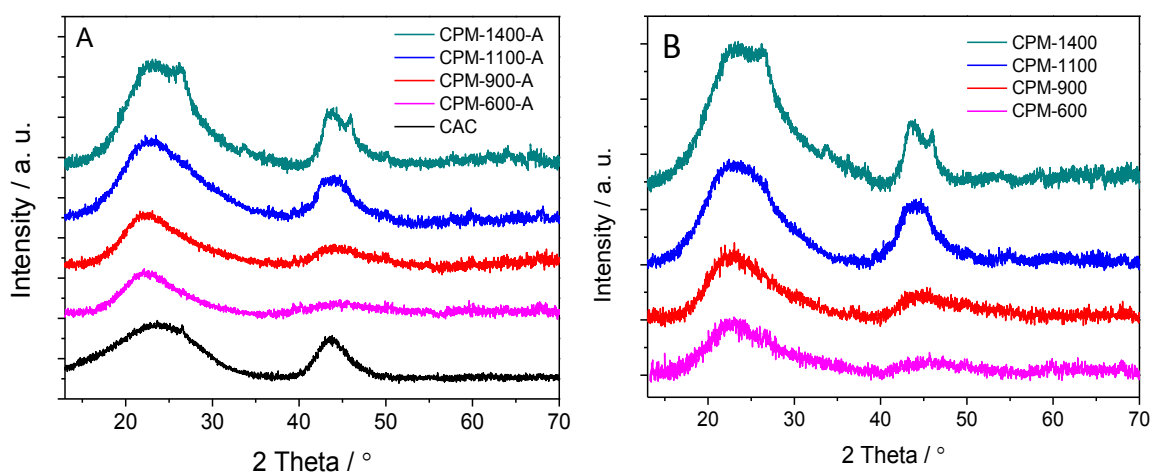


Figure 2-7: (A) XRD patterns of the activated specimens (CPM-A) and of commercial activated carbon (CAC). (B) XRD patterns of the un-activated specimens (CPM).

Figure 2-7A shows the X-ray diffraction (XRD) patterns of the CPM-A specimens along with those of baseline CAC. The XRD patterns of the CPM specimens are shown in **Figure 2-7B**. The results of the XRD analysis, along with the results of Raman and BET, are shown in **Table 2-1**. The average graphene interlayer spacing was calculated from the peak centers. The thickness and average width of the graphitic domains, L_c and L_a , are calculated based on the well-known Scherrer equation, using the FWHM values of (002) at $2\theta \sim 23^\circ$ and (100) at $2\theta \sim 43^\circ$. In the case of the CPM-1400-A there are two overlapping peaks at each position, which may be readily mathematically deconvoluted using the Voigt function. It can be seen that the 300°C activation will not appreciably alter the graphitic order/disorder. In all but the 1400°C specimens, the average thickness of the graphitic domains is ~ 1.8 nm, indicating that they are composed of 4-5 stacked graphene layers (*i.e.*, $1.8/0.38=4.7$).^{40,41} As **Table 2-1** demonstrates, the intergraphene layer (d_{002}) spacing gradually shifts toward lower values with increasing carbonization temperature. However, a comparison of the 600 , 900 and 1100°C specimens, indicates that this trend is quite weak, and that in all cases the spacing is significantly above that of equilibrium graphite (0.3354 nm). Carbonizing at 1400°C creates a clear bimodal distribution in the average d spacings, indicating that finally the temperature is high enough to form equilibrium graphite ($c/2$ measured as 0.334 nm). Based on the ratio of the deconvoluted areas of the peak doublets, the carbon to equilibrium graphite ratio is 4:1 by weight. Interestingly the remaining carbon maintains a dilated intergraphene spacing (0.383 nm), indicating that the formation of graphite occurs *via* nucleation and growth rather than by ordering and shrinkage of the existing lattice. Since the peat moss precursor is heterogeneous, graphite would be expected to form preferentially in regions originally rich in α -cellulose. For CPM-600-A, CPM-900-A, CPM-1100-A, the average value of interlayer spacing are 0.399 nm, 0.395 nm, 0.388 nm, respectively. Such open structures are known to allow for facile Na insertion/extraction between the graphene planes.²⁷ What is unique about the 1100°C

specimen, is that despite having a mean spacing far above that of graphite the material is quite ordered, having a mean graphitic domain width of over 5 nm. The only specimen that shows larger domain dimensions is CPM-1400-A, though it is composed of 20% electrochemically inactive graphite. The baseline CAC possesses comparable domain widths (4 nm), but has a smaller graphene interlayer thickness (0.372 nm). As Raman results will demonstrate, it is also much less ordered / more defective. These attributes, combined with ion diffusional limitations associated CAC's closed particulate morphology, will hinder Na ion transfer and tremendously place it at an electrochemical performance disadvantage.

Table 2-1: Physical parameters and electrochemical properties for CPM, CPM-A and CAC.

Samples	d_{002} (Å)	L_a (nm)	L_c (nm)	I_G/I_D ^a	S_{BET} (m ² g ⁻¹) ^b	V_t (cm ³ g ⁻¹) ^c	Pore vol% (<2nm)	Pore vol% (>2nm)	C_{50mAg}^{-1d} (mAhg ⁻¹)	C_{500mAg}^{-1e} (mAhg ⁻¹)
CPM-600	3.98	1.83	1.80	0.51	55.3	0.069	46.1	53.9	230	93
CPM-900	3.91	2.52	1.79	0.76	45.1	0.059	24.2	75.8	219	91
CPM-1100	3.87	5.11	1.83	0.87	24.5	0.054	4.5	95.5	325	117
CPM-1400	3.82	8.36	1.90	0.89	20.8	0.052	10.7	89.3	275	84
	/3.34	/16.21	/6.31							
CPM-600-A	3.99	1.75	1.80	0.47	369.1	0.26	72.7	27.3	267	150
CPM-900-A	3.95	2.85	1.83	0.71	271.2	0.21	64.7	35.3	280	155
CPM-1100-A	3.88	5.39	1.86	0.86	196.6	0.18	47.9	52.1	332	203
CPM-1400-A	3.83	8.51	2.21	0.91	92.2	0.12	25.2	74.8	294	139
	/3.34	/17.18	/6.25							
CAC	3.72	4.2	1.84	0.26	2050	1.17	61.7	38.3	139	38

^a I_D and I_G are the integrated intensities of D and G- band. ^b Surface area was calculated with Brunauer-Emmett-Teller (BET) method. ^c The total pore volume was determined at a relative pressure of 0.98. ^d Discharge capacity at the 2nd cycle. ^e Reversible capacity at the 35th cycle in the rate tests.

Raman spectroscopy analysis was employed to investigate the structure of the CPM-A specimens. These results, along with the same analysis performed on CAC, are shown in **Figure 2-8A**. All samples exhibit a broad disorder-induced D-band (\approx

1340 cm^{-1}) and in-plane vibrational G-band ($\approx 1580 \text{ cm}^{-1}$). The integral intensity ratio (I_G/I_D) is indicative of the degree of graphitic ordering in the carbons.⁴² The fits of the spectra are shown in **Figure 2-8**.⁴³ As shown in **Table 2-1**, increasing the carbonization temperature to 1400°C leads to a progressively more ordered structure. The 2D peak at $\approx 2680 \text{ cm}^{-1}$ may also be used as a measure of order.^{44,45,46} These are only prevalent in the 1100°C and 1400°C specimens. The CAC specimens are markedly less ordered than any of the CPM. To contrast, for CPM-1100-A and CPM-1400-A the ratio $I_G/I_D = 0.87$ and 0.91 , while for CAC the ratio is 0.26 .

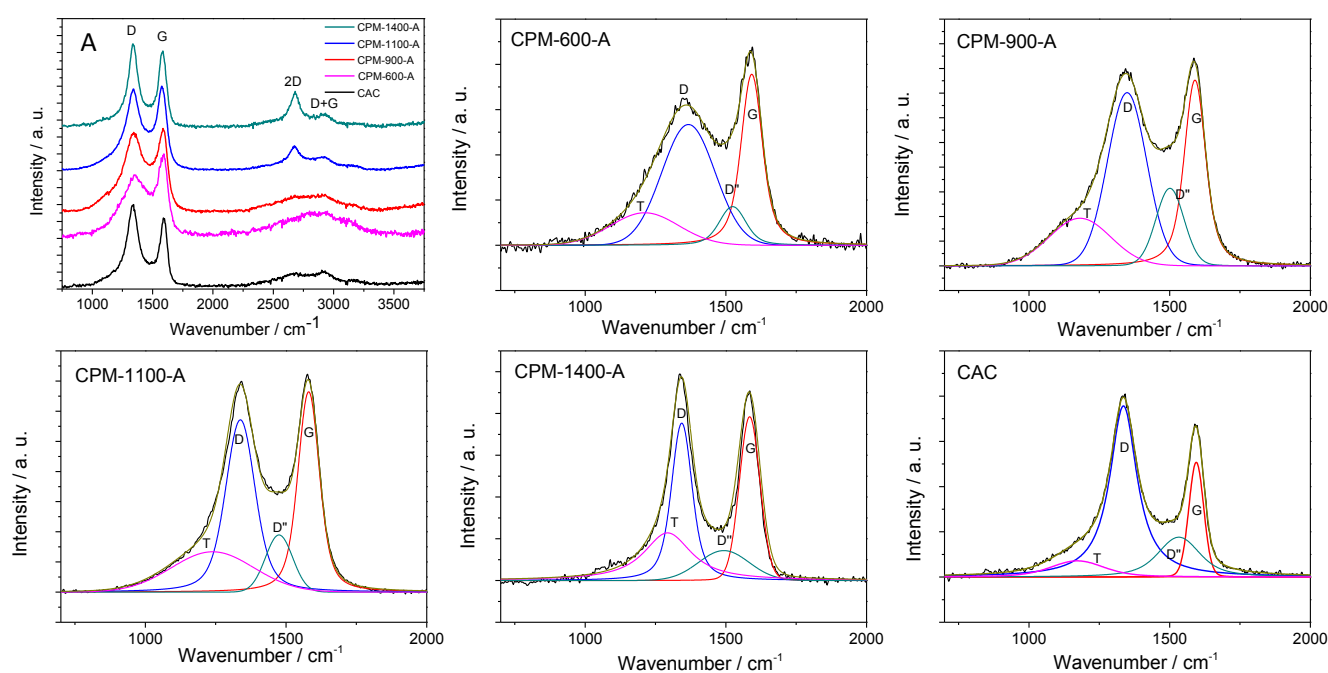


Figure 2-8: Raman spectra of CPM-A, CAC (A) and fitted Raman spectra of CPM-A and CAC specimens.

During the carbonization process, a material composed of primarily α -cellulose would readily graphitize at high temperature due to the long-scale parallel fashion of the linear polysaccharide $(\text{C}_6\text{H}_{10}\text{O}_5)_n$ chains.⁴⁷ However the main components (*ca.* 80wt%) of peat moss are actually hemicellulose (β -, γ -cellulose) and lignin. Unlike α -cellulose, the polysaccharide chain of hemicellulose is much shorter and bifurcates with glycosidically bound branches. Lignin is a three-dimensional, highly cross-linked polyphenolic polymer without any ordered repeating units.⁴⁸ The organization of the

different polymers in the cell walls of peat moss is also shown in **Figure 2-1**. The small amounts of long cellulosic microfibrils (α -cellulose) are embedded in a matrix of interwoven polysaccharides. Shorter branched hemicelluloses increase the linkage among long cellulosic fibers. High content of lignin (*ca.* 50wt%) fills the spaces between cellulose and hemicellulose, and covalently links to the cellulose and other polysaccharides within the cell wall.^{49,50} In short, despite being heterogeneous, the overall peat moss structure is highly cross-linked and non-crystalline, which prevents graphitization at low and moderate temperatures.

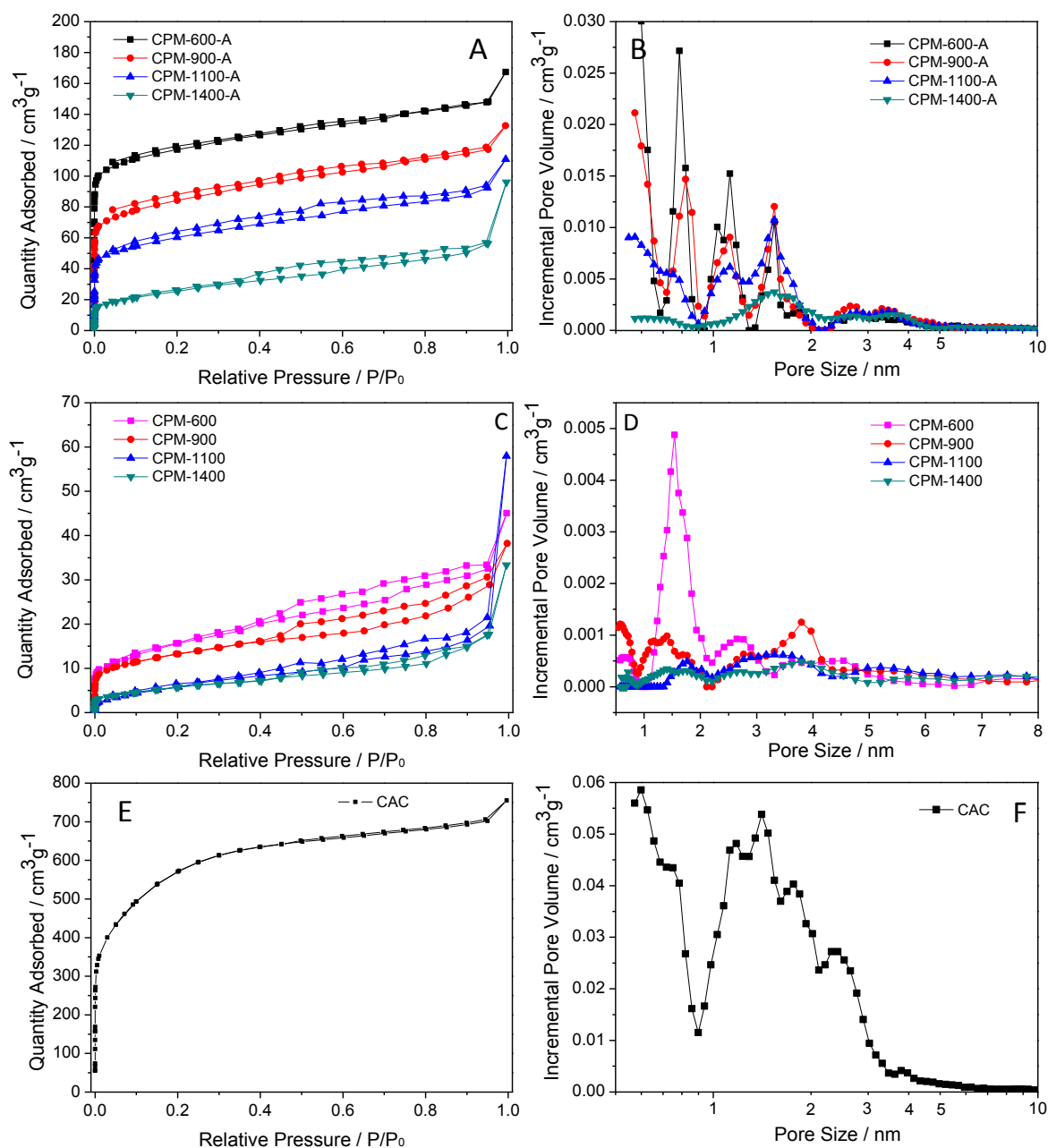


Figure 2-9: (A,C,E) Nitrogen adsorption-desorption isotherms of CPM-A, CPM and CAC specimens. (B,D,F) Pore size distribution calculated from the adsorption isotherms of CPM-A, CPM and CAC specimens, using DFT method.

Figure 2-9A shows the nitrogen adsorption-desorption isotherms CPM-A, while **Figure 2-9B** shows their resultant pore size distributions (obtained by density functional theory (DFT)). The same analysis for the CPM specimens and for CAC baseline are shown in **Figure 2-9(C-F)**. All the adsorption curves of the CPM-A specimens display type I/IV isotherms. **Table 2-1** shows the calculated BET surface

area, and the fraction of pores that are microporous *versus* mesoporous. It can be seen that while air activation does increase the amount of micro and mesoporosity in all specimens, it is progressively less effective for the more ordered/graphitic specimens. This is not unusual since graphitic carbons are known to resist oxidation better than amorphous ones.^{51,52} All the resultant materials, however, are of relatively low surface area, ranging from 55 - 21 m²g⁻¹ for CPM and from 369 - 92 m²g⁻¹ for the CPM-A. To contrast, the surface area of CAC is 2050 m²g⁻¹. Comparing CAC to CPM-1100-A, one observes almost an order of magnitude higher volume of micropores (0.722 cm³g⁻¹ vs. 0.086cm³g⁻¹) and a factor of five higher volume of mesopores (0.448 cm³g⁻¹ vs. 0.093cm³g⁻¹).

Table 2-2: Elemental composition information for CPM, CPM-A and CAC.

Samples	Elemental Analysis				XPS		
	C [wt%]	O [wt%]	N [wt%]	H [wt%]	C [wt%]	O [wt%]	N [wt%]
CPM-600	76.38	13.06	3.45	2.11	82.76	13.35	3.89
CPM-900	84.59	8.02	1.2	1.07	89.01	9.59	1.40
CPM-1100	87.11	4.93	1.03	0.51	93.65	5.28	1.07
CPM-1400	93.35	2.98	0.74	0.29	95.03	3.94	1.03
CPM-600-A	78.85	14.01	3.67	2.21	81.54	15.24	3.22
CPM-900-A	86.38	8.63	1.46	1.19	87.45	11.42	1.13
CPM-1100-A	89.35	5.13	1.05	0.49	93.41	5.84	0.75
CPM-1400-A	93.31	2.68	0.72	0.27	96.29	3.12	0.59
CAC	94.12	4.34	0.12	0.43	95.35	4.65	~0

Table 2-2 presents the combustion elemental analysis and X-ray photoelectron spectroscopy (XPS) results for the specimens, listing the weight percentages of the main elements (C, O, N, H). There is a significant content of heteroatoms both on the surface (XPS) and in the bulk (elemental) of the specimens carbonized at 600 and 900°C. XPS also shows that activation further oxidizes the surface of these more disordered carbons, but has little effect on the surface composition of the 1100°C and 1400°C specimens. As expected, with increasing carbonization temperature there is a significant decrease in the carbons' oxygen, nitrogen and hydrogen content. The

CPM-1100 and CPM-1100-A specimens show comparable oxygen and hydrogen levels to CAC. While their nitrogen content (1.05wt% bulk, 0.75wt% surface for CPM-1100-A) is higher than CAC, it is still relatively negligible in terms of its effect on the electrochemical properties.

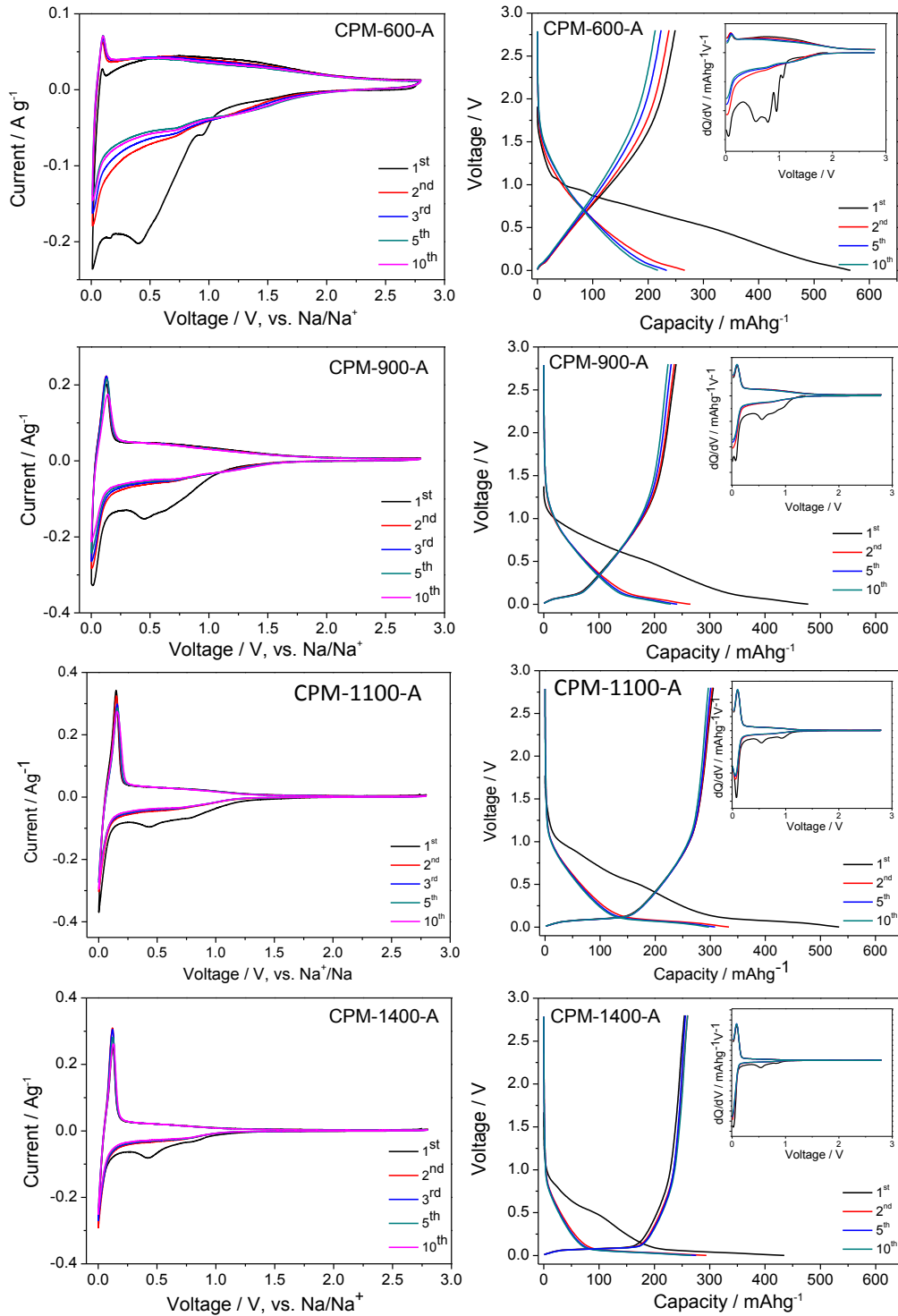


Figure 2-10: Cyclic Voltammogram of CPM-A electrodes between 0.001 and 2.8 V at

a scanning rate of 0.1 mVs^{-1} (Left panels). Galvanostatic discharge/charge curves of CPM-A electrodes at current density of 50 mAhg^{-1} (Right panels).

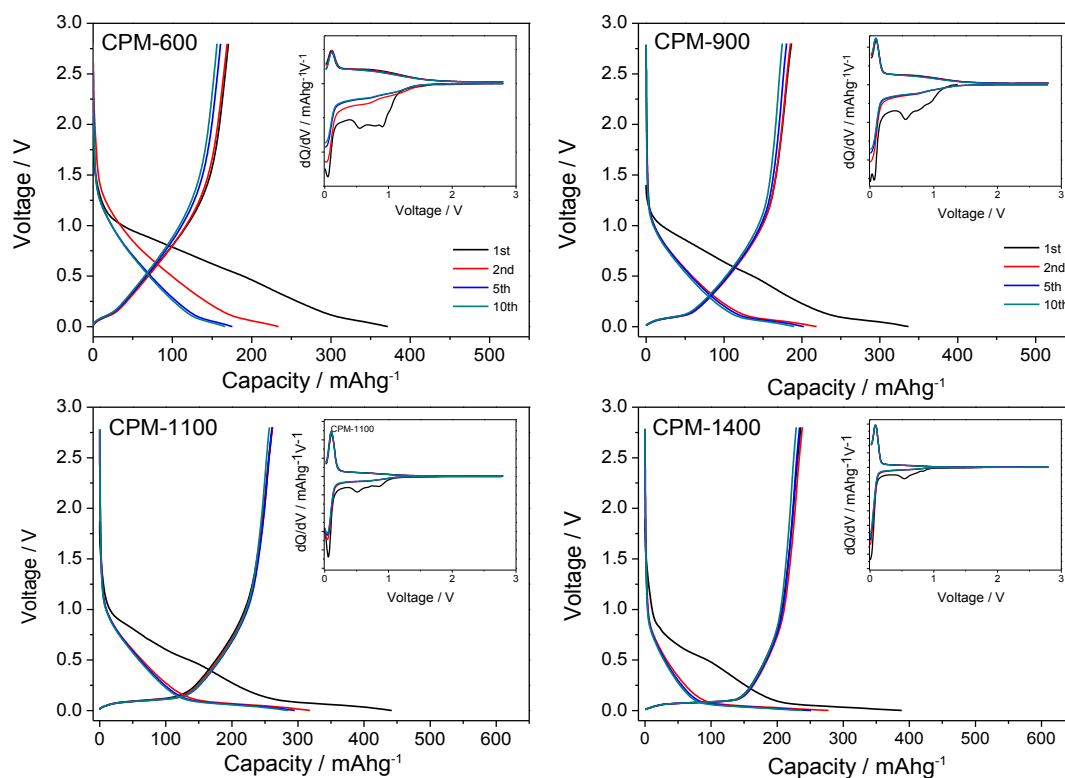


Figure 2-11: Galvanostatic discharge/charge profiles of un-activated CPM electrodes.

To investigate the electrochemical energy storage properties of the carbons we performed cyclic voltammetry (CV) and galvanostatic discharge/charge cycling. The specimens were tested between 0.001 and $2.8 \text{ V vs. Na/Na}^+$. **Figure 2-10** show the CV curve and discharge/charge profile of CPM-A specimens. The inserts of the voltage profile panels presents the derivative curves dQ/dV vs. V , which have similar shapes to the CV's. The galvanostatic data and related derivative curves for the CPM specimens are shown in **Figure 2-10**.

For CPM-1100-A, in the first CV scan, two broad cathodic peaks are visible at $\sim 0.4 \text{ V}$ and 0.75 V , disappearing in the subsequent cycling. These peaks generally attributed to the decomposition of the electrolyte and the formation of SEI (solid electrolyte interface) layer on the carbon surface.²⁹ The formation of SEI and any irreversible insertion of Na into the carbon structure are the main reasons for the initial irreversible capacity loss. At the low voltage region, there is a sharp cathodic

peak near 0 V and a counterpart anodic peak at 0.15 V, resembling the cycle voltammetry behavior of lithium insertion/extraction in graphite.⁵³ Besides the sharp peaks, there is also a pair of weak humps over a wide voltage region (0.2-1.2 V) in both the cathodic and the anodic portions. These pairs of sharp peaks and weak humps correspond to the plateau regions and the sloping regions of the galvanostatic discharge/charge profiles, respectively.

As shown in **Figure 2-10**, for CPM-1100-A the first cycle delivered specific capacities are 532 mAhg⁻¹ (discharge) and 306 mAhg⁻¹ (charge). After 10 cycles, there is still 298 mAhg⁻¹ reversible capacity remaining. This cycling performance may be considered quite outstanding, since there are very few reports of carbonaceous materials displaying over 250 mAhg⁻¹ of stable capacity as a NIB anode.^{28,29} The carbonization temperature has a profound effect on the shape of the voltage versus capacity profiles. In general, a sloping voltage plateau is associated with ion insertion into a material where the insertion sites possess a distribution of energies. A more disordered carbon would possess a wide site energy distribution, and hence would show a substantial fraction of its total capacity at higher voltages. This is the trend that we observe with CPM, with both the total amount and the relative fraction of the charge storage capacity measured above 0.2 V decreasing with I_G/I_D (**Table 2-1** lists I_G/I_D). In CPM-1100-A and CPM-1400-A, a reversible charge/discharge capacity of 196 mAhg⁻¹ (after 10 cycles at 50mAhg⁻¹) can be obtained within a narrow voltage window of 0.001- 0.2 V.

As discussed in the Introduction, this low voltage/low hysteresis plateau behavior resembles the highly attractive capacity *versus* potential profiles of graphite anodes in LIB. Moreover, examining the capacity below 0.2V (**Figure 2-10** including insert) it can be observed that both CPM-1100-A and CPM-1400-A behave quite on par with LIB graphite in terms of displaying almost a negligible charge/discharge voltage hysteresis.

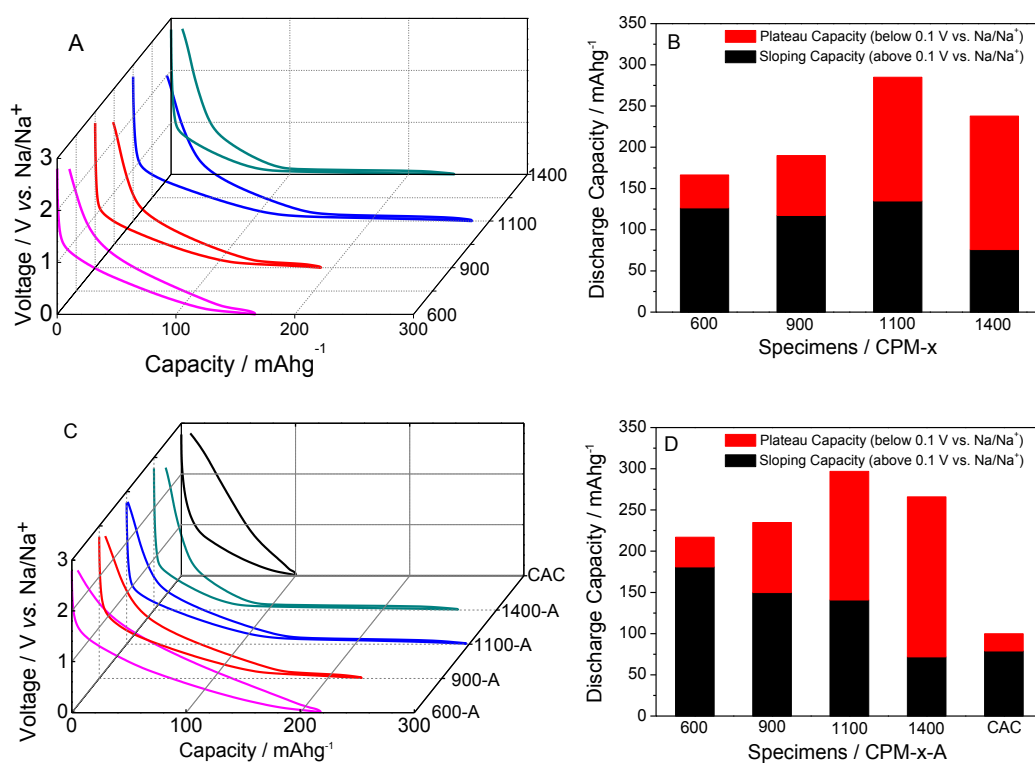


Figure 2-12: (A-C) Potential profiles of CPM, CPM-A and commercial active carbon electrodes. (B, D) Summary of capacity potential distribution of CPM, CPM-A and commercial active carbon electrodes. (10th cycle at current density of 50mAhg⁻¹ in all the figures).

Figure 2-12 shows the potential profiles of CPM-A and CAC specimens. The same type of chart is shown in **Figure 2-12A** for the CPM specimens. For CPM-A (and CPM) with increasing carbonization temperature there is an increasing capacity plateau at the low voltage region. This is interesting and somewhat unexpected since this trend is completely opposite of what one would expect if the low voltage plateau was based on filling of pores by Na metal ("nanopore filling").²¹ As **Table 2-1** demonstrates, the porosity of CPM-A specimen decreases with increasing carbonization temperature. Moreover the CAC samples are highly porous (2050 m²g⁻¹), containing both micropores and mesopores in a volume ratio of 1.6:1. Yet, the reversible capacity of CAC is low and a voltage plateau is nonexistent. Where is a strong trend however is between the total capacity and "flatness" of the low voltage plateaus in CPM and CPM-A, *versus* the degree of ordering in these carbons (I_G/I_D in

Table 2-1). The CAC specimen also fits this trend, being the least ordered of the carbons tested. This phenomenon may be explained by arguing that the more ordered domains would provide Na insertion sites that are more energetically equivalent, and hence lead to progressively flatter plateaus. Effectively the carbons would become "psedo-graphitic" to Na,⁵⁴ offering a chemically similar environment while maintaining a sufficiently dilated interlayer spacing to allow insertion/extraction. The progressive elimination of heteroatoms with increasing carbonization temperature would also help in establishing energetic equivalence of sites, though as demonstrated by the relatively pure CAC this criteria is by itself insufficient. The structure/performance of CPM-1400-A specimen is somewhat obscured by the roughly 20% graphite present in the material. Nevertheless the overall trend is unambiguous.

This trend is also summarized in histogram shown in **Figure 2-12 (B-D)**, where the fraction of the total capacity associated with the plateau below 0.1 V increases with CPM carbonization temperature (16% for CPM-600-A, 36% for CPM-900-A, 53% for CPM-1100-A, 73% for CPM-1400-A). Identical trend is observed for the CPM-600, CPM-900, CPM-1100 and CPM-1400 specimens (**Figure 2-12B**), despite none of them containing significant porosity. In fact considering 100% pore filling by Na in the un-activated CPM specimens (in our opinion a highly optimistic assumption), one obtains capacities of 78, 66, 61 and 54 mAhg⁻¹, for the CPM-600, CPM-900, CPM-1100 and CPM-1400. This is opposite in trend to the measured low voltage capacities. These values also do not account for the total low voltage measured capacities in CPM-900, CPM-1100 and CPM-1400. Conversely the low voltage capacity due to complete pore filling of CAC should be 1317 mAhg⁻¹, which is more than one order of magnitude higher than its capacity throughout the entire voltage range. While some nanopore filling by Na almost certainly occurs for all these materials at low voltages, the data leads us to hypothesize that this is not the dominant charge storage mechanism between 0.1 and 0.001 V.

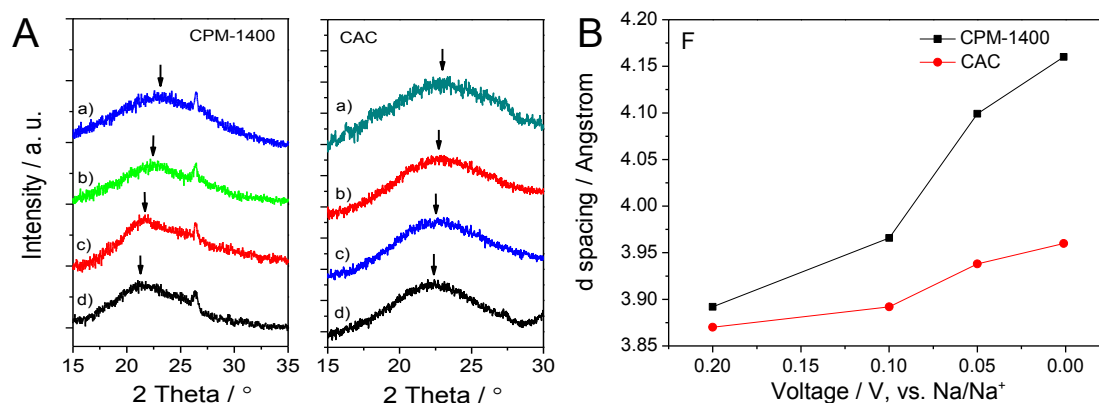


Figure 2-13: (A) XRD spectra for CPM-1400 and CAC electrodes, demonstrating Na intercalation-induced dilation of the interlayer spacing in the majority pseudographitic phase of CPM-1400. The peaks at $2\theta = 26.4^\circ$ are for the secondary (~ 20 wt.%) equilibrium graphite phase also present in CPM-1400, which is inactive and hence remains invariant with voltage. The electrodes were galvanostatically discharged to a) 0.2V, b) 0.1 V, c) 0.05 V, d) 0.001V vs. Na/Na⁺. (B) Dependence of the mean interlayer spacing on discharge voltage, values derived from (A).

Rather, we argue that because the peat moss carbons possess a unique highly ordered pseudo-graphitic structure but with a dilated graphene interlayer spacing, it is possible to achieve significant Na intercalation down to the discharge voltage. To prove this point we carried out XRD analysis to track the structural changes in CPM within the voltage region of 0.2V - 0.001V, performing identical experiments on CAC as a baseline. To obtain a "steady-state" microstructure, the half-cells first received 10 galvanostic charge-discharge cycles at 0.1C. Upon cycle 11, the electrodes were discharged to a) 0.2V, b) 0.1 V, c) 0.05 V, d) 0.001V. The cells were then disassembled in a glove box with the active material being removed from the current collector, cleaned and immediately analyzed. Specimen CPM-1400 was analyzed due to its most ordered structure of all the CPM specimens, and its largest plateau capacity (162mAhg^{-1} below 0.1V vs. Na/Na⁺). Moreover the distinct and sharp (002) Bragg peak from the roughly 20wt.% equilibrium graphite phase within this sample, being completely sodium inactive, served as a highly useful secondary *in-situ* calibration standard.

Figure 2-13A shows the raw XRD data for CPM-1400 and the CAC samples, the

broad (002) pseudo-graphitic peaks being marked by arrows. The clearly discernable shift to lower 2θ values with decreasing terminal discharge voltage reflects the increasing intergraphene spacing due to Na intercalation. **Figure 2-13B** plots the calculated mean interlayer spacing as a function of voltage. As CPM-1400 was discharged from 0.1 V to 0.001 V, the interlayer spacing expanded from 3.96 Å to 4.16 Å. Since the structure was highly ordered, the sodium occupation sites were energetically similar, leading to the observed flat voltage profile not unlike that of Li in graphite. To contrast, within the same voltage range the highly disordered CAC sample demonstrated a much lower interlayer dilation, going from 3.91 Å at 0.1 V to 3.96 Å at 0.001 V.

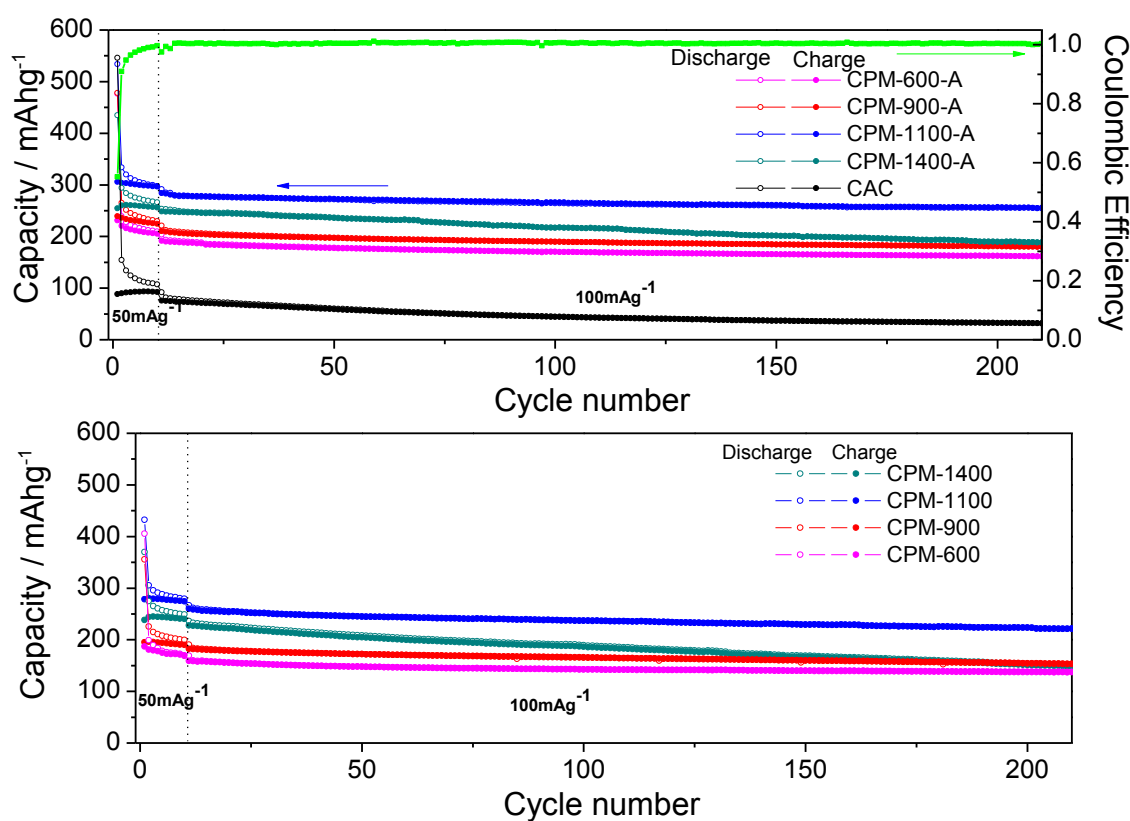


Figure 2-14: Extended cycling performance of the CPM, CPM-A and CAC electrodes, with coulombic efficiency of CPM-1100-A electrode being displayed.

Figure 2-14 (up) shows the cycling capacity retention performance of CPM-A specimens. The same plot is presented for CPM in **Figure 2-14** (bottom). The first ten

cycles were tested at a current density of 50 mAg^{-1} , and the subsequent 200 cycles were tested at 100 mAg^{-1} . As can be observed, CPM-1100-A and CPM-1100 specimens deliver the overall most favorable combination of total capacity and capacity retention, with CPM-1100-A being overall the best. The CPM-1400-A not only provides lower overall capacity but degrades at higher rates. Accelerated degradation may be perhaps related to cycling-induced growth of graphite domains at the expense of the active carbon. Alternatively pores may provide a secondary benefit of buffering the sodiation induced expansion/contraction in the material. With much lower porosity levels, CPM-1400-A may therefore partially disintegrated during cycling.

After 10 cycles at 50 mAg^{-1} the CPM-1100-A specimen demonstrates a reversible capacity of 298 mAhg^{-1} . Over the subsequent 200 discharge/charge cycles at 100 mAg^{-1} , this value decreases to 255 mAhg^{-1} . **Table 2-3** compares the cycling and rate performance behavior of our materials with several state-of-the-art carbons reported in literature. For preparing this comparison, we chose what were to our knowledge the best performing materials at that time. As can be seen, the CPM-1100-A carbon offers some of the best overall capacity and cycling capacity retention combinations.

The volume of the electrode is also a key consideration for a real packed cell. **Figure 2-15A** provides the volumetric capacity of CPM-1100-A as a function of cycle number. These values were obtained by dividing the measured gravimetric capacity by the electrode packing density (0.62 g cm^{-3}). The electrode had a mass loading of 1.2 mg and a geometric area of 1.13 cm^2 . The thickness of the electrode was $17 \text{ }\mu\text{m}$, being obtained from a cross section SEM image (**Figure 2-15B**) and confirmed using a high precision micrometer. **Figure 2-15A** demonstrates that at a rate of 50 mAg^{-1} the CPM-1100-A electrode displays a stable cycling capacity of approximately 200 mAhcm^{-3} , which is a promising volumetric energy value for practical NIBs applications.

Table 2-3: Performance comparison of CPM-1100-A *versus* state of the art NIB carbons reported in literature.

Material	Plateau capacity (capacity below 0.1 V vs. Na/Na ⁺)	Cyclability (discharge capacity)	Rate performance
Pyrolyzed glucose	150 mAhg ⁻¹ (1 st cycle)	Not reported	Not reported
Carbon fibers	<i>ca.</i> 184 mAhg ⁻¹ (1 st cycle)	Not reported	Not reported
Carbon microspheres	Not reported	285 mAhg ⁻¹ at 2 nd cycle 255 mAhg ⁻¹ at 7 th cycle 89% retention over 7 cycles at 40μAcm ⁻²	Not reported
Hard carbon particles	<i>ca.</i> 150 mAhg ⁻¹ at 25mAg ⁻¹	250 mAhg ⁻¹ at 2 nd cycle 225mAhg ⁻¹ at 100 th cycle 88% retention over 100 cycles at 25mAg ⁻¹	Not reported
Templated carbon	<i>ca.</i> 20 mAhg ⁻¹ at 74mAg ⁻¹ (10 th cycle)	180 mAhg ⁻¹ at 10 th cycle, 120mAhg ⁻¹ at 40 th cycle 66.7% retention over 30 cycles at 74mAg ⁻¹	<i>ca.</i> 140mAhg ⁻¹ at 74mAg ⁻¹ <i>ca.</i> 120mAhg ⁻¹ at 740mAg ⁻¹ <i>ca.</i> 100mAhg ⁻¹ at 1.85 Ag ⁻¹
Hollow carbon spheres	<i>ca.</i> 20 mAhg ⁻¹ at 50 mAg ⁻¹ (10 th cycle)	250 mAhg ⁻¹ at 10 th cycle, 160 mAhg ⁻¹ at 100 th cycle 64% retention over 90 cycles at 100mAg ⁻¹	175mAhg ⁻¹ at 200mAg ⁻¹ 150mAhg ⁻¹ at 500mAg ⁻¹ 100mAhg ⁻¹ at 2Ag ⁻¹ 75mAhg ⁻¹ at 5Ag ⁻¹
Hollow carbon nanowires	<i>ca.</i> 150 mAhg ⁻¹ at 50mAg ⁻¹ (10 th cycle)	<i>ca.</i> 255 mAhg ⁻¹ at 10 th cycle <i>ca.</i> 220 mAhg ⁻¹ at 200 th cycle 86% retention over 190 cycles at 50 mAg ⁻¹	<i>ca.</i> 210mAhg ⁻¹ at 250mAg ⁻¹ 149 mAhg ⁻¹ at 500mAg ⁻¹
Carbon nanosheet	<i>ca.</i> 40 mAhg ⁻¹ at 50mAg ⁻¹ (10 th cycle)	<i>ca.</i> 260mAhg ⁻¹ at 10 th cycle <i>ca.</i> 155 mAhg ⁻¹ at 200 th cycle 60% retention over 190 cycles at 50mAg ⁻¹	<i>ca.</i> 190mAhg ⁻¹ at 200mAg ⁻¹ <i>ca.</i> 125mAhg ⁻¹ at 500mAg ⁻¹ <i>ca.</i> 80 mAhg ⁻¹ at 1Ag ⁻¹ 50 mAhg ⁻¹ at 2Ag ⁻¹ 45 mAhg ⁻¹ at 5Ag ⁻¹
CPM-1100-A	161 mAhg ⁻¹ at 50 mAg ⁻¹ (10 th cycle)	284 mAhg ⁻¹ at 10 th cycle 255mAhg ⁻¹ at 210 th cycle 90% retention over 200 cycles at 100mAg ⁻¹	250 mAhg ⁻¹ at 200mAg ⁻¹ 203 mAhg ⁻¹ at 500mAg ⁻¹ 150 mAhg ⁻¹ at 1Ag ⁻¹ 106 mAhg ⁻¹ at 2Ag ⁻¹ 66 mAhg ⁻¹ at 5Ag ⁻¹

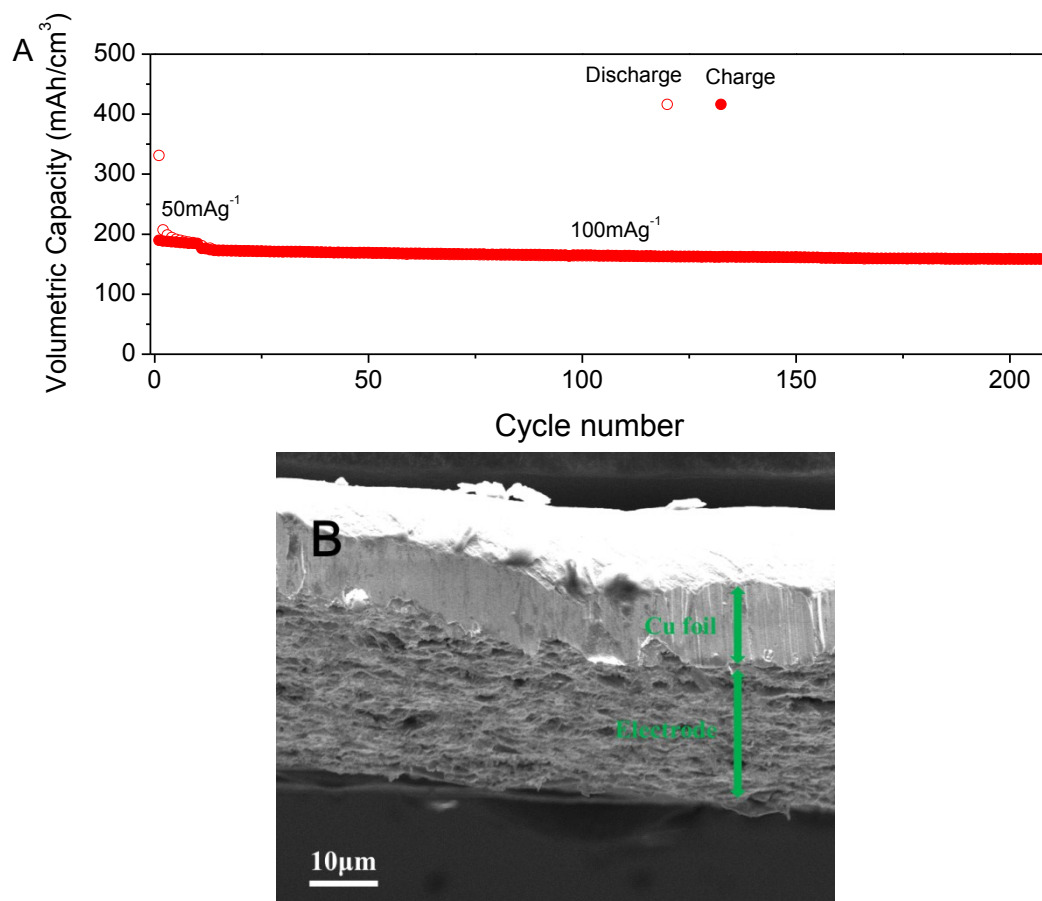


Figure 2-15: (A) Volumetric capacity of CPM-1100-A. (B) Cross section SEM image of the CPM-1100-A electrode.

The cycle 1 coulombic efficiency increased from 43.9% for CPM-600-A, to 50.1% for CPM-900-A, to 57.5% for CPM-1100-A, and 60.1% for CPM-1400-A. Similarly cycle 1 coulombic efficiency increased from 46.1% for CPM-600, to 55% for CPM-900, to 60.7% for CPM-1100, and 64.3% for CPM-1400-A. Of course a progressively decreasing surface area with carbonization temperature (less SEI formation) plays a role in this trend. However the analogous behavior of the low surface area CPM specimens indicates that a progressively lower heteroatom content (discussed ref.⁵⁵) is also critical in reducing the cycle 1 capacity loss. The initial coulombic efficiencies CPM-1100-A and CPM-1400-A are actually somewhat higher than the counterpart values reported for high performance carbonaceous materials with even lower surface areas.^{29,56} This supports the argument for the attractiveness of our materials as NIB anodes. The more ordered - less defective graphitic structures

may also reduce the extent of the irreversible capacity loss reactions in the first cycle, though the exact mechanism needs clarification. In CPM-1100-A the coulombic efficiency increases rapidly to over 90% in the second cycle and stabilizes at $\sim 100\%$ (within measurement accuracy) from the 8th cycle onwards. **Figure 2-14A** (right axis) shows the coulombic efficiency for the CPM-1100-A specimens during cycling. An analogous trend is observed for all but the CPM-1400 specimens, with $\sim 100\%$ efficiency being measured during stable cycling. CPM-1400 however never quite reaches 100% efficiency, performing between 98 - 99% for the majority of the cycling.

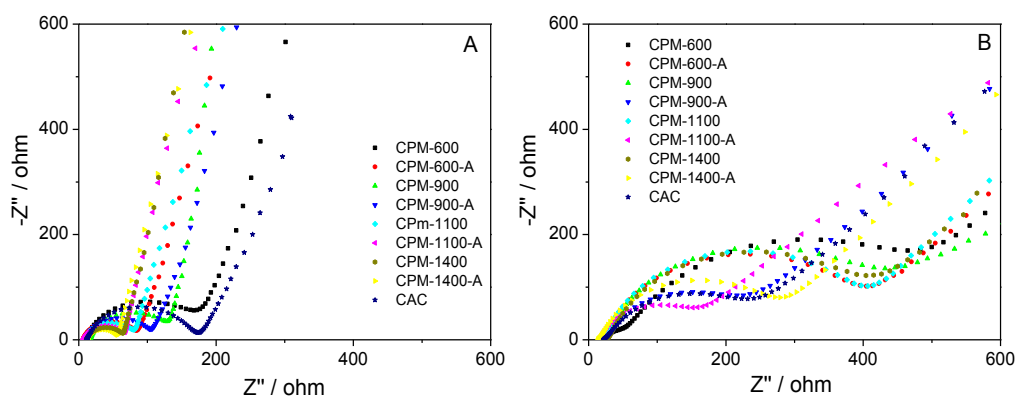


Figure 2-16: (A) Electrochemical impedance spectra of CPM, CPM-A and CAC electrodes before cycling. (B) Electrochemical impedance spectra of CPM, CPM-A and CAC electrodes after cycling for 210 cycles.

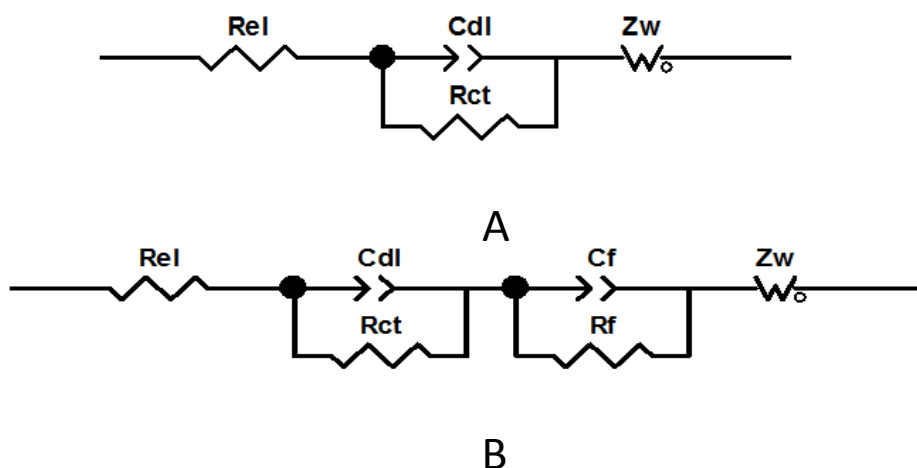


Figure 2-17: Equivalent electronic circuits used to simulate the EIS data. For the spectra of all the as prepared specimens, equivalent circuit (A) was used. R_{el} is the

sum of resistances of electrical connections in the experiment setup including ionic diffusion resistance in the electrolyte. R_{ct} reflects the charge transfer resistance and Z_w (Warburg-type element) represents Na diffusion impedance within carbon materials. For the cycled specimens with SEI layer formed (equivalent circuit B was used), another pair of resistor (R_f) and constant phase element (C_f) represent Na transport through SEI/carbon interface. $R_{ct}+R_f$ is claimed to represent the total charge transfer resistance within all the interfaces and through SEI layer.

Figure 2-16 and **Figure 2-18** show the electrochemical impedance spectra (EIS) analysis of the CPM and CPM-A specimens. **Figure 2-16A** shows the Nyquist of CPM, CPM-A and CAC specimens before cycling. **Figure 2-16B** shows the same analysis but after 210 cycles. The value of $R_{ct}+R_f$, simulated from the fit of the experimental Nyquist plots with the equivalent circuit shown in **Figure 2-17**, represents the combination of charge transfer resistance at the SEI/electrolyte interface and the resistance of Na transport through SEI layer.⁵⁷ The obtained parameters are listed in **Table 2-4**. It is the physically meaningful parameter for analysis of the cycled specimens, which is expected to increase with SEI growth. In LIB applications of graphite materials a substantial rise in $R_{ct}+R_f$ would mean that the initially low surface area electrode was creating new surfaces for SEI formation (SEI preferentially forms of fresh carbon surfaces exposed to the electrolyte rather than on the back of existing SEI), by exfoliating and/or fracturing.⁵⁸ Similarly for high surface area carbons, a cycling induced increase in $R_{ct}+R_f$ signifies some form of material disintegration. While SEI growth in NIB applications is less well understood, a qualitatively similar scenario may be expected. The CPM-1400 and CPM-1400-A specimens have the largest % increase in $R_{ct}+R_f$ versus the initial R_{ct} . These are also the specimens that demonstrate the highest rate of capacity degradation during cycling. Of all the specimens CPM-1100-A shows the lowest value of $R_{ct}+R_f$ (114.7 Ω), indicating that it's the most stable against SEI grows during cycling. For CPM-1100 $R_{ct}+R_f$ is 350.4 Ω . The difference between CPM-1100-A and CPM-1100 supports the argument that pores buffer sodiation induced expansion/contraction (*i.e.* damage) in the matrix.

Figure 2-18(A-B) show the change of $R_{ct}+R_f$ and R_{el} as a function of cycle number in CPM-1100-A and CPM-1400-A electrodes. **Figure 2-18(C-D)** show the raw Nyquist plots in the as-prepared electrodes and after 30, 100, 150 and 210 cycles. As shown in **Figure 2-18A**, the much slower increase of $R_{ct}+R_f$ in CPM-1100-A with increasing cycle number indicates a more stable SEI layer throughout cycling. A stable SEI is known to promote high capacity retention,²⁷ and is likely related to the microstructural features of CPM-1100-A *versus* CPM-1400-A previously discussed.

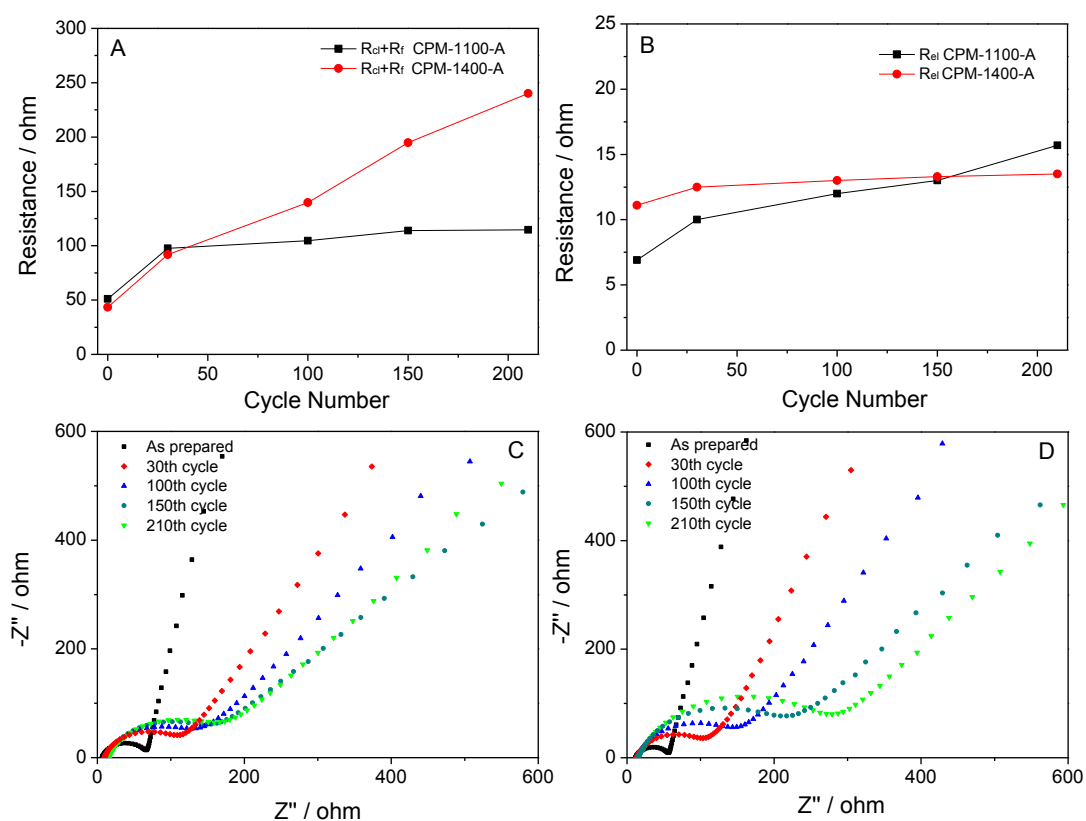


Figure 2-18: (A-B) The total charge transfer resistance within all the interfaces ($R_{ct}+R_f$) and sum of resistance of electrical connections in the experimental setup (R_{el}) changes as functions of the cycle number. (C-D) Electrochemical impedance spectra of CPM-1100-A (C) and CPM-1400-A (D) (As-prepared, 30th cycle, 100th cycle, 150th cycle and 210th cycle).

Table 2-4: Resistance values simulated from modeling the experimental impedance (**Figure 2-16**) using the equivalent circuits shown in **Figure 2-17**.

	CPM-600-A	CPM-900-A	CPM-1100-A	CPM-1400-A
As prepared electrodes				
$R_{el}(\Omega)$	6.4	9.1	6.9	11.1
$R_{ct}(\Omega)$	80.6	100.2	51.1	43.3
Cycled electrodes				
$R_{el}(\Omega)$	15.2	23.8	15.7	13.5
$R_{ct}+R_f(\Omega)$	324.5	182.7	114.7	240.1

	CPM-600	CPM-900	CPM-1100	CPM-1400
As prepared electrodes				
$R_{el}(\Omega)$	9.3	16.1	8.5	11.2
$R_{ct}(\Omega)$	172	119.7	72.1	52.6
Cycled electrodes				
$R_{el}(\Omega)$	24.2	22.8	20.1	23.2
$R_{ct}+R_f(\Omega)$	396	306.1	350.4	335.3

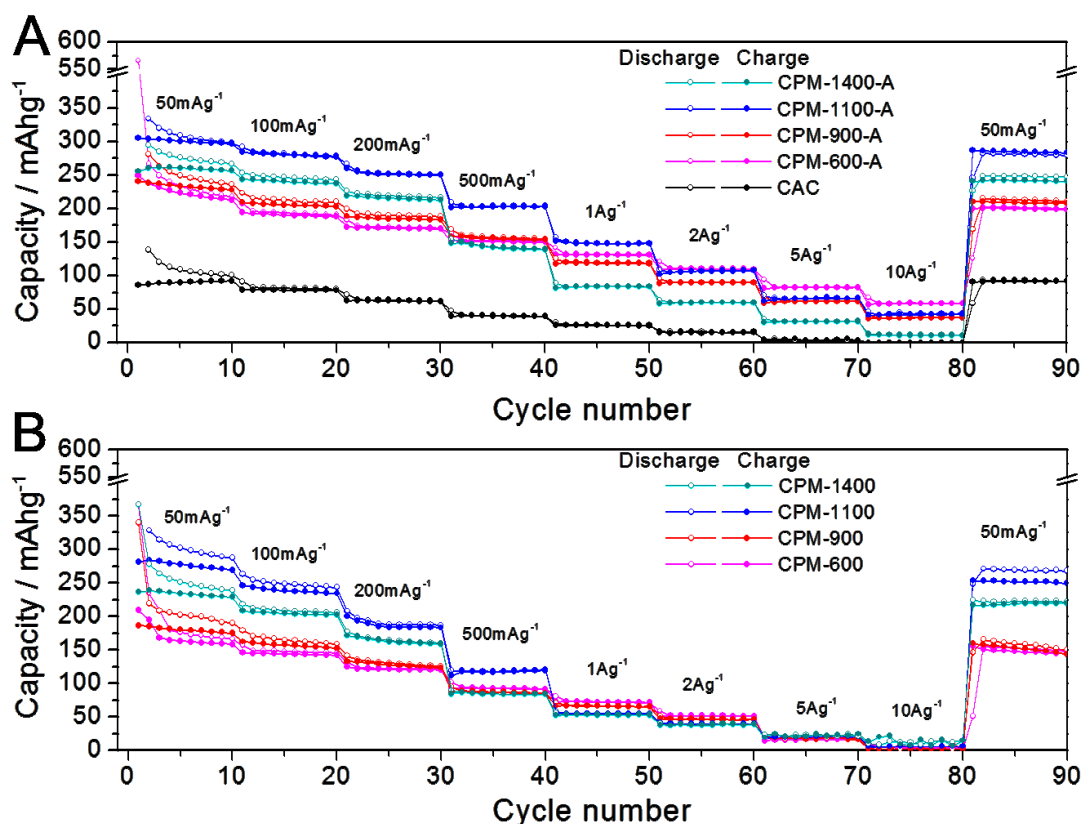


Figure 2-19: Rate performance of CPM-A (A) and CPM (B) electrodes.

Where the really interesting difference between the CPM and CPM-A specimens emerges is in their rate capability, shown in **Figure 2-19**. At high charge rates, such as at 2 and 5 Ag⁻¹, the un-activated samples show effectively negligible capacity.

Conversely the CPM-1100-A, CPM-900-A and CPM-600-A all still perform. The CPM-1100-A specimens provide stable capacities of 203 mAhg⁻¹ at 500mA g⁻¹, 150 mAhg⁻¹ at 1Ag⁻¹, 106 mAhg⁻¹ at 2Ag⁻¹, and 66 mAhg⁻¹ at 5Ag⁻¹, rates over 1Ag⁻¹ being considered very high (e.g. assuming a capacity of 200 mAhg⁻¹, 1Ag⁻¹ is equal to 5C !).

As we argued earlier in the text, the introduction of limited porosity will in effect reduce the required Na ion diffusion distances since the electrolyte will be able to penetrate into the pores. Where this seems to matter the most is at high rates, where it is logical to surmise that Na diffusion in the *bulk* of the carbon may be the rate limited step. Solid-state diffusion of ions has been argued to be the limiting factor for the high rate performance of bulk intercalation electrodes.^{4,5,8,59} The activation process would not affect the solid-state diffusion values of Na in carbon, but could substantially reduce the diffusion distances necessary for full sodiation of the material. Since time is proportional to the diffusion distance squared (Fick's first law), if all else being equal, thinner walls of carbon would sodiate faster. The CPM-1400-A samples have by far the lowest surface area of all the activated specimens (less than 1/2 the surface area of CPM-1100-A), indicating less penetrating porosity and explaining the worse rate capability. Were nano-pore filling to become an important Na storage mechanism in the specimens at high charge/discharge rates, activation would similarly facilitate increased capacity. Comparing the CPM-1100-A specimens to the carbons presented in **Table 2-3**, demonstrates its highly promising rate capability, on par with the more exotic open structures such as hollow carbon spheres and carbon nanosheets. In fact for a given current density in the range of 0.2-2 Ag⁻¹, CPM-1100-A exceeds all the counterpart capacities.

2.4 Conclusion

In this study we synthesized and tested carbons derived from a ubiquitously found biomass precursor, namely peat moss. Taking advantage of the cross-linked

organization of the polymers in the peat moss cell wall, we achieved highly ordered pseudo-graphic structures with a highly dilated graphene interlayer spacing. This allowed for facile Na intercalation into the carbons' bulk, while the high level of order created a chemically homogenous environment for the inserted ions and hence relatively flat voltage profiles. The intrinsically open macroporous structure of the peat moss resulted in sheet-like walls in the post-pyrolyzed carbons that were as thin as 60 nm. To improve the high rate performance we employed mild air activation (300°C) to create sufficient porosity to further reduce the Na diffusion distances. The resultant carbons display superb (some of the best reported in literature) electrochemical performance in numerous respects, including total reversible capacity, cycling stability, rate capability, charge/discharge voltage hysteresis. The exceptional performance, combined with the green and economical method for synthesis, should make carbonized peat moss a highly attractive practical NIB anode material.

2.5 References

- 1 M. D. Slater, D. Kim, E. Lee, C. S. Johnson, *Adv. Funct. Mater.*, 2013, **23**, 947-958.
- 2 H. L. Pan, Y. S. Hu, L. Q. Chen, *Energy Environ. Sci.*, 2013, **6**, 2338-2360.
- 3 Y. L. Cao, L. F. Xiao, W. Wang, D. W. Choi, Z. M. Nie, J. G. Yu, L. V. Saraf, Z. G. Yang, J. Liu, *Adv. Mater.*, 2011, **23**, 3155-3160.
- 4 N. Yabuuchi, M. Kajiyama, J. Iwatate, H. Nishikawa, S. Hitomi, R. Okuyama, R. Usui, Y. Yamada, S. Komaba, *Nat. Mater.*, 2012, **11**, 512-517.
- 5 Y. Shao, J. Xiao, W. Wang, M. Engelhard, X. Chen, Z. Nie, M. Gu, L. Saraf, G. Exarhos, J. Zhang, *et al.*, *Nano Lett.*, 2013, **8**, 3909-3914.
- 6 P. Senguttuvan, G. Rousse, V. Seznec, J. M. Tarascon, M. R. Palacin, *Chem. Mater.*, 2011, **23**, 4109-4111.
- 7 Y. Park, D. S. Shin, S. H. Woo, N. S. Choi, K. H. Shin, S. M. Oh, K. T. Lee, S. Y. Hong, *Adv. Mater.*, 2012, **24**, 3562-3567.

- 8 H. L. Zhu, Z. Jia, Y. C. Chen, N. Weadock, J. Y. Wan, O. Vaaland, X. G. Han, T. Li, L. B. Hu, *Nano Lett.*, 2013, **13**, 3093-3100.
- 9 A. Darwiche, C. Marino, M. T. Sougrati, B. Fraisse, L. Stievano, L. Monconduit, *J. Am. Chem. Soc.*, 2012, **134**, 20805-20811.
- 10 J. W. Wang, X. H. Liu, S. X. Mao, J. Y. Huang, *Nano Lett.*, 2012, **12**, 5897-5902.
- 11 Y. W. Zhu, S. Murali, M. D. Stoller, K. J. Ganesh, W. W. Cai, P. J. Ferreira, A. Pirkle, R. M. Wallace, K. A. Cychoz, M. Thommes, *et al.*. *Science*, 2011, **332**, 1537-1541.
- 12 M. D. Stoller, S. J. Park, Y. W. Zhu, J. H. An, R. S. Ruoff, *Nano Lett.*, 2008, **8**, 3498-3502.
- 13 K. Jost, C. R. Perez, J. K. McDonough, V. Presser, M. Heon, G. Dion, Y. Gogotsi, *Energy Environ. Sci.*, 2011, **4**, 5060-5067.
- 14 L. L. Zhang, X. S. Zhao, *Chem. Soc. Rev.*, 2009, **38**, 2520-2531.
- 15 X. Zhao, C. M. Hayner, M. C. Kung, H. H. Kung, *Adv. Energy Mater.*, 2011, **1**, 1079-1084.
- 16 M. Winter, J. O. Besenhard, M. E. Spahr, P. Novak, *Adv. Mater.*, 1998, **10**, 725-763.
- 17 D. Linden, T. B. Reddy, *Handbook of Batteries*; McGRAW-HILL, INC; New York, 2002.
- 18 J. R. Dahn, *Phys. Rev. B*, 1991, **44**, 9170-9177.
- 19 E. Peled, C. Menachem, D. BarTow, A. Melman, *J. Electrochem. Soc.*, 1996, **143**, 4-7.
- 20 Z. G. Yang, J. L. Zhang, M. C. W. Kintner-Meyer, X. C. Lu, D. W. Choi, J. P. Lemmon, J. Liu, *Chem. Rev.*, 2011, **111**, 3577-3613.
- 21 D. A. Stevens, J. R. Dahn, *J. Electrochem. Soc.*, 2001, **148**, 803-811.
- 22 D. A. Stevens, J. R. Dahn, *J. Electrochem. Soc.*, 2000, **147**, 1271-1273.
- 23 P. Thomas, D. Billaud, *Electrochim. Acta*, 2000, **46**, 39-47.

- 24 R. Alcantara, P. Lavela, G. F. Ortiz, J. L. Tirado, *Electrochem. Solid St.*, 2005, **8**, 222-225.
- 25 S. Komaba, W. Murata, T. Ishikawa, N. Yabuuchi, T. Ozeki, T. Nakayama, A. Ogata, K. Gotoh, K. Fujiwara, *Adv. Funct. Mater.*, 2011, **21**, 3859-3867.
- 26 S. Wenzel, T. Hara, J. Janek, P. Adelhelm, *Energy Environ. Sci.*, 2011, **4**, 3342-3345.
- 27 K. Tang, L. J. Fu, R. J. White, L. H. Yu, M. M. Titirici, M. Antonietti, J. Maier, *Adv. Energy Mater.*, 2012, **2**, 873-877.
- 28 H. G. Wang, Z. Wu, F. L. Meng, D. L. Ma, X. L. Huang, L. M. Wang, X. B. Zhang, *ChemSusChem*, 2013, **6**, 56-60.
- 29 Y. Cao, L. Xiao, M. L. Sushko, W. Wang, B. Schwenzer, J. Xiao, Z. Nie, L. V. Saraf, Z. Yang, J. Liu, *Nano Lett.*, 2012, **12**, 3783-3787.
- 30 C. R. Perez, S. H. Yeon, J. Segalini, V. Presser, P. L. Taberna, P. Simon, Y. Gogotsi, *Adv. Funct. Mater.*, 2013, **23**, 1081-1089.
- 31 J. T. Zhang, X. S. Zhao, *ChemSusChem*, 2012, **5**, 818-841.
- 32 M. M. Titirici, A. Thomas, S. H. Yu, J. O. Muller, M. Antonietti, *Chem. Mater.*, 2007, **19**, 4205-4212.
- 33 C. G. Bain, A. Bonn, R. Stoneman, S. Chapman, A. Coupar, M. Evans, B. Gearey, M. Howat, C. Keenleyside, J. Labadz, *et al.* IUCN UK *Commission of Inquiry on Peatlands* 2011.
- 34 N. T. Plank, *Am. J. Bot.*, 1946, **33**, 335-337.
- 35 J. R. Dahn, T. Zheng, Y. H. Liu, J. S. Xue, *Science*, 1995, **270**, 590-593.
- 36 H. C. Bold, *Morphology of Plants*; Joanna Cotler Books; 1967; pp 225-229.
- 37 D. Klemm, B. Heublein, H. P. Fink, A. Bohn, *Angew. Chem., Int. Ed.*, 2005, **44**, 3358-3393.
- 38 D. Y. Kim, Y. Nishiyama, M. Wada, S. Kuga, *Carbon*, 2001, **39**, 1051-1056.
- 39 Y. P. Wu, C. R. Wan, C. Y. Jiang, S. B. Fang, Y. Y. Jiang, *Carbon*, 1999, **37**,

1901-1908.

- 40 B. E. Warren, *J. Chem. Phys.*, 1934, **2**, 551-555.
- 41 A. K. Kercher, D. C. Nagle, *Carbon*, 2003, **41**, 15-27.
- 42 C. Portet, G. Yushin, Y. Gogotsi, *Carbon*, 2007, **45**, 2511-2518.
- 43 S. Yamauchi, Y. Kurimoto, *J. Wood Sci.*, 2003, **49**, 235-240.
- 44 G. Eda, M. Chhowalla, *Adv. Mater.*, 2010, **22**, 2392-2415.
- 45 C. Y. Su, Y. P. Xu, W. J. Zhang, J. W. Zhao, X. H. Tang, C. H. Tsai, L. J. Li, *Chem. Mater.*, 2009, **21**, 5674-5680.
- 46 S. A. Shojaee, A. Zandiatashbar, N. Koratkar, D. A. Lucca, *Carbon*, 2013, **62**, 510-513.
- 47 C. E. Byrne, D. C. Nagle, *Carbon*, 1997, **35**, 259-266.
- 48 R. K. Sharma, J. B. Wooten, V. L. Baliga, X. H. Lin, W. G. Chan, M. R. Hajaligol, *Fuel*, 2004, **83**, 1469-1482.
- 49 K. Iiyama, T. B. T. Lam, B. A. Stone, *Plant Physiol.*, 1994, **104**, 315-320.
- 50 M. Chabannes, K. Ruel, A. Yoshinaga, B. Chabbert, A. Jauneau, J. P. Joseleau, A. M. Boudet, *Plant J.*, 2001, **28**, 271-282.
- 51 Y. Ando, X. Zhao, H. Shimoyama, *Carbon*, 2001, **39**, 569-574.
- 52 Y. S. Park, Y. C. Choi, K. S. Kim, D. C. Chung, D. J. Bae, K. H. An, S. C. Lim, X. Y. Zhu, Y. H. Lee, *Carbon*, 2001, **39**, 655-661.
- 53 Y. L. Cao, L. F. Xiao, X. P. Ai, H. X. Yang, *Electrochem. Solid St.*, 2003, **6**, 30-33.
- 54 S. Flandrois, B. Simon, *Carbon*, 1999, **37**, 165-180.
- 55 Y. Mao, H. Duan, B. Xu, L. Zhang, Y. S. Hu, C. C. Zhao, Z. X. Wang, L. Q. Chen, Y. S. Yang, *Energy Environ. Sci.*, 2012, **5**, 7950-7955.
- 56 Z. H. Wang, L. Qie, L. X. Yuan, W. X. Zhang, X. L. Hu, Y. H. Huang, *Carbon*, 2013, **55**, 328-334.
- 57 E. Barsoukov, J. H. Kim, J. H. Kim, C. O. Yoon, H. Lee, *Solid State Ion.*, 1999, **116**, 249-261.

58 M. D. Levi, D. Aurbach, *J. Phys. Chem. B*, 1997, **101**, 4630-4640.

59 Z. Chen, V. Augustyn, X. L. Jia, Q. F. Xiao, B. Dunn, Y. F. Lu, *ACS Nano*, 2012, **6**, 4319-4327.

3

Peanut Shell Hybrid Sodium Ion Capacitor with Extreme Energy - Power Rivals Lithium Ion Capacitors*

3.1 Introduction

Electrical energy storage (EES) systems play a crucial role in consumer electronics, automotive, aerospace and stationary markets. Due to sodium's effectively inexhaustible and democratically distributed reserves, Na - ion based energy storage devices are a promising alternative to the well-developed Li - ion technologies.^{1,2,3,4,5,6,7,8,9,10,11,12,13,14,15,16} There are primarily two types of devices for energy storage; batteries *e.g.*^{17, 18, 19, 20, 21} and electrochemical capacitors *e.g.*^{22,23,24,25,26,27,28,29,30,31,32,33,34}. The former offers a high energy density while the later offers high power. For instance, commercial lithium ion batteries deliver a specific energy upwards of 200 Whkg⁻¹, but with a maximum specific power being below 350 Wkg⁻¹. By contrast most electrochemical capacitors possess specific power values as high as 10 kW kg⁻¹, but with specific energies in the 5 Wh kg⁻¹ range. Yet a key target for an advanced electrical energy storage device is to deliver both high energy and high power in a single system.^{35,36}

A hybrid ion capacitor is a relatively new device that is intermediate in energy and powder between batteries and supercapacitors. Since there is the potential to span the

* Material in this chapter has been published in:
Jia Ding, Huanlei Wang, Zhi Li, Kai Cui, Dimitre Karpuzov, Xuehai Tan, Alireza Kohandehghan, David Mitlin, *Energy & Environmental Science*, 2015, 8, 941-955.

energy-power divide between the two systems, hybrid devices are attracting increasing scientific attention.^{37,38,39,40,41,42,43,44,45,46,47,48} The hybrid ion capacitor couples a high capacity bulk intercalation based battery-style negative electrode (anode) and a high rate surface adsorption based capacitor-style positive electrode (cathode). When employing Na^+ and counter ions such as ClO_4^- as charge carriers, the device is termed NIC, *i.e.* sodium ion capacitor.^{38,43,45}

Overall, the NIC field is quite young, with more research into improved electrode materials being desirable. Previously, researchers have primarily focused on improving the power capability of the anode in order to catch up with the fast kinetics of the capacitive cathode.^{39,42,44,46} NIC devices have been recently fabricated using the following anode-cathode combinations: $\text{V}_2\text{O}_5/\text{CNT}//\text{AC}$,³⁸ $\text{Na}_x\text{H}_{2-x}\text{Ti}_3\text{O}_7//\text{AC}$ ⁴³, with AC meaning conventional activated carbon. This creates a necessity to include excess mass (*i.e.* volume), generally several times more than that of the anode, in order to achieve the charge balance between the two electrodes.^{39,43,44} The Na ion insertion processes into the bulk of the negative electrodes are known to be substantially more kinetically sluggish than those for Li,^{4,49,50} posing a secondary major challenge to achieving attractive Na ion - based hybrid devices.

An inexpensive carbon-based negative electrode with a Na redox potential near Na/Na^+ would not only provide a cost advantage over the inherently more costly inorganic materials but would also maximize the device energy density.^{11,40,49,51,52} Ideally such electrode materials would also be truly green,^{7,8,20,26,30,31,33,47,53,54,55,56,57,58,59,60,61} being derived from organic waste products that otherwise possess no economic value. Peanuts are a globally cultivated legume food staple, with the peanut shells having only limited commercial end-use as filler in animal feed or as charcoal.⁶² In 2010 the peanut plant was cultivated on 21 million hectares worldwide,⁶³ producing approximately 20 million tons, with an estimated value of 9 billion USD.⁶⁴ This produces roughly 6 million tons of peanut shell waste. Researchers have prepared activated carbons from peanut shells and explored their

applications in environmental science (*e.g.* sorbents for organic and metal pollutants removal^{65,66}) and energy storage (*e.g.* supercapacitor,^{67,68} lithium ion battery^{69,70}). These "classical" activated carbons were prepared by direct pyrolysis followed by high temperature activation.^{62,67,71,72} In terms of the synthesis methodology and by the resultant structure and performance, such ACs are analogous to commercial products, which are micro-scale particulates with tortuous 3D pore networks. In terms of the synthesis methodology and by the resultant structure and performance, such ACs are analogous to commercial products, which are micro-scale particulates with tortuous 3D pore networks. In this work we take an alternative approach: We tailor the synthesis process to take full advantage of the unique structure of the peanut shell and actually achieve two fundamentally different (anode *vs.* cathode) very high performance electrodes from the same precursor.

3.2 Experimental procedures

3.2.1 Materials

We employed shells from the peanuts grown and roasted in the Shandong region of China, bags of which the author (HW) gave to the research group as a going away gift. The obtained biomass was firstly soaked in ethanol for 2 weeks, and then washed with MQ-water (Ultrapure water with 18.2 M Ω ·cm at 25 °C obtained in Milli-Q water purifier system, Millipore Corporation) and thoroughly dried before use. Rough grinding was used to separate the inner from the outer peanut shell. The PSNC cathode materials were synthesized as follows: A ratio of 1.5 g of outer shell, 2.5 mL of concentrated sulfuric acid and 50 mL of MQ-water were sealed in a 100 mL stainless steel autoclave. The autoclave was heated at 180°C for 48 h and then cooled down naturally. The resulting biochar was collected by filtration, washed with MQ-water and then dried. The yield of biochar is approximately 0.8 g. The dried biochar and activation agent (KOH), in a mass ratio of 1:2 or 1:3, were thoroughly

ground and mixed using an agate mortar and pestle. Activation was carried out in a tubular furnace at 800 or 850 °C for 1h under argon flow. The activated samples were thoroughly washed with 2M HCl and MQ-water, and finally dried in an oven at 100°C overnight. The final yield of the PSNC carbons was in the 19 - 29% range (based on the weight of the biochar). The PSOC anode materials were synthesized as follows: A mass of 2g of the inner shell carbonized in argon at 1200°C for 6 h. This resulted in a yield of approximately 0.7 g, *i.e.* 35%. To remove impurities the obtained carbon was thoroughly washed using 20% KOH at 70°C for 2h, and 2M HCl at 60°C for 15 h, followed by MQ-water. Activation for the PSOC-A was performed at 300°C for 9 h with dry air flown at 50 sccm min⁻¹. The activated carbons were then washed again using the above procedure.

3.2.2 Material characterization

The surface area and porous texture of carbon materials are characterized by nitrogen adsorption at 77 K (Quantachrome Autosorb⁻¹). Prior to the gas sorption measurements, the samples were outgassed at 250 °C for 4 h under a vacuum. The pore size distribution (PSD) being calculated using density functional theory (DFT) model from the adsorption branch. The pore size distributions were evaluated by a nonlocal DFT method using nitrogen adsorption data and assuming slit-pore geometry. To characterize the morphology of the carbon samples, field emission scanning electron microscopy (FE-SEM) (Hitachi S-4800) and transmission electron microscopy (TEM) (JEOL 2200FS, 200 kV) are used. Low loss electron energy loss spectroscopy (EELS) was performed with scanning TEM (STEM) mode with a nominal electron beam size of 0.5nm. The carbon compact's electrical conductivity was measured using Pro4 from Lucas Laboratories. X-ray photoelectron spectroscopy (XPS) measurements are performed on an ULTRA (Kratos Analytical) spectrometer using monochromatic Al-K_α radiation ($h\nu= 1486.6$ eV) run at 210 W. Before XPS analysis, the samples were dried at 110 °C in vacuum oven overnight to remove the

absorbed water. X-ray diffraction (XRD) analysis was performed using a Bruker AXS D8 Discover diffractometer with the Cu K α radiation. The Raman spectra were recorded with a confocal microprobe Raman system (Thermo Nicolet Almega XR Raman Microscope).

3.2.3 Electrochemical testing

All the electrodes were prepared by coating electrodes slurries (75 wt% active material, 15 wt% carbon black, and 10 wt% polyvinylidenedifluoride dissolved in *N*-methylpyrrolidone) on stainless steel spacers, and then dried at 120°C under vacuum overnight. The typical mass loading of the electrodes was 0.4 mg cm⁻² and each electrode has area of 1.77cm². To ensure that this mass loading was adequate for representing the electrochemical performance of a higher loaded electrode, additional testing was performed on both the cathodes and the anodes loaded with 2 mg cm⁻². Commercial mass loading electrodes (15 mg cm⁻²) were prepared identically but pressed at 100 MPa in the final step. Half cells were constructed using standard 2032 button cells, with Na metal as the counter electrode, a polyethylene-based separator, and 1M NaClO₄ in 1:1 (volume ratio) ethylene carbonate (EC): die1thyl carbonate (DEC) as the electrolyte. Button cell - based Na-ion capacitor (NIC) devices were constructed using opposing carbon electrodes with the same separator and electrolyte. All the cell fabrication and disassembly was performed inside an Ar filled glove box with sub-0.1 ppm water and oxygen contents. To confirm that passivation of Na metal was avoided we cycled Na-Na cells. There is no degradation of Na-Na cell during the tested 5,000 cycles. Galvanostatic charge/discharge profiles were performed using the BT2000 Arbin electrochemical workstation. Cycling voltammetry and electrochemical impedance spectroscopy (EIS) measurements performed using a Solartron 1470 Multistat system.

3.3 Results and discussion

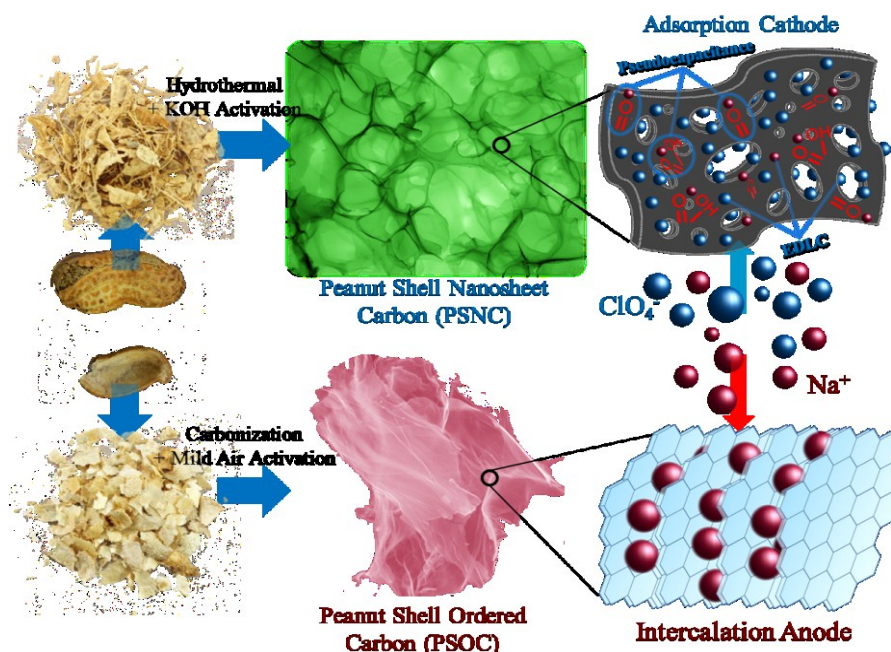


Figure 3-1: Material synthesis process employed for each of the electrodes and the relevant cathode/anode charge storage mechanisms in the sodium ion capacitor (NIC).

Figure 3-1 illustrates the material synthesis process employed for each of the electrodes, as well as the relevant cathode/anode charge storage mechanisms, to be discussed later in the text. The peanut shell was firstly separated into two parts. The inner portion of the shell was used as the precursor for the negative electrode (designated "anode"). The anodes were prepared by carbonization (1200°C) in argon, followed by a mild low temperature (300°C) activation treatment in air. Unlike conventional high temperature activation, typically performed in excess of 600°C, this treatment was unique in introducing sufficient porosity but not destroying the macroscopic sheet-like architecture of the precursor. Because of their resultant structure, these materials are labelled Peanut Shell Ordered Carbon PSOC. Since not all specimens were activated, we added the ending "-A" *i.e.* PSOC-A to the ones that were. The outer rough shell was employed as the precursor for the positive electrodes ("cathode"). These carbons were prepared by hydrothermal treatment (described in experimental) followed by KOH chemical activation at 800 - 850 °C in argon.

Because of their resultant structure, these carbons are labelled Peanut Shell Nanosheet Carbon PSNC. The specific nomenclature is PSNC- x - y , where x refer to the mass ratio between the KOH and the biochar obtained after the hydrothermal treatment, while y refer to the activation temperature. A high surface area Commercial Activated Carbon (NORIT A SUPRA, steam activated), labeled CAC, was also employed as baseline for cathode testing.

The decision to employ the inner shell as the anode and the outer shell as the cathode was based on our understanding of the differences in their plant structure, and how those may be transformed to the target final electrodes' microstructure. The peanut shell is primarily a combination of cellulose, hemicellulose and lignin. However its tissue is highly heterogeneous, with the inner versus the outer shell containing different relative fractions and distribution of each phase. Our sodium ion capacitor (NIC) device consists of an intercalation anode and an adsorption cathode, requiring carbons with fundamentally different degrees of graphene ordering, surface area/porosity, and surface functionality for each electrode.

We chose the inner shell for the anode because it is the most homogenous portion of the shell, being primarily composed of lignin. Lignin is a three-dimensional, highly cross-linked polyphenolic polymer without any ordered repeating units. This lignin-rich tissue prevented large-scale formation of equilibrium graphite during high temperature pyrolysis but allowed for pseudographitic ordering of the defective graphene planes. Such ordering results in a structure composed of highly inter-dilated graphene layers (as compared to equilibrium graphite), which is thus able to easily intercalate the large Na ions. The NIC's battery-like ion intercalation anode does not need to possess a high surface area, as ion adsorption was not a significant charge storage mechanism. Therefore the inner shell's relative homogeneity was not a major concern, as it did not require to be separated into nanosheets, etc. through preferential chemical etching.

Conversely the NICs capacitor-like adsorption cathode required a very high

surface area and facile ion diffusion/access through the electrolyte. We were looking for a precursor that ideally could be transformed in to an electrochemically graphene-like analogue. From our previous work on processing plant-based materials we knew that the key to achieving such properties is to begin with a precursor that is highly heterogeneous but with nano-scale periodicity. We needed something where one or several of the phases could be preferentially etched while leaving behind intact sheets or other 2-D structures. The outer skin of the peanut shell was cellulose-rich but highly heterogeneous. It consists of an interconnected cellulosic fibril network (crystalline cellulose), with the individual microfibrils being roughly 10 - 30 nm in diameter. These microfibrils are interlinked by a minority phase of much shorter branched polysaccharide tethers (hemicellulose) and polyphenolic polymers (lignin).⁷³ Such multi-phase tissue, abundant in cellulose fibrils, is an ideal precursor to achieve interconnected carbon nanosheets through a hydrothermal + chemical activation process, which in parallel adds capacitance enhancing surface functional groups.

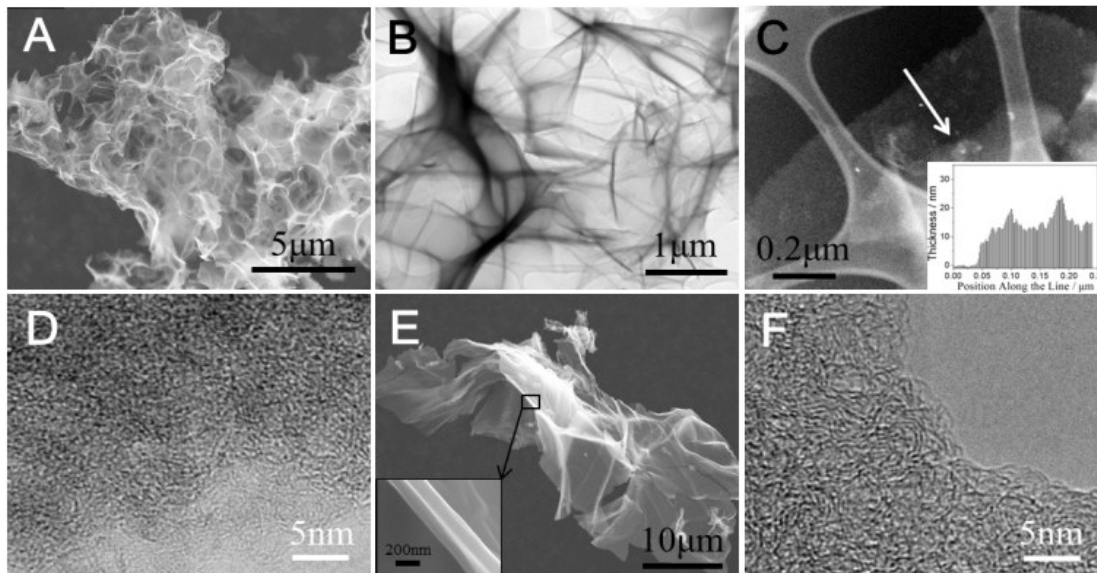


Figure 3-2: (A) Low magnification SEM micrograph illustrating the macroscopic morphology of PSNC-3-800. (B) TEM micrograph of PSNC-3-800 highlighting the morphology of the carbon nanosheets. (C) HAADF image (holey carbon support also visible) and insert of a thickness profile of PSNC-3-800, measured with low loss EELS along the white arrow. (D) HRTEM micrograph of PSNC-3-800. (E) Low magnification SEM micrograph highlighting the morphology of PSOC-A with an insert highlighting the thickness of the carbon sheet. (F) HRTEM micrograph of

PSOC-A.

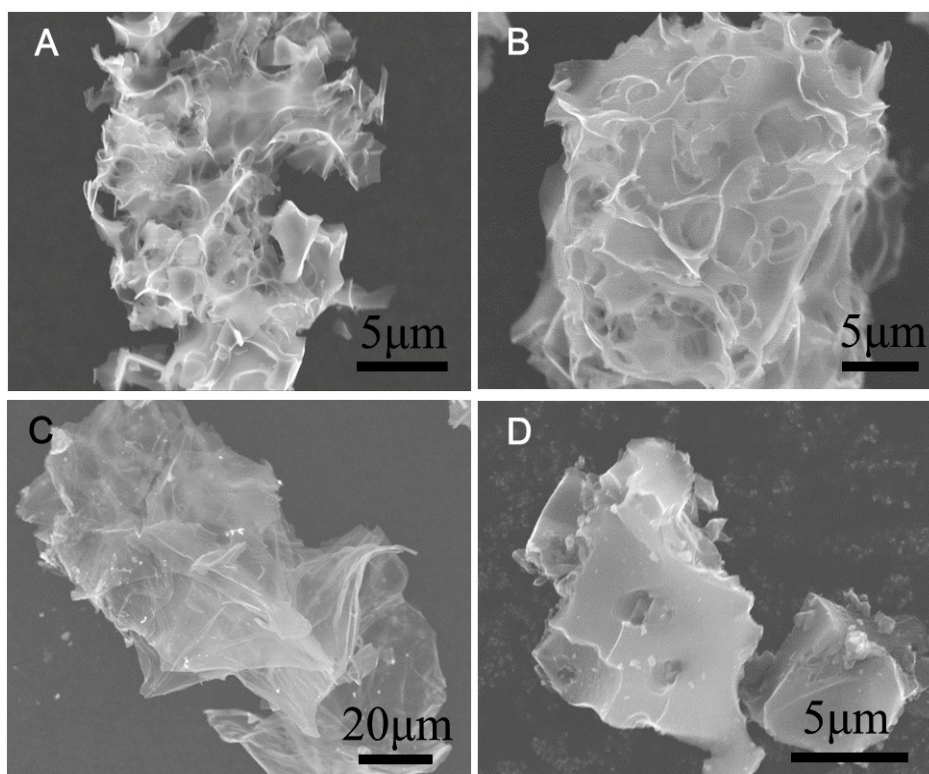


Figure 3-3: SEM micrographs of (A) PSNC-3-850 and (B) PSNC-2-800, (C) PSOC, (D) the baseline commercial activated carbon (CAC).

Figure 3-2 displays a low magnification scanning electron microscopy (SEM) micrograph of PSNC-3-800. **Figure 3-3D** shows CAC, which is a micron - scale 3D particulate. Conversely, PSNC-3-800 morphologically resembles a macroscopically open sponge. **Figure 3-3(A-B)** display the SEM micrographs of PSNC-3-850 and PSNC-2-800. Both carbons possess an analogous morphology as PSNC-3-800, although with decreasing levels of macroscopic "openness" in the same order.

The morphology of PSNC is attributable to a synthesis strategy that is tailored to take the maximum advantage of the structure of the outer peanut shell. Under the relatively aggressive conditions of a hydrothermal treatment, the minority non-crystalline components are hydrolyzed and dissolved. However the interconnected cellulosic fibril network is not fully dissolved. Rather, the hydrothermal process degrades the overall crystallinity and loosens the connections between the microfibrils. The hydrothermal process also partially carbonizes them, resulting in the preservation of a cellulose "scaffold" on the micron-scale, as observed

in the SEM images. During chemical activation the pores left over from the dissolution of non-crystalline components serve as channels for the capillarity-driven infiltration of liquid KOH, further loosening the microfibril networks to create the carbon nanosheets and punching secondary micro and meso porosity into the structures. A similar phenomenology was employed to explain the formation of sheet like carbon layers from other multi-phase composites containing cellulose fibrils precursors, *e.g.* hemp fiber.⁷⁴ In order to reinforce the discussion concerning the rationale for precursor selection, we employed the entire peanut shell as a single precursor, with the same synthesis procedures as PSNC-3-800. **Figure 3-5A** shows SEM micrograph of the resultant carbon specimen. The carbon particle did not display the essential macroscopically open sheet-like morphology.

During electrochemical testing the open architecture of PSNC will allow full access of the electrolyte to the active surfaces, minimizing high rate diffusional losses through the liquid. By contrast, commercial activated carbons including CAC are known to contain a tortuous pore network that penetrates microns deep into the particulates. Especially at high scan rates / current densities this will result in significant ion diffusional losses.

Figure 3-2B shows a transmission electron microscopy (TEM) micrograph of PSNC-3-800, further illustrating the structure of the carbon, which consists of three-dimensional arrays carbon nanosheets. **Figure 3-2C** and **Figure 3-4(A-B)** show high angle annular dark field (HAADF) scanning TEM (STEM) micrographs and low-loss electron energy loss spectroscopy (EELS) thickness profiles of the PSNC specimens. PSNC-3-800 has carbon nanosheet thickness in the range of 15 - 25nm, which is thinner than that of PSNC-3-850 (40 - 60nm). Due to the insufficient chemical etching, PSNC-2-800 has the largest carbon sheet thicknesses, being up to 140 nm. **Figure 3-2D** presents a high resolution TEM (HRTEM) micrograph of PSNC-3-800, demonstrating the low degree of ordering in the material. The other PSNC specimens were similarly disordered, being shown in **Figure 3-2 C and D**.

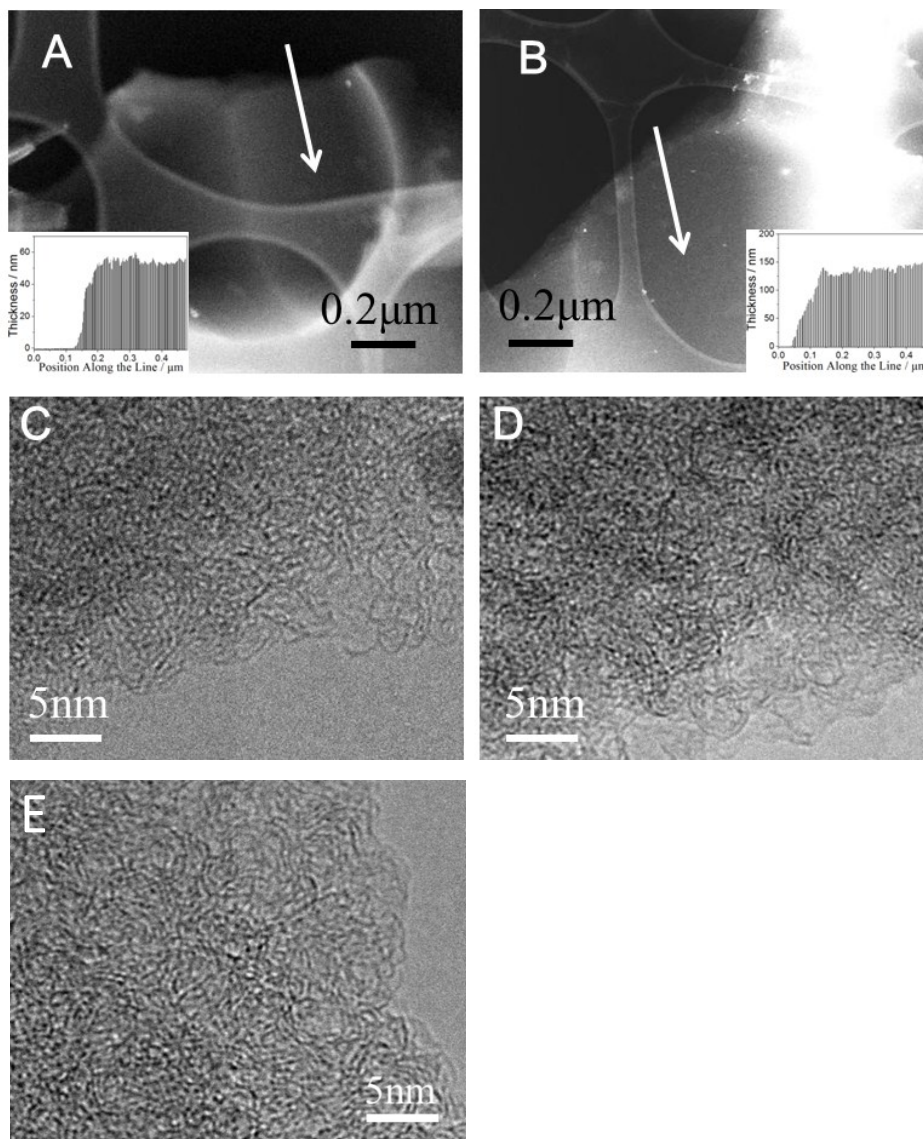


Figure 3-4: HAADF TEM micrographs and thickness profiles (insert) of (A) PSNC-3-850 and (B) PSNC-2-800, measured from low-loss EELS along the white arrows. HRTEM micrographs of (C) PSNC-3-850, (D) PSNC-2-800, and (E) PSOC.

The morphology of the PSOC-A and PSOC, which are synthesized from the inner peanut shell, is shown in **Figure 3-2E** and **Figure 3-3C**. These materials also exhibit a macroscopically open structure, which is unaffected by activation. The insert in **Figure 3-2E** highlights the typical sheet thickness, which is on the order of 300 nm. As shown in **Figure 3-5B**, the specimen derived from the integral peanut shell is mainly solid μm-size irregular-shaped carbon particles lacking macroscopic openness. The tissue of the inner peanut shell possesses a much higher content of three-dimensional highly cross-linked lignin. During high temperature pyrolysis such

a precursor will act as a "hard" carbon, preventing large-scale formation of equilibrium graphite at temperatures high as 1400°C.⁴⁹ However during carbonization the material will order locally, creating pseudo-graphitic arrays with dilated intergraphene spacing. As the HRTEM images in **Figure 3-2F** and **Figure 3-4E** illustrate, PSOC and PSOC-A primarily consist of partially ordered graphene domains, which may be described as "pseudographitic".

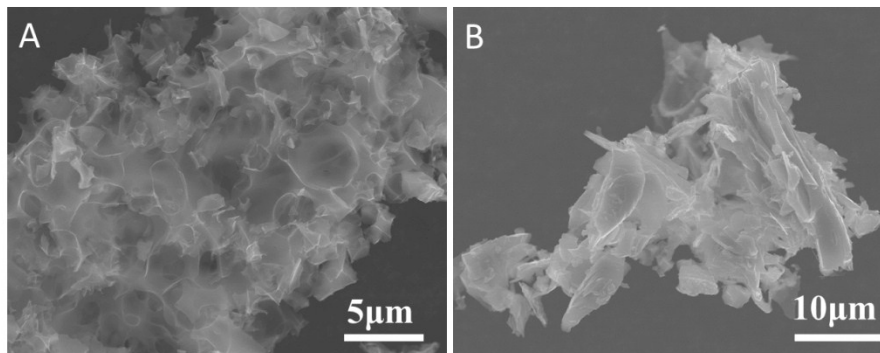


Figure 3-5: SEM micrographs of cathode and anode carbons achieved when employing the entire peanut shell as a single precursor for either synthesis process. (A) cathode carbon. (B) anode carbon.

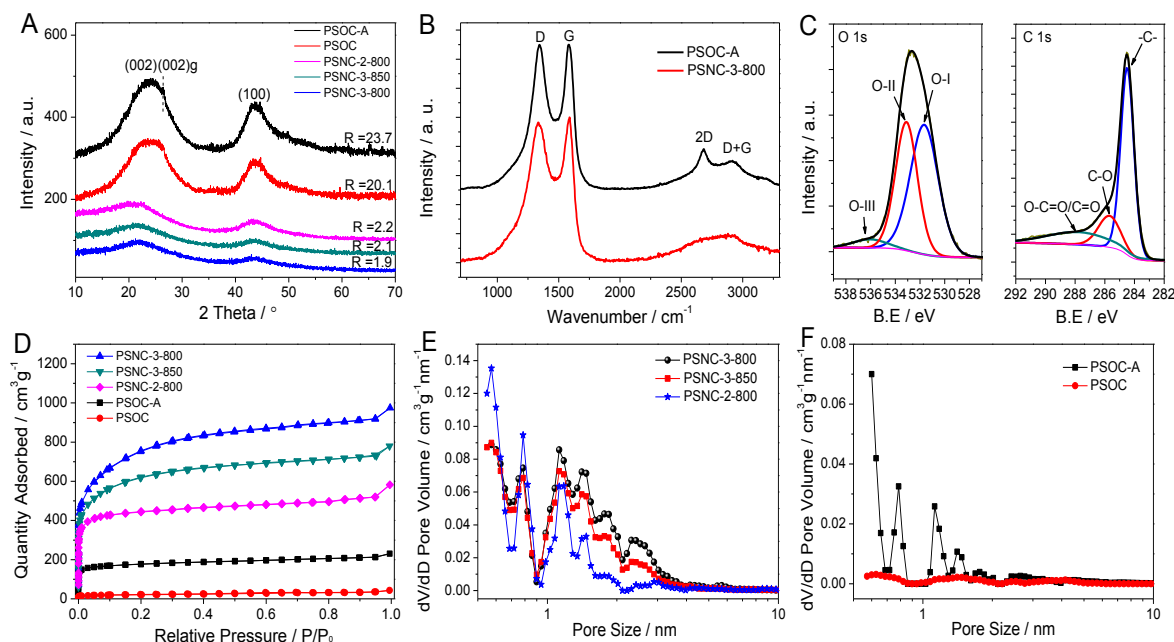


Figure 3-6: (A) XRD patterns of the PSNC and PSOC specimens. (B) Raman spectra of PSNC-3-800 and PSOC-A. (C) O 1s and C 1s core level XPS spectra fits for PSNC-3-800. (D) Nitrogen adsorption-desorption isotherms of PSNC and PSOC. (E) Pore size distribution of PSNCs. (F) Pore size distribution of PSOCs, calculated from the adsorption isotherms using DFT method.

Figure 3-6A shows the X-ray diffraction (XRD) patterns of the PSOC and PSNC. The patterns of PSOC show two broad diffraction peaks that are indexed as (002) and (100) of the pseudographitic domains. These peaks are barely discernible in PSNC, indicative of its much lower ordering. Moreover the PSOC patterns display the presence of a minor amount (estimated to be ~ 1 wt%) of equilibrium graphite, which is indexed separately. The average graphene interlayer spacing can be calculated from the center position of (002) peaks. As **Table 3-1** shows, the mean intergraphene layer spacing (d_{002}) for PSOC is significantly larger than that of graphite (0.3354 nm). We will demonstrate that this dilated intergraphene spacing allows for facile Na ion intercalation into the bulk of the PSOC-based negative electrode. To further understand the graphene plane arrangement in our materials, we employ an empirical parameter (R), defined as the ratio of height of the (002) Bragg peak to the surrounding background.⁷⁵

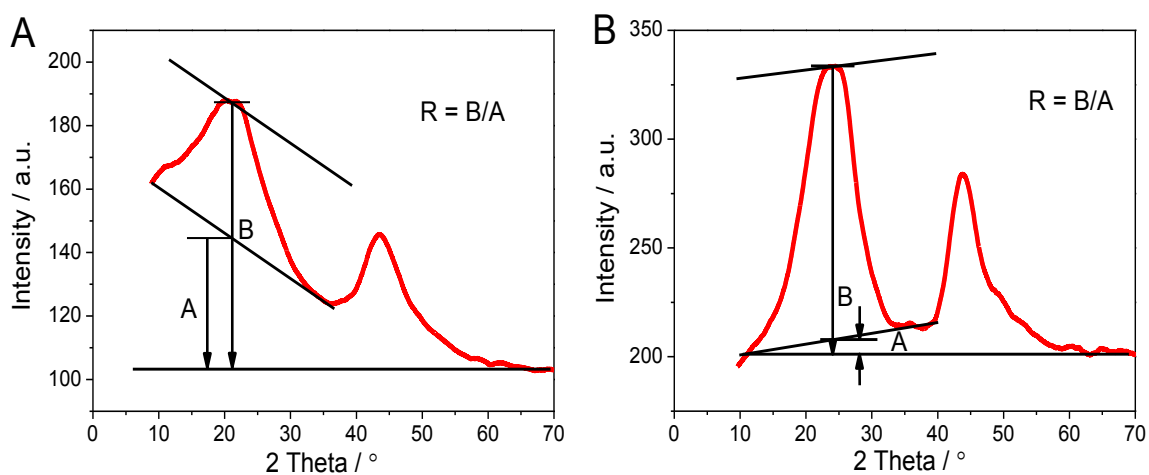


Figure 3-7: Scheme illustrating the R values calculation based on XRD patterns for PSNCs (A) and PSOCs (B).

A schematic depicting how R was calculated is shown in **Figure 3-7**. It has been argued that the value of R could credibly characterize the concentration of the graphene sheets arranged as single layer, with a larger R indicating a lower percentage of single graphene sheets within a carbon.⁷⁵ The R values for PSOC are an order of magnitude higher than they are for PSNC (20-23 vs. ~ 2), agreeing with our

interpretation of the HRTEM images. Activation of PSOC does increase R from 20.1 to 23.7, presumably by preferentially volatilizing to CO_2 the less ordered portions of the material. The average dimensions of the ordered graphene domains (L_a , L_c) could be calculated by the well-known Scherrer equation, using the full width at half maximum values of (002) and (100) peaks, respectively. As shown in Table 1, the domain thickness is relatively invariant from sample to sample (including for CAC), ranging from 1.51 - 1.84 nm. However with domain width is twice as large for PSOC *versus* PSNC or CAC (~ 8 nm *vs.* ~ 4 nm).

The structure of the carbons was further investigated by Raman spectroscopy. As shown in **Figure 3-6B** and **Figure 3-8**, all the specimens exhibit broad disorder-induced D-bands (≈ 1340 cm^{-1}) and in-plane vibration G-bands (≈ 1580 cm^{-1}). The values of the integral intensity of D- and G- bands could be obtained by fitting the spectra (**Figure 3-8**), with I_G/I_D being employed to index the degree of graphitic ordering. As **Table 3-1** shows, for PSOC the I_G/I_D values are 1.01 - 1.1, for PSNC they are 0.41 - 0.62, while for CAC the ratio is 0.26. PSOC also exhibited second order 2D and D+G peaks, which are also associated with their more ordered structure.⁷⁶ PSNC displayed an electrical conductivity in the range of 181 - 227 S cm^{-1} , being a factor of five higher than that of CAC (43 S cm^{-1}). Although we were unable to press PSOC into sufficiently dense "pucks" as to perform satisfactory 4 point probe conductivity measurements, it is expected that these highly ordered - low surface area carbons will be similarly much more conductive than CAC.

Figure 3-6D shows the nitrogen adsorption-desorption isotherms of PSNC and PSOC, while **Figure 3-6 (E-F)** shows their pore size distributions (obtained by density functional theory (DFT)). The same analysis for the CAC baseline is shown in **Figure 3-9**. **Table 3-1** provides the porosity characteristics of the peanut shell derived materials and of CAC. Type I/IV isotherms could be found for all the PSNC specimens, which all possess considerable porosity and high surface areas. The surface area and the pore volume fraction of micropores *vs.* of mesopores (and total

pore volume) depend on the activation conditions. Overall both the highest surface area ($2396 \text{ m}^2 \text{ g}^{-1}$, being desirable for maximizing the total ion adsorption) and the highest fraction of mesopores (35.4%, being desirable for rapid electrolyte diffusion) were achieved in the PSNC-3-800. A higher activation temperature or a lower ratio of KOH to carbon resulted in a reduction of both attributes. CAC actually possesses an on par surface area ($2050 \text{ m}^2 \text{ g}^{-1}$) and mesopore content (32.3%). However due to its lower electrical conductivity and a "closed" particulate morphology CAC will be demonstrated to be a far inferior electrode at high charge rates.

Table 3-1: Carbon structure, electrical conductivity and textural properties of Peanut Shell Nanosheet Carbon (PSNC) and Peanut Shell Ordered Carbon (PSOC), with baseline commercial activated carbon CAC also shown.

Sample	Carbon Structure					σ (S cm^{-1})	Textural Properties			
	d_{002} (\AA)	R	L_a (nm)	L_c (nm)	I_G/I_D^a		S_{BET} ($\text{m}^2 \text{ g}^{-1}$) ^b	V_t ($\text{cm}^3 \text{ g}^{-1}$) ^c	micropores %	mesopores %
PSNC-3-850	4.12	2.1	4.43	1.51	0.56	227	1998	1.21	70.2	29.8
PSNC-3-800	4.13	1.9	3.75	1.71	0.41	181	2396	1.31	64.5	35.4
PSNC-2-800	4.11	2.2	4.49	1.55	0.62	192	1376	0.91	77.5	22.5
PSOC	3.78	20.1	7.95	1.80	1.10	-	78	0.074	45	55
PSOC-A	3.79	23.7	8.04	1.84	1.01	-	476	0.31	77.8	22.2
CAC	3.72	3.8	4.20	1.84	0.26	43	2050	1.17	67.7	32.3

^a I_D and I_G are the integrated intensities of D- and G- band. ^b Surface area was calculated with Brunauer-Emmett-Teller (BET) method. ^c The total pore volume was determined at a relative pressure of 0.98.

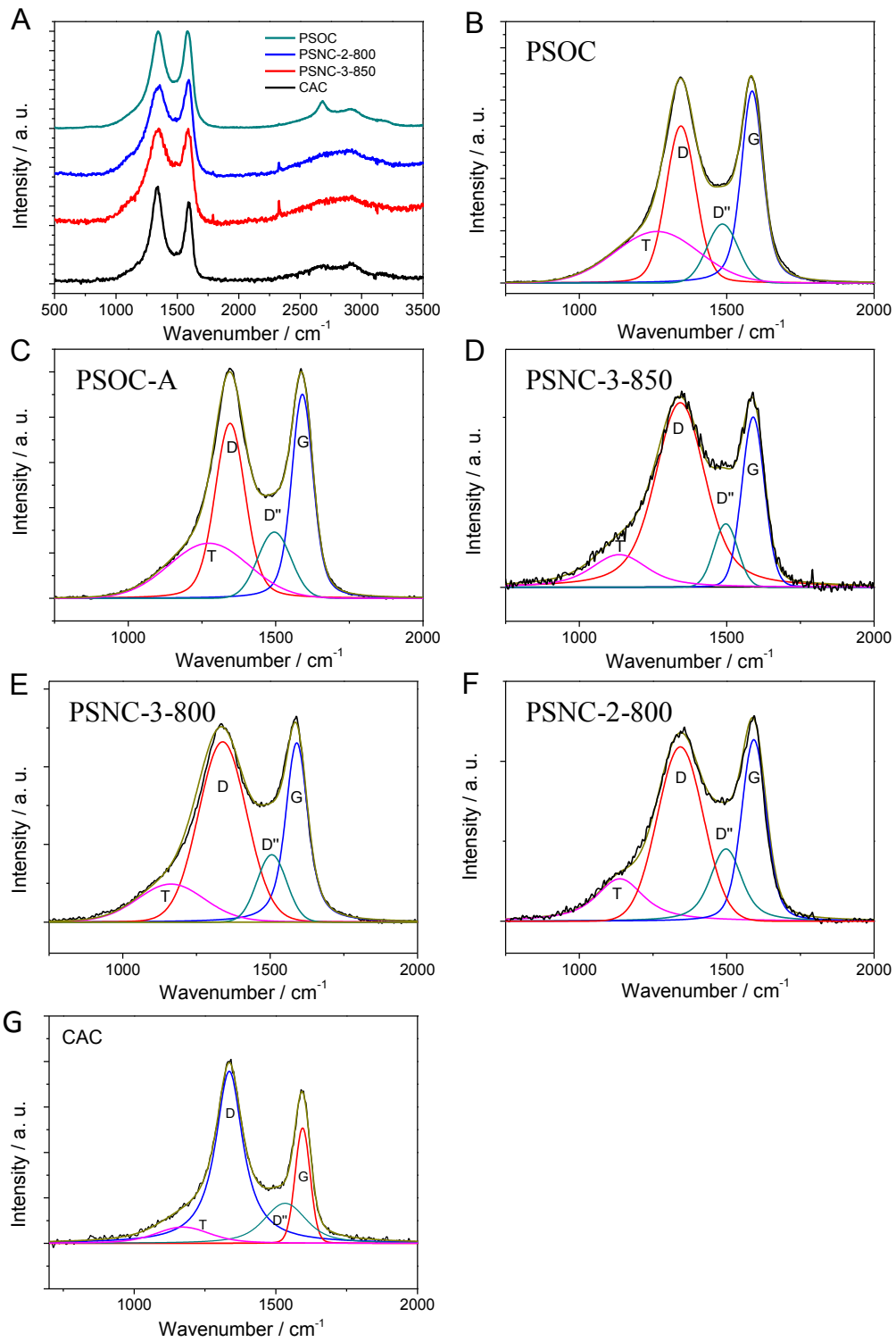


Figure 3-8: (A) Raman spectra of PSNC-2-800, PSNC-3-850 and PSOC specimens. (B-G) Fitted Raman spectra of PSOC, PSNC and CAC.

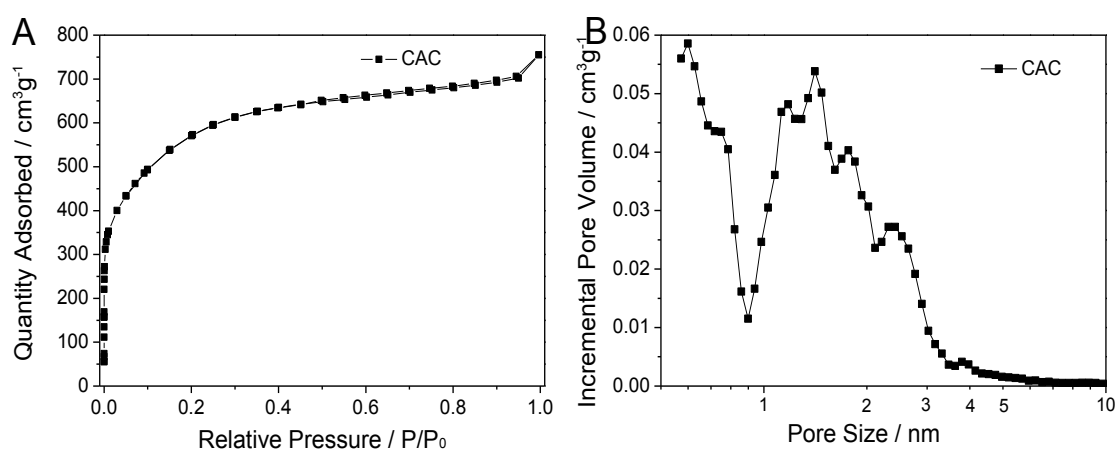


Figure 3-9: (A)-(B) Nitrogen adsorption-desorption isotherms and pore size distributions of CAC.

X-ray photoelectron spectroscopy (XPS) and combustion elemental analysis were employed to investigate the surface and bulk chemical composition of PSNC and PSOC. **Figure 3-10** displays the XPS survey and fitted high-resolution spectra. **Table 3-2** lists the surface composition of the carbons, the oxygen functionalities, and the bulk C, O, N and H results of the elemental analysis. Based on the XPS survey spectra, the content of impurities (Si, Cl) is 0.9 wt% in total. Other potential impurities that may be present in plant-based precursors (*e.g.* P, K, Mg, Ca) were below the detection limits of XPS analysis, being both volatilized during synthesis and further removed by the post-synthesis HCl wash.

Table 3-2: Surface chemistry of PSNC and PSOC, with baseline CAC also shown.

Sample	Surface Chemistry (XPS)			Functionality (% of total O 1s)			Elemental analysis ^a			
	C (wt%)	N (wt%)	O (wt%)	O-I	O-II	O-III	C (wt%)	N (wt%)	O (wt%)	H (wt%)
PSNC-3-850	89.45	0.85	9.70	44.15	51.87	3.98	90.44	0.93	7.41	0.21
PSNC-3-800	85.91	0.58	13.51	53.94	41.83	4.23	86.51	0.65	12.21	0.13
PSNC-2-800	87.31	0.96	11.73	44.58	43.04	12.38	88.31	0.94	9.97	0.33
PSOC	93.70	0.73	5.57	55.72	29.44	14.83	92.82	0.46	5.04	1.08
PSOC-A	92.94	0.97	6.09	39.41	55.28	5.31	91.85	0.74	5.71	1.10
CAC	95.35	~0	4.65	45.32	47.15	7.53	94.12	0.12	4.34	0.43

^a Weight percent of elements obtained from combustion analysis.

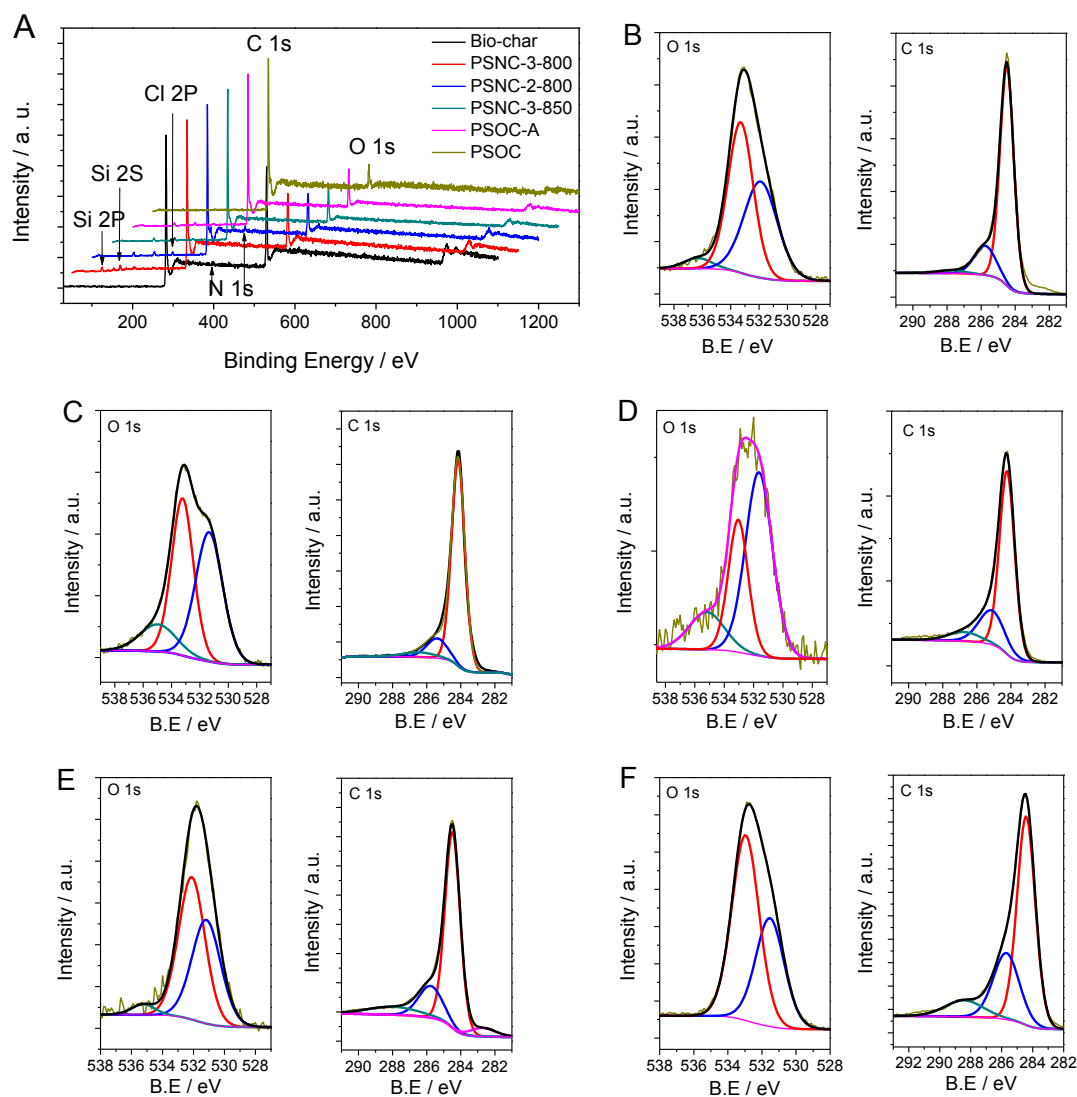


Figure 3-10: (A) XPS survey spectra of PSNC, PSOC and hydrothermal biochar. Magnified views of the C 1s, N 1s and O 1s core level XPS spectra with fits for (B) PSNC-3-850, (C) PSNC-2-800, (D) PSOC, (E) PSOC-A, (F) hydrothermal obtained biochar.

The unactivated biochar obtained after the hydrothermal process possessed a significant content of O (34.2wt%, results not shown). After chemical activation, a large portion of oxygen heteroatoms is preserved, with 11.7wt%, 13.5wt% and 9.7wt% oxygen content for PSNC-2-800, PSNC-3-800 and PSNC-3-850 respectively. The high-resolution O 1s and C 1s XPS spectra of PSNC-3-800 is shown in **Figure 3-6C**, with the same data for the other materials being displayed in **Figure 3-10 (B-F)**. The

high resolution O 1s spectra could be deconvoluted using 3 peaks representing the 3 different types of oxygen functional groups: C=O quinone type groups (O-I, 531 eV), C-OH phenol/C-O-C ether groups (O-II, 532.4 eV), and COOH carboxylic groups (O-III, 535.4 eV). The surfaces in all the specimens are primarily covered by O-I and O-II functionalities, with O-III being a relative minority. For instance in PSNC-3-800 the relative weight percent is 53.9% for O-I, 41.8% for O-II and 4.2% for O-III. In PSOC and PSOC-A the amount of O was much lower, being 5.6wt% and 6.1wt%. In all PSNC and PSOC the N content was below 1wt%. Baseline CAC contained 4.65wt% O and negligible N. The N content in all carbons is sufficiently low that it is not expected to meaningfully contribute to the charge storage capacity.

Figure 3-11 shows the electrochemical performance results for PSNC, which will be employed as the cathode in the hybrid NIC device. Here PSNC was tested in a half-cell configuration *versus* Na metal, in a voltage window previously employed for hybrid Na-based cathodes (1.5 - 4.2V). This range maximized the operating voltage window without decomposing the electrolyte, or intercalating ions into the bulk of the carbons to an appreciable extent.^{49,77,78} Upon positive polarization the PSNC electrode will reversibly adsorb ClO_4^- and reversibly release Na^+ . Capacitance is achieved both by EDLC of ClO_4^- , and through a pseudocapacitive interaction of Na^+ with surface defects and oxygen functionalities.

As shown in **Figure 3-11A**, the CV curves of PSNC-3-800 electrode display a box-like shape, indicative of typical EDLC behavior, overlaid with pseudocapacitive humps. **Figure 3-12(A-C)** shows the same CV data for PSNC-3-850, PSNC-2-800 and CAC carbons. The level of *IR* loss - induced distortion in the CVs at higher scan rates for the materials goes effectively in the order of the "openness" of the structures: With increasing scan rate (0.2 - 10 mVs^{-1}) the PSNC-3-800 specimen displayed negligible shape distortion. PSNC-3-850 was the second least distorted, the PSNC-2-800 was the third least distorted. Of all the carbons, the high scan rate CVs of the particulate-like CAC were by far the most distorted.

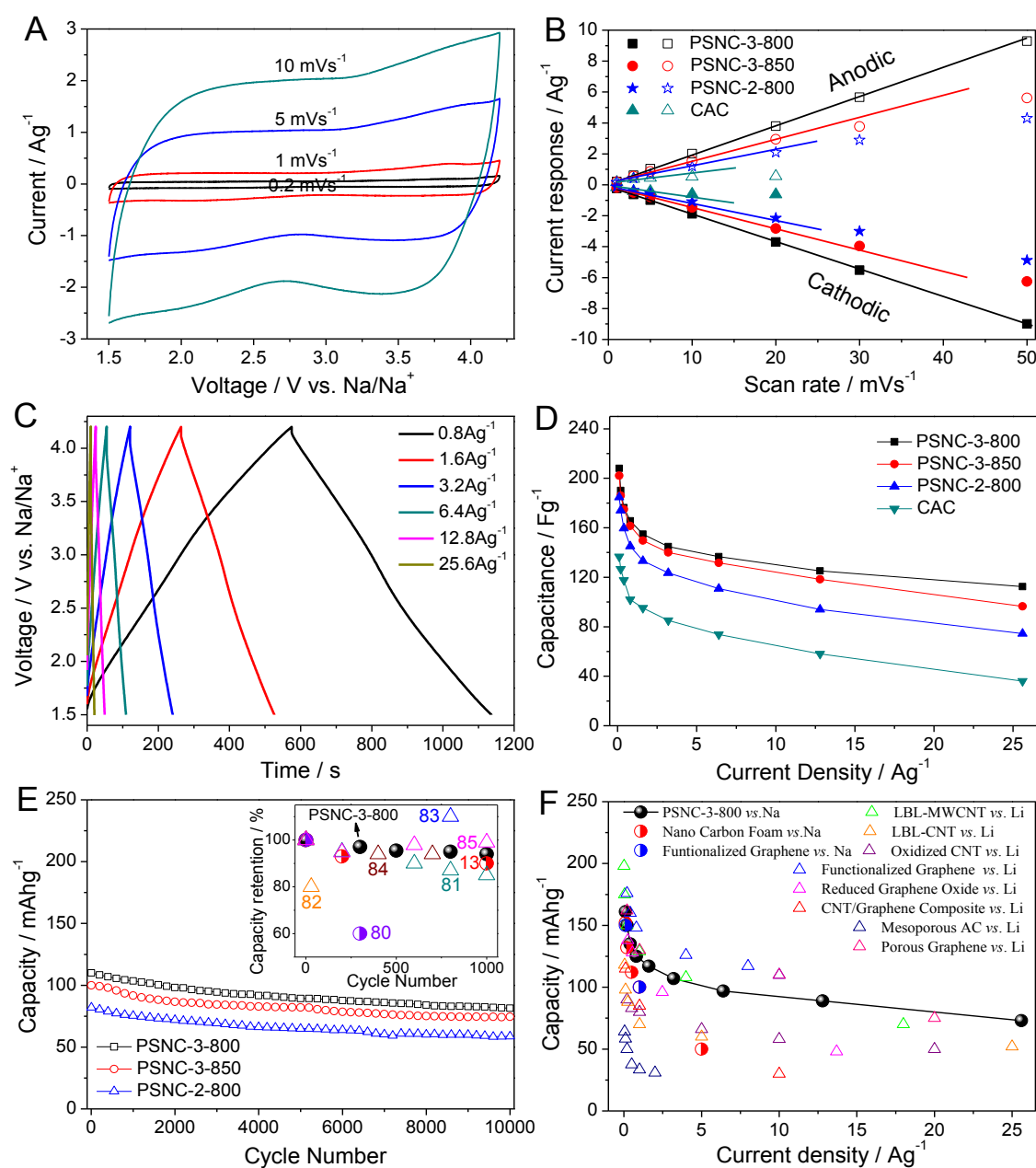


Figure 3-11: Half – cell performance of PSNC and CAC, tested between 1.5 - 4.2 V vs. Na metal. (A) Cyclic voltammograms (CVs) of PSNC-3-800. (B) Dependence of anodic and cathodic current (at 2.75 V) on scan rate, indicating the deviation from linear behavior. (C) Galvanostatic discharge/charge profiles of PSNC-3-800, at current densities from 0.8 to 25.6 Ag⁻¹. (D) Specific capacitance of PSNC versus current density. (E) Cycling stability of PSNC (tested at 3.2 Ag⁻¹ for 10,000 cycles), with an insert comparison to state-of-the-art Na and Li cathodes in hybrid devices. (F) Specific capacity vs. current density for PSNC-3-800, comparing with best literature reports for both Na (tested at same voltage window) and Li (tested at the wider 1.5-4.5 V vs. Li/Li⁺) hybrid cathodes.

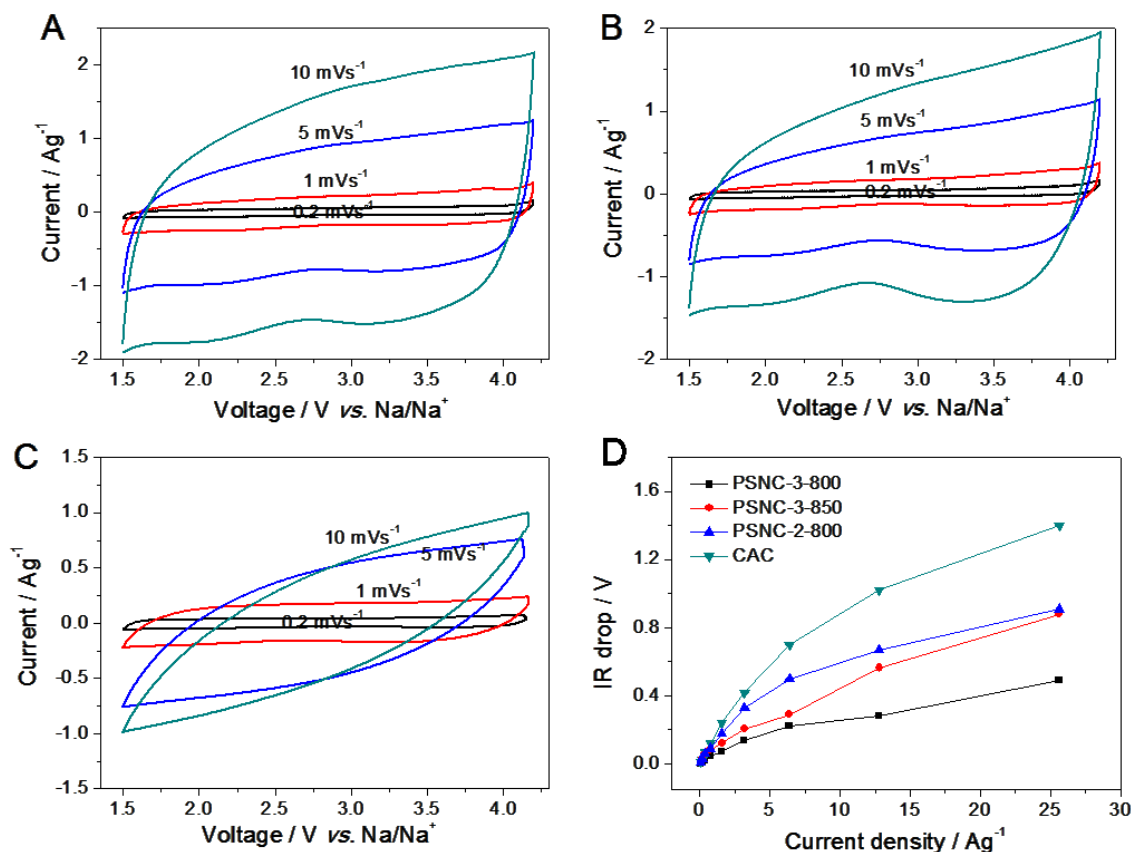


Figure 3-12: (A-C) Cyclic voltammograms (CVs) of PSNC-3-850, PSNC-2-800, and CAC, respectively. (D) IR drops of PSNC specimens and CAC in half cells.

Figure 3-11B displays the current dependence on the CV scan rate, measured at 2.75 V. At scan rates from 1 to 50 mV s⁻¹ the PSNC-3-800 electrode maintained linearity. For PSNC-3-850 and PSNC-2-800, the onset for deviation from linearity is 25 mV s⁻¹ and 15 mV s⁻¹, respectively. For CAC, the charge storage reaction became diffusion limited at very low rates, *i.e.* below 5 mV s⁻¹. A transition from a linear dependence of current to square root dependence is considered an indicator of the onset of diffusion-limited reactions,⁷⁹ and supports the argument that the ion transfer kinetics for the open PSNC structures is much more facile as compared to CAC. Since the charge storage mechanisms for PSNC are surface adsorption based, one can argue that the carbons' open structure reduces the ion diffusional limitations in the electrolyte (rather than in the bulk). Differences in pore shapes may also play an important role. Pores in PSNC could provide smoother inner-pore transport channels

for ions as compared to conventional activated carbons, reducing the "traffic jam" effect discussed in ref.^{30,74}

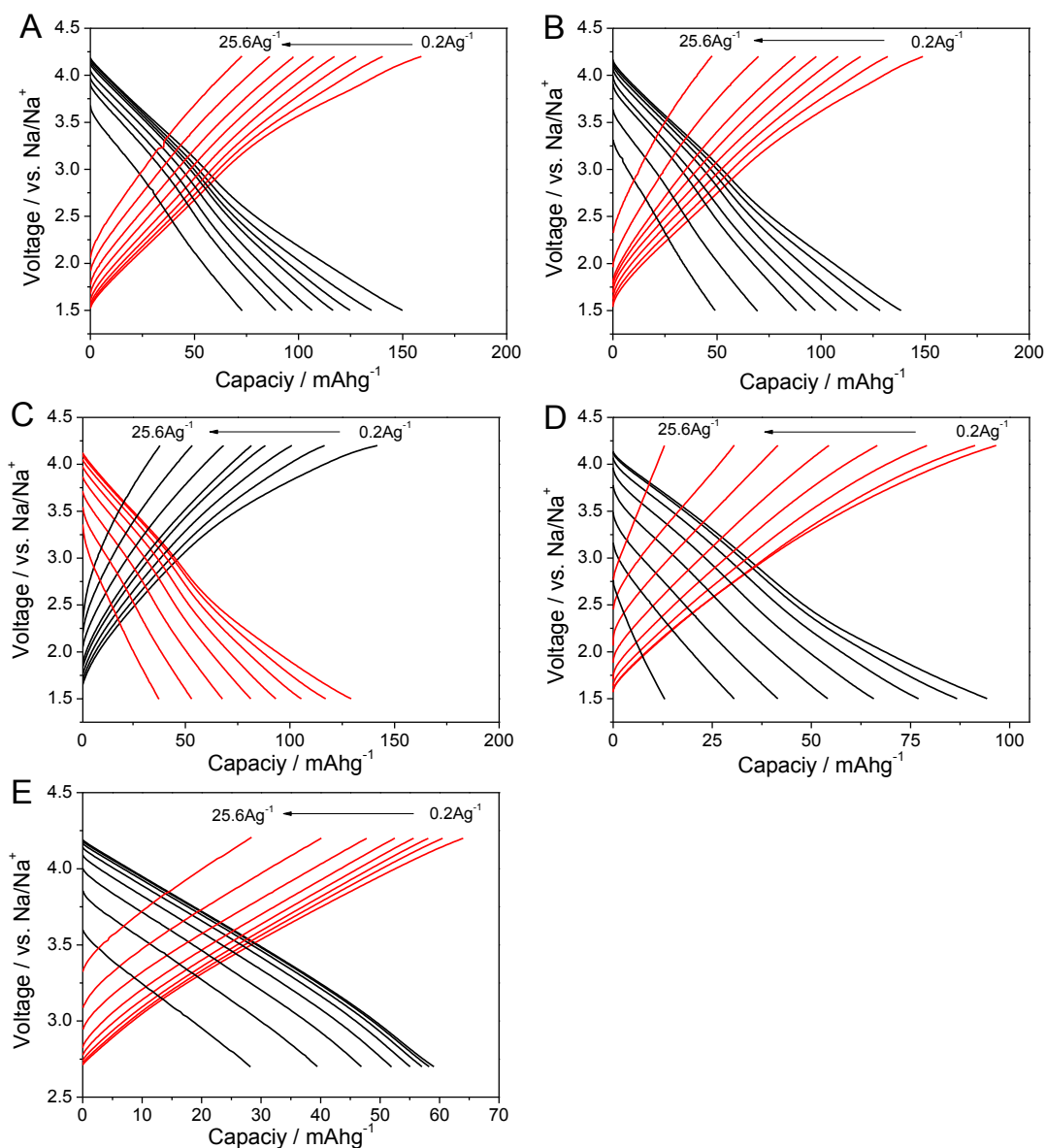


Figure 3-13 : Galvanostatic discharge/charge profiles of (A) PSNC-3-800, (B) PSNC-3-850, (C) PSNC-2-800 and (D) CAC, (E) PSNC-3-800 within voltage region of 2.7-4.2 V vs. Na/Na⁺.

Figure 3-11C and **Figure 3-13** show the galvanostatic charge/discharge profiles for PSNC as well as for CAC. For the PSNC electrodes the curves are symmetrical with low *IR* drops. Conversely, CAC is quite distorted at higher current densities (**Figure 3-13D**). **Figure 3-13D** displays the measured *IR* drop of each carbon at various

current densities. As indicated, CAC's pore tortuosity and inferior electrical conductivity both contribute to the larger CV distortion at high rates and the higher IR drops.

Figure 3-11D shows the specific capacitance of the PSNC and the CAC electrodes as a function of current density. The optimized PSNC-3-800 delivered a capacitance of 213Fg^{-1} at current density of 0.1Ag^{-1} , which gave surface normalized capacitance of $8.9\ \mu\text{Fcm}^{-2}$ (based on BET surface area). The PSNC electrodes consistently outperform CAC through the entire current range of testing. However the performance difference is most stark at the very high currents, where electrolyte diffusional limitations the manifest: At $25.6\ \text{Ag}^{-1}$ PSNC-3-800 delivers $119\ \text{Fg}^{-1}$ while CAC delivers $36\ \text{F/g}$. **Figure 3-14** shows the electrochemical data for the cathode carbon derived from the integral peanut shell as the precursor. Its inferior capacitance further proves the essential function of the macroscopic openness and the sheet-like morphology of PSNC-3-800.

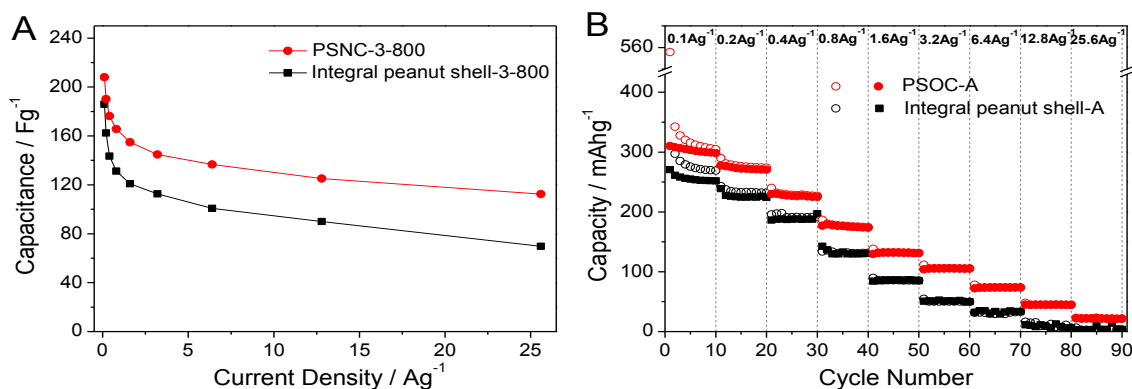


Figure 3-14: The electrochemical performance of cathode carbon (A) and anode carbon (B) that were derived from the entire peanut shell without separation.

Overall the PSNC-3-800 electrode offers the best performance, which may be attributed to its optimum combination of O content, surface area and mesopore content, the later becoming critical at high scan rates. The most reactive oxygen functional groups should be the quinone type groups ($\text{C}=\text{O}/\text{O}-\text{C}=\text{O}$, O-I type) due to the unsaturated carbon-oxygen double bond. As covered earlier, all PSNC materials possess significant O-I content, with PSNC-3-800 being the richest both in terms of

weight fraction (53.94%) and the total amount. It has been previously argued that between 1.5-4.2V *vs.* Na/Na⁺ there is substantial charge storage capacity associated with reversible Na⁺ binding to this moiety.^{13,80} This therefore is another reason for the optimum performance in PSNC-3-800 *versus* PSNC-3-850 or PSNC-2-800. While CAC contains an analogous fraction of O-I, its overall oxygen content is three times lower.

The cycling performance of PSNC, tested at 3.2 Ag⁻¹, is shown in **Figure 3-11E**. The figure also contains an insert that compares our data to state-of-the-art Na and Li cathodes previously employed in hybrid devices and published in scientific literature. For a consistency with the PSOC data, these results are presented in terms of specific capacities (mAhg⁻¹) rather than capacitances. The capacitance C (F g⁻¹) is defined as $C = i \times t / V$, where i is the active mass normalized current density and t is discharge time obtained from the galvanostatic discharge curve. The voltage window V is defined as $V = V_{\max} - V_{\min}$, where V_{\max} is the voltage at the beginning of discharge after the IR drop and V_{\min} is the voltage at the end of discharge. The specific capacity Q of a half-cell is $Q = i \times t$. Thus a conversion of a measured capacitance to a measured capacity requires a straightforward multiplication of C by V . For instance a capacitance of 140 F/g with a voltage window of 2.7 V will yield a specific capacity of 105 mAhg⁻¹ (*i.e.* $140 \times 2.7/3.6$).

It is important to point out that the scientific convention for cycling of electrodes in hybrid battery - supercapacitor Li and Na devices remains similar to that for testing of conventional battery materials, rather than to materials employed for EDLC supercapacitors or for faradaic pseudocapacitors (*e.g.* surface redox oxides such as Co₃O₄). In literature for hybrid Na and Li electrodes, cycling is often completed as early as after 1,000 cycles, with testing being rarely performed beyond 5,000 cycles. The PSNC-3-800, PSNC-3-850 and PSNC-2-800 electrodes retained 94%, 91% and 92% of the initial capacity after the usual 1,000 cycle test span employed for qualifying hybrid system cathodes^{13,81,82,83,84,85}. Previously published cycling results

are overlaid with our data, Na being half full circles and Li being open triangles. PSNC cycling performance is among the state-of-the-art for both Li^{81,82,83,84,85} and Na^{13,80} systems, which is notable since researchers empirically observe Na electrodes cycling worse than Li electrodes. The PSNC cathodes kept working well throughout the 10,000 cycles tested. At the 5,000th cycle, PSNC-3-800, PSNC-3-850 and PSNC-2-800 retained 82%, 84% and 81% of the initial capacity. After 10,000 cycles these values were 73%, 74%, 73%. We attribute the cycling loss to a gradual degradation of the surface oxygen moieties rather than to bulk changes of the carbons' structure. By contrast the CAC electrode retained only 61% of its initial capacity after 5,000 cycles.

Figure 3-11F displays the current density dependence of the capacity in PSNC-3-800 and compares it to various advanced carbon-based materials previously employed as cathodes in both Na and Li hybrid devices. The PSNC-3-800 electrode (black circles) is quite attractive in comparison to published Na-based systems (half full circles) tested at an identical voltage window^{13,80}. In fact it actually performs on par with some of the best cathodes for hybrid Li devices (open triangles), which are normally expected to display higher capacities and rate capabilities than Na. The fact that our Na adsorption cathode is competitive with Li adsorption cathodes is highly notable since Na is a 39% larger ion that is much more prone to electrolyte solution diffusional limitations while inside the pores of the carbon (a key rate limiting step for ion adsorption electrodes). The Li cathodes are also tested with a wider voltage window (1.5-4.5 V), further giving them a "leg up" over Na in terms of the measured capacity. The Li electrodes include mesoporous AC's,⁸⁶ functionalized graphene,^{82,83,87} CNT/graphene composite,⁸⁸ and functionalized CNTs^{81,85,89}.

We also prepared PSNC-3-800 electrode with a mass loading of 2 mg cm⁻² and tested it identically. As shown in **Figure 3-15A**, although the mass loading is 5 times higher, the capacities were at maximum 17% lower. To estimate the density of an electrode which would operate in a commercial device, we prepared a 15 mg cm⁻²

mass loading electrode in a pressed state (100 MPa). As shown in **Figure 3-17A**, the PSNC-3-800 electrode was approximately 240 μm thick, giving a packing density of 0.62 g cm^{-3} . This is on par with the 210 μm , 0.71 g cm^{-3} of an identically mass loaded and pressed CAC electrode. We calculated the volumetric capacity of the PSNC-3-800 electrode based on the above density value, with the results being shown in **Figure 3-16A**.

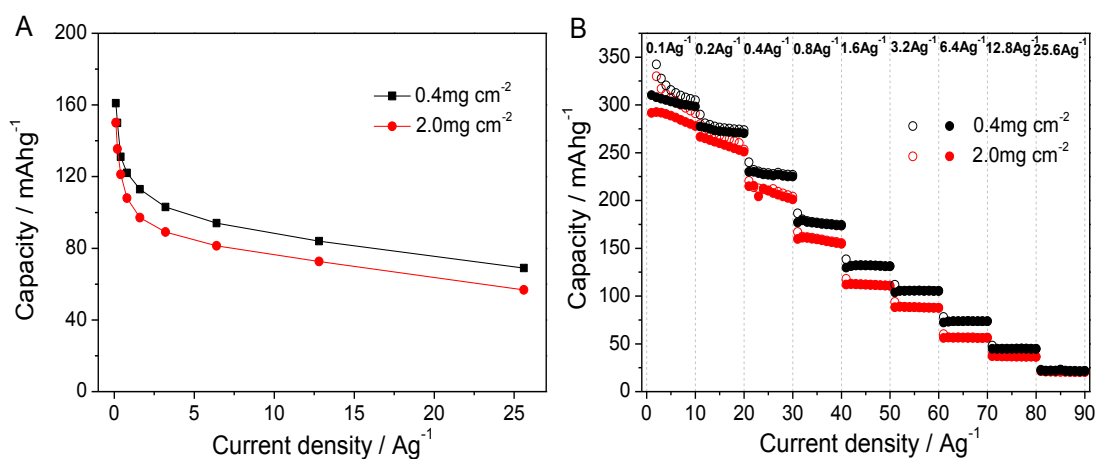


Figure 3-15: The electrochemical performance of PSNC-3-800 (A) and PSOC-A (B) with two different electrode mass loadings.

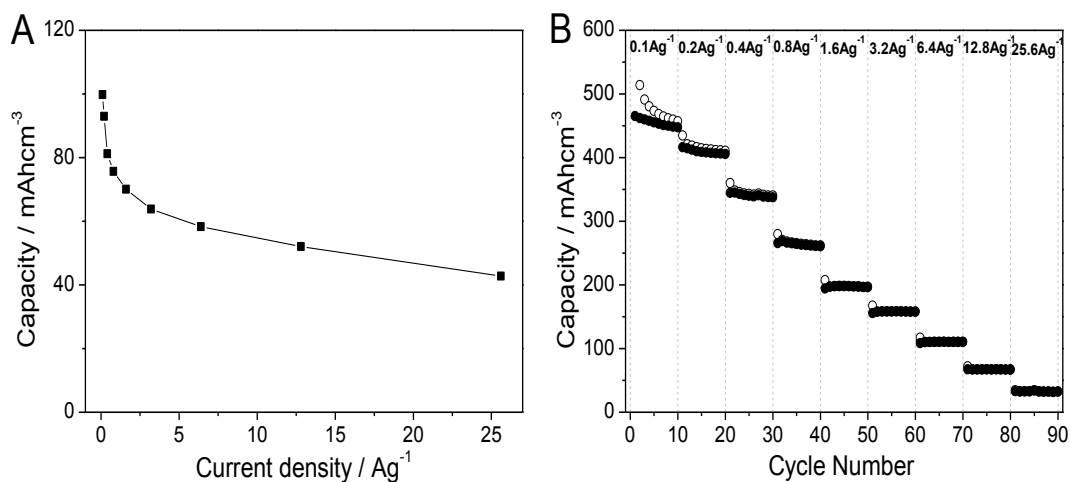


Figure 3-16: The volumetric capacity of PSNC-3-800 (A) and PSOC-A (B).

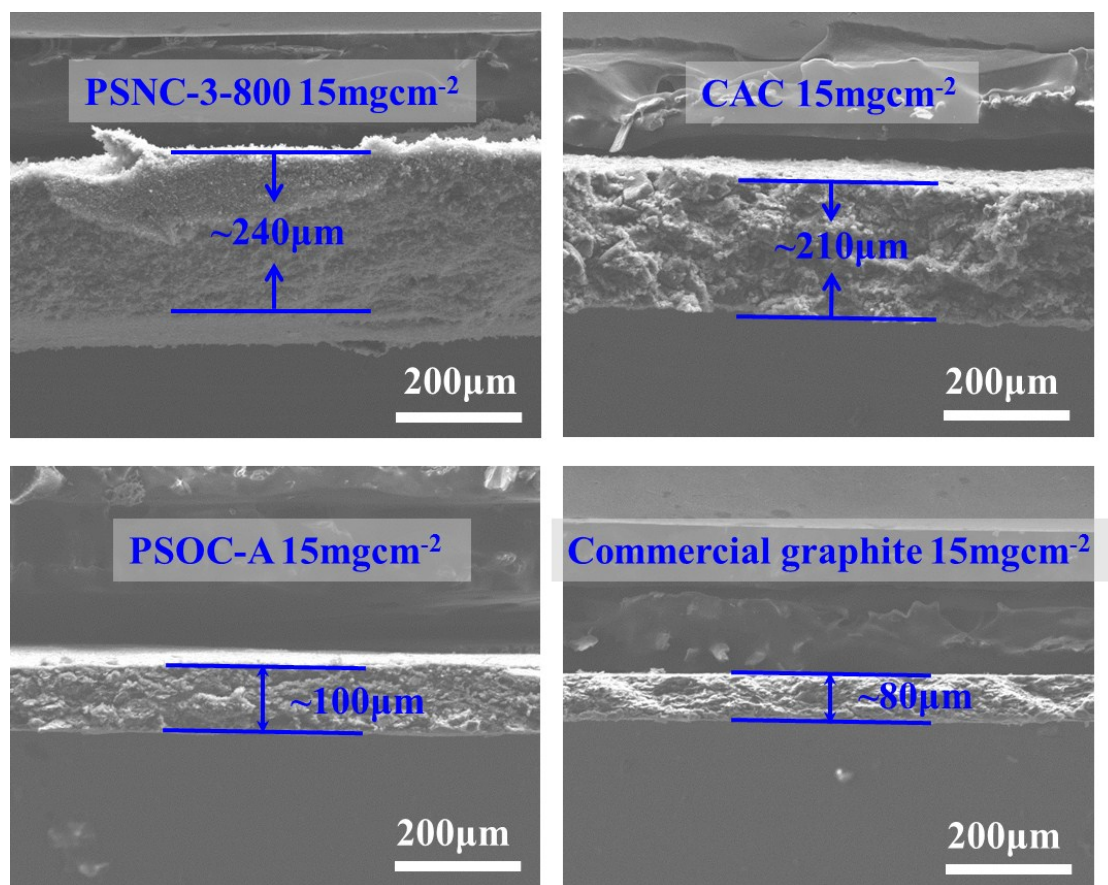


Figure 3-17: Cross section SEM images of (A) PSNC-3-800 (B) CAC, (C) PSOC-A and (D) commercial graphite thin film electrodes with commercial mass loadings.

Figure 3-18 shows the electrochemical performance results for PSOC, which will be employed as the anode in the hybrid device. Here PSOC was tested in a half-cell configuration *versus* Na metal. **Figure 3-18A** and **Figure 3-19** display the CV curves of PSOC-A and PSOC half-cells, tested between 0.001 and 3V. The CV's display a pair of sharp cathodic (centered at 0.016 V) and anodic peaks (centered at 0.11 V), indicating minimum hysteresis between the charge and the discharge process. **Figure 3-18B** shows the galvanostatic data for PSOC-A tested at a current density of 0.1 A g^{-1} ($\sim 1/3C$), at cycles 1, 2, 5 and 10. The same charts for PSOC and the galvanostatic curves as a function of current density (at 5th cycle at each current density) are shown in **Figure 3-19B**. As shown in **Figure 3-18B**, galvanostatic curves possess relatively flat charge - discharge profiles, with the majority of the capacity (discharge: 181 of 315 mAhg^{-1}) being accumulated below 0.1 V. The flat charge - discharge plateau and

the low voltage are desirable for maximizing both the energy density and the voltage profiles of full devices.

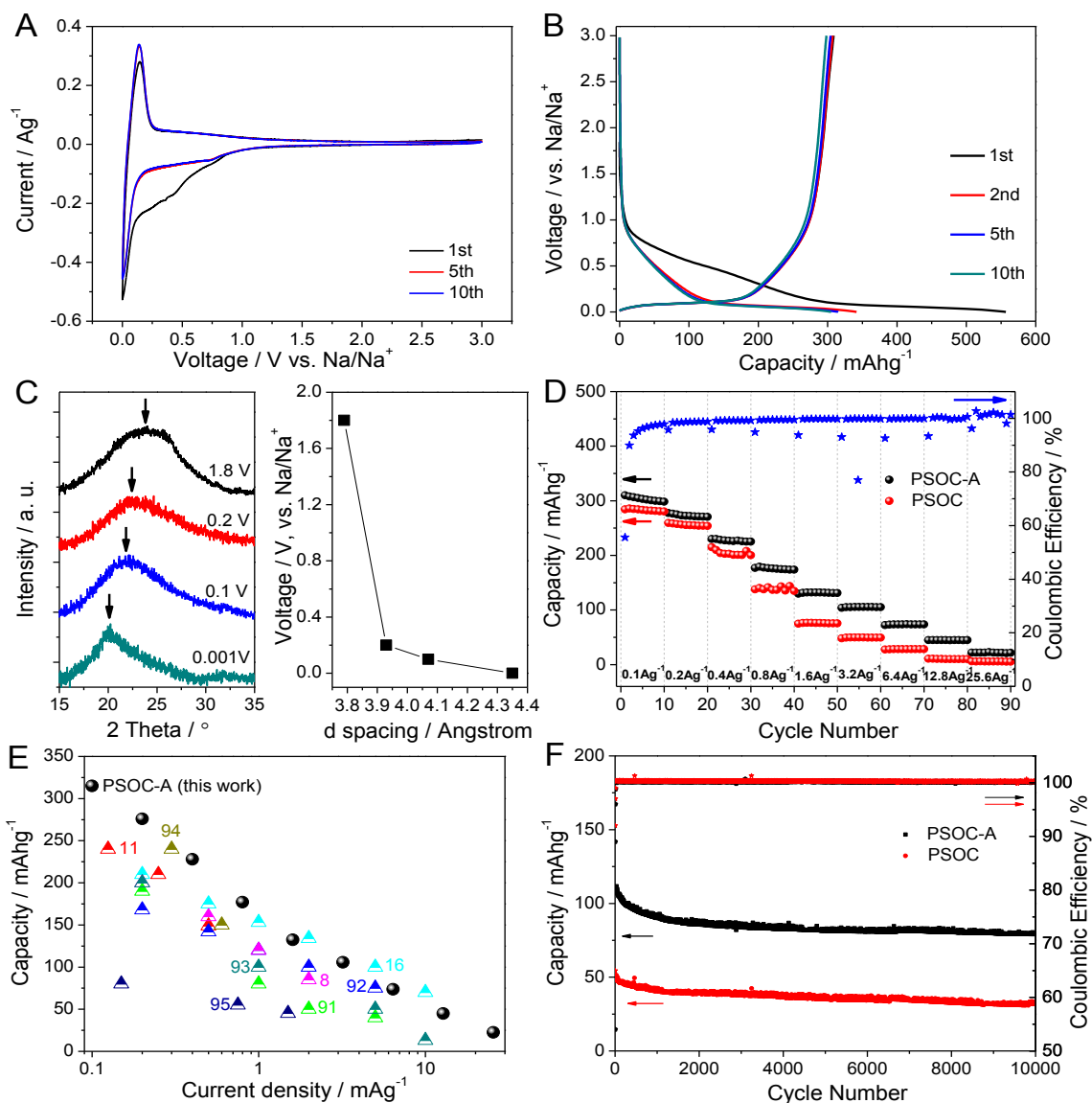


Figure 3-18: Half - cell performance of PSOC and PSOC-A. (A) CVs of PSOC-A, tested at 0.1 mVs⁻¹. (B) Galvanostatic discharge/charge profiles of PSOC-A, tested at 0.1Ag⁻¹. (C) (left) XRD spectra for PSOC discharged at 50 mAhg⁻¹ to 0.2, 0.1 and 0.001 V. (right) The mean interlayer spacing at several cut-off voltages. (D) Rate performance and CE of PSOC and PSOC-A. (E) Rate capability comparison of PSOC-A with the literature published carbonaceous materials employed as Na anodes. (F) Cycling capacity retention and CE of PSOC and PSOC-A, tested at 3.2 Ag⁻¹ for 10,000 cycles.

Figure 3-18C displays the *ex-situ* XRD patterns of PSOC electrodes discharged to different cut-off voltages (1.8, 0.2, 0.1 and 0.001 V vs. Na/Na⁺) at a current density of

50 mAg⁻¹. The sodiated carbons were kept in an argon container up to the point of XRD testing. The raw XRD plots along with the insert of the calculated mean *d*-spacing demonstrate sodiation-induced dilation of the intergraphene layers that is synonymous with ion intercalation. This is fundamentally different low voltage charge storage behavior as compared to nanoporous carbons tested against Li metal, where metal plating was indeed experimentally proven to be a key contributor to the total capacity.⁹⁰

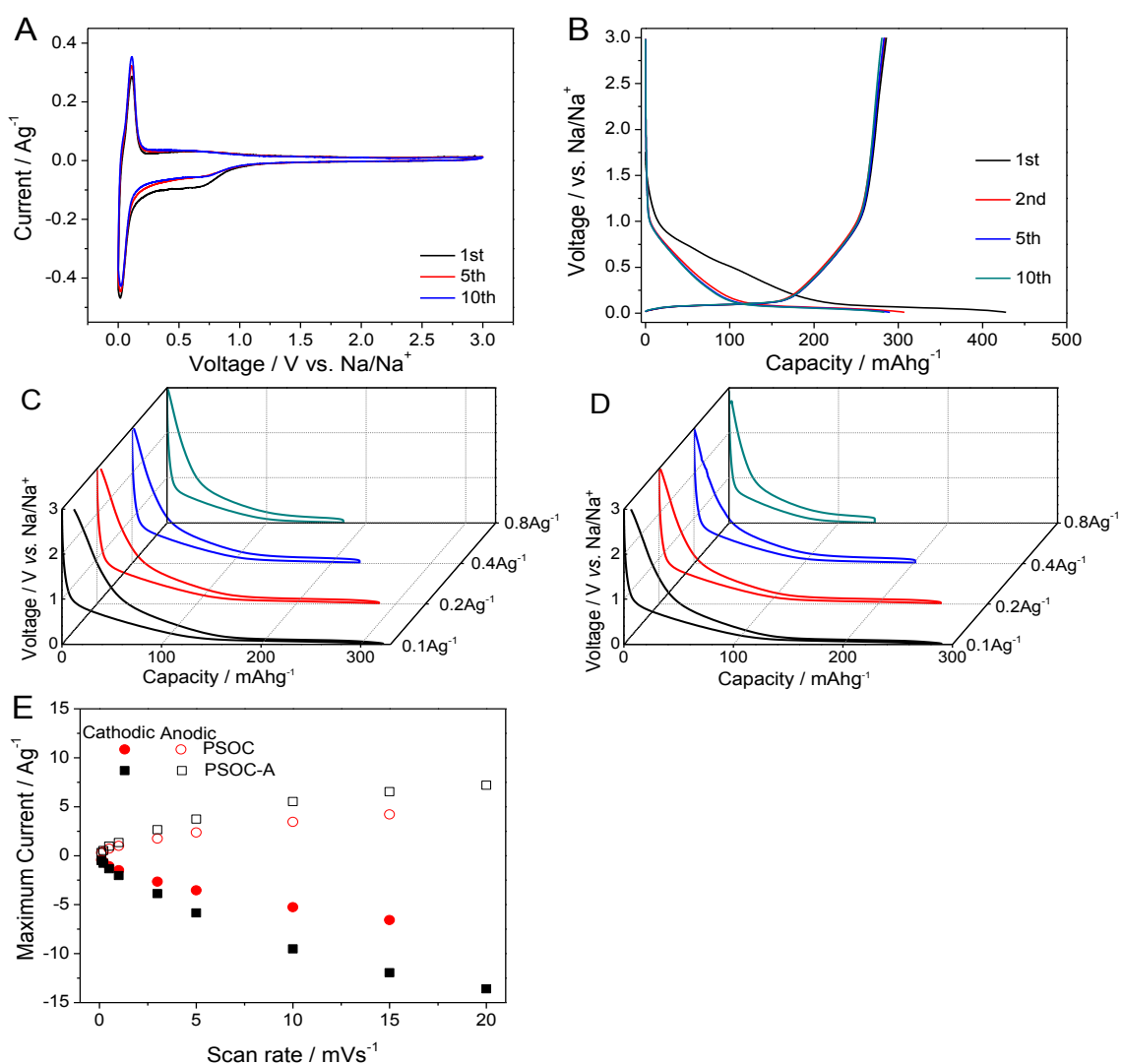


Figure 3-19: (A) CVs of PSOC specimen at a scan rate of 0.1mVs⁻¹. (B) Galvanostatic discharge/charge profiles of PSOC at density of 0.1Ag⁻¹. (C-D) Galvanostatic discharge/charge profiles of PSOC-A (C) and PSOC (D) at current densities of 0.1, 0.2, 0.4 and 0.8Ag⁻¹. (E) Dependence of anodic and cathodic peak currents on scan rate for PSOC and PSOC-A. (F) Galvanostatic discharge/charge profiles of PSNC-3-800//PSOC-A hybrid Na-ion capacitor at low current densities.

We employed air activation to introduce limited additional porosity into the PSOC electrodes. This would both improve the electrolyte access to the bulk of the material and reduced the solid-state diffusion distances due to a lower effective sheet thickness. As shown in **Figure 3-19E**, through the entire scan rate range of interest, both the unactivated and the activated electrodes display nearly a square root dependence of the peak current on scan rate. This indicates that the charge storage process for both PSOC and PSOC-A is diffusion-limited, which is expected for intercalation. However as shown in **Figure 3-18D**, PSOC-A exhibited much improved rate capability. At low currents the capacities are not that dissimilar, for example being 315 vs. 290 mAhg⁻¹ at 0.1 Ag⁻¹. At higher currents, such as 3.2 Ag⁻¹ (~ 10C), activation makes a tremendous difference; effectively doubling the capacity from 51 to 107 mAh/g. According to **Figure 3-18E** the rate performance of PSOC-A is among the most favorable in comparison to various carbonaceous materials previously tested as anodes in Na half-cells.^{8,11,91,92,93,94,95}

As shown in **Figure 3-15B**, at the 2 mg cm⁻² mass loading the current density dependence of specific capacity of PSOC is only slightly lower relative to the 0.4 mg cm⁻² loading values. Tested within the current density range 0.1 to 25.6 Ag⁻¹, the capacity of the 2 mg cm⁻² electrode is at most lower by 15%. **Figure 3-17** shows that in a pressed state the 15 mg cm⁻² PSOC-A electrode is 100 μm thick with a packing density of 1.5 g cm⁻³, while electrodes identically synthesized from commercial LIB-electrode grade graphite are 80 μm and 1.87 g cm⁻³. **Figure 3-16B** displays the volumetric capacity of PSOC-A electrode at various currents, the calculation being based on an electrode packing density of 1.5 g cm⁻³.

According to **Figure 3-18F** the cycled PSOC-A electrode retained 75% of its original capacity after 10,000 cycles, with coulombic efficiency being at 100% (within the resolution of the instrument) after the first 5 cycles. Such results are highly unusual even for Li anode systems (apart from commercial graphite), since electrode decrepitation and concomitant loss of electrical contact with the current collector

inevitably occurs due to repeated volume expansion/contraction associated with charging. However such cycling stability is even more unique for anodes that employ Na as charge carriers due to their larger diameter. The favorable cycling performance of PSOC-A compared to previously published materials may be attributed to its unique "pseudographitic" structure that allows for facile intercalation of large amounts of Na at low voltages. The excellent rate capability results from the very short diffusion distances due the carbons' intrinsic sheet-like morphology further boosted by activation-introduced porosity. As shown in **Figure 3-14B**, the carbons derived from the integral peanut shells exhibit much worse rate performances. Materials such as CAC, which are much less ordered and less diffusionally accessible, will offer neither the low-voltage flat-capacity plateau nor the rate capability.

We combined the two peanut derived carbons to create hybrid sodium ion capacitors (NICs) with an unparalleled performance for Na class of hybrid devices that actually rivals Li ion capacitors (LICs). For the reasons outlined earlier, one normally does not expect NICs to perform as well as LICs in either rate capability or cycling stability. The rationale for employing PSNC as the cathode and PSOC as the anode is as follows: The PSNC is ideally suited as the cathode since it possesses a relatively large charge storage capability and rate performance in the high voltage region, *i.e.* 1.5 - 4.2V *vs.* Na/Na⁺. When employing the PSOC as the anode we can fully utilize the large plateau capacity in the low voltage region, *i.e.* near and below 0.1 V *vs.* Na/Na⁺. We point out that the device would have poor performance if the electrodes were to be swapped. The PSOC anode is a low surface area insertion electrode, with almost all of its capacity being below 0.5 V *vs.* Na/Na⁺. It would store negligible charge if employed as cathode swinging through a positive voltage range in a device.

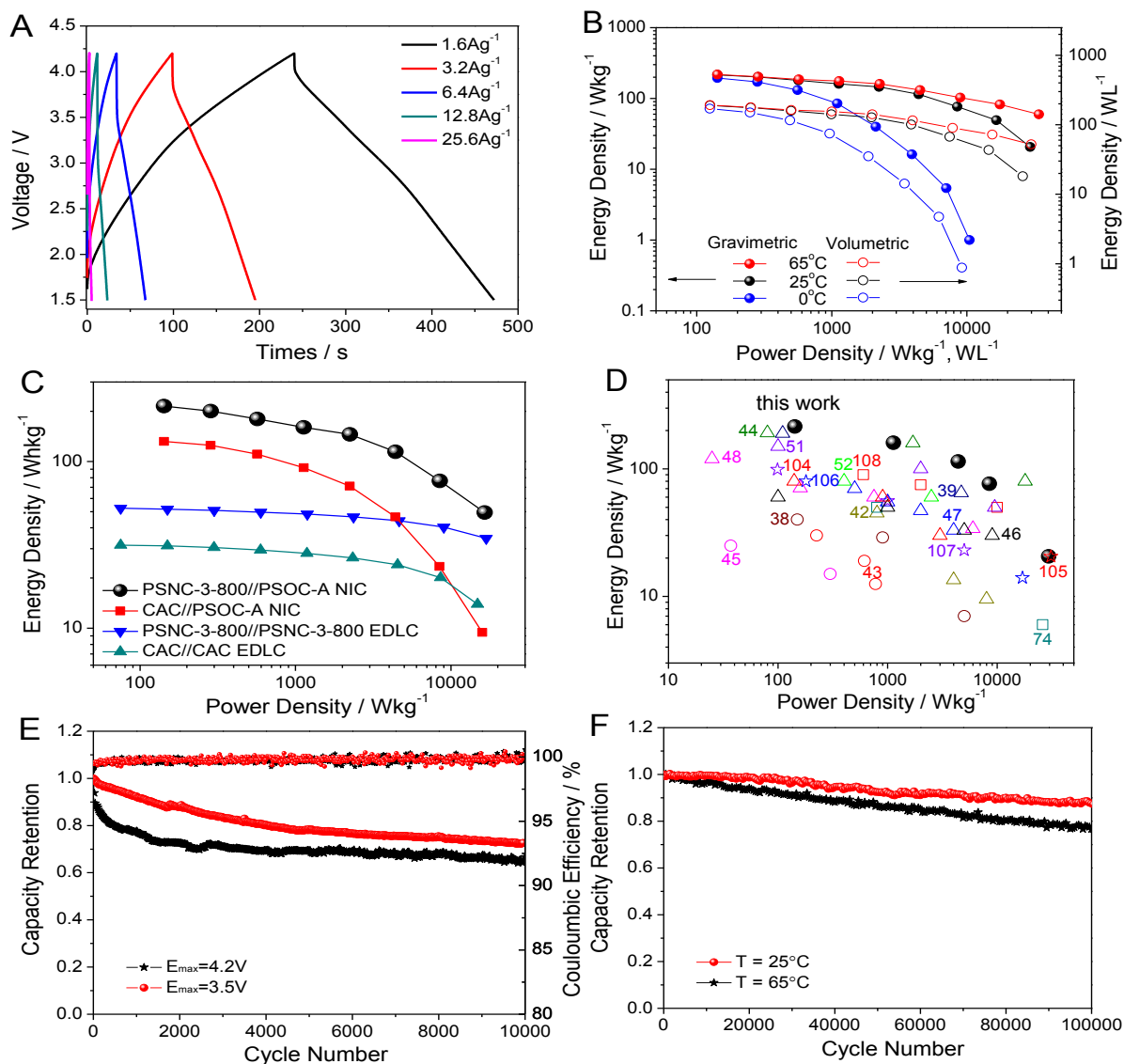


Figure 3-20: Electrochemical performance of the hybrid Na-ion capacitors (NICs). (A) Galvanostatic profiles of PSNC-3-800//PSOC-A, the low current density results being shown in **Figure 3-21A**. (B) Ragone plot of PSNC-3-800//PSOC-A at 0°C, 25°C and 65°C. The calculated energy and power densities are based on the total mass (solid) or volume (hollow) of the active electrodes. (C) Ragone plot (active mass normalized) comparing a device based on PSNC//PSOC to CAC//PSOC and to symmetric PSNC//PSNC and CAC//CAC systems. The PSNC//PSNC and CAC//CAC store charge based on EDLC only. (D) Energy - power density performance comparison (all active mass normalized) of PSNC-3-800//PSOC-A *versus* state-of-the-art reported energy storage systems in literature. (\circ : Na-ion capacitor, Δ : Li-ion capacitor, \star : Aqueous asymmetric EDCL + faradaic capacitor, \square : Ionic liquid EDLC capacitor). (E) Cycling stability and coulombic efficiency of PSNC-3-800//PSOC-A, tested at 6.4 Ag^{-1} for 10,000 cycles. (F) PSNC-3-800//PSOC-A devices were tested at 25°C and at 65°C, in both cases undergoing 100,000 cycles at 51.2 Ag^{-1} within a voltage window of 1.5-3.5V.

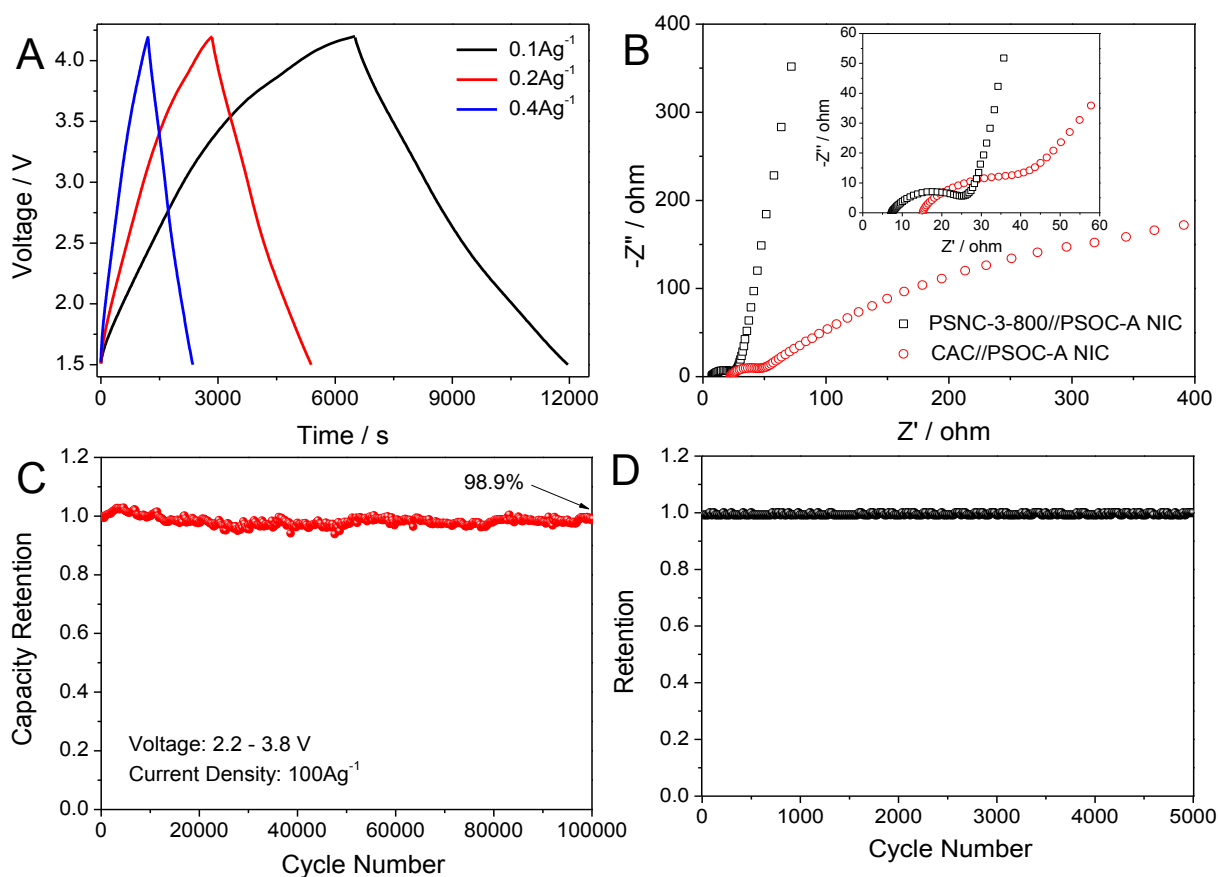


Figure 3-21: (A) Galvanostatic discharge/charge profiles of PSNC-3-800//PSOC-A hybrid Na-ion capacitor at low current densities. (B) Nyquist plots of PSNC-3-800//PSOC-A and CAC//PSOC-A after rate tests. (C) Cycling stability of PSNC-3-800//PSOC-A hybrid ion capacitor at a current density of 100Ag^{-1} and voltage window of 2.2-3.8V. (D) The cyclability of Na-Na cell.

Optimizing device performance consists of achieving the widest possible working voltage window without decomposing the electrolyte, while maximizing the capacity of both electrodes. Both of these targets could be realized when the PSOC anode operates within its plateau region while PSNC cathode swings through the high voltages. In accordance with the principle of balanced charge passing through the cathode and the anode ($Q_{\text{cathode}} = Q_{\text{anode}}$), the electrode mass ratio ($m_{\text{cathode}}/m_{\text{anode}}$) was kept at 1:1. This is based on a capacity of 161mAhg^{-1} for PSNC-3-800 (discharged at 0.1A g^{-1} to 1.5V vs. Na/Na^+) and a 0.1V vs. Na/Na^+ plateau capacity of 181mAh g^{-1} for PSOC-A at the same rate. The total voltage window for the NIC was 2.7V . It is important to differentiate the total voltage window for the assembled device presented

in **Figure 3-20**, from the voltage windows for the half-cells vs. Na/Na⁺ presented in **Figure 3-11**. The device voltage range was purposely kept at 1.5 - 4.2 V (rather than at 0 - 2.7 V) so as to maintain the cathode operating in the ion surface adsorption regime while limiting ion insertion. Since the capacities of the two electrodes are roughly balanced, upon charging of the device the cathode positively swings by ~ 2.6 V, while the anode negatively swings by ~ 0.1 V (*i.e.* the flat plateau) to become fully sodiated.

Prior to assembly and testing of the NIC devices, both electrodes were preconditioned in half-cells (*i.e.* vs. Na/Na⁺). The PSOC anode was firstly galvanostatically (50 mA g⁻¹) cycled three times between 0.001 - 3 V vs. Na/Na⁺, and then discharged to a cut-off voltage of 0.1 V vs. Na/Na⁺. This left it right above the onset of its high capacity intercalation plateau. The PSNC cathode was discharged (50 mA g⁻¹) to a cut-off voltage of 1.5 V vs. Na/Na⁺, leaving it sodiated to its target capacity. The specific energy and specific power values of assembled NICs were calculated as follows: $E = P \times t$, $P = \Delta V \times i$, $\Delta V = (V_{\max} + V_{\min})/2$, in this case i being the current normalized by the total active mass in both electrodes, V_{\max} is the voltage at the beginning of discharge after the IR drop and V_{\min} is the voltage at the end of discharge.

The performance of the NIC device is shown in **Figure 3-20**. Results in **Figure 3-20(A-E)** show devices tested at 1.5 - 4.2 V. **Figure 3-20E** and **Figure 3-20F** also shows devices tested in a narrower voltage window of 1.5 - 3.5 V. **Figure 3-21C** shows a device tested in a voltage window of 2.2 - 3.8 V, which is the identical range specified for an advanced hybrid Li ion capacitor that is commercially available.⁹⁶

Figure 3-20A and **Figure 3-21A** provide the galvanostatic charge and discharge profiles of the hybrid NIC devices at intermediate/high and at low current densities, respectively. The profiles display the desirable symmetric characteristics with low IR drops. At a current density (normalized by mass of anode) of 3.2, 6.4 and 12.8 A g⁻¹, the discharge capacity normalized by that active mass is 83, 57 and 36 mAh g⁻¹. This

equals 41.5, 28.5 and 18 mAh g⁻¹ (*i.e.* 60 Fg⁻¹×2.5V/3.6, 44.3 Fg⁻¹×2.32 V/3.6, and 30 Fg⁻¹×2.15 V/3.6) when normalized by the active mass in the device.

Figure 3-21B shows the Nyquist plots of PSNC-3-800//PSOC-A and CAC//PSOC-A devices. The spectra were fitted by an electric equivalent circuit model shown in **Figure 3-22**. The lower equivalent series resistance (R_{es}) for PSNC-3-800//PSOC-A (7.47 Ω) *vs.* CAC//PSOC-A (15.85 Ω) is attributed to a combination of superior electrical conductivity and reduced ion diffusion losses. The PSNC-3-800//PSOC-A device also demonstrated a lower charge transfer resistance (R_{ct} =12.01 Ω *vs.* 21.44 Ω), which may also be attributed to a less tortuous pore network.

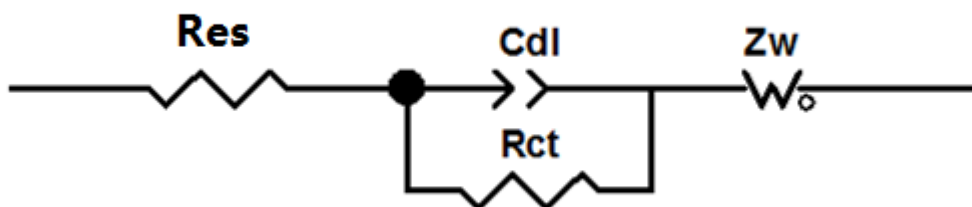


Figure 3-22: Equivalent electronic circuits used to simulate the EIS data. R_{es} is the sum of resistances of electrical connections in the experiment setup including ionic diffusion resistance in the electrolyte. R_{ct} reflects the charge transfer resistance and Z_w (Warburg-type element) represents Na diffusion impedance within carbon materials.

Figure 3-20B displays the Ragone plot of PSNC-3-800//PSOC-A NIC at different temperatures, tested at 1.5-4.2V. The gravimetric energy and power density is based on the total active mass in both electrodes. The volumetric energy and power is also plotted, being estimated from a rule of mixtures of the experimentally measured volume of the active cathode and anode. The device worked well at a wide temperature range (*i.e.* 0-65°C), yielding very promising energy and power combinations. At 65°C, a superb gravimetric energy density of 60 Wh kg⁻¹ is obtained at a power density as high as 34,000 W kg⁻¹. At the same temperature a volumetric energy density of 52 Wh L⁻¹ is achieved at a power density of 30,000 W L⁻¹. A factor

of 1/5 could be used to extrapolate the volumetric performance of a device with realistic mass loading from the performance based on the active materials alone.^{97,98} This conversion qualitatively (different device size, packaging, etc.) places our button cells in the range of commercial LIC devices.⁹⁹ A volumetric (active electrode or device) based comparison with scientific LIC and NIC literature is difficult as energy/power data is presented normalized by mass only.^{38,39,43,44,45,47,48,51,52}

Figure 3-20C displays the Ragone plot of PSNC-3-800//PSOC-A NIC at room temperature, with the specific energy/power density being based on the total mass of the active materials. The figure also shows a NIC based on CAC//PSOC-A, as well as symmetric EDLC devices based on CAC//CAC and PSNC-3-800//PSNC-3-800. Here the voltage window was 1.5 - 4.2 V, except for the symmetric EDLC devices which were tested within a voltage of 0 - 3V, *i.e.* actually a wider window than for the hybrids. However the EDLC systems are markedly inferior to the PSNC-3-800//PSOC-A configuration. In fact, the PSNC-3-800//PSOC-A system is superior at both low and high power, sacrificing nothing to the EDLC configurations, which are supposed to be superior at high rates. This is a direct testament of the exquisite high-rate intercalation kinetics of the PSOC anode, since solid-state diffusion is normally considered the rate-limiting step for Na battery electrodes. Even at the very power of 16,500 Wkg⁻¹ the PSNC-3-800//PSOC-A device delivers a respectable 50 Whkg⁻¹ of energy.

It is instructive to compare the energy - power characteristics of our device to the state-of-the-art reported in literature. This is shown in **Figure 3-20D**. The figure actually plots four types of systems: NICs, LICs, classical asymmetric aqueous electrolyte based supercapacitors, and ionic liquid electrolyte based supercapacitors that store charge by EDLC. A key distinction between NICs/LICs versus asymmetric aqueous electrolyte based supercapacitors (often also termed "hybrids"), is that for the latter electrical charge is primarily stored by a combination of EDLC and surface pseudocapacitance. Unlike for NICs and LICs, there is negligible ion insertion into

the bulk of the anode. While pure EDLC systems may cycle for up to 1,000,000 cycles (albeit at a lower energy), optimized asymmetric aqueous electrolyte based supercapacitors typically last 10,000 cycles and may fail by dissolution and/or coarsening of the oxide^{100,101,102,103}.

The Li/Na ion capacitors listed include various systems coupling a battery anode and a capacitor cathode, such as, AC//graphite (Li⁺),⁵¹ AC//hard carbon (Li⁺),⁵² AC//Li₄Ti₅O₁₂ (Li⁺),^{47,48} AC//TiO₂-RGO (Li⁺),⁴² 3D-porous graphene-sucrose//Li₄Ti₅O₁₂/G (Li⁺),¹⁰⁴ AC//3D-TiO₂/CNT (Li⁺),⁴⁶ 3D-Graphene//Fe₃O₄-graphene (Li⁺),³⁹ AC//V₂O₅-CNT (Na⁺),³⁸ AC//Na_xH_{2-x}Ti₃O₇ (Na⁺),⁴³ AC//NiCo₂O₄ (Na⁺),⁴⁵ AC//AC/MnO (Li⁺)⁴⁴. The supercapacitors mentioned include asymmetric aqueous systems like activated-graphene//MnO₂/activated-graphene,¹⁰⁵ Ni(OH)₂-graphene//porous graphene,¹⁰⁶ graphene//2D-MnO₂,¹⁰⁷ and symmetric liquid ion systems.^{74,108} As may be seen from this master comparison plot, the system developed in the current study is overall quite promising.

The cycling stability of the PSNC-3-800//PSOC-A NIC was firstly investigated at a current density of 6.4 Ag⁻¹. As shown in **Figure 3-20E**, using a maximum voltage of 4.2 V the device will retain 79% of its initial capacity after 1,000 cycles, 69% after 5,000 cycles, and 66% after 10,000 cycles. When we employed a smaller cut-off voltage of 3.5 V, the capacity retention increases to 81% at cycle 5,000 and 72% at cycle 10,000. We hypothesize that this improvement corresponds to reduced rates of degradation in the PSNC oxygen functionalities at the lower potential window. At both voltage windows the hybrid capacitors displayed excellent coulombic efficiencies, being near 100% during cycling. As a comparison, NIC device reported in previous literature displayed 27, 22 or 37% capacity decay after a limited number of cycles (~1,000, or 2,000) at lower voltage region (below 3V).^{38,43,45} As **Table 3-3** demonstrates, our cyclability is actually comparable to the previously published LIC devices.^{39,40,44,47,51,52,109} For reasons ascribed to the higher levels of

volume expansion for a comparable capacity associated with Na vs. Li insertion, achieving an on par cyclability with a NIC is indeed a notable feat.

Table 3-3: Capacity retention comparison with literature reported hybrid devices.

Hybrid system	Voltage Window	Current density	Energy density (Whkg ⁻¹)	Power density (Wkg ⁻¹)	Cycled number	Capacity retention	Ref.
PSNC-3-800//PSOC-A (Na ⁺)	1.5-4.2V	6.4Ag ⁻¹	50-75	~8000	1000/5000/10000	79%/69%/66%	This work
PSNC-3-800//PSOC-A (Na ⁺)	1.5-3.5V	6.4Ag ⁻¹	30-38	~7000	1000/5000/10000	92%/78%/72%	This work
PSNC-3-800//PSOC-A (Na ⁺)-65°C	1.5-3.5V	51.2Ag ⁻¹	~20	~55000	100000	78%	This work
PSNC-3-800//PSOC-A (Na ⁺)	1.5-3.5V	51.2Ag ⁻¹	~8	~50000	100000	88%	This work
AC//Na _x H _{2-x} Ti ₃ O ₇ (Na ⁺)	0-3V	0.25Ag ⁻¹	20-30	~200	1000	73%	43
AC//V ₂ O ₅ /CNT (Na ⁺)	0-2.8V	60C	16-20	~1700	900	78%	38
AC//NiCo ₂ O ₄ (Na ⁺)	0-3V	0.15Ag ⁻¹	11-18	~200	2000	62.5%	45
AC//V ₂ O ₅ /CNT (Li ⁺)	0.1-2.7V	30C	24-30	~850	10000	80%	106
CNS//MnO/CNS (Li ⁺)	0-4V	5Ag ⁻¹	50-70	~6000	5000	82%	44
3DGraphene//Fe ₃ O ₄ /Graphene (Li ⁺)	1-4V	2Ag ⁻¹	60-90	2500	1000	68%	39
AC//Li ₄ Ti ₅ O ₁₂ (Li ⁺)	1-3V	1.5Ag ⁻¹	22-28	~3000	2000	80%	47
AC//Soft carbon (Li ⁺)	0-4.4V	0.74Ag ⁻¹	50-80	~2000	10000	65%	40
AC//graphite (Li ⁺)	1.5-5.0V	0.65Ag ⁻¹	60-90	~1056	10000	63%	51
AC//hard carbon (Li ⁺)	1.5-3.9V	10C	60-75	~750	10000	82%	52

Finally, we also followed the cycling test parameters similar to those employed by a commercial LIC device manufacturer (Ultimo™), which are listed on their website⁹⁶. As shown in **Figure 3-21C**, the devices were tested for 100,000 cycles between 1.5-3.5 V (51.2 Ag⁻¹), both at 25°C and at 65°C. Our NICs achieved energy/power densities of 8-20 Wh kg⁻¹ at ~50000 Wkg⁻¹ (active material normalized), retaining 88% and 78% of their capacity after 100,000 cycles at 25 and 65°C. **Figure 3-21C** shows the cycling stability of PSNC-3-800//PSOC-A NIC at a current density of 100Ag⁻¹ and a voltage window of 2.2-3.8V, which are the current density and voltage window quoted in ref. 96. After 100,000 cycles our NICs capacity degraded by only 1.2%. These values are fully competitive with Ultimo LICs according to the information provided on the manufacturer website. Once again this highlights the attractiveness of our approach considering that our electrode materials are fabricated from waste peanut shells and hence to use the expression "cost peanuts", run on Na rather than on Li, and should be further improvable with industrial-style engineering optimization (electrode fabrication process, electrolyte component adjustment, *etc.*).

3.4 Conclusion

To summarize, we created a high performance hybrid sodium ion capacitor (NIC) with the active materials in both electrodes being approximately balanced in their capacity and derived entirely from a single precursor of biomass waste peanut shells. The device offers some of the most promising energy-power-cycling stability combinations reported in literature for either Na or Li ion hybrid systems.

3.5 References

- 1 M. D. Slater, D. Kim, E. Lee and C. S. Johnson, *Adv. Funct. Mater.*, 2013, **23**, 947-958.
- 2 V. Palomares, P. Serras, I. Villaluenga, K. B. Hueso, J. Carretero-Gonzalez and T.

- Rojo, *Energy Environ. Sci.*, 2012, **5**, 5884-5901.
- 3 L. Ji, M. Gu, Y. Shao, X. Li, M. H. Engelhard, B. W. Arey, W. Wang, Z. Nie, J. Xiao, C. Wang, J. Zhang and J. Liu, *Adv. Mater.*, 2014, **26**, 2901-2908.
- 4 J. F. Qian, Y. Xiong, Y. L. Cao, X. P. Ai, H. X. Yang, *Nano Lett.*, 2014, **14**, 1865-1869.
- 5 Y. Wen, K. He, Y. Zhu, F. Han, Y. Xu, I. Matsuda, Y. Ishii, J. Cumings and C. Wang, *Nat. Commun.*, 2014, **5**, 4033.
- 6 D. Datta, J. W. Li and V. B. Shenoy, *ACS Appl. Mater. Inter.*, 2014, **6**, 1788-1795.
- 7 H. L. Zhu, Z. Jia, Y. C. Chen, N. Weadock, J. Y. Wan, O. Vaaland, X. G. Han, T. Li and L. B. Hu, *Nano Lett.*, 2013, **13**, 3093-3100.
- 8 W. Luo, J. Schardt, C. Bommier, B. Wang, J. Razink, J. Simonsen and X. L. Ji, *J. Mater. Chem. A*, 2013, **1**, 10662-10666.
- 9 C. D. Wessells, M. T. McDowell, S. V. Peddada, M. Pasta, R. A. Huggins and Y. Cui, *ACS Nano*, 2012, **6**, 1688-1694.
- 10 Y. L. Cao, L. F. Xiao, M. L. Sushko, W. Wang, B. Schwenzer, J. Xiao, Z. M. Nie, L. V. Saraf, Z. G. Yang and J. Liu, *Nano Lett.*, 2012, **12**, 3783-3787.
- 11 C. Bommier, W. Luo, W. Gao, A. Greaney, S. Ma and X. Ji, *Carbon*, 2014, **76**, 165-174.
- 12 T. H. Hwang, D. S. Jung, J. S. Kim, B. G. Kim and J. W. Choi, *Nano Lett.*, 2013, **13**, 4532-4538.
- 13 Y. Y. Shao, J. Xiao, W. Wang, M. Engelhard, X. L. Chen, Z. M. Nie, M. Gu, L. V. Saraf, G. Exarhos, J. G. Zhang and J. Liu, *Nano Lett.*, 2013, **13**, 3909-3914.
- 14 D. W. Su and G. X. Wang, *ACS Nano*, 2013, **7**, 11218-11226.
- 15 Y. Liu, F. Fan, J. Wang, Y. Liu, H. Chen, K. L. Jungjohann, Y. Xu, Y. Zhou, D. Bigio, T. Zhu and C. Wang, *Nano Lett.*, 2014, **14**, 3445-3452.
- 16 L. J. Fu, K. Tang, K. P. Song, P. A. van Aken, Y. Yu and J. Maier, *Nanoscale*, 2014, **6**, 1384-1389.

- 17 B. R. Liu, P. Soares, C. Checkles, Y. Zhao and G. H. Yu, *Nano Lett.*, 2013, **13**, 3414-3419.
- 18 Y. J. Gong, S. B. Yang, L. Zhan, L. L. Ma, R. Vajtai and P. M. Ajayan, *Adv. Funct. Mater.*, 2014, **24**, 125-130.
- 19 S. M. Oh, S. T. Myung, C. S. Yoon, J. Liu, J. Hassoun, B. Scrosati, K. Amine, Y. K. Sun, *Nano Lett.*, 2014, **14**, 1620-1626.
- 20 R. Mukherjee, R. Krishnan, T. M. Lu and N. Koratkar, *Nano Energy*, 2012, **1**, 518-533.
- 21 C. B. Zhu, K. P. Song, P. A. van Aken, J. Maier and Y. Yu, *Nano Lett.*, 2014, **14**, 2175-2180.
- 22 C. Z. Wu, X. L. Lu, L. L. Peng, K. Xu, X. Peng, J. L. Huang, G. H. Yu and Y. Xie, *Nat. Commun.*, 2013, **4**, 2431.
- 23 J. X. Zhu, L. J. Cao, Y. S. Wu, Y. J. Gong, Z. Liu, H. E. Hoster, Y. H. Zhang, S. T. Zhang, S. B. Yang, Q. Y. Yan, P. M. Ajayan, R. Vajtai, *Nano Lett.*, 2013, **13**, 5408-5413.
- 24 C. H. Xu, B. H. Xu, Y. Gu, Z. G. Xiong, J. Sun and X. S. Zhao, *Energy Environ. Sci.*, 2013, **6**, 1388-1414.
- 25 J. Han, L. L. Zhang, S. Lee, J. Oh, K. S. Lee, J. R. Potts, J. Y. Ji, X. Zhao, R. S. Ruoff and S. Park, *ACS Nano*, 2013, **7**, 19-26.
- 26 W. Luo, B. Wang, C. G. Heron, M. J. Allen, J. Morre, C. S. Maier, W. F. Stickle and X. L. Ji, *Nano Lett.*, 2014, **14**, 2225-2229.
- 27 L. Qie, W. M. Chen, H. H. Xu, X. Q. Xiong, Y. Jiang, F. Zou, X. L. Hu, Y. Xin, Z. L. Zhang and Y. H. Huang, *Energy Environ. Sci.*, 2013, **6**, 2497-2504.
- 28 S. Boukhalfa, D. Gordon, L. L. He, Y. B. Melnichenko, N. Nitta, A. Magasinski and G. Yushin, *ACS Nano*, 2014, **8**, 2495-2503.
- 29 M. R. Lukatskaya, O. Mashtalir, C. E. Ren, Y. Dall'Agnese, P. Rozier, P. L. Taberna, M. Naguib, P. Simon, M. W. Barsoum and Y. Gogotsi, *Science*, 2013, **341**,

1502-1505.

30 L. Wei, M. Sevilla, A. B. Fuertes, R. Mokaya and G. Yushin, *Adv. Energy Mater.*, 2011, **1**, 356-361.

31 W. J. Qian, F. X. Sun, Y. H. Xu, L. H. Qiu, C. H. Liu, S. D. Wang and F. Yan, *Energy Environ. Sci.*, 2014, **7**, 379-386.

32 L. L. Peng, X. Peng, B. R. Liu, C. Z. Wu, Y. Xie and G. H. Yu, *Nano Lett.*, 2013, **13**, 2151-2157.

33 Z. Li, L. Zhang, B. S. Amirkhiz, X. H. Tan, Z. W. Xu, H. L. Wang, B. C. Olsen, C. M. B. Holt and D. Mitlin, *Adv. Energy Mater.*, 2012, **2**, 431-437.

34 M. Ghaffari, Y. Zhou, H. P. Xu, M. R. Lin, T. Y. Kim, R. S. Ruoff and Q. M. Zhang, *Adv. Mater.*, 2013, **25**, 4879-4885.

35 N. S. Choi, Z. H. Chen, S. A. Freunberger, X. L. Ji, Y. K. Sun, K. Amine, G. Yushin, L. F. Nazar, J. Cho and P. G. Bruce, *Angew. Chem., Int. Edit.*, 2012, **51**, 9994-10024.

36 P. Simon, Y. Gogotsi and B. Dunn, *Science*, 2014, **343**, 1210-1211.

37 K. Naoi, S. Ishimoto, J. Miyamoto and W. Naoi, *Energy Environ. Sci.*, 2012, **5**, 9363-9373.

38 Z. Chen, V. Augustyn, X. L. Jia, Q. F. Xiao, B. Dunn and Y. F. Lu, *ACS Nano*, 2012, **6**, 4319-4327.

39 F. Zhang, T. F. Zhang, X. Yang, L. Zhang, K. Leng, Y. Huang and Y. S. Chen, *Energy Environ. Sci.*, 2013, **6**, 1623-1632.

40 M. Schroeder, M. Winter, S. Passerini and A. Balducci, *J. Power Sources*, 2013, **238**, 388-394.

41 Q. Wang, Z. H. Wen and J. H. Li, *Adv. Funct. Mater.*, 2006, **16**, 2141-2146.

42 H. Kim, M. Y. Cho, M. H. Kim, K. Y. Park, H. Gwon, Y. Lee, K. C. Roh and K. Kang, *Adv. Energy Mater.*, 2013, **3**, 1500-1506.

43 J. Yin, L. Qi and H. Y. Wang, *ACS Appl. Mater. Inter.*, 2012, **4**, 2762-2768.

- 44 H. L. Wang, Z. W. Xu, Z. Li, K. Cui, J. Ding, A. Kohandehghan, X. H. Tan, B. Zahiri, B. C. Olsen, C. M. B. Holt and D. Mitlin, *Nano Lett.*, 2014, **14**, 1987-1994.
- 45 R. Ding, L. Qi and H. Wang, *Electrochim. Acta*, 2013, **114**, 726-735.
- 46 Z. Chen, Y. Yuan, H. H. Zhou, X. L. Wang, Z. H. Gan, F. S. Wang and Y. F. Lu, *Adv. Mater.*, 2014, **26**, 339-345.
- 47 A. Jain, V. Aravindan, S. Jayaraman, P. S. Kumar, R. Balasubramanian, S. Ramakrishna, S. Madhavi and M. P. Srinivasan, *Sci. Rep.*, 2013, **3**, 3002.
- 48 H. S. Choi, J. H. Im, T. Kim, J. H. Park and C. R. Park, *J. Mater. Chem.*, 2012, **22**, 16986-16993.
- 49 J. Ding, H. L. Wang, Z. Li, A. Kohandehghan, K. Cui, Z. W. Xu, B. Zahiri, X. H. Tan, E. M. Lotfabad, B. C. Olsen and D. Mitlin, *ACS Nano*, 2013, **7**, 11004-11015.
- 50 N. Yabuuchi, M. Kajiyama, J. Iwatate, H. Nishikawa, S. Hitomi, R. Okuyama, R. Usui, Y. Yamada and S. Komaba, *Nat. Mater.*, 2012, **11**, 512-517.
- 51 V. Khomenko, E. Raymundo-Pinero and F. Beguin, *J. Power Sources*, 2008, **177**, 643-651.
- 52 J. H. Kim, J. S. Kim, Y. G. Lim, J. G. Lee and Y. J. Kim, *J. Power Sources*, 2011, **196**, 10490-10495.
- 53 B. Hu, K. Wang, L. H. Wu, S. H. Yu, M. Antonietti and M. M. Titirici, *Adv. Mater.*, 2010, **22**, 813-828.
- 54 Z. Gui, H. L. Zhu, E. Gillette, X. G. Han, G. W. Ruoff, L. B. Hu and S. B. Lee, *ACS Nano*, 2013, **7**, 6037-6046.
- 55 L. Wei and G. Yushin, *Nano Energy*, 2012, **1**, 552-565.
- 56 N. A. Liu, K. F. Huo, M. T. McDowell, J. Zhao and Y. Cui, *Sci. Rep.*, 2013, **3**, 1919.
- 57 S. Dutta, A. Bhaumik and C. W. Wu, *Energy Environ. Sci.*, 2014, **7**, 3574-3592.
- 58 R. J. White, V. Budarin, R. Luque, J. H. Clark and D. J. Macquarrie, *Chem. Soc. Rev.*, 2009, **38**, 3401-3418.

- 59 M. Latorre-Sanchez, A. Primo and H. Garcia, *Angew. Chem., Int. Edit.*, 2013, **52**, 11813-11816.
- 60 L. Sun, C. G. Tian, M. T. Li, X. Y. Meng, L. Wang, R. H. Wang, J. Yin and H. G. Fu, *J. Mater. Chem. A*, 2013, **1**, 6462-6470.
- 61 M. Biswal, A. Banerjee, M. Deo and S. Ogale, *Energy Environ. Sci.*, 2013, **6**, 1249-1259.
- 62 K. Wilson, H. Yang, C. W. Seo and W. E. Marshall, *Bioresource Technol.*, 2006, **97**, 2266-2270.
- 63 X. Y. Zhao, J. Chen and F. L. Du, *J. Food Sci. Tech. Mys.*, 2012, **49**, 521-529.
- 64 A. S. Chang, A. Sreedharan and K. R. Schneider, *Food Control*, 2013, **32**, 296-303.
- 65 E. I. El-Shafey, *J. Environ. Manage*, 2007, **84**, 620-627.
- 66 Z. A. Al-Othman, R. Ali and M. Naushad, *Chem. Eng. J.*, 2012, **184**, 238-247.
- 67 X. J. He, P. H. Ling, J. S. Qiu, M. X. Yu, X. Y. Zhang, C. Yu and M. D. Zheng, *J. Power Sources*, 2013, **240**, 109-113.
- 68 P. Z. Guo, Q. Q. Ji, L. L. Zhang, S. Y. Zhao and X. S. Zhao, *Acta. Phys-Chim. Sin.*, 2011, **27**, 2836-2840.
- 69 G. T. K. Fey, Y. Y. Lin, K. P. Huang, Y. C. Lin, T. P. Kumar, Y. D. Cho and H. M. Kao, *Adv. Mater. Res.*, 2012, **415-417**, 1572-1585.
- 70 I. Watanabe, T. Doi, J. I. Yamaki, Y. Y. Lin and G. T. K. Fey, *J. Power Sources*, 2008, **176**, 347-352.
- 71 M. Ahmad, S. S. Lee, X. Dou, D. Mohan, J. K. Sung, J. E. Yang and Y. S. Ok, *Bioresour Technol.*, 2012, **118**, 536-544.
- 72 Z. Y. Zhong, Q. Yang, X. M. Li, K. Luo, Y. Liu and G. M. Zeng, *Ind. Crop. Prod.*, 2012, **37**, 178-185.
- 73 X. D. Zhang, M. Xu, R. F. Sun and L. Sun, *J. Eng. Gas Turb. Power*, 2006, **128**, 493-496.

- 74 H. Wang, Z. W. Xu, A. Kohandehghan, Z. Li, K. Cui, X. H. Tan, T. J. Stephenson, C. K. King'ondeu, C. M. B. Holt, B. C. Olsen, J. K. Tak, D. Harfield, A. O. Anyia and D. Mitlin, *ACS Nano*, 2013, **7**, 5131-5141.
- 75 Y. H. Liu, J. S. Xue, T. Zheng and J. R. Dahn, *Carbon*, 1996, **34**, 193-200.
- 76 C. Y. Su, Y. P. Xu, W. J. Zhang, J. W. Zhao, X. H. Tang, C. H. Tsai and L. J. Li, *Chem. Mater.*, 2009, **21**, 5674-5680.
- 77 C. Vidal-Abarca, P. Lavela, J. L. Tirado, A. V. Chadwick, M. Alfredsson and E. Kelder, *J. Power Sources*, 2012, **197**, 314-318.
- 78 A. Bhide, J. Hofmann, A. K. Durr, J. Janek and P. Adelhelm, *Phys. Chem. Chem. Phys.*, 2014, **16**, 1987-1998.
- 79 V. Augustyn, J. Come, M. A. Lowe, J. W. Kim, P. L. Taberna, S. H. Tolbert, H. D. Abruna, P. Simon and B. Dunn, *Nat. Mater.*, 2013, **12**, 518-522.
- 80 H. Kim, Y. U. Park, K. Y. Park, H. D. Lim, J. Hong and K. Kang, *Nano Energy*, 2014, **4**, 97-104.
- 81 S. Y. Kim, J. Hong, R. Kaviani, S. W. Lee, M. N. Hyder, Y. Shao-Horn and P. T. Hammond, *Energy Environ. Sci.*, 2013, **6**, 888-897.
- 82 S. H. Ha, Y. S. Jeong and Y. J. Lee, *ACS Appl. Mater. Inter.*, 2013, **5**, 12295-12303.
- 83 H. Kim, H. D. Lim, S. W. Kim, J. Hong, D. H. Seo, D. C. Kim, S. Jeon, S. Park and K. Kang, *Sci. Rep.*, 2013, **3**, 1506.
- 84 M. N. Hyder, S. W. Lee, F. C. Cebeci, D. J. Schmidt, Y. Shao-Horn and P. T. Hammond, *ACS Nano*, 2011, **5**, 8552-8561.
- 85 S. W. Lee, N. Yabuuchi, B. M. Gallant, S. Chen, B. S. Kim, P. T. Hammond and Y. Shao-Horn, *Nat. Nanotechnol.*, 2010, **5**, 531-537.
- 86 W. T. Gu, N. Peters and G. Yushin, *Carbon*, 2013, **53**, 292-301.
- 87 F. Y. Tu, S. Q. Liu, T. H. Wu, G. H. Jin and C. Y. Pan, *Powder Technol.*, 2014, **253**, 580-583.

- 88 H. R. Byon, B. M. Gallant, S. W. Lee and Y. Shao-Horn, *Adv. Funct. Mater.*, 2013, **23**, 1037-1045.
- 89 S. W. Lee, B. M. Gallant, Y. Lee, N. Yoshida, D. Y. Kim, Y. Yamada, S. Noda, A. Yamada and Y. Shao-Horn, *Energy Environ. Sci.*, 2012, **5**, 5437-5444.
- 90 R. Mukherjee, A. V. Thomas, D. Datta, E. Singh, J. W. Li, O. Eksik, V. B. Shenoy and N. Koratkar, *Nat. Commun.*, 2014, **5**, 3710.
- 91 H. G. Wang, Z. Wu, F. L. Meng, D. L. Ma, X. L. Huang, L. M. Wang and X. B. Zhang, *ChemsusChem*, 2013, **6**, 56-60.
- 92 K. Tang, L. J. Fu, R. J. White, L. H. Yu, M. M. Titirici, M. Antonietti and J. Maier, *Adv. Energy Mater.*, 2012, **2**, 873-877.
- 93 X. Zhou, Y. G. Guo, *ChemElectroChem*, 2014, **1**, 83-86.
- 94 A. Ponrouch, A. R. Goni and M. R. Palacin, *Electrochem. Commun.*, 2013, **27**, 85-88.
- 95 V. G. Pol, E. Lee, D. H. Zhou, F. Dogan, J. M. Calderon-Moreno and C. S. Johnson, *Electrochim. Acta*, 2014, **127**, 61-67.
- 96 http://www.jmenergy.co.jp/en/products_cell_can.html
- 97 Y. Gogotsi, P. Simon, *Science*, 2011, **334**, 917-918.
- 98 Y. W. Zhu, S. Murali, M. D. Stoller, K. J. Ganesh, W. W. Cai, P. J. Ferreira, A. Pirkle, R. M. Wallace, K. A. Cychosz, M. tomme, D. Su, E. A. Stach, R. S. Ruoff, *Science*, 2011, **332**, 1537-1541.
- 99 <http://www.jsrmicro.com/index.php/EnergyAndEnvironment>
- 100 H. Wang, C. M. Holt, Z. Li, X. Tan, B. S. Amirkhiz, Z. Xu, B. Olsen, T. Stephenson, D. Mitlin, *Nano Res.*, 2012, **5**, 605-617.
- 101 W. Wei, X. Cui, W. Chen, D. Ivey, *Chem. Soc. Rev.*, 2011, **40**, 1697-1721.
- 102 D. Cericola, R. Kotz, *Electrochim. Acta*, 2012, **72**, 1-17.
- 103 G. Wang, L. Zhang, J. Zhang, *Chem. Soc. Rev.*, 2012, **41**, 797-828.
- 104 K. Leng, F. Zhang, L. Zhang, T. F. Zhang, Y. P. Wu, Y. H. Lu, Y. Huang and Y. S.

Chen, *Nano Res.*, 2013, **6**, 581-592.

105 X. Zhao, L. L. Zhang, S. Murali, M. D. Stoller, Q. H. Zhang, Y. W. Zhu and R. S. Ruoff, *ACS Nano*, 2012, **6**, 5404-5412.

106 J. Yan, Z. J. Fan, W. Sun, G. Q. Ning, T. Wei, Q. Zhang, R. F. Zhang, L. J. Zhi and F. Wei, *Adv. Funct. Mater.*, 2012, **22**, 2632-2641.

107 S. Shi, C. J. Xu, C. Yang, Y. Y. Chen, J. J. Liu and F. Y. Kang, *Sci. Rep.*, 2013, **3**, 2598.

108 C. G. Liu, Z. N. Yu, D. Neff, A. Zhamu and B. Z. Jang, *Nano Lett.*, 2010, **10**, 4863-4868.

109 Z. Chen, V. Augustyn, J. Wen, Y. W. Zhang, M. Q. Shen, B. Dunn and Y. F. Lu, *Adv. Mater.*, 2011, **23**, 791-795.

4

Sodiation vs. Lithiation Phase Transformations in a High Rate - High Stability SnO₂ in Carbon Nanocomposite*

4.1 Introduction

Electrical energy storage systems are critical technologies to address the global energy shortage and emerging environmental issues. As one of the most important EES systems, lithium ion batteries (LIBs), have been widely applied in electric vehicles, portable devices and grid storages.^{1,2,3} Due to the increasing concern about lithium's cost and continued availability, sodium ion batteries (NIBs) are currently under extensive investigation as an alternative to LIBs.^{4,5,6,7,8,9,10,11} There have been good recent successes in developing NIB cathodes^{12,13,14,15}. Moreover, highly ordered but non-graphitic carbons,^{16, 17, 18, 19} titanium oxides/compounds^{20, 21, 22, 23} and alloys^{24,25,26,27,28,29} are emerging promising NIB anode materials. Candidates for alloy - dealloying anodes include Sn,^{30,31,32} Si,^{33,34,35} Ge,³⁶ Sb,^{37,38} SnO_x,^{39,40,41,42,43,44,45,46} Sb₂O₃^{47,48} etc.

Tin dioxide (SnO₂) is a promising LIB anode material, which has recently been applied to the Na system.^{41,49,50,51,52,53,54,55,56} In a LIB application, based on systematic *in-situ* TEM,⁵⁷ atomic scale HRTEM characterization⁵⁸ and *ex-situ* XPS, TEM analysis⁵², it is commonly proposed that the charge storage mechanism of SnO₂ is based on a reversible conversion reaction ($\text{SnO}_2 + 4\text{Li} + 4\text{e}^- \leftrightarrow \text{Sn} + \text{Li}_2\text{O}$) combined

* Material in this chapter has been published in:

Jia Ding, Huanlei Wang, Zhi Li, Kai Cui, Dimitre Karpuzov, Xuehai Tan, Alireza Kohandehghan, David Mitlin., *Journal of Materials Chemistry A*, 2015, 3(13), 7100-7111.

with an alloying reaction ($\text{Sn} + 4.4\text{Li}^+ + 4.4\text{e}^- \leftrightarrow \text{Li}_{22}\text{Sn}_5$),⁵⁸ resulting to a theoretical capacity of 1494 mAhg^{-1} for the combined reactions. In the recent studies applying SnO_2 as LIBs anode, the practical capacities obtained have generally been in that range.^{51,52,59} With Na the capacity should be only somewhat lower (1378 mAhg^{-1} , assuming that SnO_2 follows a parallel conversion ($\text{SnO}_2 + 4\text{Na}^+ + 4\text{e}^- \leftrightarrow \text{Sn} + \text{Na}_2\text{O}$, 711 mAhg^{-1}), and then an alloying reaction ($\text{Sn} + 3.75\text{Na}^+ + 3.75\text{e}^- \leftrightarrow \text{Na}_{15}\text{Sn}_4$, 667 mAhg^{-1} normalized to the mass of SnO_2).⁶⁰ By contrast for the case of Na, the experimentally measured capacity of SnO_2 based materials are generally much lower than the theoretical value.^{54,55,61,62,63,64} To date this discrepancy remains unresolved, and it would be desirable to test and analyze the same material against Na and against Li to ascertain the key mechanistic differences in the charging - discharging behavior.

A key issue for broad range of NIB anode materials is that they appear to undergo significant capacity fading during cycling, on a scale that is substantially worse than for comparable LIB anodes. While there may be numerous reasons for this degradation, the commonly observed factors in both LIBs and NIBs are material pulverization (loss of electrical contact) and/or agglomeration of nanoparticulates (worsening of kinetics due to loss of nano-scale diffusion distances).⁶⁵ For the oxides (*e.g.* SnO_2) especially, material agglomeration will also impede the reversibility of the conversion reaction.^{51,52} In order to minimize this problem, researchers introduce secondary carbon phases (*e.g.* CNT,^{66,67} graphene,^{40,51,68,69} carbon fibers,^{70,71} disordered carbon,^{72,73} *etc.*) that both accommodate the volume expansion and prevent the aggregation of the active materials. Substantial success has been achieved applying this strategy for LIBs, with this approach becoming applied for NIBs as well.^{27,61,74} However NIB anodes undergo a larger volumetric expansion than their LIB counterparts (due to the larger diameter of the former ion: 1.06 \AA Na *vs.* 0.76 \AA).⁷⁵ This raises a bigger challenge in buffering the stress during sodiation and in preventing the capacity decay due to the materials pulverization/agglomeration issues.

In this work, we prepared a unique nanostructured SnO_2 - carbon composite through a self-assembly process under hydrothermal conditions. The C- SnO_2

electrode exhibited quite promising electrochemical performance as anodes for both NIBs and LIBs. We systemically investigated the phase transformations associated with SnO₂ reacting with Na, providing a systematic and broadly applicable picture of the origin of the capacity difference of this material for NIB vs. for LIB applications.

4.2 Experimental procedure

4.2.1 Materials preparation

C-SnO₂ materials were prepared by a modified hydrothermal synthesis method followed by a carbonization process. In a typical synthesis, hexadecyltrimethylammonium bromide (CTAB, (C₁₆H₃₃)N(CH₃)₃Br, 0.5g) was firstly dispersed in 15mL MQ-water. After stirring for 2h, 1.2g glucose was dissolved afterwards. Finally, 0.35g sodium stannate (Na₂SnO₃) trihydrate was dissolved in the former solution under vigorously stirring for 0.5h. Then the final aqueous solution was placed in a 50 mL stainless steel autoclave. The autoclave was sealed, soaked at 160°C for 1h and at 180°C for another 1.5h before it was allowed to cool to room temperature. The reaction mechanism of stannate hydrolysis under the modified hydrothermal condition will be further discussed in the Results and Discussion section. The resulting brown product was thoroughly washed by both ethanol and MQ-water, then collected by filtration and dried at 80°C overnight. The further carbonization is carried out in a horizontal tube furnace at 510°C for 3h under argon flow. SnO₂ nanoparticle baseline was prepared by the same procedure but without glucose and CTAB. The pure carbon reference was prepared without CTAB and stannate salt.

4.2.2 Material characterization

For the morphologies of the material, a Hitachi S-4800 SEM equipped with field emission gun is used. TEM analysis is performed using a JEOL JEM-2010 TEM, with an accelerating voltage of 200 kV. XRD analysis was performed using a Bruker AXS D8 Discover diffractometer with the Cu K_α radiation. XPS spectra were obtained on

an Axis Ultra spectrometer. Nitrogen adsorption-desorption analysis was performed using Quantachrome Instruments (U.S.A) Autosorb-1 at 77 K. Thermogravimetric analysis (TGA, Perkin-Elmer TGA 4000) was measured with a heating rate of 5°C min⁻¹ under 200 mL min⁻¹ of flowing air.

4.2.3 Electrochemical measurements

Electrochemical tests were carried out using coin cell CR2032. Typically, a slurry of 80% active materials, 10% carbon black (Super-P), and 10% poly(vinylidenedifluoride) in N-methylpyrrolidone was coated onto a stainless steel disk and then dried at 110°C overnight in a vacuum oven. The mass loading of the electrodes was 1.5 mg cm⁻². For Na half cells, Na metal was used as counter electrode and separated from the working electrode with polyethene separator. 1 M NaClO₄ dissolved in a mixture of ethylene carbonate (EC) and diethyl carbonate (DEC) with a volume ratio of 1:1 was utilized as the electrolyte. For Li half cells, Li metal as used as counter electrode, 1M LiPF₆ solvated in EC-DEC-DMC (dimethyl carbonate), 1:1:1 volumetric ratio was used as electrolyte. All the cyclic voltammetry measurements were conducted on a Solartron 1470 Multistat system. The galvanostatic charge-discharge tests were performed using an Arbin BT2000 Potentiostat. Before the CV, galvanostatic cycling and rate performance tests, the assembled batteries were first stored at ambient for 8 hours. All electrochemical tests were conducted at room temperature.

4.3 Result and discussion

4.3.1 As-synthesized microstructure

The nanocomposite was prepared through one-pot hydrothermal synthesis, followed by annealing in Ar. Sodium stannate is a commonly employed precursor for SnO₂ materials synthesis.^{76,77,78,79} Firstly, after being dissolved in aqueous solution the Na₂SnO₃ is dissociated into ions of Na⁺ and SnO₃²⁻. The hydrothermal treatment

of glucose would create a mild acidic condition in the reaction system.⁸⁰ In this environment, SnO_3^{2-} would react with H_2O (*i.e.* hydrolysis) forming precipitate particles⁸¹, which would be amorphous tin oxides or tin hydrates. The reaction routes have been described as $\text{SnO}_3^{2-} + 3\text{H}_2\text{O} \rightarrow \text{Sn}(\text{OH})_4 + 2\text{OH}^-$, or $\text{SnO}_3^{2-} + \text{H}_2\text{O} \rightarrow \text{SnO}_2 + 2\text{OH}^-$ ^{76,81}, with the hydrates transforming into oxides during the subsequent annealing process.⁸¹ Based on the ultimate morphology of the resultant SnO_2 crystals, the pristine hydrolysis products should be sub-5nm in size. Precipitation of carbon-rich polysaccharide took place following stannate hydrolysis, resulting in a self-assembled hierarchical nanostructure of the two phases. The Ar annealing at the relatively low temperature (510°C) further carbonized the polysaccharide but without reducing the oxide. The obtained material consisted of SnO_2 nanoparticle assemblies embedded in a continuous matrix of amorphous carbon and is termed "C- SnO_2 ". For a baseline we synthesized carbon-free SnO_2 nanoparticle specimens, naming them " SnO_2 ".

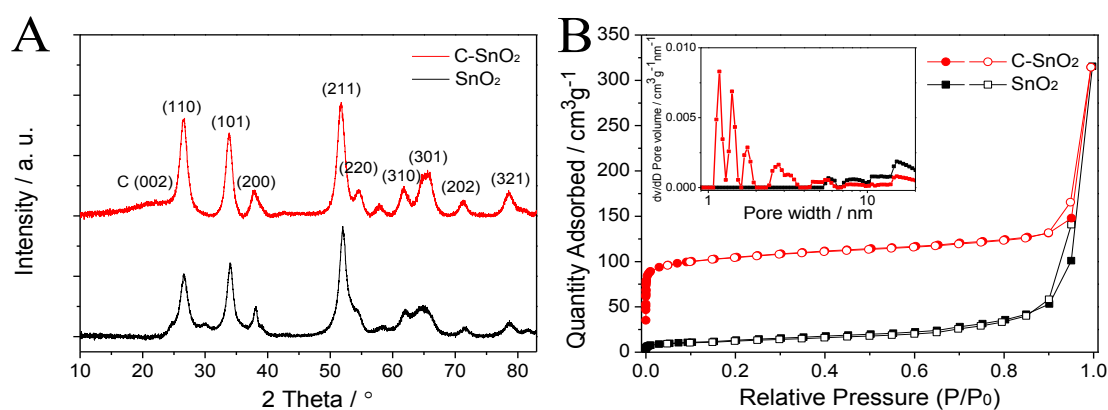


Figure 4-1: As-synthesized microstructures. (A) Indexed XRD pattern of C- SnO_2 and SnO_2 specimens, showing SnO_2 being present as the rutile phase. (B) Nitrogen adsorption-desorption isotherms of C- SnO_2 and SnO_2 , and pore size distribution of both specimens (insert).

The crystalline structure of both C- SnO_2 and SnO_2 was characterized by X-ray diffraction (XRD). As shown in **Figure 4-1A**, the patterns of both specimens are indexed as rutile SnO_2 ,⁸² with no other Sn oxide phases being detected (*e.g.* SnO , orthorhombic SnO_2). The broad hump centered at $\sim 22^\circ$ for C- SnO_2 is due to the carbon. As the carbon phase in C- SnO_2 is highly structurally disordered, it does not

possess a graphitic structure and has few intact graphene planes. However, there is short-range order between nearest – neighbor C atoms, with their relative positions being described by a radial distribution of distances. Because there is a frequency maximum in the radial distribution of first and second nearest neighbors, the XRD pattern contains two broad humps (rather than sharp Bragg peaks), with first one being much more intense.⁸³ In amorphous carbons the first hump occurs at roughly 22°, and may be extrapolated to yield the mean C nearest neighbor position in the disordered array similarly to the way Bragg’s law may be employed for long-range ordered phases.

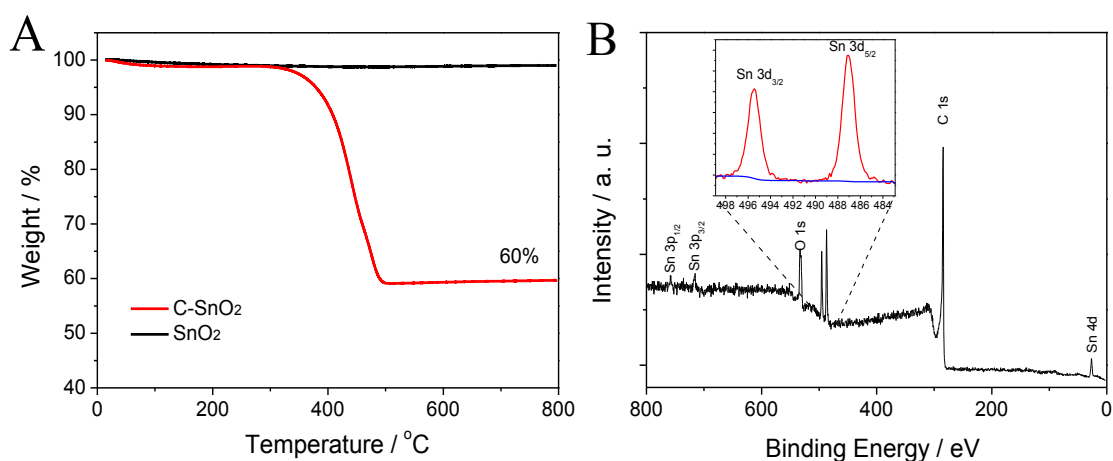


Figure 4-2: (A) Thermogravimetric curves of C-SnO₂ and SnO₂ specimens. (B) XPS survey spectrum of C-SnO₂ and high resolution spectrum of Sn 3d level (insert).

The weight percent of SnO₂ in C-SnO₂ is 60wt%, as evaluated by thermogravimetric analysis (TGA) performed in air and shown in **Figure 4-2A**. Combustion of the carbon occurs in the range of 310 - 500°C, with no additional changes in weight at higher temperatures. **Figure 4-1B** shows the nitrogen adsorption-desorption isotherms of C-SnO₂ and SnO₂ specimens. The corresponding pore size distribution results (obtained by density functional theory (DFT)) are shown in the figure insert. C-SnO₂ displays type I isotherm, with a high specific BET surface area of 338 m²g⁻¹ and total pore volume of 0.48 cm³g⁻¹. Most of the porosity is located in the micro and sub-3nm mesopore regime. Conversely, the SnO₂ specimen possesses a surface area of 48 m²g⁻¹ and inter-particle voids larger than 10 nm. The

near-surface structure of C-SnO₂ was characterized by X-ray photoelectron spectroscopy (XPS). **Figure 4-2B** displays its survey spectrum, while the insert shows the high resolution spectrum of the Sn 3d double peaks. The peaks at 487 eV and 495.5 eV are ascribed to Sn 3d_{5/2} and Sn 3d_{3/2} respectively. These peak positions are characteristic of the Sn⁴⁺ chemical state, further confirming the oxidation state of Sn as SnO₂.

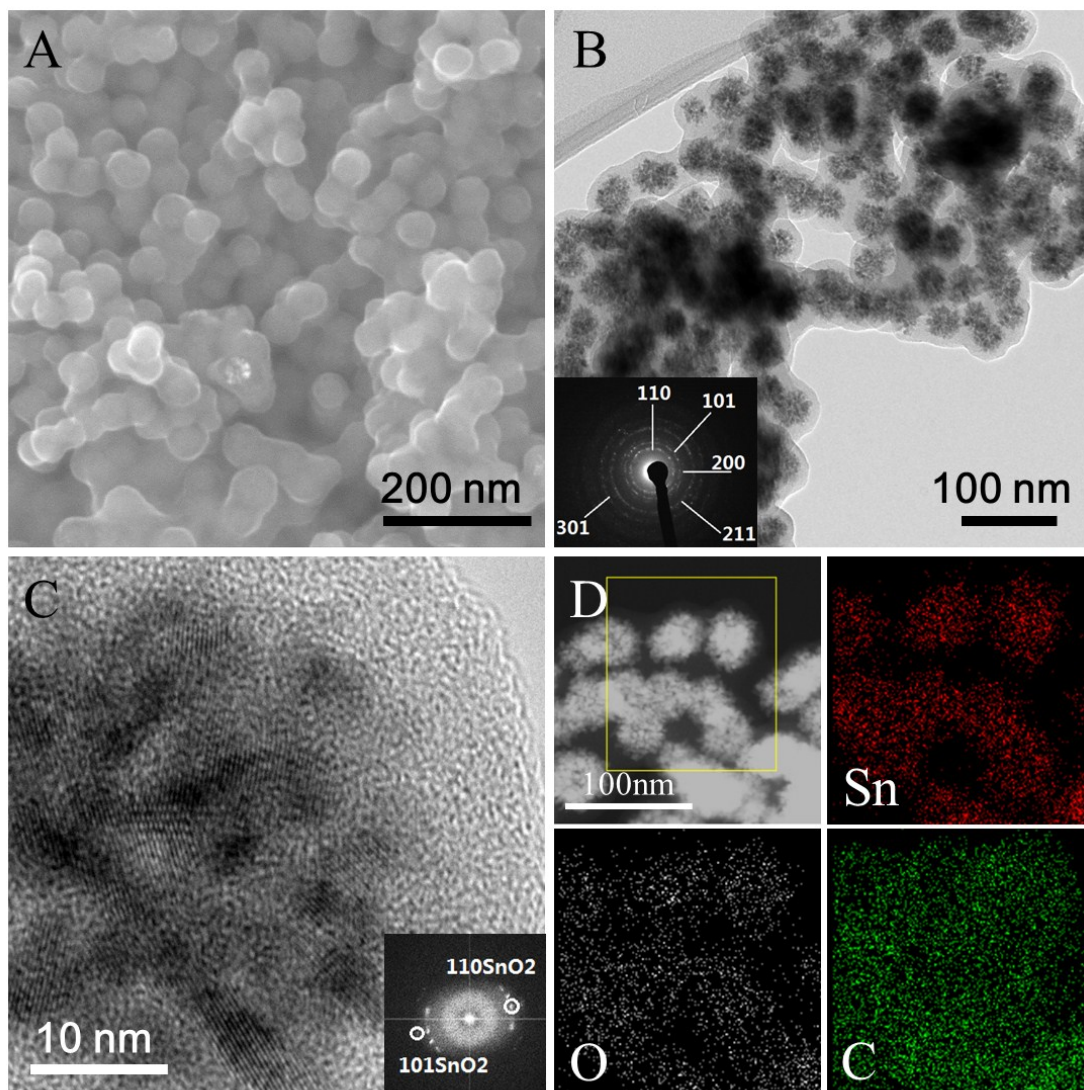


Figure 4-3: (A) SEM micrograph revealing the continuous macroscopic morphology of the nanocomposite. (B) Conventional bright field TEM micrograph and indexed SAD further highlighting the highly interconnected architecture with rutile SnO₂ phase embedded in the carbon. (C) HRTEM micrograph of one such cluster of SnO₂ nanocrystallites within the carbon. (D) HAADF TEM micrograph and EELS elemental maps of Sn, O and C.

Figure 4-3A is a SEM micrograph showing a low magnification image of C-SnO₂. On a macroscopic scale the material displays a highly interconnected morphology, reminiscent of a dense coral reef. **Figure 4-3B** shows a conventional bright field TEM micrograph and the corresponding indexed selected area diffraction pattern (SAD). The image further highlights the highly interconnected architecture of C-SnO₂, which contains dense assemblies sub-5 nm rutile SnO₂ nanocrystals encapsulated by carbon. **Figure 4-3C** shows a HRTEM micrograph of one such assembly containing numerous nanocrystallites. As illustrated by the HAADF TEM micrographs and EELS elemental maps shown in **Figure 4-3D**, the assemblies are 50 – 70 nm in scale, with more carbon between them.

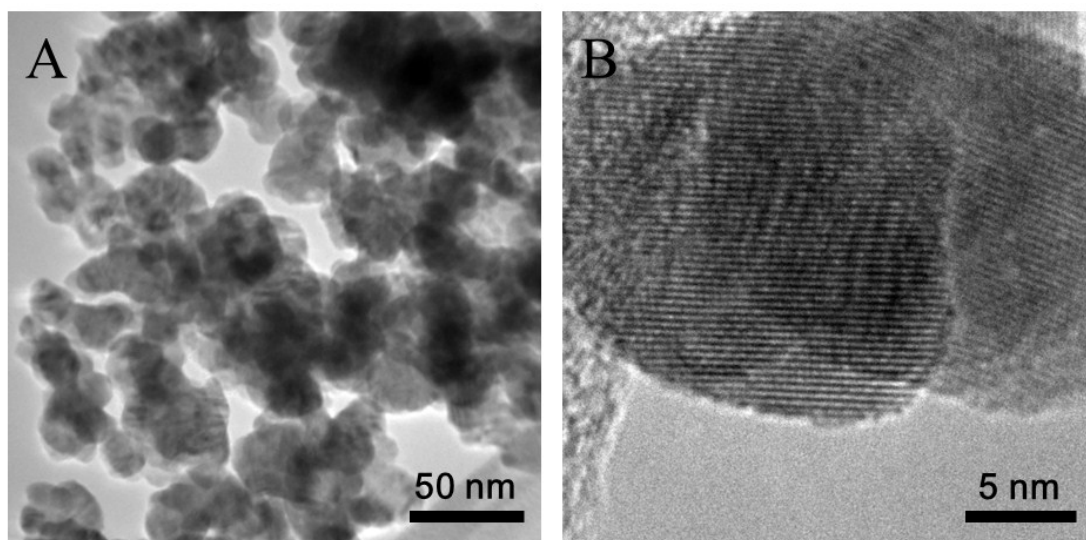


Figure 4-4: (A) Conventional TEM micrograph of the baseline SnO₂ specimen. (B) HRTEM micrograph of two overlapping SnO₂ particles.

As shown in **Figure 4-4**, baseline SnO₂ consists of nearly spherical particles in the size range of around 25 nm, without any additional features.

4.3.2 Electrochemical performance and phase transformations vs. Li

C-SnO₂ and SnO₂ were tested as half-cells against Li and Na in the range of 0.01 to 3 V and at 0.01 to 1.5 V vs. Li/Li⁺ or vs. Na/Na⁺. The mass loading of the electrodes was 1.5 mg cm⁻². As most published literature data on SnO₂ is based on

approximately the 0.01 to 3 V range, those results are used for the performance comparisons. For each literature comparison we will list the actual voltage window employed in that study. Since testing is being done of half-cells rather than of full batteries, lithiation (sodiation) is defined as "discharge", while delithiation (desodiation) is defined as "charge". For C-SnO₂ the specific capacity is always calculated based on the weight of both the SnO₂ and the carbon. A reversible capacity is defined as the capacity at delithiation/desodiation.

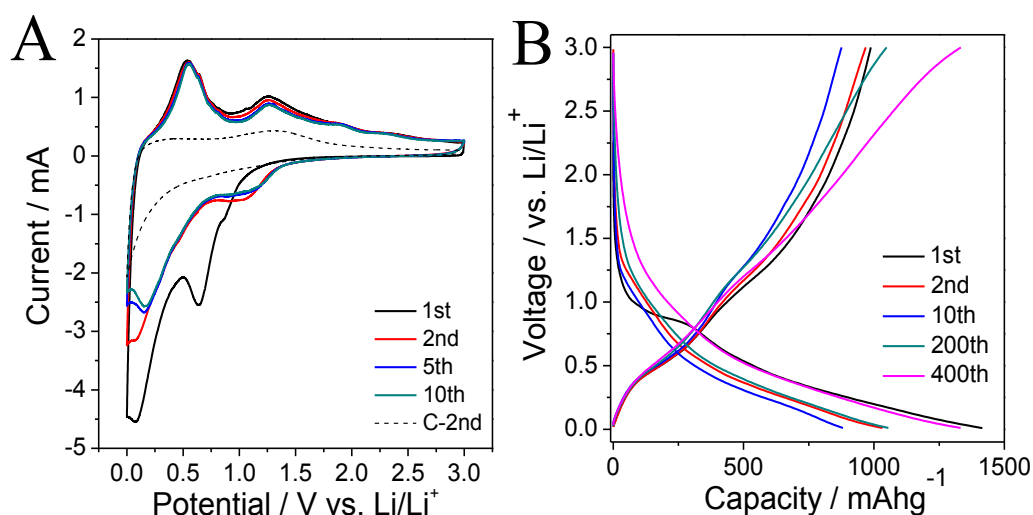


Figure 4-5: Electrochemical performance of C-SnO₂ *versus* Li, tested between 0.01 and 3V. (A) Cyclic voltammograms (CVs) at 0.1 mVs⁻¹ for the first 10 cycles, also showing the 2nd CV of the baseline pure carbon. (B) Galvanostatic discharge/charge profiles at 0.5 Ag⁻¹ for cycles 1 – 400.

The lithiation results are presented first. **Figure 4-5A** shows the cyclic voltammograms (CVs) of C-SnO₂ electrode for the initial 10 cycles, at a scan rate of 0.1 mVs⁻¹. Also shown is the 2nd CV of the pure carbon phase, employed as a baseline to help identify the Sn and SnO₂ - specific redox peaks. As supported by XRD analysis shown later, the lithiation peak at 1.1V and the delithiation peak at 1.25V correspond to the reversible conversion reaction of tin oxide when it is truly nanostructured: SnO₂ + 4Li⁺ + 4e⁻ ↔ Sn + 2Li₂O. The position and the relative intensity of the conversion reaction peaks is almost constant between cycle 2-10, indicating excellent reversibility. Good reversibility of the conversion reaction is only

observed among the ultra-fine SnO_2 materials. More coarse scale SnO_2 does not reverse fully at normal charging rates. The redox peak pair at 0.2V (lithiation) and 0.6V (delithiation) are caused by the reversible alloying process leading to a terminal intermetallic $\text{Li}_{22}\text{Sn}_5$ phase: $\text{Sn} + 4.4\text{Li}^+ + 4.4\text{e}^- \leftrightarrow \text{Li}_{22}\text{Sn}_5$. In the first discharging branch of the CV, an exaggerated broad peak at 0-1 V can be observed. This is due to the formation of the solid electrolyte interface (SEI) layer.

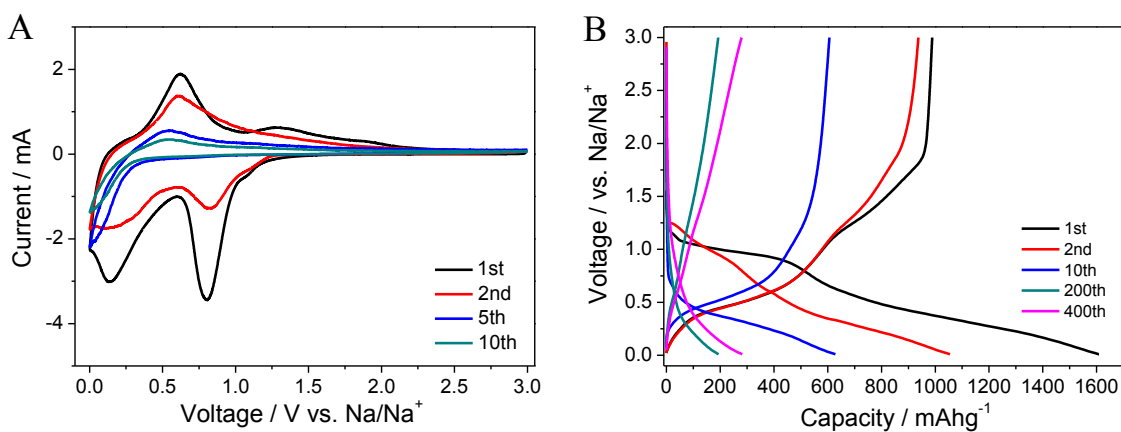


Figure 4-6: Electrochemical performance of SnO_2 vs. Li. (A) CVs of SnO_2 , tested at 0.1 mVs^{-1} . (B) Galvanostatic discharge/charge profiles of SnO_2 , tested at 0.5 Ag^{-1} .

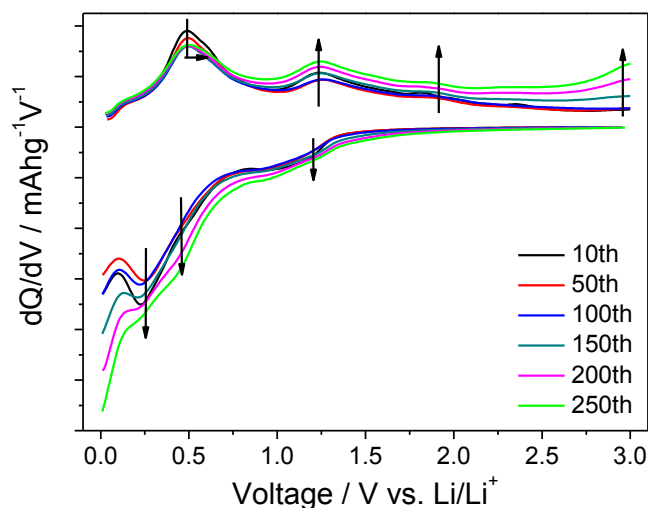


Figure 4-7: Derivate curves dQ/dV vs. V for C- SnO_2 electrode against Li.

Figure 4-6 shows the electrochemical performance of the baseline SnO_2 vs. Li, with **Figure 4-6A** being the CVs and **Figure 4-6B** being the galvanostatic profiles. Two key differences are observed with this coarser structure. First there is

substantially more capacity fade during cycling. Second, the conversion peaks are much less pronounced, supporting previous findings regarding the kinetic difficulty of the reaction for larger crystallite sizes.⁵²

Figure 4-5B shows the galvanostatic discharge/charge profiles at 0.5Ag^{-1} for cycles 1 – 400. **Figure 4-7** shows the derivative curves (dQ/dV vs. V) of those results. The intensity of the anodic 0.6 V peak decreased slightly during the initial 50 cycles and remains constant thereafter, supporting the high reversibility of alloy/dealloy reaction upon extended cycling. According to **Figure 4-5B**, a reversible capacity of 1023mAhg^{-1} is obtained in the second cycle.

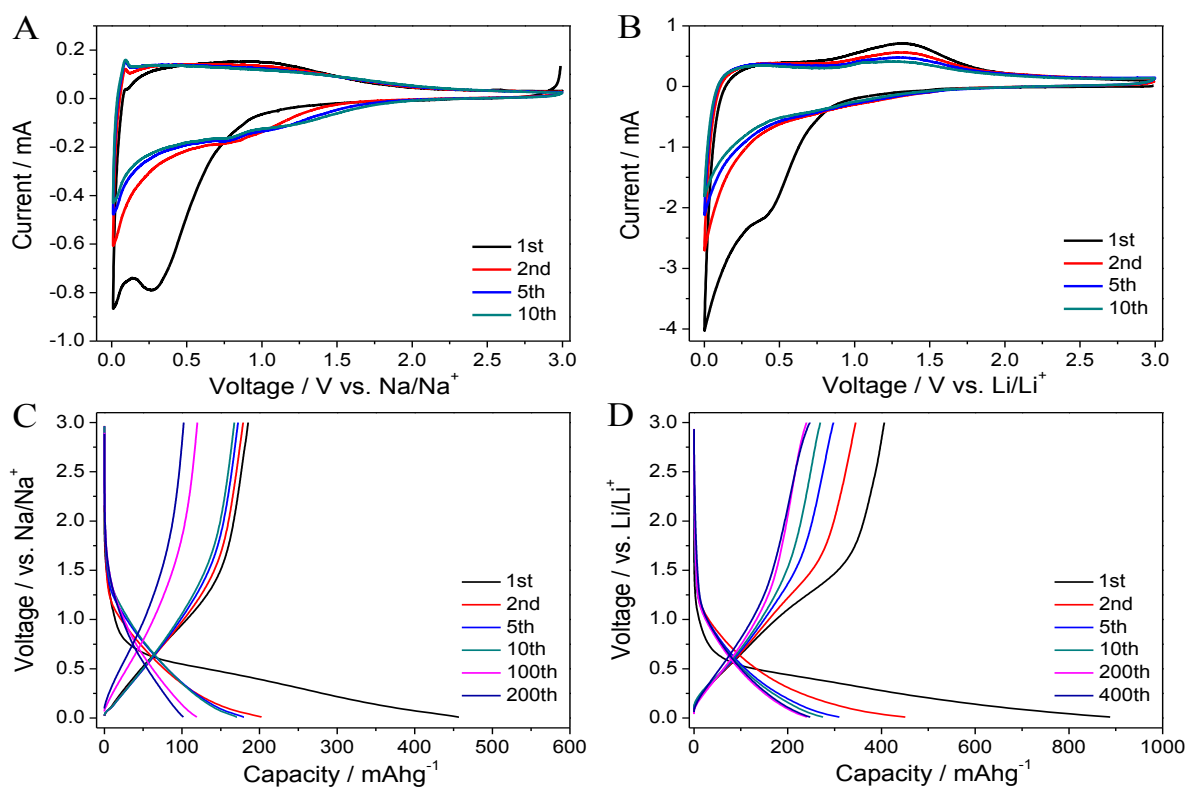


Figure 4-8: Electrochemical performance of pure carbon in a half-cell vs. Na, Li. (A) CVs of pure carbon electrode for the cycle 1 – 10 vs. Na, tested at 0.1mVs^{-1} . (C) Galvanostatic discharge/charge profiles of pure carbon electrode, tested at 0.08Ag^{-1} . (B) CVs of pure carbon electrode for the cycle 1 – 10 vs. Li, tested at 0.1mVs^{-1} . (D) Galvanostatic discharge/charge profiles of pure carbon electrode, tested at 0.5Ag^{-1} vs. Li.

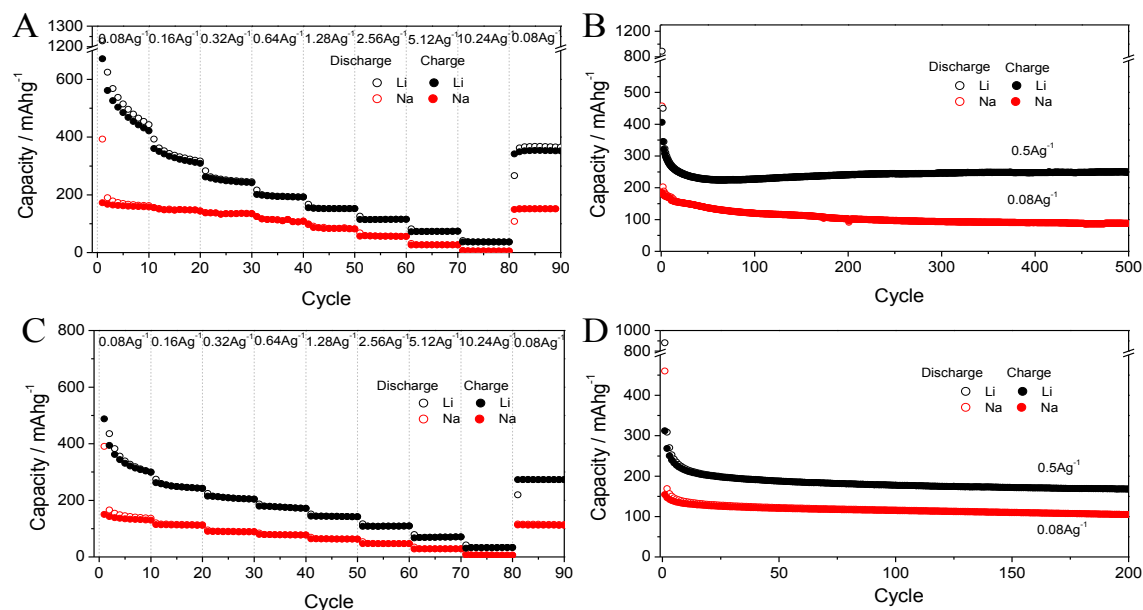


Figure 4-9: (A) Rate performance of the baseline pure amorphous carbon electrodes vs. Na and vs. Li, tested 0.01-3V. (B) Cycling performance of pure carbon electrodes, tested 0.01-3V. (C) Rate performance of the baseline pure amorphous carbon electrodes vs. Na and vs. Li, tested 0.01-1.5V. (D) Cycling performance of pure carbon electrodes, tested 0.01-1.5V.

The galvanostatic data for the identically synthesized pure hydrothermal carbon, tested against Li and against Na, is presented in **Figure 4-8** and **Figure 4-9**. At 0.5 A/g the capacity of the carbon is $\sim 450 \text{ mAhg}^{-1}$. Thus a reversible capacity of 1023 mAhg^{-1} is close (95%) to the expected value by rule of mixtures of the two Li active materials ($1494 \text{ mAhg}^{-1} \times 0.6 + 450 \text{ mAhg}^{-1} \times 0.4$). This ratio proves the full utilization of SnO_2 for both the reversible alloying and conversion reactions.⁵¹

Beyond cycle 90 the capacity progressively increases, hitting 1367 mAhg^{-1} at cycle 400. A likely explanation for the extra capacity is the formation of a reversible polymer gel on the nanostructured conversion electrode's surface during lithiation, with its consequent dissolution upon delithiation to potentials roughly above 1.5 V. Such a faradic process has been compared to the redox reactions in polymer-based electrochemical capacitors, being highly reversible and imparting a negligible coulombic efficiency penalty.^{84,85,86} Similar high CE cycling-induced capacity gains

have been reported for a range of conversion oxide electrodes when tested against Li, including SnO_2 ^{51,91} MnO ⁸⁷ and MoO_2 ⁸⁸. Since our electrochemical instrument will measure CE with $\geq 1\%$ accuracy, we will refer to computer generated CE values of 100% as being $>99\%$. From cycle 8 onward the CE of C- SnO_2 is $>99\%$.

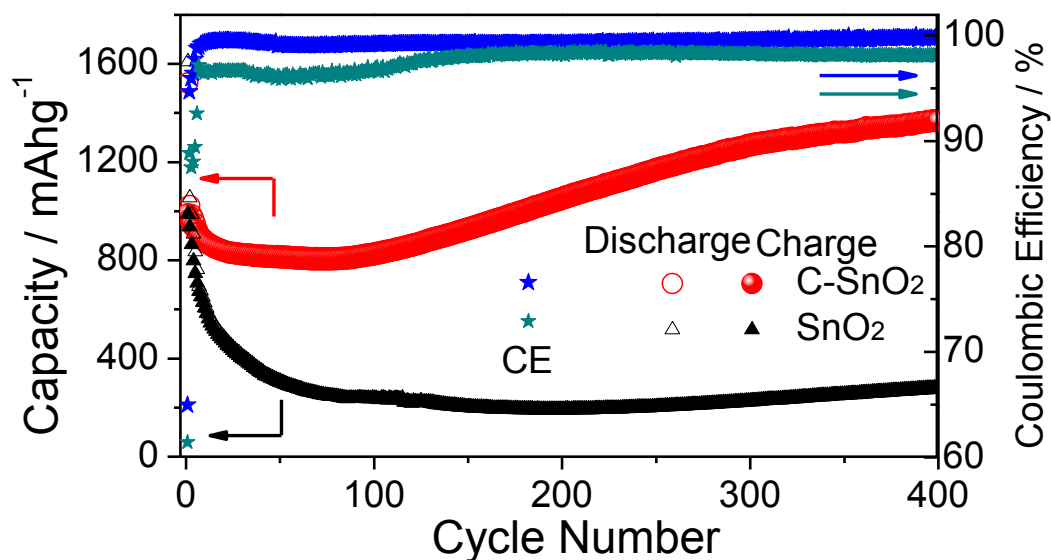


Figure 4-10: Cycling performance of C- SnO_2 and SnO_2 (0.5 Ag^{-1}), with corresponding coulombic efficiency (CE) displayed on the right axis.

Figure 4-10 shows the cycling results of C- SnO_2 electrodes, with SnO_2 being presented as a baseline. For C- SnO_2 a reversible capacity of 1367 mAhg^{-1} was obtained after 400 cycles at current density of 0.5 Ag^{-1} . At first cycle the coulombic efficiency is 65%, agreeing with previously reported values for SnO_2 tested against Li^{52,73}. By the second cycle CE is over 95%, and stabilizes to $>99\%$ from the 8th cycle onward. Conversely the baseline SnO_2 electrode exhibits only 29% capacity retention after 400 cycles, with CE being never going above 99% through cycling.

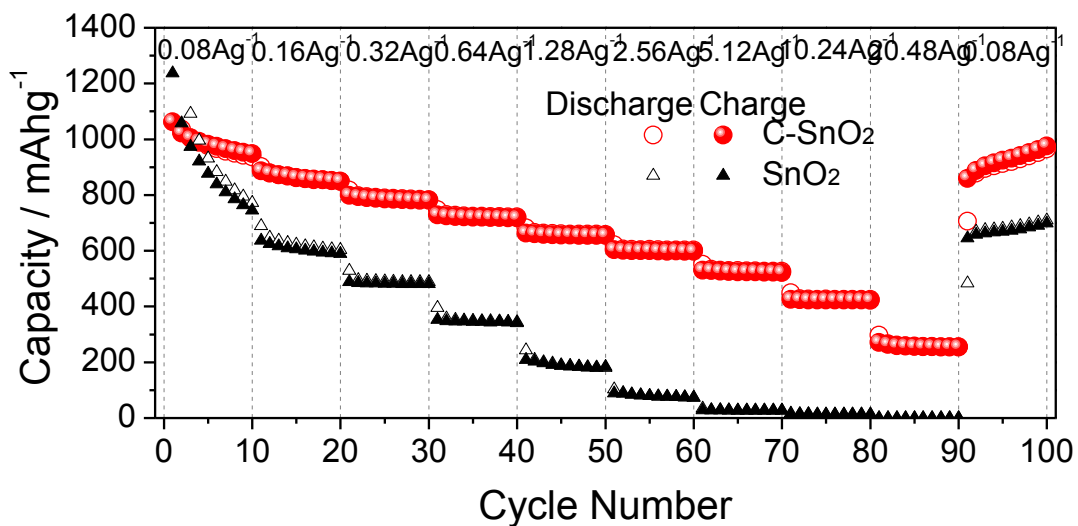


Figure 4-11: Rate performance of C-SnO₂ and SnO₂.

The rate performance of C-SnO₂ and SnO₂ is shown in **Figure 4-11**. At current densities of 1.28, 2.56, 5.12, 10.24, 20.48 Ag⁻¹, the C-SnO₂ electrode maintained a capacity of 663, 608, 527, 422 and 255 mAhg⁻¹, respectively.

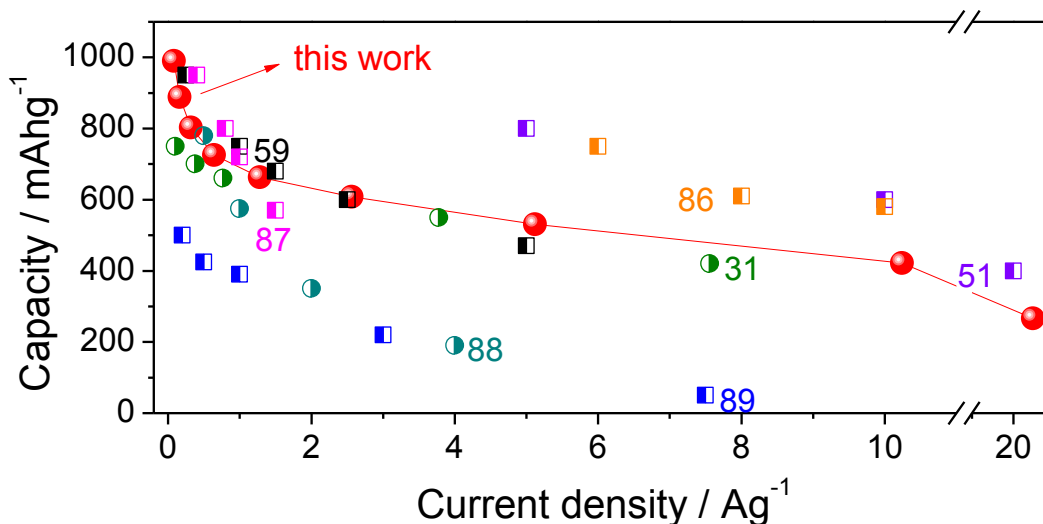


Figure 4-12: Rate capability comparison of C-SnO₂ with state-of-the-art SnO₂ (■), Sn (●) based LIBs anodes from literature. All plotted literature capacities were obtained from tests also performed with a 0.01-3V voltage window.

Figure 4-12 shows a rate capability comparison of C-SnO₂ with state-of-the-art previously published electrodes based on both SnO₂ (■) and on Sn (●). Overall our

system is quite promising, being on par with some of the best architectures that have been created. Specifically C-SnO₂ is competitive with potentially more expensive systems based on graphene oxide^{89,90}, N-doped graphene⁵¹ supports. C-SnO₂ also shows favorable performance in comparison with amorphous carbon - Sn(SnO₂) composites.^{31,59,91,92} It is important to point out that for this broad comparison we plotted literature results obtained from a comparable 0.01 V to 3V testing range. We did not include any results for a lower terminal anodic voltage (such as 1.5V) where less reversible capacity is expected.

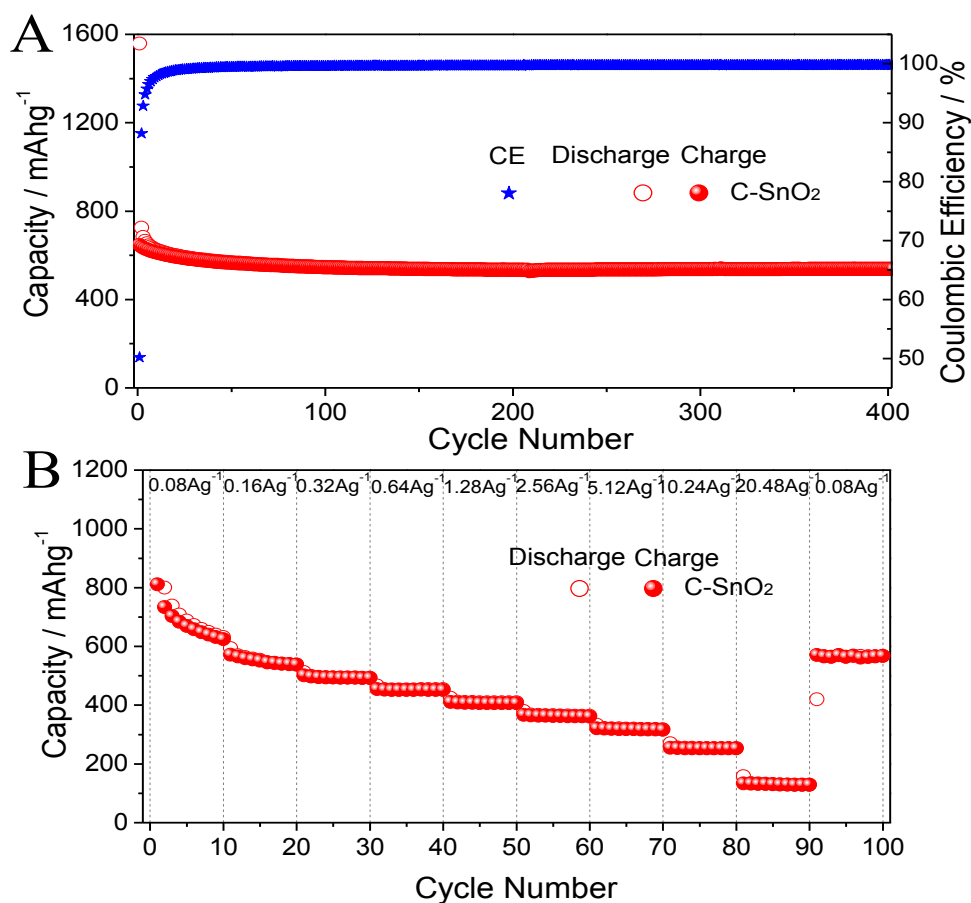


Figure 4-13: Electrochemical performance of C-SnO₂ versus Li, tested between 0.01 and 1.5 V. (A) Cycling performance of C-SnO₂ (0.5 Ag⁻¹), with corresponding coulombic efficiency (CE) displayed on the right axis. (B) Rate performance of C-SnO₂.

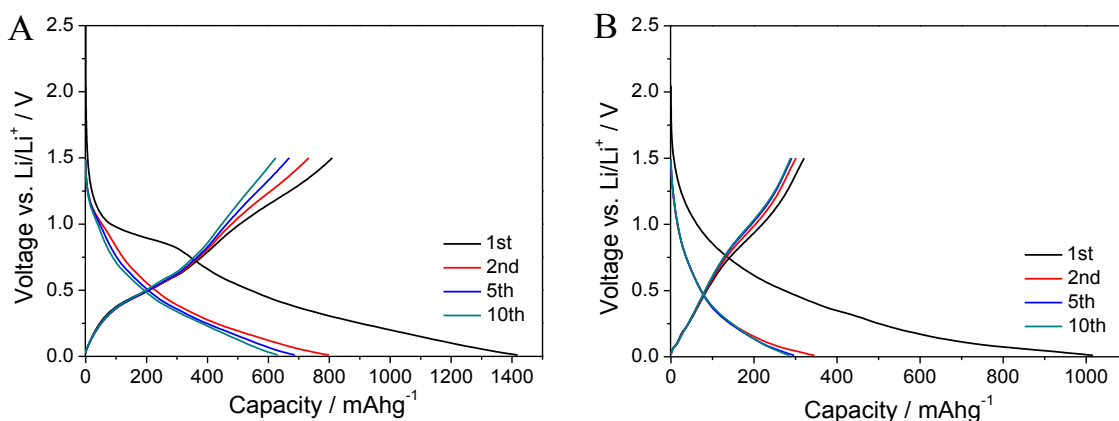


Figure 4-14: The raw galvanostatic discharge/charge profiles

We investigated the electrochemical performance of C-SnO₂ against Li at a window of 0.01-1.5V, which may be more (depending on the cathode material) representative of a voltage excursion of an anode in a full battery cell. As will be demonstrated by the XRD and XPS analysis, with a cut-off voltage of 1.5V, Li storage is based on a fully reversible alloying/dealloying reaction and a partially reversible conversion reaction. According to **Figure 4-13A**, the initial reversible capacity of the electrode is 633 mAhg⁻¹ (at 0.5Ag⁻¹), retaining 85% of this value after 400 cycles. The 1st cycle coulombic efficiency is 42%, lower than the 65% when charged up to 3V. However, the coulombic efficiency during cycling is good, stabilizing in the > 99% range by cycle 23. At all currents the specific capacity is lower than when the electrodes were charged to 3V, agreeing with findings by ref.⁵². This is due to the incompleteness of the oxide conversion reaction at 1.5V.

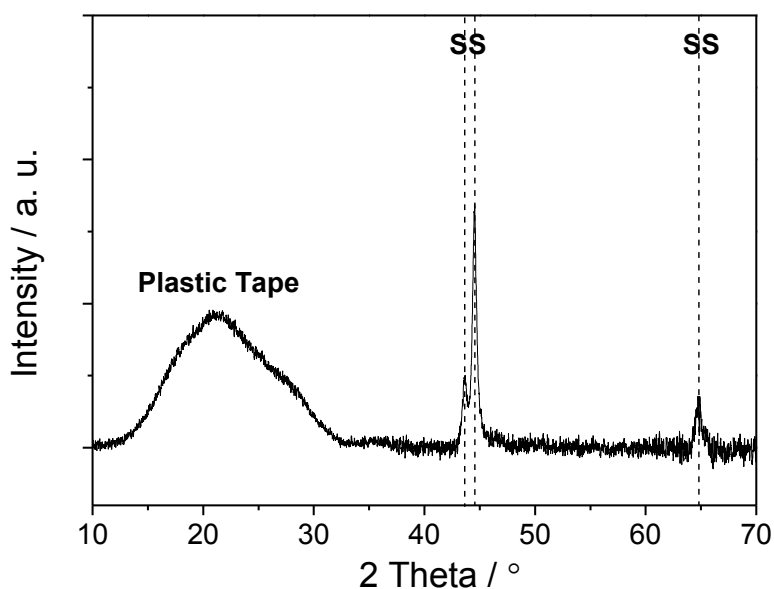


Figure 4-15: XRD pattern for the plastic tape on the stainless steel current collector.

We performed XRD characterization to track the phase transformations in C-SnO₂ vs. Li at various cut - off voltages. The electrodes were discharged/charged galvanostatically at $\sim 1/20C$ (0.05 Ag^{-1}) to the cut-off voltage, and held there until the float current decreased to below 5% of the galvanostatic current. A special sample preparation procedure was employed in order to minimize exposure of the materials to air, oxygen or water vapor. After disassembly in the glove box, the electrodes were firstly washed by DEC to remove remaining salts and EC/DMC, dried in vacuum for 10 minutes and then sealed in plastic tape. **Figure 4-15** shows the XRD pattern for the plastic tape on the stainless steel current collector, without the electrode material, displaying a plastic tape hump at $\sim 22^\circ$ and the characteristic sharp Bragg peaks for the fcc steel.

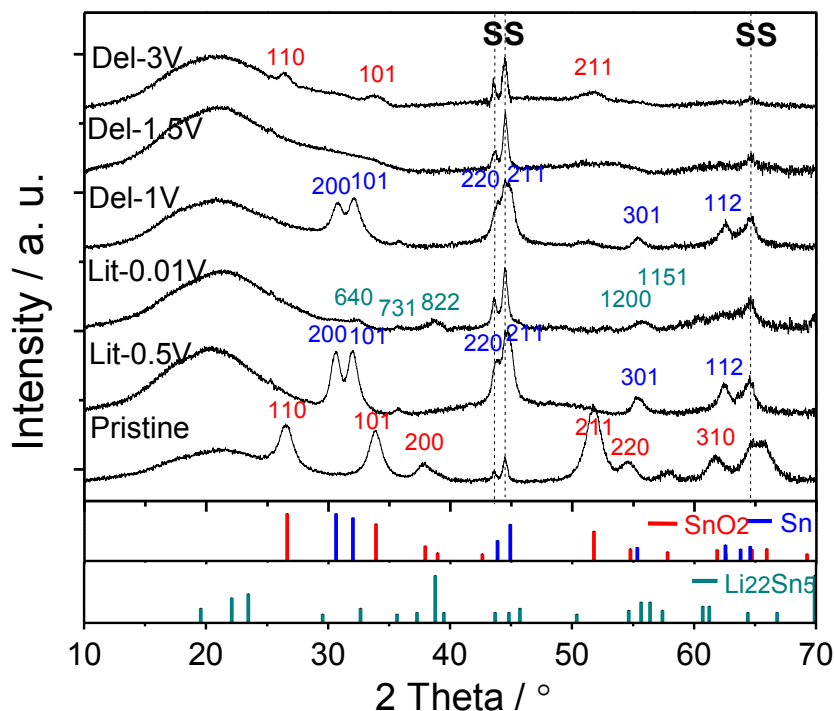


Figure 4-16: XRD patterns of C-SnO₂ at various cut-off voltages: first lithiation to 0.5V, first lithiation to 0.01 V, first delithiation to 1V, first delithiation to 1.5V, first delithiation to 3V.

The resultant patterns are shown in **Figure 4-16**. When the pristine electrode is first lithiated to 0.5 V Li/Li⁺, the reduction reaction of SnO₂ ($\text{SnO}_2 + 4\text{Li}^+ + 4\text{e}^- \rightarrow \text{Sn} + \text{Li}_2\text{O}$) is effectively complete since no SnO₂ signal is detected in the "Lit-0.5V" spectrum. When the electrode is further lithiated down to 0.01 V, Bragg peaks of β -Sn are no longer detectable. Instead, broad peaks ascribed to the Li₂₂Sn₅ intermetallic phase are present, with the (640), (731), (822), (12 00) and (11 51) reflections being discernable. The β -Sn peaks re-appear after the electrode is charged back to 1V, indicating full reversibility of the alloying reaction. When charged to 1.5V the β -Sn peaks disappear, while a weak (110) SnO₂ signal becomes visible, being superimposed on a broad XRD hump associated with the plastic tape. Overall, however, the majority of the material is amorphous at 1.5V. When charged to 3V, the characteristic SnO₂ (110), (101) and (211) peaks are detectable but not well pronounced. This is likely caused by a combination of peak broadening due to the SnO₂ nanocrystalline size and/or a substantial portion of it remaining amorphous.

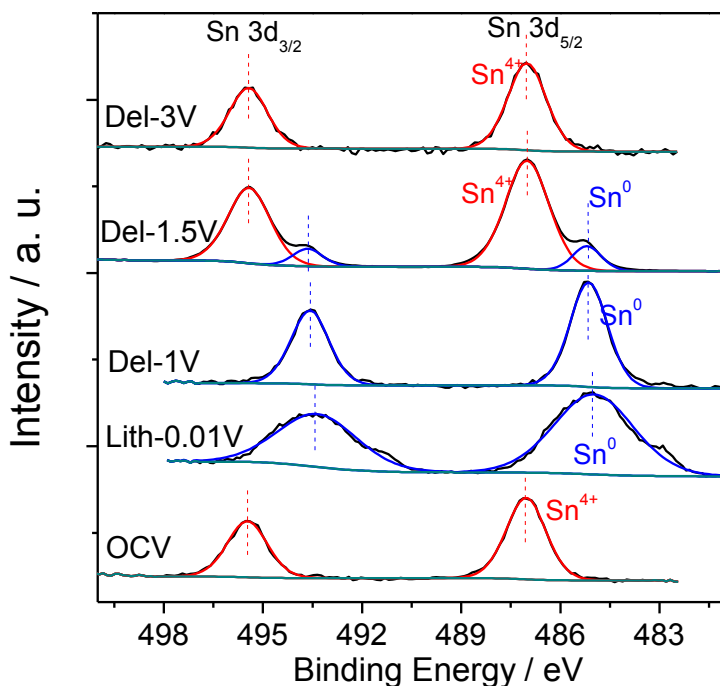


Figure 4-17: XPS spectra for Sn 3d levels of C-SnO₂ at open circuit voltage (prior to testing, used as a baseline), first lithiation to 0.01V, first delithiation to 1V, first delithiation to 1.5V, first delithiation to 3V.

We performed XPS analysis to track the chemical state of Sn in the C-SnO₂ specimens as a function of voltage. Samples that were lithiated down to 0.01 V were first etched by Ar plasma as to blast off most of the surface SEI which otherwise obscured the analysis. The results for those experiments are presented in **Figure 4-17**, which shows the oxidation state of Sn as a function of voltage. Also shown in the figure are the baseline results for the as-synthesized specimen left at open circuit voltage (OCV). The associated O 1s and C 1s XPS data are shown **Figure 4-18**. At 0.01 V, the Sn 3d peaks were present at 493.4 and 485.04 eV, indicating Sn⁰ state associated with the Li₂₂Sn₅ intermetallic (and/or Li-Sn alloys). Analogously at 1V the Sn 3d peaks also showed primarily the Sn⁰ state. After delithiated to 1.5V, the Sn 3d peaks could be deconvoluted into a majority Sn⁴⁺ and minority Sn⁰, indicating that the conversion reaction has proceeded but not entirely to completion. Since no Sn signal with intermediate chemical state was detected, it could be concluded that LiO₂ is reduced directly to SnO₂ and Li. At 3V, the Sn⁰ peaks are no longer detectable,

indicating full reversibility of the LiO_2 to SnO_2 conversion reaction between 0.01 and 3 V.

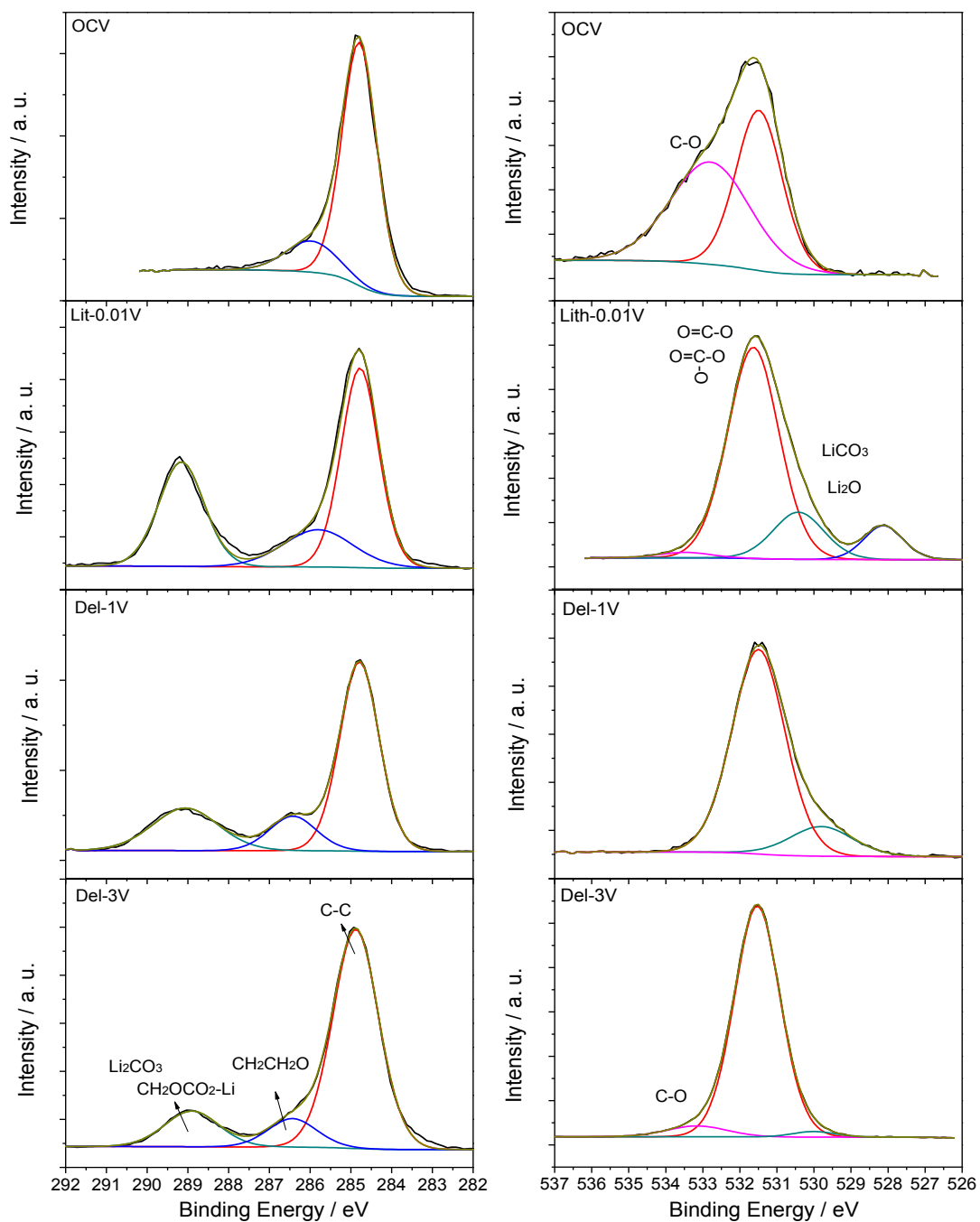


Figure 4-18: XPS spectra for C 1s (left) and O 1s (right) of C-SnO₂ electrodes at the same cut-off voltages.

4.3.3 Electrochemical performance and phase transformations vs. Na

Figure 4-19A shows the CVs of C-SnO₂ during the first 10 cycles, as well as the 2nd cycle CV of the pure carbon baseline. It may be seen that compared to the CV data for Li, the redox peaks for the Na conversion and alloying reactions are much broader and washed out. The peaks' overall intensity is also lower for Na than for Li, which will be shown to agree well with a substantially lower capacity. In the cathodic portion of the scan, a broad peak initiates near 1.7V vs. Na/Na⁺, with its intensity increasing all the way down to full discharge. As will be demonstrated through XRD analysis, this peak corresponds primarily to the oxide conversion reaction, with the Sn-Na alloying reaction not running to completion. As may be seen from **Figure 4-8**, Na insertion into the carbon phase contributes to the broad "background" of the CV curve, but does not add any sharp redox peaks. In the first cycle, the formation of SEI also contributes to the total CV current, producing the small hump at around 0.4V.^{27,55}

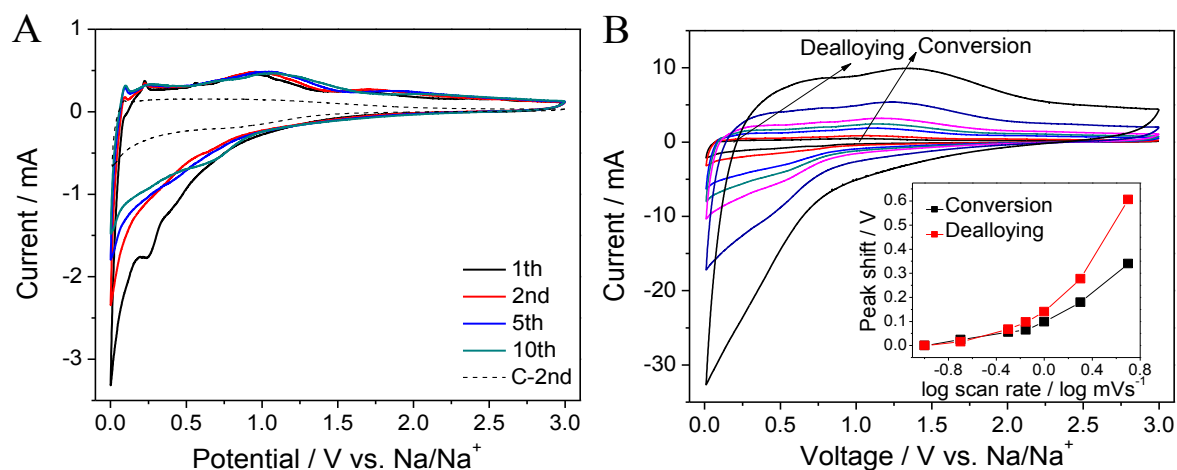


Figure 4-19: Electrochemical performance of C-SnO₂ and SnO₂ vs. Na, tested between 0.01 and 3V. (A) CVs of C-SnO₂ for the cycle 1 - 10, tested at 0.1 mVs⁻¹. (B) CVs of electrode at various scan rates from 0.1 to 5 mVs⁻¹. The shift of the conversion/dealloying peaks as function of scan rate (inset).

In the anodic portion of the CV, the first small peak appears at ~ 0.1 V and is ascribed to the Na extraction from the carbon phase.¹⁶ The small sharp peaks at ~ 0.23

and ~ 0.56 V have been ascribed to the progressive dealloying reactions from $\text{Na}_{15}\text{Sn}_4$ (crystalline) to Na_9Sn_4 (amorphous) and then to NaSn (amorphous) and to NaSn_5 (amorphous).^{27,74} Judging from the alloying peaks' small relative intensity, it is unlikely that all of the Sn in the electrode transforms accordingly. XRD analysis will demonstrate that at 0.01V a notable fraction of the material remains as β -Sn, while complementary HRTEM will highlight a co-presence of small and isolated $\text{Na}_{15}\text{Sn}_4$ intermetallics. In the anodic portion of the CV, the expected position of the final dealloying peak (i.e. formation of β -Sn) overlaps with two other broad anodic peaks. These will be shown to be associated with the Na_2O to SnO_2 conversion reaction that proceeds through an intermediate SnO phase.

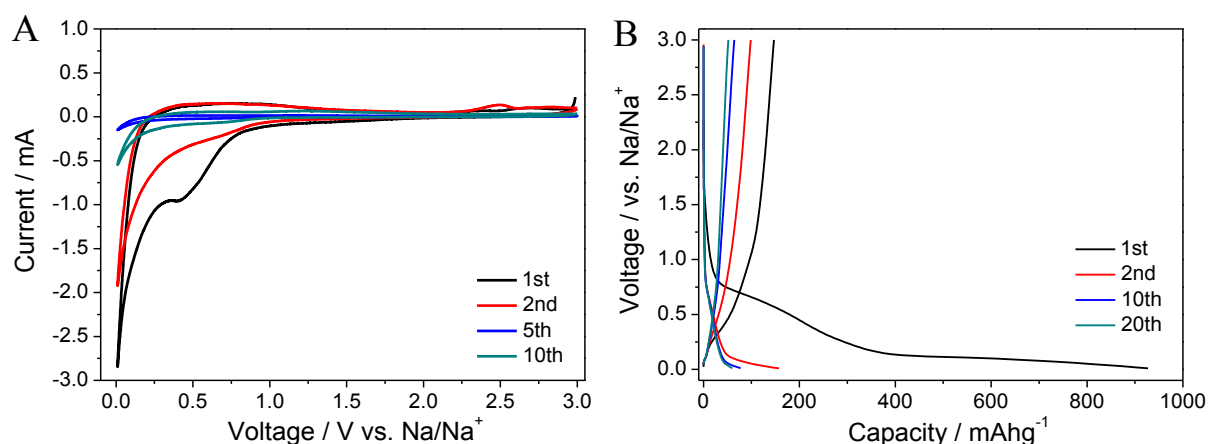


Figure 4-20: Electrochemical performance of SnO_2 versus Na. (A) Cyclic voltammograms (CVs) of SnO_2 electrode. (B) Galvanostatic discharge/charge profiles of SnO_2 electrode at current density of 0.08Ag^{-1} .

The CV curve of the baseline SnO_2 (**Figure 4-20**) shows very poorly defined redox peaks. As the XRD results will demonstrate, in the coarser baseline SnO_2 both conversion and alloying are kinetically difficult. In that system the total current quickly degrades with cycle number.

We further analyzed the sodiation kinetics of C- SnO_2 by performing CV tests at various scan rates, $0.1 - 5 \text{ mVs}^{-1}$. Those results are shown in **Figure 4-19B**. It can be observed from the anodic portion of the graph that both the dealloying and the conversion reaction peaks shift to higher voltages with increasing scan rate, but that the alloying peak shows a larger shift than the conversion peak. The magnitude of the

shift (*i.e.* the overpotential) for a given reaction is indicative of its kinetic feasibility, and demonstrates that Na-Sn alloying is more difficult than the conversion.

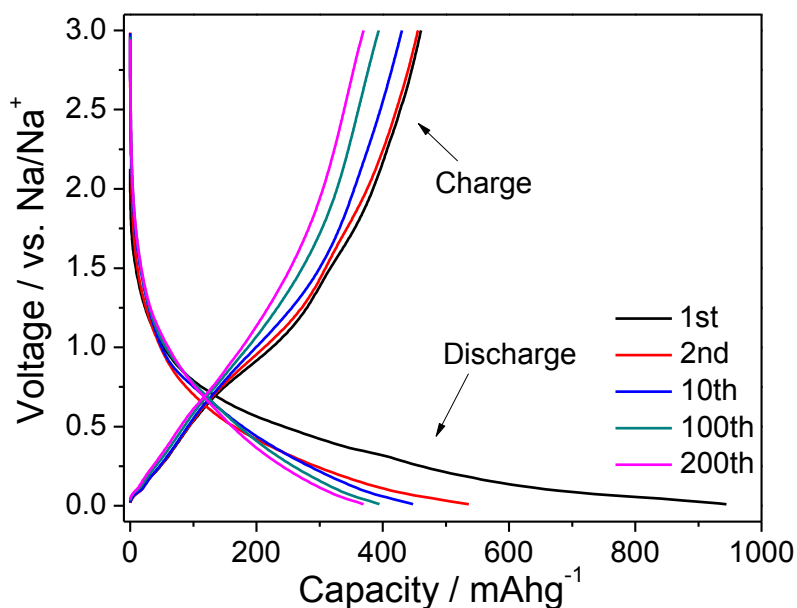


Figure 4-21: Galvanostatic discharge/charge profiles of C-SnO₂, tested at 80 mA g⁻¹.

Figure 4-21 shows the galvanostatic charge/discharge profiles of C-SnO₂ electrode at current density of 0.08 Ahg⁻¹. A capacity of 946 mAhg⁻¹ was obtained in the first sodiation. A reversible capacity of 459 mAhg⁻¹ is obtained at cycle 1, resulting in a CE of 48.5%. As may be observed from **Figure 4-9**, the sodiation capacity of baseline amorphous carbon is lower than for lithiation. For Na at cycle 1 the reversible capacity of the baseline carbon is 195 mAhg⁻¹, while at cycle 500 it is 95 mAhg⁻¹. Conversely with Li these values are 450 mAhg⁻¹ and 250 mAhg⁻¹. These results show that the exact same SnO₂ based material and the exact same carbon tested against Na will display less than half the reversible capacity as when tested against Li.

Figure 4-22A shows the cycling capacity retention performance of C-SnO₂ and of the baseline SnO₂. The electrodes were tested in the voltage at current density of 0.08 Ag⁻¹. The C-SnO₂ electrode displayed excellent cyclability; a specific capacity of 372 mAhg⁻¹ was obtained after 200 full charge/discharge cycles, which is 81% of the initial charge value. By contrast, the reversible capacity of baseline SnO₂ rapidly

decays, going from 147 to 49 mAhg⁻¹ after 50 cycles. **Figure 4-22A** also shows the cycling CE for both materials. In C-SnO₂ the CE grows to over 90% by the 3rd cycle, and stabilized to 98% to >99% from cycle 20 onward. The cycling CE of SnO₂ is much lower, never going above 90%.

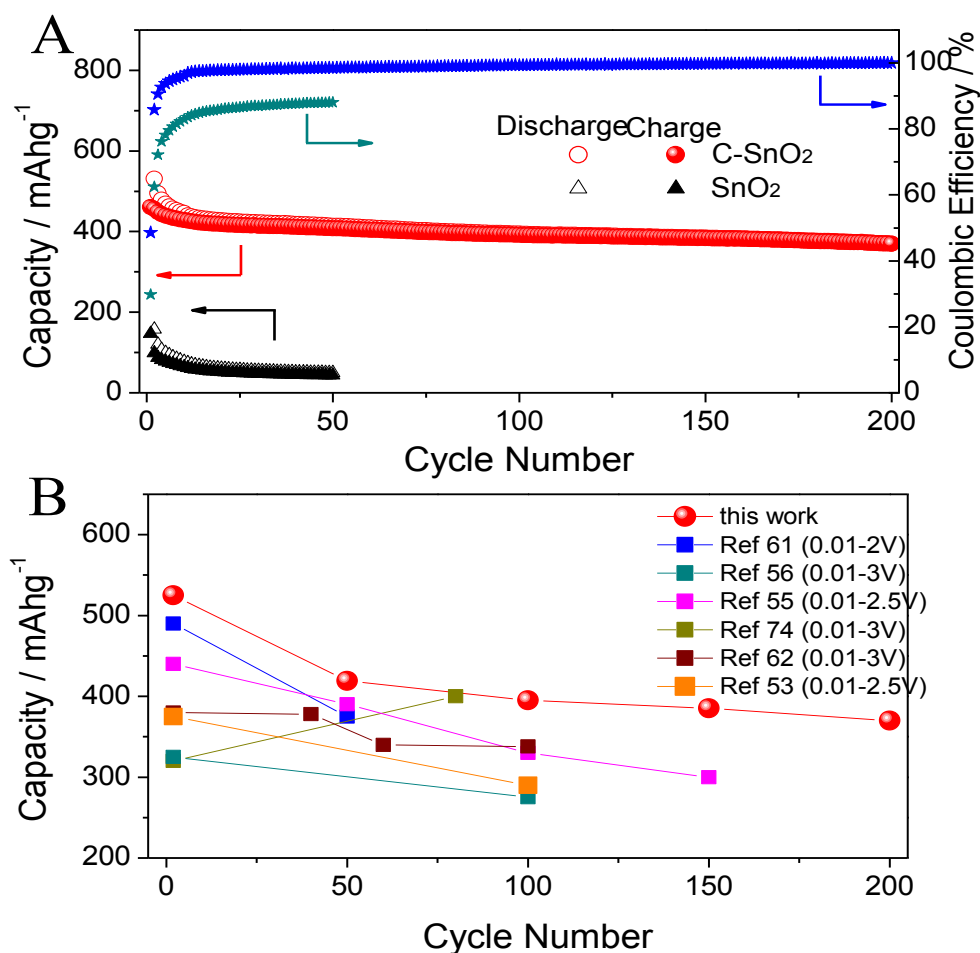


Figure 4-22: (A) Cycling performance of C-SnO₂ and SnO₂ (0.08 Ag⁻¹), with corresponding CE displayed on the right axis. (B) Cycling capacity retention comparison of C-SnO₂ with state-of-the-art SnO₂ based NIBs anodes from literature.

Figure 4-22B shows a comparison of the cycling performance of C-SnO₂ to the state-of-the-art nanomaterials based on SnO₂.^{53,54,55,56,61,62,74} In the figure, the data legend lists the exact testing voltage window along with the associated citation. The anodic upper limit varied from study to study, being in the 2 – 3 V range. Examining previously published results one concludes that there does not appear to be a correlation in the capacity versus cycle number values with the upper anodic limit, as

long as it is at or above 2V. Rather, performance seems to be dictated by the microstructure of the electrode. We did not include any metallic Sn results from literature, as this would not be an appropriate comparison. Since sodiation/lithiation of metallic Sn do not involve conversion reactions (apart from the native surface oxide), one would be essentially comparing “apples to oranges” in terms of both phase transformations and the performance measures.

As may be observed, C-SnO₂ is among the most favorable both in terms of the total reversible capacity and the cycling capacity retention. It is important to note that the cyclability performance in this work was achieved using normal PVDF binder and practical organic electrolyte (*i.e.* 1 mol NaClO₄ in EC/DEC mixture). We did not employ any SEI stabilizing additive (*e.g.* fluoroethylene carbonate, FEC), which would be expected to further boost the cycling performance.^{32,55,93,94}

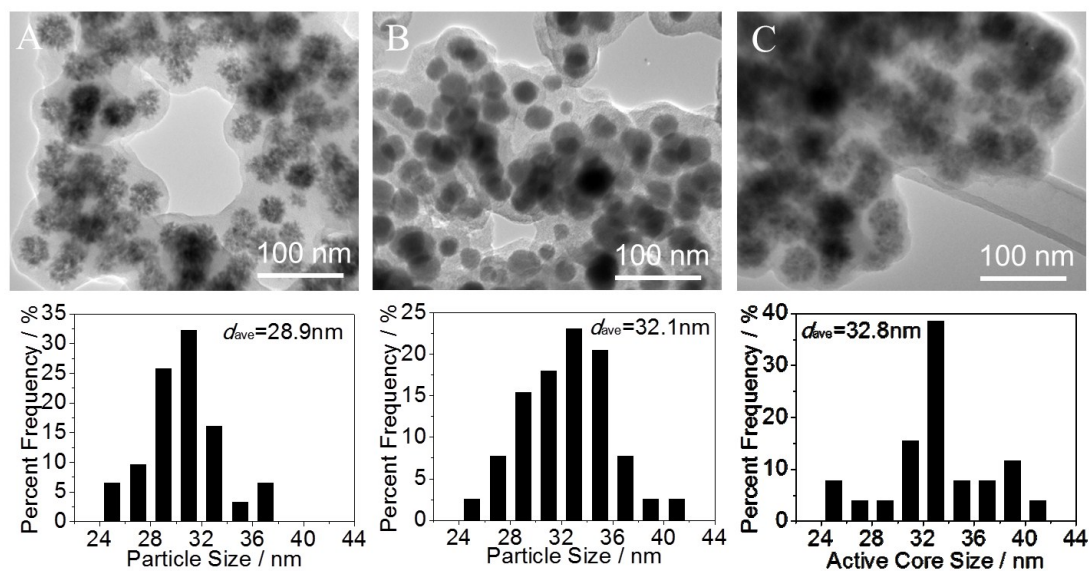


Figure 4-23: (A-C) TEM micrographs of C-SnO₂ with corresponding histograms for the size of the active SnO₂ nanocrystal assemblies (not individual crystallites). (A) Open circuit potential. (B) Sodiated to 0.01V. (C) Desodiated to 3V.

A straightforward explanation for the superior cycling performance of C-SnO₂ lies in its monocoque microstructure that is distinct from the usual nanocomposites consisting of particulate assemblies. During cycling the carbon frame carries the sodiation/lithiation stresses while preventing cycling-induced agglomeration of the individual crystals. **Figure 4-23** show TEM micrographs of C-SnO₂ showing the

microstructure at open circuit potential (prior to cycling), sodiated once to 0.01V and desodiated once to 3V. The figure also shows corresponding histograms for the size of the active SnO₂ nanocrystal assemblies (not individual crystallites) at each condition. The histograms were obtained using Gwddion software from ~80 assemblies on 5 separate micrographs. According to the measured size distribution the initial SnO₂ crystallite assembly mean diameter is 29 nm. The cluster diameter is 32 nm at full sodiation, and is the same after full desodiation. This demonstrates that while the expansion of the active SnO₂ phases is upwards of several hundred percent (exact value will depend on the degree of completion of the alloying and conversion reactions), the surrounding carbon matrix acts as a buffer to minimize the macroscopic strain on the electrode and prevents its decrepitation. As may be seen from the HRTEM image in **Figure 4-3C** the carbon engulfs the individual SnO₂ nanocrystallites, which is expected to minimize their agglomeration during cycling.

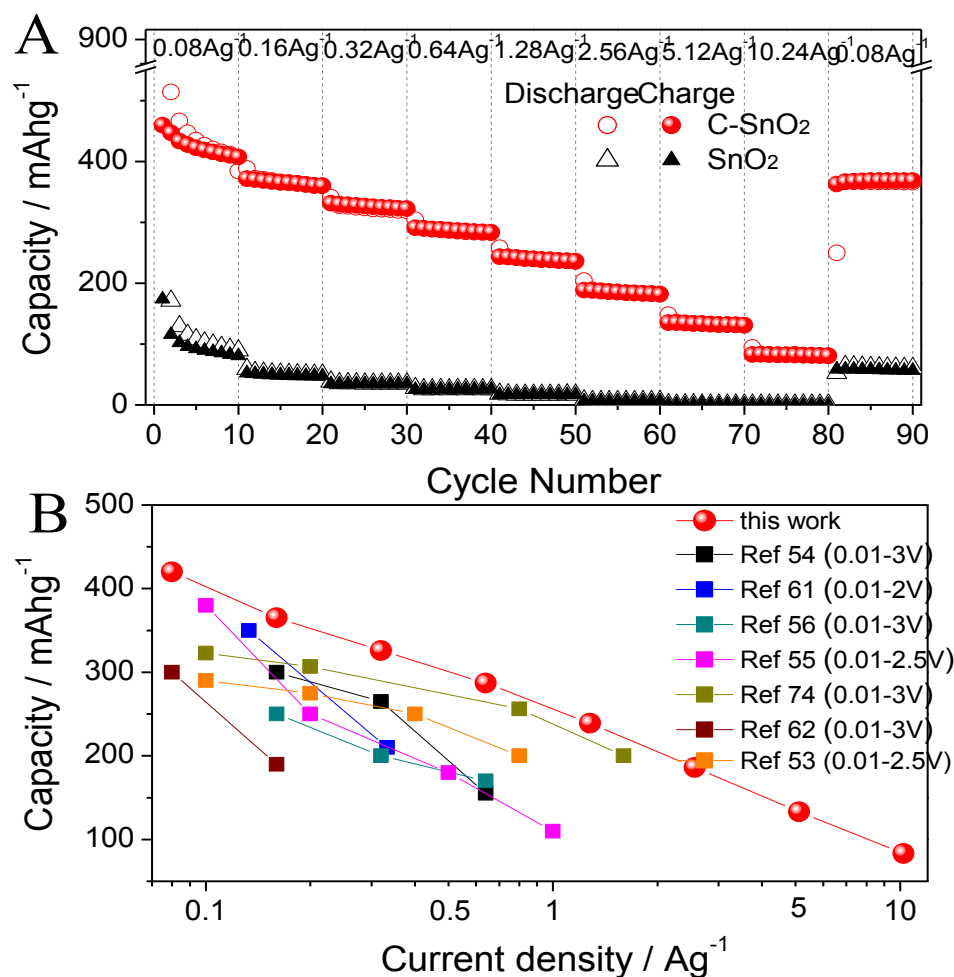
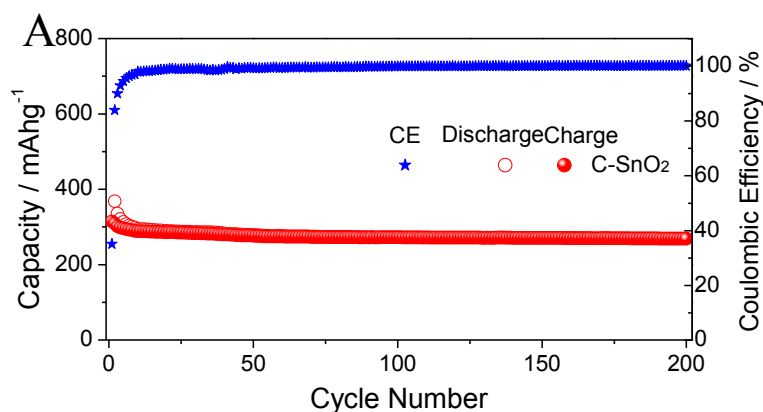


Figure 4-24: (A) Rate performance of C-SnO₂ and SnO₂ electrodes. (B) Rate capability comparison of C-SnO₂ with state-of-the-art SnO₂ based NIBs anodes from literature.

Figure 4-24A shows the capacity of C-SnO₂ and of SnO₂ at various current densities. Overall the C-SnO₂ electrode exhibits outstanding rate performance, far superior to SnO₂ that has effectively negligible capacity at higher rates. The C-SnO₂ possesses the dual advantage of the carbon frame and the sub 5 nm - scale of the individual SnO₂ crystallites. The Na active carbon frame imparts excellent electrical conductivity to the electrode and allows for rapid diffusion of Na and Li ions. The fine scale of the crystallites shortens the diffusion distance, reducing the time needed for both the alloying and the conversion reactions. Since the diffusion time is proportional to the diffusion length squared, the sub 5 nm crystallites in C-SnO₂ will have a tremendous kinetic advantage over the 50 nm crystallites in baseline SnO₂. For C-SnO₂, capacities of 187, 136 and 80 mAhg⁻¹ are obtained at current densities of 2.56, 5.12 and 10.28 Ag⁻¹. A comparison of our materials rate capability with the best SnO₂ materials from literature is shown in **Figure 4-24B**. In the range of 2 – 3 V, there does not appear to be a correlation in the capacity versus current density values with the upper anodic limit. Previously published architectures include SnO₂@graphene nanocomposites,^{54,55} SnO₂ anchored CNT,⁶¹ octahedral SnO₂ nanocrystals.⁶² It may be observed that overall the C-SnO₂ electrode looks quite favorable.



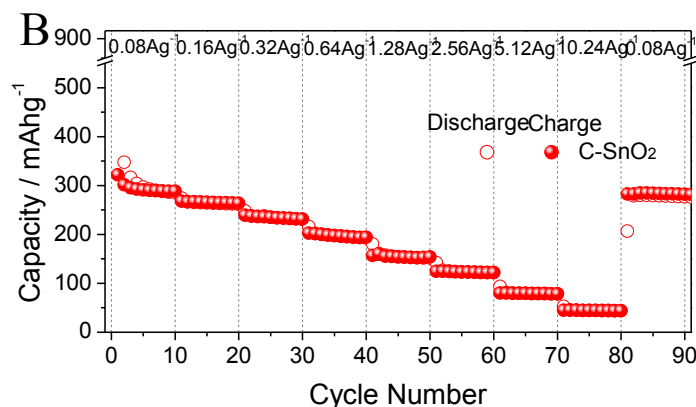


Figure 4-25: Electrochemical performance of C-SnO₂ versus Na, tested between 0.01 and 1.5 V. (A) Cycling performance (0.08 Ag⁻¹), with corresponding CE displayed on the right axis. (B) Rate performance.

Figure 4-25 shows the cycling and the rate performance of C-SnO₂ electrodes against Na, tested between 0.01-1.5V. As shown in **Figure 4-25A**, although C-SnO₂ exhibits a lower total reversible capacity than when it is charged to 3V, the cyclability is actually improved. At cycle 1 the reversible capacity is 314 mAh/g, while at cycle 200 it is 270 mAh/g, *i.e.* only a 86 % degradation. We attribute enhanced cycling to a greater structural stability of the SEI with the lower voltage window. This explanation makes the most sense if the SEI is considered to be a dynamically evolving product, which partially dissolves and/or changes in composition/structure during anodic polarization. The superior cycling up to 1.5V also gives great hope for the performance of a full sodium ion battery cell, where the anodic swing on the negative electrode will be closer to that range. The coulombic efficiency of the electrode increased to 90% by the 3rd cycle, to over 98% by the 12th cycle, and > 99 % from the 21th cycle onwards. As shown in **Figure 4-25B**, capacities of 150, 125 and 80 mAhg⁻¹ were obtained at current densities of 1.2, 2.5 and 5 Ag⁻¹.

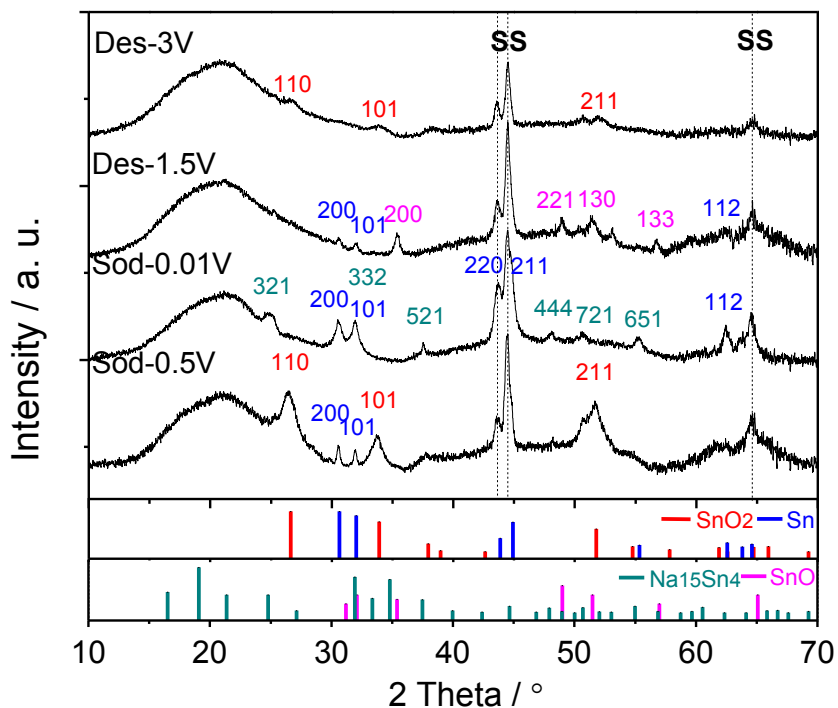


Figure 4-26: (A) XRD patterns of C-SnO₂ at various cut-off voltages: first sodiation to 0.5V, first sodiation to 0.01 V, first desodiation to 1.5V, first desodiation to 3V.

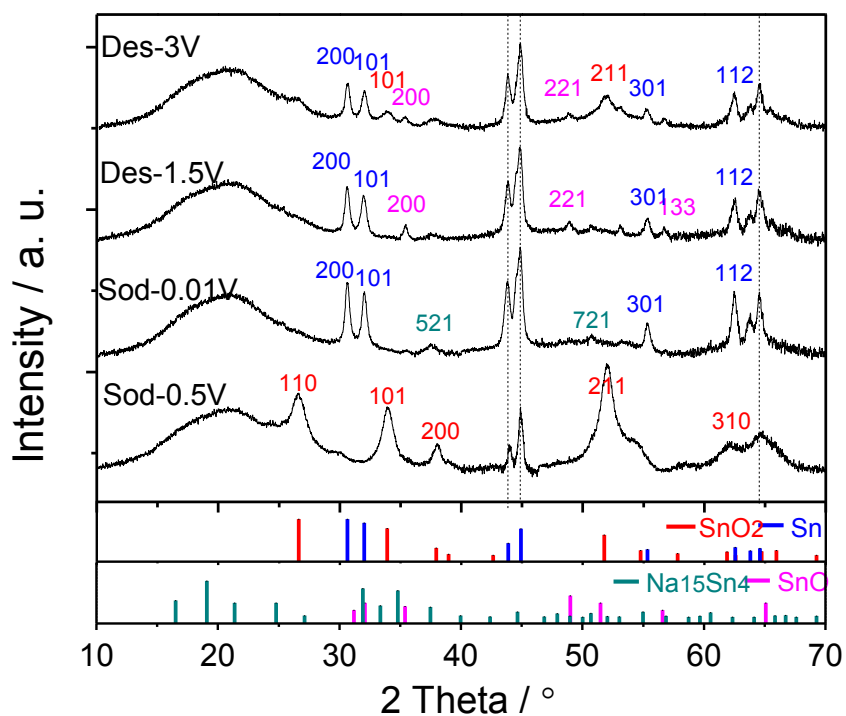


Figure 4-27: (A) XRD patterns of SnO₂ electrodes at various cut-off voltages: first sodiation to 0.5V, first sodiation to 0.01 V, first desodiation to 1.5V, first desodiation to 3V.

We performed XRD characterization to track the phase transformations in C-SnO₂ vs. Na at various cut - off voltages, with the resultant patterns being shown in **Figure 4-26**. Upon first sodiation to 0.5 V new peaks ascribed to β -Sn appeared besides the original SnO₂ peaks. This change indicates the occurrence of conversion reaction $\text{SnO}_2 + 4\text{Na}^+ + 4\text{e}^- \rightarrow \text{Sn} + \text{Na}_2\text{O}$. The Na₂O phase had been reported to be amorphous, which explains the lack of associated Bragg peaks. As the electrode was further discharged down to 0.01 V the SnO₂ phase completely disappeared, while peaks associated with the Na₁₅Sn₄ intermetallic arose. However at 0.01 V the crystalline Sn peaks remained intense, indicating that the alloying reaction $\text{Sn} + 3.75 \text{Na}^+ + 3.75 \text{e}^- \rightarrow \text{Na}_{15}\text{Sn}_4$ is not fully completed. The fact that crystalline Sn is present means that some portion of the material has not even sodiated to one of the intermediate amorphous Na-Sn compositions^{60,75}.

We attribute the unreacted Sn to be the root cause of the much lower capacity of C-SnO₂ with Na than with Li: A substantial portion of the initial SnO₂ phase that is reduced to metallic Sn by the Na does not further participate in the sodiation reaction. This is most likely due to the lower diffusivity of Na in Sn, as well as perhaps due to sluggish interfacial reaction kinetics. Another contributing factor to the incomplete reaction may include poor diffusion of Na through the Na₂O shell that surrounds the metallic Sn after the conversion reaction, as compared to diffusion of Li through the Li₂O shell. A thicker and structurally different SEI will also block or reduce the rates of sodiation *versus* lithiation in the same material. It is important to point out that we did not employ the most stable electrolyte available (one containing FEC). Thus the contribution of the SEI layer on both the C-SnO₂ electrode and on the Na counter electrode may be significant enough to overshadow the intrinsic diffusivity differences.

The same XRD characterization was performed on baseline SnO₂ electrodes. The resultant patterns are shown in **Figure 4-27**. The β -Sn peaks with high intensity in Sod-0.01V spectrum indicate the large amount of unalloyed Sn phase after the first sodiation process. When the electrode was desodiated to 1.5 V the Na₁₅Sn₄ peaks

disappeared, to be replaced by an intermediate orthorhombic SnO phase. This is a distinct difference from the case for C-SnO₂ with Li, where the conversion reaction proceeds from LiO₂ to SnO₂ with no intermediates. Relatively weak crystalline β -Sn peaks were also present at 1.5 V. When desodiated to 3 V the β -Sn peaks completely disappeared, indicating that the material is back to being oxidized. At 3 V there is some evidence of rutile SnO₂, although just like the case for SnO₂ with Li, much of the reformed oxide is nanocrystalline and/or amorphous.

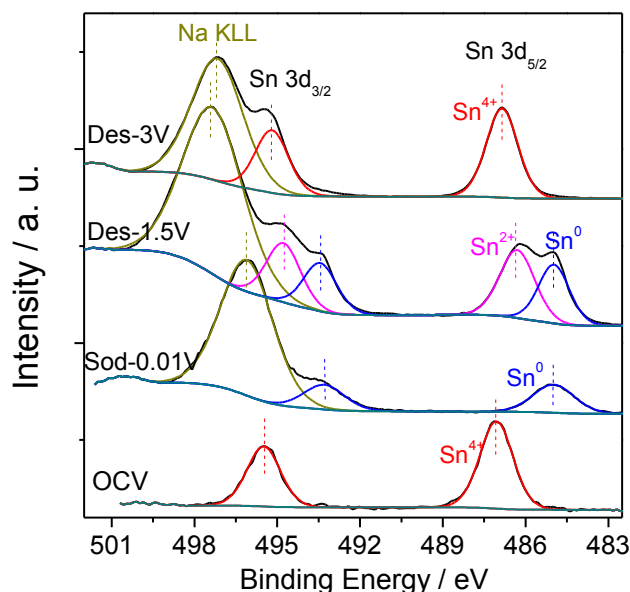


Figure 4-28: XPS spectra for Sn 3d levels of C-SnO₂ at open circuit voltage, first sodiation to 0.01 V, first desodiation to 1.5V, first desodiation to 3V.

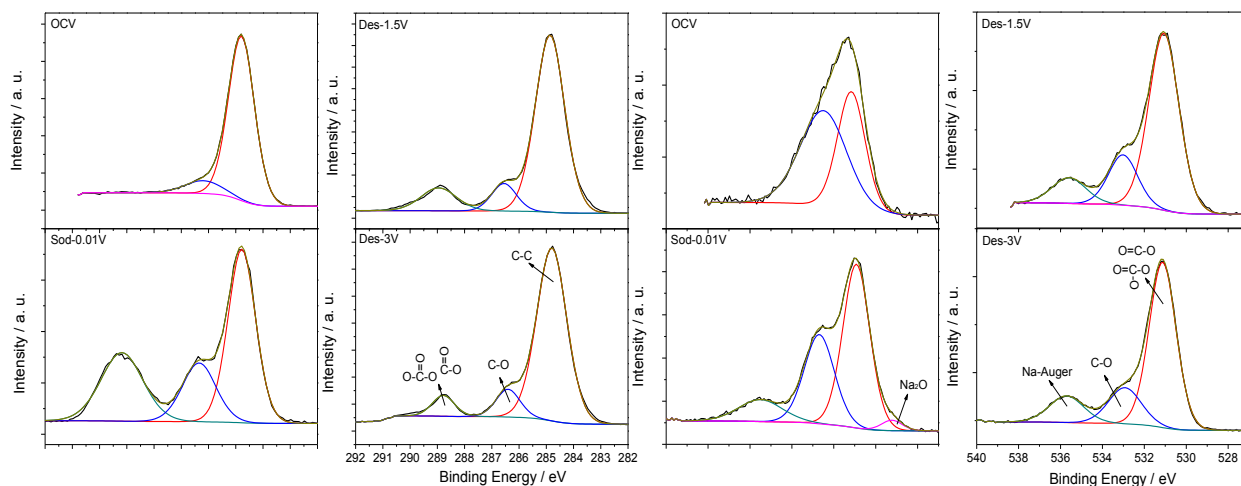


Figure 4-29: XPS spectra for C 1s (left panel) and O 1s (right panel) levels of C-SnO₂

electrodes at various cut-off voltages (open circuit voltage, first sodiated to 0.01 V, first desodiated to 1.5V, first desodiated to 3V vs. Na/Na⁺).

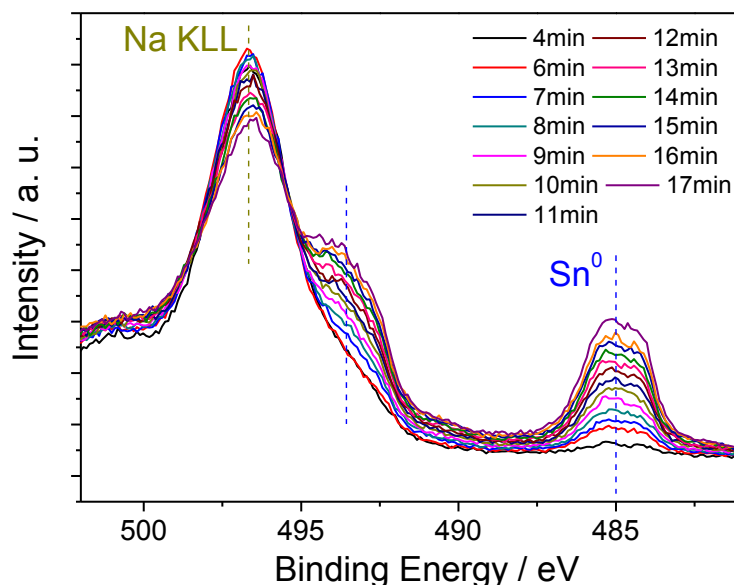


Figure 4-30: XPS depth profiling for Sn 3d levels of C-SnO₂ upon sodiation to 0.01V with Ar etching rate of 5 nm/min.

XPS tests were performed to track the chemical state of Sn in C-SnO₂ electrode during sodiation/desodiation. The results for those experiments are presented in **Figure 4-28** and in **Figure 4-29** for O 1s and C 1s. After discharging to 0.01V from OCV, the Sn 3d peaks shifted to 485 and 493.2 eV, indicating the complete reduction of Sn⁴⁺ to Sn⁰ in the first sodiation process. At 1.5V the Sn 3d peaks are deconvoluted into two components. According to the binding energies, there are both Sn⁰ and Sn²⁺ states detected at this voltage, agreeing with the XRD results. After further desodiation to 3V, the Sn 3d peaks shifted to the Sn⁴⁺ position, characterizing the reformation of SnO₂.

Figure 4-30 shows the XPS depth profiling for Sn 3d levels of C-SnO₂ upon sodiation to 0.01V. The sample was etched by Ar sputtering at a rate of 5nm/min. As shown in the spectra, the binding energy of Sn 3d did not shift as the depth increased, which indicated the homogeneity of the *ex-situ* samples.

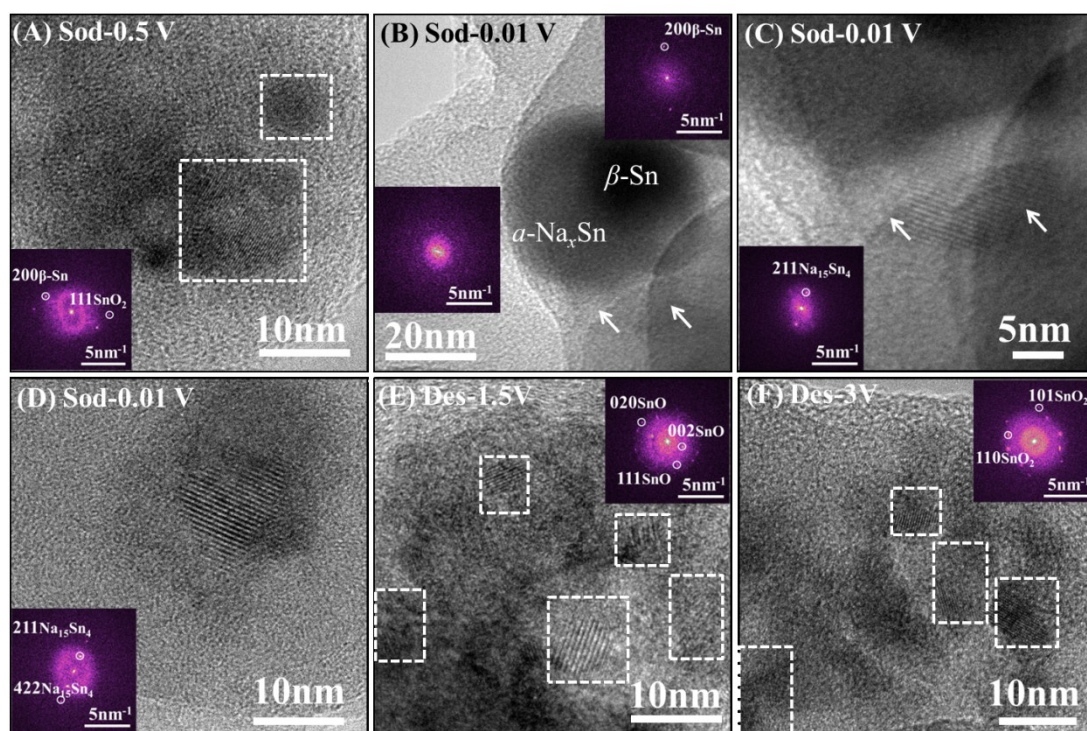


Figure 4-31: HRTEM micrographs of C-SnO₂ electrodes with corresponding indexed FFT patterns corresponding to regions in white squares. (A) first sodiation to 0.5 V. (B,C,D) first sodiation to 0.01 V. The regions indicated by double arrows in (B) (C) are the same region with different magnification. (E) first desodiation to 1.5V, (F) first desodiation to 3V.

Figure 4-31 shows HRTEM micrographs of C-SnO₂ electrodes with corresponding indexed FFT patterns. For these specimens the electrodes were discharged/charged galvanostatically (0.025 Ag⁻¹) to the cut-off voltages, and held there until the float current decreased to below 5% of the galvanostatic current. Results are shown after the first sodiation to 0.5 V, after the first sodiation to 0.01 V, after the first desodiation to 1.5V and after the first desodiation to 3V. When sodiated to 0.5 V we observe both crystalline β -Sn and SnO₂ interspersed in an amorphous matrix. At 0.01 V, unreacted β -Sn is still present. Here it is surrounded by a shell of amorphous high atomic mass material (distinct from amorphous carbon) that is likely some intermediate Na_xSn alloy. Small and isolated Na₁₅Sn₄ crystallites are observed, although they by no means constitute the majority of the Sn in the material. For instance, one such intermetallic is marked in **Figure 4-31B** (indicated by double arrows), with a higher magnification image of the marked area being shown in **Figure**

4-31C. The lattice fringes of this crystallite correspond to (211) $\text{Na}_{15}\text{Sn}_4$. Another isolated $\text{Na}_{15}\text{Sn}_4$ crystallite is shown in **Figure 4-31D**. The electrode desodiated to 1.5 V shows a distribution sub-10 nm SnO crystallites as well as an amorphous matrix. When desodiated to 3 V the crystalline phase returns to SnO_2 .

4.4 Conclusion

To summarize, we used a hydrothermal self-assembly method to create a nanocomposite based on sub- 5nm SnO_2 nanocrystallites in carbon that had excellent bifunctionality as a lithium and a sodium ion battery anode. Especially when tested against Na, the material displayed capacity, cyclability and high-rate capability that are promising relative to published results. Additionally we provide a systematic comparison examination of the sodiation *versus* the lithiation related phase transformations in nanostructured SnO_2 , and establish the fundamental microstructural causes for the much lower capacity observed with Na as compared to Li.

4.5 References

- 1 M. Armand, J. M. Tarascon, *Nature*, 2008, **451**, 652-657.
- 2 J. H. Pikul, H. G. Zhang, J. Cho, P. V. Braun, W. P. King, *Nat. Commun.*, 2013, **4**, 1732.
- 3 M. S. Whittingham, *Chem. Rev.*, 2014, **114**, 11414-11443.
- 4 N. Yabuuchi, K. Kubota, M. Dahbi, S. Komaba, *Chem. Rev.*, 2014, **114**, 11636-11682.
- 5 V. Palomares, P. Serras, I. Villaluenga, K. B. Hueso, J. Carretero-Gonzalez, T. Rojo, *Energy Environ. Sci.*, 2012, **5**, 5884-5901.
- 6 V. Palomares, M. Casas-Cabanas, E. Castillo-Martinez, M. H. Han, T. Rojo, *Energy Environ. Sci.*, 2013, **6**, 2312-2337.
- 7 S. W. Kim, D. H. Seo, X. H. Ma, G. Ceder, K. Kang, *Adv. Energy Mater.*, 2012, **2**, 710-721.

- 8 M. D. Slater, D. Kim, E. Lee, C. S. Johnson, *Adv. Funct. Mater.*, 2013, **23**, 947-958.
- 9 L. Wang, Y. H. Lu, J. Liu, M. W. Xu, J. G. Cheng, D. W. Zhang, J. B. Goodenough, *Angew. Chem. Int. Edit.*, 2013, **52**, 1964-1967.
- 10 B. Koo, S. Chattopadhyay, T. Shibata, V. B. Prakapenka, C. S. Johnson, T. Rajh, E. V. Shevchenko, *Chem. Mater.*, 2013, **25**, 245-252.
- 11 M. Han, E. Gonzalo, G. Singh, T. Rojo, *Energy Environ. Sci.*, 2015, **8**, 81-102.
- 12 N. Yabuuchi, M. Kajiyama, J. Iwatate, H. Nishikawa, S. Hitomi, R. Okuyama, R. Usui, Y. Yamada, S. Komaba, *Nat. Mater.*, 2012, **11**, 512-517.
- 13 Y. Jung, C. Lim, D. Kim, *J. Mater. Chem. A*, 2013, **1**, 11350-11354.
- 14 S. Li, Y. Dong, L. Xu, X. Xu, L. He, L. Mai, *Adv. Mater.*, 2014, **26**, 3545-3553.
- 15 W. Song, X. Cao, Z. Wu, J. Chen, K. Huangfu, X. Wang, Y. Huang, X. Ji, *Phys. Chem. Chem. Phys.*, 2014, **16**, 17681-17687.
- 16 J. Ding, H. L. Wang, Z. Li, A. Kohandehghan, K. Cui, Z. W. Xu, B. Zahiri, X. H. Tan; E. M. Lotfabad, B. C. Olsen, D. Mitlin, *ACS Nano*, 2013, **7**, 11004-11015.
- 17 W. Luo, J. Schardt, C. Bommier, B. Wang, J. Razink, J. Simonsen, X. Ji, *J. Mater. Chem. A*, 2013, **1**, 10662-10666.
- 18 J. Ding, H. Wang, Z. Li, K. Cui, D. Karpuzov, X. Tan, A. Kohandehghan, D. Mitlin, *Energy Environ. Sci.*, 2015, **8**, 941-955.
- 19 K. Tang, L. J. Fu, R. J. White, L. H. Yu, M. M. Titirici, M. Antonietti, J. Maier, *Adv. Energy Mater.*, 2012, **2**, 873-877.
- 20 H. Cha, H. Jeong, J. Kang, *J. Mater. Chem. A*, 2014, **2**, 5182-5186.
- 21 Y. Xu, E. M. Lotfabad, H. L. Wang,; B. Farbod, Z. W. Xu,; A. Kohandehghan, D. Mitlin, *Chem. Commun.*, 2013, **49**, 8973-8975.
- 22 P. Senguttuvan, G. Rouse, V. Seznec, J. M. Tarascon, M. R. Palacin, *Chem. Mater.*, 2011, **23**, 4109-4111.
- 23 H. L. Pan, X. Lu, X. Q. Yu, Y. S. Hu, H. Li, X. Q. Yang, L. Q. Chen, *Adv. Energy Mater.*, 2013, **3**, 1186-1194.
- 24 Y. Zhu, P. Nie, L. Shen, S. Dong, Q. Sheng, H. Li, H. Luo, X. Zhang, *Nanoscale*, 2015, **7**, 3309-3315..

- 25 L. Baggetto, H. Y. Hah, J. C. Jumas, C. E. Johnson, J. A. Johnson, J. K. Keum, C. A. Bridges, G. M. Veith, *J. Power Sources*, 2014, **267**, 329-336.
- 26 L. F. Xiao, Y. L. Cao, J. Xiao, W. Wang, L. Kovarik, Z. M. Nie, J. Liu, *Chem. Commun.*, 2012, **48**, 3321-3323.
- 27 Y. H. Xu, Y. J. Zhu, Y. H. Liu, C. S. Wang, *Adv. Energy Mater.*, 2013, **3**, 128-133.
- 28 B. Farbod, K. Cui, W. P. Kalisvaart, M. Kupsta, B. Zahiri, A. Kohandehghan, E. M. Lotfabad, Z. Li, E. J. Lubber, D. Mitlin, *ACS Nano*, 2014, **8**, 4415-4429.
- 29 L. Baggetto, K. J. Carroll, H. Y. Hah, C. E. Johnson, D. R. Mullins, R. R. Unocic, J. A. Johnson, Y. S. Meng, G. M. Veith, *J. Phys. Chem. C*, 2014, **118**, 7856-7864.
- 30 V. Kulish, O. Malyi, M. Ng, Z. Chen, S. Manzhos, P. Wu, *Phys. Chem. Chem. Phys.*, 2014, **16**, 4260-4267.
- 31 Y. H. Xu, Q. Liu, Y. J. Zhu, Y. H. Liu, A. Langrock, M. R. Zachariah, C. S. Wang, *Nano Lett.*, 2013, **13**, 470-474.
- 32 D. Bresser, F. Mueller, D. Buchholz, E. Paillard, S. Passerini, *Electrochim. Acta*, 2014, **128**, 163-171.
- 33 C. K. Chan, H. L. Peng, G. Liu, K. McIlwrath, X. F. Zhang, R. A. Huggins, Y. Cui, *Nat. Nanotechnol.*, 2008, **3**, 31-35.
- 34 X. Zhu, H. Chen, Y. Wang, L. Xia, Q. Tan, H. Li, Z. Zhong, F. Su, X.S. Zhao, *J. Mater. Chem. A*, 2013, **14**, 4483-4489.
- 35 Y. Yao, N. Liu, M. T. McDowell, M. Pasta, Y. Cui, *Energy Environ. Sci.*, 2012, **5**, 7927-7930.
- 36 M. H. Seo, M. Park, K. T. Lee, K. Kim, J. Kim, J. Cho, *Energy Environ. Sci.*, 2011, **4**, 425-428.
- 37 T. Ramireddy, M. Rahman, T. Xing, Y. Chen, A. M. Glushenkov, *J. Mater. Chem. A*, 2014, **2**, 4282-4291.
- 38 A. Darwiche, C. Marino, M. T. Sougrati, B. Fraisse, L. Stievano, L. Monconduit, *J. Am. Chem. Soc.*, 2012, **134**, 20805-20811.
- 39 Y. Wang, F. Su, JY. Lee, X.S. Zhao, *Chem. Mater.*, 2006, **18**, 1347-1353.
- 40 X. Wang, X. Q. Cao, L. Bourgeois, H. Guan, S. M. Chen, Y. T. Zhong, D. M. Tang,

- H. Q. Li, T. Y. Zhai, L. Li, Y. Bando, D. Golberg, *Adv. Funct. Mater.*, 2012, **22**, 2682-2690.
- 41 H. W. Song, N. Li, H. Cui, C. X. Wang, *J. Mater. Chem. A*, 2013, **1**, 7558-7562.
- 42 J. Liu, H. G. Zhang, J. Wang, J. Cho, J. H. Pikul, E. S. Epstein, X. Huang, J. Liu, W. P. King, P. V. Braun, *Adv. Mater.*, 2014, **26**, 7096-7101.
- 43 N. Yesibolati, M. Shahid, W. Chen, M. N. Hedhili; M. C. Reuter, F. M. Ross, H. N. Alshareef, *Small*, 2014, **10**, 2849-2858.
- 44 D. W. Su, X. Q. Xie, G. X. Wang, *Chem-Eur. J.*, 2014, **20**, 3192-3197.
- 45 M. Shimizu, H. Usui, H. Sakaguchi, *J. Power Sources*, 2014, **248**, 378-382.
- 46 M. Shahid, N. Yesibolati, M. C. Reuter, F. M. Ross, Whittingham, *J. Power Sources*, 2014, **263**, 239-245.
- 47 H. Bryngelsson, J. Eskhult, L. Nyholm, M. Herranen, O. Alm, K. Edstrom, *Chem. Mater.*, 2007, **19**, 1170-1180.
- 48 V. Aravindan, P. Vickraman, *Solid State Sci.*, 2007, **9**, 1069-1073.
- 49 X. Fan, J. Shao, X. Xiao, X. Wang, S. Li, H. Ge, L. Chen, C. S. Wang, *J. Mater. Chem. A*, 2014, **2**, 18367-18374.
- 50 L. Zhang, H. Wu, B. Liu, X. Lou, *Energy Environ. Sci.*, 2014, **7**, 1013-1017.
- 51 X. S. Zhou, L. J. Wan, Y. G. Guo, *Adv. Mater.*, 2013, **25**, 2152-2157.
- 52 Z. X. Chen, M. Zhou, Y. L. Cao, X. P. Ai, H. X. Yang, J. Liu, *Adv. Energy Mater.*, 2012, **2**, 95-102.
- 53 S. Li, Y. Wang, J. Qiu, M. Ling, H. Wang, W. Martens, S. Zhang, *RSC Adv.*, 2014, **4**, 50148-50152.
- 54 D. W. Su, H. J. Ahn, G. X. Wang, *Chem. Commun.*, 2013, **49**, 3131-3133.
- 55 Y. X. Wang, Y. G. Lim, M. S. Park, S. L. Chou, J. H. Kim, H. K. Liu, S. X. Dou, Y. J. Kim, *J. Mater. Chem. A*, 2014, **2**, 529-534.
- 56 X. Xie, D. Su, J. Zhang, S. Chen, A. Mondal, G. Wang, *Nanoscale*, 2015, **7**, 3164-3172..
- 57 J. Y. Huang,; L. Zhong,; C. M. Wang,; J. P. Sullivan,; W. Xu,; L. Q. Zhang,; S. Mao, X,; N. S. Hudak,; X. H. Liu,; A. Subramanian,; H. Y. Fan,; L. A. Qi,; A.

- Kushima,; J. Li, *Science*, 2010, **330**, 1515-1520.
- 58 A. M. Nie, L. Y. Gan, Y. C. Chong, H. Asayesh-Ardakani, Q. Q. Li, C. Z. Dong, R. Z. Tao, F. Mashayek, H. T. Wang, U. Schwingenschlogl, R. F. Klie, R. S. Yassar, *ACS Nano*, 2013, **7**, 6203-6211.
- 59 G. M. Zhou, D. W. Wang, L. Li, N. Li, F. Li, H. M. Cheng, *Nanoscale*, 2013, **5**, 1576-1582.
- 60 L. D. Ellis, T. D. Hatchard, M. N. Obrovac, *J. Electrochem. Soc.*, 2012, **159**, A1801-A1805.
- 61 Y. Wang, D. W. Su, C. Y. Wang, G. X. Wang, *Electrochem. Commun.*, 2013, **29**, 8-11.
- 62 D. W. Su, C. Y. Wang, H. Ahn, G. X. Wang, *Phys. Chem. Chem. Phys.*, 2013, **15**, 12543-12550.
- 63 J. Park, J. W. Park, J. H. Han, S. W. Lee, K. Y. Lee, H. S. Ryu, K. W. Kim, G. X. Wang, J. H. Ahn, H. J. Ahn, *Mater. Res. Bull.*, 2014, **58**, 186-189.
- 64 M. Shahid, N. Yesibolati, M. C. Reuter, F. M. Ross, H. N. Alshareef, *J. Power Sources*, 2014, **263**, 239-245.
- 65 W. J. Zhang, *J. Power Sources*, 2011, **196**, 13-24.
- 66 H. X. Zhang, C. Feng, Y. C. Zhai, K. L. Jiang, Q. Q. Li, S. S. Fan, *Adv. Mater.*, 2009, **21**, 2299-2304.
- 67 Y. Wang, H. C. Zeng, J. Y. Lee, *Adv. Mater.*, 2006, **18**, 645-649.
- 68 S. M. Paek, E. Yoo, I. Honma, *Nano Lett.*, 2009, **9**, 72-75.
- 69 X. D. Huang, X. F. Zhou, L. Zhou, K. Qian, Y. H. Wang, Z. P. Liu, C. Z. Yu, *ChemPhysChem*, 2011, **12**, 278-281.
- 70 C. A. Bonino, L. W. Ji, Z. Lin, O. Toprakci, X. W. Zhang, S. A. Khan, *ACS Appl. Mater. Inter.*, 2011, **3**, 2534-2542.
- 71 X. Zhang, J. Liang, G. X. Gao, S. J. Ding, Z. L. Yang, W. Yu, B. Q. Li, *Electrochim. Acta*, 2013, **98**, 263-267.
- 72 L. Zhang, G. Q. Zhang, H. B. Wu, L. Yu, X. W. Lou, *Adv. Mater.*, 2013, **25**, 2589-2593.

- 73 M. He, L. X. Yuan, X. L. Hu, W. X. Zhang, J. Shu, Y. H. Huang, *Nanoscale*, 2013, **5**, 3298-3305.
- 74 Y. Zhang, J. Xie, S. Zhang, P. Zhu, G. Cao, X. Zhao, *Electrochim. Acta*, 2015, **151**, 8-15.
- 75 J. W. Wang, X. H. Liu, S. X. Mao, J. Y. Huang, *Nano Lett.*, 2012, **12**, 5897-5902.
- 76 X. W. Lou, C. Yuan, L. A. Archer, *Small*, 2007, **3**, 262-265.
- 77 W. S. Kim, Y. Hwa, H. C. Kim, J. H. Choi, H. J. Sohn, S. H. Hong, *Nano Res.*, 2014, **7**, 1128-1136.
- 78 A. Z. Adamyan, Z. N. Adamian, V. M. Aroutiounian, *Sensors*, 2003, **3**, 438-442.
- 79 X. W. Lou, Y. Wang, C. Yuan, J. Lee, L. A. Archer, *Adv. Mater.*, 2006, **18**, 2325-2329.
- 80 S. Ikeda, K. Tachi, Y. H. Ng, Y. Ikoma, T. Sakata, H. Mori, T. Harada, M. Matsumura, *Chem. Mater.*, 2007, **19**, 4335-4340.
- 81 X. W. Lou, J. S. Chen, P. Chen, L. A. Archer, *Chem. Mater.*, 2009, **21**, 2868-2874.
- 82 C. Wang, Y. Zhou, M. Y. Ge, X. B. Xu, Z. L. Zhang, J. Z. Jiang, *J. Am. Chem. Soc.*, 2010, **132**, 46-47.
- 83 T. Egami, S. J. L. Billinge, *Underneath the Bragg Peaks: Structural analysis of Complex Materials*, Elsevier Ltd., 2003.
- 84 A. Ponrouch, P. L. Taberna, P. Simon, M. R. Palacin, *Electrochim. Acta*, 2012, **61**, 13-18.
- 85 S. Grugeon, S. Laruelle, L. Dupont, J.-M. Tarascon, *Solid State Sci.*, 2003, **5**, 895-940.
- 86 S. Laruelle, S. Grugeon, P. Poizot, M. Dolle, L. Dupont, J.-M. Tarascon, *J. Electrochem. Soc.*, 2002, **149**, 627-634.
- 87 H. L. Wang, Z. W. Xu, Z. Li, K. Cui, J. Ding, A. Kohandehghan, X. H. Tan, B. Zahiri, B. C. Olsen, C. M. B. Holt, D. Mitlin, *Nano Lett.*, 2014, **14**, 1987-1994.
- 88 Z. W. Xu, H. L. Wang, Z. Li, A. Kohandehghan, J. Ding, J. Chen, K. Cui, D. Mitlin, *J. Phys. Chem. C*, 2014, **118**, 18387-18396.
- 89 Y. Chen, B. Song, R. Chen, L. Lu, J. Xue, *J. Mater. Chem. A*, 2014, **2**, 5688-5695.

- 90 F. Han, W. Li, M. Li, A. Lu, *J. Mater. Chem.*, 2012, **22**, 9645-9651.
- 91 Y. H. Xu, J. C. Guo, C. S. Wang, *J. Mater. Chem.*, 2012, **22**, 9562-9567.
- 92 X. W. Lou, C. M. Li, L. A. Archer, *Adv. Mater.*, 2009, **21**, 2536-2539.
- 93 K. Dai, H. Zhao, Z. Wang, X. Song, V. Battaglia, G. Liu, *J. Power Sources*, 2014, **263**, 276-279.
- 94 S. A. Webb, L. Baggetto, C. A. Bridges, G. M. Veith, *J. Power Sources*, 2014, **248**, 1105-1117.

5

Concluding remarks

This thesis was devoted to developing promising electrode materials for Na ion based energy storage devices including sodium ion batteries and sodium ion capacitors. In addition to the materials design and preparation, we also completed systemic investigations on the fundamental Na storage mechanisms of the related electrode materials, which could contribute significantly to the whole field.

The first work (chapter 2) focused on exploring carbon materials as sodium ion battery anodes. In this study, we utilized a ubiquitously found biomass named peat moss as the precursor, and for the first time synthesized carbons combining all the desired features for Na storage, including dilated graphene interlayer spacing, short bulk Na ion diffusion length and facile Na ion transport pathway. The resultant carbon anode displayed superb electrochemical performances in terms of high overall capacity, good cycling stability, excellent rate capability and negligible charge/discharge voltage hysteresis. Based on the systemic investigation of the synthesis-structure-performance relationship of the peat moss derived carbons, we for the first time discovered that the highly ordered pseudographitic domains in carbons (*i.e.* domains with larger interlayer spacing than that of equilibrium graphite) can provide energy homogeneous intercalation sites for Na ions, which create a flat plateau on the voltage profile. Moreover, we also discovered the positive correlation between the degree of carbon's graphitic order and the plateau capacity of the corresponding anode. These findings have already guided the carbon anode developments in the following studies.

The second work (chapter 3) developed carbon materials utilized for hybrid Na

ion capacitor (NIC) devices. We have for the first time built a totally carbon-based NIC device with state-of-the-art performance in terms of energy, power and cyclability. In order to achieve this target, both the electrode materials and working style of the full device were optimized. Firstly, we try to push the envelope of the electrode performances. In order to increase the overall specific capability of the cathode, we introduced extra pseudo-capacitance by surface redox reaction between Na^+ and oxygen functional groups, in addition to the normal EDLC capacitance by electrostatic surface adsorption. Secondly, by purposely restraining the intercalation capacity of the anode within a narrow voltage window at the low voltage region, we successfully balanced the mass and capacity between the cathode and anode as a ratio of 1:1, which has maximized the voltage window and energy/power densities of the full device. It should also be noted that all the electrode carbons were prepared from a totally valueless peanut shell biowaste, which is globally generated at over 6 million tons per year but with little application. The exceptional performance, combining with the green and low cost synthesis method, should make the peanut shell derived carbons highly practical for NICs.

Motivated by the increasing demand for high volumetric capacity electrodes, the third study (chapter 4) was devoted to exploring SnO_2 based anode materials for both NIBs and LIBs. Firstly, based on a systematic investigation of the phase transformation of nanostructured SnO_2 during sodiation and lithiation processes, we have provided a clear picture of the charge storage mechanisms of SnO_2 based anodes in LIBs and NIBs. Secondly, we discovered the fundamental causes of the much lower experimental capacity of SnO_2 based anode against Na than that of against Li, which is due to the kinetic difficulty for the full completeness of the Na-Sn alloying reaction. Based on the side-by-side comparison between our SnO_2 -C nanocomposite and normal SnO_2 nanoparticles, we also discovered that the special nanostructure could help improve both the kinetics of the alloying reaction and the reversibility of the conversion reaction. In more detail, the SnO_2 -C nanocomposite consists of a unique continuous carbon frame with internally imbedded sub-5nm SnO_2 crystallites.

The frame imparts excellent electrical conductivity to the active material, allows for rapid diffusion of Na ions. It can also effectively buffer the sodiation/desodiation stresses and prevent cycling-induced agglomeration of the active crystals. Benefiting from this unique nanostructure, the SnO₂-C anodes exhibited very outstanding cyclability and rate performances in both LIBs and NIBs.

For future research, the main targets we can focus on will be to obtain better electrode materials and higher energy/power density devices. Firstly, due to the complexity of carbon properties, the charge storage mechanism of carbons, especially for the heavily heteroatom-doped ones, still remains largely unknown. More works could be done developing better carbon electrodes for Na storage. Secondly, more researches are highly desired preparing high volumetric capacity Sn-based anodes. Compounds such as tin sulfide (SnS, SnS₂) and tin phosphide (Sn₃P₄) could also be very promising anodes for NIBs. Finally, in place of the traditional intercalation cathode typically limited by low reversible capacity, sulfur and selenium based materials could be next generation cathode candidates due to their much higher reversible capacities for Na storage.

Bibliography

1. M. Armand, J. M. Tarascon, *Nature*, 2008, **451**, 652-657.
2. P. Simon, Y. Gogotsi, *Nat. Mater.*, 2008, **7**, 845-854.
3. Y. -M. Chiang, *Science*, 2010, **330**, 1485-1486.
4. H. L. Pan, Y. S. Hu, L. Q. Chen, *Energy Environ. Sci.*, 2013, **6**, 2338-2360.
5. H. K. Liu, G. X. Wang, Z. P. Guo, J. Z. Wang, K. Konstantinov, *J. Nanosci. Nanotechnol.*, 2006, **6**, 1-15.
6. M. Wakihara, O. Yamamoto, *Lithium Ion Batteries, Fundamentals and Performance*, Wiley-VCH, Japan, 1998.
7. R. Liu, J. Duay, S. B. Lee, *Chem. Commun.*, 2011, **47**, 1384-1404.
8. X. Zuo, C. Fan, X. Xiao, J. Liu, J. Nan, *J. Power Sources*, 2012, **219**, 94-99.
9. S. Flandrois, B. Simon, *Carbon*, 1999, **37**, 165-180.
10. L. Yuan, Z. Huang, W. Zhang, X. Hu, J. Chen, Y. Huang, J. B. Goodenough, *Energy Environ. Sci.*, 2011, **4**, 269-284.
11. M. Winter, J. O. Besenhard, M. E. Spahr, P. Novak, *Adv. Mater.*, 1998, **10**, 725-763.
12. M. D. Slater, D. Kim, E. Lee, C. S. Johnson, *Adv. Funct. Mater.*, 2013, **23**, 947-958.
13. G. E. Pascal and M. Fouletier, *Solid State Ionics*, 1988, **28**, 1172-1175.
14. M. M. Doeff, Y. P. Ma, S. J. Visco and L. C. Dejonghe, *J. Electrochem. Soc.*, 1993, **140**, 169-170.
15. P. Thomas and D. Billaud, *Electrochim. Acta*, 2002, **47**, 3303-3307.
16. D. A. Stevens and J. R. Dahn, *J. Electrochem. Soc.*, 2000, **147**, A1271-A1273.
17. D. A. Stevens and J. R. Dahn, *J. Electrochem. Soc.*, 2001, **148**, A803-A811.
18. R. Alcántara, P. Lavela, G. F. Ortiz and J. L. Tirado, *Electrochem. Solid-State Lett.*, 2005, **8**, A222-A225.
19. S. Wenzel, T. Hara, J. Janek and P. Adelhelm, *Energy Environ. Sci.*, 2011, **4**, 3342-3345.

20. K. Tang, L. Fu, R. J. White, L. Yu, M.-M. Titirici, M. Antonietti and J. Maier, *Adv. Energy Mater.*, 2012, **2**, 873-877.
21. H. G. Wang, Z. Wu, F. L. Meng, D. L. Ma, X. L. Huang, L. M. Wang and X. B. Zhang, *ChemSusChem*, 2013, **6**, 56-60.
22. Y. Cao, L. Xiao, M. L. Sushko, W. Wang, B. Schwenzer, J. Xiao, Z. Nie, L. V. Saraf, Z. Yang and J. Liu, *Nano Lett.*, 2012, **12**, 3783-3787.
23. Li, W.; Zeng, L.; Yang, Z.; Gu, L.; Wang, J.; Liu, X.; Cheng, J.; Yu, Y. *Nanoscale*, 2014, **6**, 693-698.
24. Luo, W.; Schardt, J.; Bommier, C.; Wang, B.; Razink, J.; Simonsen, J.; Ji, X. C. *J. Mater. Chem. A*, 2013, **1**, 10662-10666.
25. V. G. Pol, E. Lee, D. Zhou, F. Dogan, J. M. Calderon-Moreno, C. S. Johnson, *Electrochim. Acta*, 2014, **127**, 61-67.
26. C. Bommier, W. Luo, W. Gao, A. Greaney, S. Ma, X. Ji, *Carbon*, 2014, **76**, 165-174.
27. W. -J. Zhang, *J. Power Sources*, 2011, **196**, 13-24.
28. L. Baggetto, H. Y. Hah, J. C. Jumas, C. E. Johnson, J. A. Johnson, J. K. Keum, C. A. Bridges, G. M. Veith, *J. Power Sources*, 2014, **267**, 329-336.
29. L. Baggetto, J. K. Keum, J. F. Browning, G. M. Veith, *Electrochem. Commun.*, 2013, **34**, 41-44.
30. J. Qian, X. Wu, Y. Cao, X. Ai, H. Yang, *Angew. Chem.*, 2013, **125**, 4731-4734.
31. Y. Kim, Y. Park, A. Choi, N. S. Choi, J. Kim, J. Lee, J. H. Ryu, S. M. Oh, K. T. Lee, *Adv. Mater.*, 2013, **25**, 3045-3049.
32. M. He, K. Kravchyk, M. Walter, M. V. Kovalenko, *Nano Lett.*, 2014, **14**, 1255-1262.
33. K. J. Rhodes, R. Meisner, M. Kirkham, N. Dudney, C. Daniel, *J. Electrochem. Soc.*, 2012, **159**, 294-299.
34. L. D. Ellis, T. D. Hatchard, M. N. Obrovac, *J. Electrochem. Soc.*, 2012, **159**, 1801-1805.
35. M. K. Datta, R. Epur, Partha Saha, Karan Kadakia, S. K. Park, P. N. Kumta, *J.*

- Power Sources*, 2013, **225**, 316-322.
36. Y. Xu, Y. Zhu, Y. Liu, C. S. Wang, *Adv. Energy Mater.*, 2013, **3**, 128-133.
37. M. Gu, A. Kushima, Y. Shao, J. Zhang, J. Liu, N. D. Browning, J. Li, C. Wang, *Nano Lett.*, 2013, **13**, 5203-5211.
38. D. Buchholz, A. Moretti, R. Kloepsch, S. Nowak, V. Siozios, M. Winter, and S. Passerini, *Chem. Mater.*, 2013, **25**, 142-148.
39. J. W. Wang, X. H. Liu, S. X. Mao, J. Y. Huang, *Nano Lett.*, 2012, **12**, 5897-5902.
40. J. Y. Huang, L. Zhong, C. M. Wang, J. P. Sullivan, W. Xu, L. Q. Zhang, S. X. Mao, N. S. Hudak, X. H. Liu, A. Subramanian, H. Fan, L. Qi, A. Kushima, J. Li, *Science*, 2010, **330**, 1515-1520.
41. H. Zhu, Z. Jia, Y. Chen, N. Weadock, J. Wan, O. Vaaland, X. Han, T. Li, L. Hu, *Nano Lett.*, 2013, **13**, 3093-3100.
42. D. Nam, T. Kim, K. S. Hong, H. S. Kwon, *ACS Nano*, 2014, **8**, 11824-11835.
43. M. Shimizu, H. Usui, H. Sakaguchi, *J. Power Sources*, 2014, **248**, 378-382.
44. D. W. Su, X. Q. Xie, G. X. Wang, *Chem-Eur. J.*, 2014, **20**, 3192-3197.
45. Z. Chen, M. Zhou, Y. Cao, X. Ai, H. Yang, J. Liu, *Adv. Energy Mater.*, 2012, **2**, 95-102.
46. C. Guan, X. H. Wang, Q. Zhang, Z. X. Fan, H. Zhang, H. J. Fan, *Nano Lett.*, 2014, **14**, 4852-4858.
47. X. S. Zhou, L. J. Wan, Y. G. Guo, *Adv. Mater.*, 2013, **25**, 2152-2157.
48. X. Fan, J. Shao, X. Xiao, X. Wang, S. Li, H. Ge, L. Chen, C. S. Wang, *J. Mater. Chem. A*, 2014, **2**, 18367-18374.
49. D. Su, H. Ahn, G. Wang, *Chem. Commun.*, 2013, **49**, 3131-3133.
50. Y. Wang, Y. Lim, M. Park, S. Chou, J. H. Kim, H. K. Liu, S. X. Dou, Y. J. Kim, *J. Mater. Chem. A*, 2014, **2**, 529-534.
51. Y. Wang, D. Su, C. Wang, G. Wang, *Electrochem. Commun.*, 2013, **29**, 8-11.
52. Patrice Simon, Yury Gogotsi, Bruce Dunn, *Science*, 2014, **343**, 1210-1211.
53. N. Choi, Z. Chen, S. A. Freunberger, X. Ji, Y. Sun, K. Amine, G. Yushin, L. F. Nazar, J. Cho, and P. G. Bruce. *Angew. Chem. Int. Ed.*, 2012, **51**, 9994-10024.

54. B. R. Liu, P. Soares, C. Checkles, Y. Zhao and G. H. Yu, *Nano Lett.*, 2013, **13**, 3414-3419.
55. Y. J. Gong, S. B. Yang, L. Zhan, L. L. Ma, R. Vajtai and P. M. Ajayan, *Adv. Funct. Mater.*, 2014, **24**, 125-130.
56. S. M. Oh, S. T. Myung, C. S. Yoon, J. Liu, J. Hassoun, B. Scrosati, K. Amine, Y. K. Sun. *Nano Lett.*, 2014, **14**, 1620-1626.
57. R. Mukherjee, R. Krishnan, T. M. Lu and N. Koratkar, *Nano Energy*, 2012, **1**, 518-533.
58. C. B. Zhu, K. P. Song, P. A. van Aken, J. Maier and Y. Yu, *Nano Lett.*, 2014, **14**, 2175-2180.
59. J. X. Zhu, L. J. Cao, Y. S. Wu, Y. J. Gong, Z. Liu, H. E. Hoster, Y. H. Zhang, S. T. Zhang, S. B. Yang, Q. Y. Yan, P. M. Ajayan, R. Vajtai, *Nano Lett.*, 2013, **13**, 5408-5413.
60. J. Han, L. L. Zhang, S. Lee, J. Oh, K. S. Lee, J. R. Potts, J. Y. Ji, X. Zhao, R. S. Ruoff and S. Park, *ACS Nano*, 2013, **7**, 19-26.
61. L. Qie, W. M. Chen, H. H. Xu, X. Q. Xiong, Y. Jiang, F. Zou, X. L. Hu, Y. Xin, Z. L. Zhang and Y. H. Huang, *Energy Environ. Sci.*, 2013, **6**, 2497-2504.
62. M. R. Lukatskaya, O. Mashtalir, C. E. Ren, Y. Dall'Agnese, P. Rozier, P. L. Taberna, M. Naguib, P. Simon, M. W. Barsoum and Y. Gogotsi, *Science*, 2013, **341**, 1502-1505.
63. W. J. Qian, F. X. Sun, Y. H. Xu, L. H. Qiu, C. H. Liu, S. D. Wang and F. Yan, *Energy Environ. Sci.*, 2014, **7**, 379-386.
64. Z. Li, L. Zhang, B. S. Amirkhiz, X. H. Tan, Z. W. Xu, H. L. Wang, B. C. Olsen, C. M. B. Holt and D. Mitlin, *Adv. Energy Mater.*, 2012, **2**, 431-437.
65. F. Beguin, E. Frackowiak, Ed., *Supercapacitors: Materials, Systems and Applications*, Wiley-VCH, Weinheim, Germany, 2013.
66. J. R. Miller, P. Simon, *Science*, 2008, **321**, 651-652.
67. P. Simon, Y. Gogotsi, *Acc. Chem. Res.*, 2013, **46**, 1094-1103.
68. K. Brezesinski, J. Wang, J. Haetge, C. Reitz, S. O. Steinmueller, S. H. Tolbert, B.

- M. Smarsly, B. Dunn, T. Brezesinski, *J. Am. Chem. Soc.*, 2012, **132**, 6982-6990.
69. C. Hu, K. Chang, M. Lin, Y. Wu, *Nano Lett.*, 2006, **6**, 2690-2695.
70. G. Yu, L. Hu, M. Vosgueritchian, H. Wang, X. Xie, J. R. McDonough, X. Cui, Y. Cui, Z. Bao, *Nano Lett.*, 2011, **11**, 2905-2911.
71. Y. He, W. Chen, X. Li, Z. Zhang, J. Fu, C. Zhao, E. Xie, *ACS Nano*, 2013, **7**, 174-182.
72. J. W. Kim, V. Augustyn, B. Dunn, *Adv. Energy Mater.*, 2012, **2**, 141-148.
73. V. Augustyn, J. Come, M. A. Lowe, J. W. Kim, P. L. Taberna, S. H. Tolbert, H. D. Abruna, P. Simon and B. Dunn, *Nat. Mater.*, 2013, **12**, 518-522.
74. K. Naoi, S. Ishimoto, J. Miyamoto and W. Naoi, *Energy Environ. Sci.*, 2012, **5**, 9363-9373.
75. Z. Chen, Y. Yuan, H. H. Zhou, X. L. Wang, Z. H. Gan, F. S. Wang and Y. F. Lu, *Adv. Mater.*, 2014, **26**, 339-345.
76. A. Jain, V. Aravindan, S. Jayaraman, P. S. Kumar, R. Balasubramanian, S. Ramakrishna, S. Madhavi and M. P. Srinivasan, *Sci. Rep.*, 2013, **3**, 3002.
77. Z. Chen, V. Augustyn, X. L. Jia, Q. F. Xiao, B. Dunn and Y. F. Lu, *ACS Nano*, 2012, **6**, 4319-4327.
78. J. Yin, L. Qi and H. Y. Wang, *ACS Appl. Mater. Inter.*, 2012, **4**, 2762-2768.
79. R. Ding, L. Qi and H. Wang, *Electrochim. Acta*, 2013, **114**, 726-735.
80. V. Khomenko, E. Raymundo-Pinero and F. Beguin, *J. Power Sources*, 2008, **177**, 643-651.
81. A. Yoshino, T. Tsubata, M. Shimoyamada, H. Satake, Y. Okana, S. Mori and S. Yata, *J. Electrochem. Soc.*, 2004, **151**, 2180-2182.
82. H. L. Wang, Z. W. Xu, Z. Li, K. Cui, J. Ding, A. Kohandehghan, X. H. Tan, B. Zahiri, B. C. Olsen, C. M. B. Holt and D. Mitlin, *Nano Lett.*, 2014, **14**, 1987-1994.
83. K. Leng, F. Zhang, L. Zhang, T. F. Zhang, Y. P. Wu, Y. H. Lu, Y. Huang and Y. S. Chen, *Nano Res.*, 2013, **6**, 581-592.
84. S. Shi, C. J. Xu, C. Yang, Y. Y. Chen, J. J. Liu and F. Y. Kang, *Sci. Rep.*, 2013, **3**, 2598.

85. X. Zhao, L. L. Zhang, S. Murali, M. D. Stoller, Q. H. Zhang, Y. W. Zhu and R. S. Ruoff, *ACS Nano*, 2012, **6**, 5404-5412.
86. H. Kim, M. Y. Cho, M. H. Kim, K. Y. Park, H. Gwon, Y. Lee, K. C. Roh and K. Kang, *Adv. Energy Mater.*, 2013, **3**, 1500-1506.
87. F. Zhang, T. F. Zhang, X. Yang, L. Zhang, K. Leng, Y. Huang and Y. S. Chen, *Energy Environ. Sci.*, 2013, **6**, 1623-1632.
88. S. R. Sivakkumar, A. G. Pandolfo, *J. Appl. Electrochem.*, 2014, **44**, 105-113.
89. N. Mosier, C. Wyman, B. Dale, R. Elander, Y. Lee, M. Holtzapple, M. Ladisch, *Bioresour. Technol.*, 2005, **96**, 673-688.
90. J. B. Binder, R. T. Raines, *J. Am. Chem. Soc.*, 2009, **131**, 1979-1985.
91. Y. Zhai, Y. Dou, D. Zhao, P. F. Fulvio, R. T. Mayes, S. Dai, *Adv. Mater.*, 2011, **23**, 4828-4850.
92. E. Raymundo-Pinero, M. Cadek, F. Beguin, *Adv. Funct. Mater.*, 2009, **19**, 1032-1039.
93. H. Wang, Z. Li, D. Mitlin, *ChemElectroChem*, 2014, **1**, 332-337.
94. M. Sevilla, A. B. Fuertes, R. Mokaya, *Energy Environ. Sci.*, 2011, **4**, 1400-1410.
95. B. Hu, K. Wang, L. Wu, S. Yu, M. Antonietti, M. M. Titirici, *Adv. Mater.*, 2010, **22**, 813-828.
96. M. M. Titirici, A. Thomas, S. H. Yu, J. O. Muller, M. Antonietti, *Chem. Mater.*, 2007, **19**, 4205-4212.
97. D. Klemm, B. Heublein, H. P. Fink, A. Bohn, *Angew. Chem., Int. Ed.*, 2005, **44**, 3358-3393.
98. D. Y. Kim, Y. Nishiyama, M. Wada, S. Kuga, *Carbon*, 2001, **39**, 1051-1056.
99. N. Shibuya, A. Misaki, *Agric. Bio. Chem.*, 1978, **42**, 2267-2274.
100. R. K. Sharma, J. B. Wooten, V. L. Baliga, X. H. Lin, W. G. Chan, M. R. Hajaligol, *Fuel*, 2004, **83**, 1469-1482.
101. H. Yang, R. Yan, H. Chen, D. H. Lee, C. Zheng, *Fuel*, 2007, **86**, 1781-1788.
102. M. V. Ramiah, *J. Appl. Polym. Sci.*, 1970, **14**, 1323-1337.
103. T. Hosoya, H. Kawamoto, S. Saka, *J. Anal. Appl. Pyrolysis*, 2007, **80**, 118-125.

104. G. Liu, X. Li, J. Lee, B. N. Popov, *Catal. Sci. Technol.*, 2011, **1**, 207-217.
105. Z. Yong, V. G. Mata, A. E. Rodrigues, *Adsorption*, 2001, **7**, 41-50.
106. Z. Yong, V. Mata, A. E. Rodrigues, *Sep. Purif. Technol.*, 2002, **26**, 195-205.
107. E. Frackowiak, F. Beguin, *Carbon*, 2001, **39**, 937-950.
108. L. L. Zhang, X. S. Zhao, *Chem. Soc. Rev.*, 2009, **38**, 2520-2531.
109. V. C. Menon, *J. Porous Mater.*, 1998, **5**, 43-58.
110. P. Hadi, M. Xu, C. Ning, C. S. K. Lin, G. McKay, *Chem. Eng. J.*, 2015, **260**, 895-906.
111. S. H. Yu, X. J. Cui, L. L. Li, K. Li, B. Yu, M. Antonietti, H. Colfen, *Adv. Mater.*, 2004, **16**, 1636-1640.
112. F. Shafizadeh, *J. Anal. Appl. Pyrolysis*, 1982, **3**, 283-305.
113. D. Mohan, C. U. Pittman, P. H. Steele, *Energy Fuel*, 2006, **20**, 848-889.
114. K. Raveendran, A. Ganesh, K. C. Khilar, *Fuel*, 1996, **75**, 987-998.
115. A. Rabenau, *Angew. Chem. Int. Ed.*, 1985, **24**, 1026-1040.
116. S. Somiya, R. Roy, *Bull. Mater. Sci.*, 2000, **23**, 453-460.
117. H. Schafer, *Annu. Rev. Mater. Sci.*, 1985, **15**, 1-41.
118. S. Feng, R. Xu, *Acc. Chem. Res.*, 2001, **34**, 239-247.
119. T. Fujino, J. M. Calderon-Moreno, S. Swamy, T. Hirose, M. Yoshimura, *Solid State Ionics*, 2002, **151**, 197-203.
120. Y. Yang, J. Cui, M. Zheng, C. Hu, S. Tan, Y. Xiao, Q. Yang, Y. Liu, *Chem. Commun.*, 2012, **48**, 380-382.
121. M. M. Titirici, M. Antonietti, *Chem. Soc. Rev.*, 2010, **39**, 103-116.
122. N. Baccile, G. Laurent, F. Babonneau, F. Fayon, M. M. Titirici, M. Antonietti, *J. Phys. Chem. C*, 2009, **113**, 9644-9654.
123. M. M. Titirici, M. Antonietti, N. Baccile, *Green Chem.*, 2008, **10**, 1204-1212.
124. X. C. Ma, F. Xu, Y. Du, L. Y. Chen, J. M. Shen, L. C. Wang, Y. T. Qian, *Carbon*, 2006, **44**, 2861-2864.
125. T. Luo, L. S. Gao, J. W. Liu, L. Y. Chen, J. M. Shen, L. C. Wang, Y. T. Qian, *J. Phys. Chem. B*, 2005, **109**, 15272-15277.

126. H. Wang, Z. W. Xu, A. Kohandehghan, Z. Li, K. Cui, X. H. Tan, T. J. Stephenson, C. K. King'ondeu, C. M. B. Holt, B. C. Olsen, J. K. Tak, D. Harfield, A. O. Anyia and D. Mitlin, *ACS Nano*, 2013, **7**, 5131-5141.
127. Q. Wang, H. Li, Q. Chen, X. J. Huang, *Carbon*, 2001, **39**, 2211-2214.
128. R. Demir-Cakan, N. Baccile, M. Antonietti, M. M. Titirici, *Chem. Mater.*, 2009, **21**, 484-490.
129. Y. L. Cao, L. F. Xiao, W. Wang, D. W. Choi, Z. M. Nie, J. G. Yu, L. V. Saraf, Z. G. Yang, J. Liu, *Adv. Mater.*, 2011, **23**, 3155-3160.
130. Y. Shao, J. Xiao, W. Wang, M. Engelhard, X. Chen, Z. Nie, M. Gu, L. Saraf, G. Exarhos, J. Zhang, *et al. Nano Lett.*, 2013, **8**, 3909-3914.
131. P. Senguttuvan, G. Rouse, V. Seznec, J. M. Tarascon, M. R. Palacin, *Chem. Mater.*, 2011, **23**, 4109-4111.
132. Y. Park, D. S. Shin, S. H. Woo, N. S. Choi, K. H. Shin, S. M. Oh, K. T. Lee, S. Y. Hong, *Adv. Mater.*, 2012, **24**, 3562-3567.
133. A. Darwiche, C. Marino, M. T. Sougrati, B. Fraisse, L. Stievano, L. Monconduit, *J. Am. Chem. Soc.*, 2012, **134**, 20805-20811.
134. J. W. Wang, X. H. Liu, S. X. Mao, J. Y. Huang, *Nano Lett.*, 2012, **12**, 5897-5902.
135. Y. W. Zhu, S. Murali, M. D. Stoller, K. J. Ganesh, W. W. Cai, P. J. Ferreira, A. Pirkle, R. M. Wallace, K. A. Cychosz, M. Thommes, *et al.. Science*, 2011, **332**, 1537-1541.
136. M. D. Stoller, S. J. Park, Y. W. Zhu, J. H. An, R. S. Ruoff, *Nano Lett.*, 2008, **8**, 3498-3502.
137. K. Jost, C. R. Perez, J. K. McDonough, V. Presser, M. Heon, G. Dion, Y. Gogotsi, *Energy Environ. Sci.*, 2011, **4**, 5060-5067.
138. X. Zhao, C. M. Hayner, M. C. Kung, H. H. Kung, *Adv. Energy Mater.*, 2011, **1**, 1079-1084.
139. D. Linden, T. B. Reddy, *Handbook of Batteries*; McGRAW-HILL, INC; New York, 2002.

140. J. R. Dahn, *Phys. Rev. B*, 1991, **44**, 9170-9177.
141. E. Peled, C. Menachem, D. BarTow, A. Melman, *J. Electrochem. Soc.*, 1996, **143**, 4-7.
142. Z. G. Yang, J. L. Zhang, M. C. W. Kintner-Meyer, X. C. Lu, D. W. Choi, J. P. Lemmon, J. Liu, *Chem. Rev.*, 2011, **111**, 3577-3613.
143. P. Thomas, D. Billaud, *Electrochim. Acta*, 2000, **46**, 39-47.
144. R. Alcantara, P. Lavela, G. F. Ortiz, J. L. Tirado, *Electrochem. Solid St.*, 2005, **8**, 222-225.
145. S. Komaba, W. Murata, T. Ishikawa, N. Yabuuchi, T. Ozeki, T. Nakayama, A. Ogata, K. Gotoh, K. Fujiwara, *Adv. Funct. Mater.*, 2011, **21**, 3859-3867.
146. C. R. Perez, S. H. Yeon, J. Segalini, V. Presser, P. L. Taberna, P. Simon, Y. Gogotsi, *Adv. Funct. Mater.*, 2013, **23**, 1081-1089.
147. J. T. Zhang, X. S. Zhao, *ChemSusChem*, 2012, **5**, 818-841.
148. C. G. Bain, A. Bonn, R. Stoneman, S. Chapman, A. Coupar, M. Evans, B. Gearey, M. Howat, C. Keenleyside, J. Labadz, *et al.* IUCN UK *Commission of Inquiry on Peatlands* 2011.
149. N. T. Plank, *Am. J. Bot.*, 1946, **33**, 335-337.
150. J. R. Dahn, T. Zheng, Y. H. Liu, J. S. Xue, *Science*, 1995, **270**, 590-593.
151. H. C. Bold, *Morphology of Plants; Joanna Cotler Books*; 1967; pp 225-229.
152. Y. P. Wu, C. R. Wan, C. Y. Jiang, S. B. Fang, Y. Y. Jiang, *Carbon*, 1999, **37**, 1901-1908.
153. B. E. Warren, *J. Chem. Phys.*, 1934, **2**, 551-555.
154. A. K. Kercher, D. C. Nagle, *Carbon*, 2003, **41**, 15-27.
155. C. Portet, G. Yushin, Y. Gogotsi, *Carbon*, 2007, **45**, 2511-2518.
156. S. Yamauchi, Y. Kurimoto, *J. Wood Sci.*, 2003, **49**, 235-240.
157. G. Eda, M. Chhowalla, *Adv. Mater.*, 2010, **22**, 2392-2415.
158. C. Y. Su, Y. P. Xu, W. J. Zhang, J. W. Zhao, X. H. Tang, C. H. Tsai, L. J. Li, *Chem. Mater.*, 2009, **21**, 5674-5680.
159. S. A. Shojaee, A. Zandiatashbar, N. Koratkar, D. A. Lucca, *Carbon*, 2013, **62**,

510-513.

160. C. E. Byrne, D. C. Nagle, *Carbon*, 1997, **35**, 259-266.
161. K. Iiyama, T. B. T. Lam, B. A. Stone, *Plant Physiol.*, 1994, **104**, 315-320.
162. M. Chabannes, K. Ruel, A. Yoshinaga, B. Chabbert, A. Jauneau, J. P. Joseleau, A. M. Boudet, *Plant J.*, 2001, **28**, 271-282.
163. Y. Ando, X. Zhao, H. Shimoyama, *Carbon*, 2001, **39**, 569-574.
164. Y. S. Park, Y. C. Choi, K. S. Kim, D. C. Chung, D. J. Bae, K. H. An, S. C. Lim, X. Y. Zhu, Y. H. Lee, *Carbon*, 2001, **39**, 655-661.
165. Y. L. Cao, L. F. Xiao, X. P. Ai, H. X. Yang, *Electrochem. Solid St.*, 2003, **6**, 30-33.
166. Y. Mao, H. Duan, B. Xu, L. Zhang, Y. S. Hu, C. C. Zhao, Z. X. Wang, L. Q. Chen, Y. S. Yang, *Energy Environ. Sci.*, 2012, **5**, 7950-7955.
167. Z. H. Wang, L. Qie, L. X. Yuan, W. X. Zhang, X. L. Hu, Y. H. Huang, *Carbon*, 2013, **55**, 328-334.
168. E. Barsoukov, J. H. Kim, J. H. Kim, C. O. Yoon, H. Lee, *Solid State Ion.*, 1999, **116**, 249-261.
169. M. D. Levi, D. Aurbach, *J. Phys. Chem. B*, 1997, **101**, 4630-4640.
170. V. Palomares, P. Serras, I. Villaluenga, K. B. Hueso, J. Carretero-Gonzalez and T. Rojo, *Energy Environ. Sci.*, 2012, **5**, 5884-5901.
171. L. Ji, M. Gu, Y. Shao, X. Li, M. H. Engelhard, B. W. Arey, W. Wang, Z. Nie, J. Xiao, C. Wang, J. Zhang and J. Liu, *Adv. Mater.*, 2014, **26**, 2901-2908.
172. J. F. Qian, Y. Xiong, Y. L. Cao, X. P. Ai, H. X. Yang, *Nano Lett.*, 2014, **14**, 1865-1869.
173. Y. Wen, K. He, Y. Zhu, F. Han, Y. Xu, I. Matsuda, Y. Ishii, J. Cumings and C. Wang, *Nat. Commun.*, 2014, **5**, 4033.
174. D. Datta, J. W. Li and V. B. Shenoy, *ACS Appl. Mater. Inter.*, 2014, **6**, 1788-1795.
175. C. D. Wessells, M. T. McDowell, S. V. Peddada, M. Pasta, R. A. Huggins and Y. Cui, *ACS Nano*, 2012, **6**, 1688-1694.

176. T. H. Hwang, D. S. Jung, J. S. Kim, B. G. Kim and J. W. Choi, *Nano Lett.*, 2013, **13**, 4532-4538.
177. Y. Y. Shao, J. Xiao, W. Wang, M. Engelhard, X. L. Chen, Z. M. Nie, M. Gu, L. V. Saraf, G. Exarhos, J. G. Zhang and J. Liu, *Nano Lett.*, 2013, **13**, 3909-3914.
178. D. W. Su and G. X. Wang, *ACS Nano*, 2013, **7**, 11218-11226.
179. Y. Liu, F. Fan, J. Wang, Y. Liu, H. Chen, K. L. Jungjohann, Y. Xu, Y. Zhou, D. Bigio, T. Zhu and C. Wang, *Nano Lett.*, 2014, **14**, 3445-3452
180. L. J. Fu, K. Tang, K. P. Song, P. A. van Aken, Y. Yu and J. Maier, *Nanoscale*, 2014, **6**, 1384-1389.
181. C. Z. Wu, X. L. Lu, L. L. Peng, K. Xu, X. Peng, J. L. Huang, G. H. Yu and Y. Xie, *Nat. Commun.*, 2013, **4**, 2431.
182. C. H. Xu, B. H. Xu, Y. Gu, Z. G. Xiong, J. Sun and X. S. Zhao, *Energy Environ. Sci.*, 2013, **6**, 1388-1414.
183. W. Luo, B. Wang, C. G. Heron, M. J. Allen, J. Morre, C. S. Maier, W. F. Stickle and X. L. Ji, *Nano Lett.*, 2014, **14**, 2225-2229.
184. S. Boukhalifa, D. Gordon, L. L. He, Y. B. Melnichenko, N. Nitta, A. Magasinski and G. Yushin, *ACS Nano*, 2014, **8**, 2495-2503.
185. L. Wei, M. Sevilla, A. B. Fuertes, R. Mokaya and G. Yushin, *Adv. Energy Mater.*, 2011, **1**, 356-361.
186. L. L. Peng, X. Peng, B. R. Liu, C. Z. Wu, Y. Xie and G. H. Yu, *Nano Lett.*, 2013, **13**, 2151-2157.
187. M. Ghaffari, Y. Zhou, H. P. Xu, M. R. Lin, T. Y. Kim, R. S. Ruoff and Q. M. Zhang, *Adv. Mater.*, 2013, **25**, 4879-4885.
188. M. Schroeder, M. Winter, S. Passerini and A. Balducci, *J. Power Sources*, 2013, **238**, 388-394.
189. Q. Wang, Z. H. Wen and J. H. Li, *Adv. Funct. Mater.*, 2006, **16**, 2141-2146.
190. H. S. Choi, J. H. Im, T. Kim, J. H. Park and C. R. Park, *J. Mater. Chem.*, 2012, **22**, 16986-16993.
191. J. Ding, H. L. Wang, Z. Li, A. Kohandehghan, K. Cui, Z. W. Xu, B. Zahiri, X. H.

- Tan, E. M. Lotfabad, B. C. Olsen and D. Mitlin, *ACS Nano*, 2013, **7**, 11004-11015.
192. N. Yabuuchi, M. Kajiyama, J. Iwatate, H. Nishikawa, S. Hitomi, R. Okuyama, R. Usui, Y. Yamada and S. Komaba, *Nat. Mater.*, 2012, **11**, 512-517.
193. J. H. Kim, J. S. Kim, Y. G. Lim, J. G. Lee and Y. J. Kim, *J. Power Sources*, 2011, **196**, 10490-10495.
194. Z. Gui, H. L. Zhu, E. Gillette, X. G. Han, G. W. Rubloff, L. B. Hu and S. B. Lee, *ACS Nano*, 2013, **7**, 6037-6046.
195. L. Wei and G. Yushin, *Nano Energy*, 2012, **1**, 552-565.
196. N. A. Liu, K. F. Huo, M. T. McDowell, J. Zhao and Y. Cui, *Sci. Rep.*, 2013, **3**, 1919.
197. S. Dutta, A. Bhaumik and C. W. Wu, *Energy Environ. Sci.*, 2014, **7**, 3574-3592.
198. R. J. White, V. Budarin, R. Luque, J. H. Clark and D. J. Macquarrie, *Chem. Soc. Rev.*, 2009, **38**, 3401-3418.
199. M. Latorre-Sanchez, A. Primo and H. Garcia, *Angew. Chem., Int. Edit.*, 2013, **52**, 11813-11816.
200. L. Sun, C. G. Tian, M. T. Li, X. Y. Meng, L. Wang, R. H. Wang, J. Yin and H. G. Fu, *J. Mater. Chem. A*, 2013, **1**, 6462-6470.
201. M. Biswal, A. Banerjee, M. Deo and S. Ogale, *Energy Environ. Sci.*, 2013, **6**, 1249-1259.
202. K. Wilson, H. Yang, C. W. Seo and W. E. Marshall, *Bioresource Technol.*, 2006, **97**, 2266-2270.
203. X. Y. Zhao, J. Chen and F. L. Du, *J. Food Sci. Tech. Mys.*, 2012, **49**, 521-529.
204. A. S. Chang, A. Sreedharan and K. R. Schneider, *Food Control*, 2013, **32**, 296-303.
205. E. I. El-Shafey, *J. Environ. Manage*, 2007, **84**, 620-627.
206. Z. A. Al-Othman, R. Ali and M. Naushad, *Chem. Eng. J.*, 2012, **184**, 238-247.
207. X. J. He, P. H. Ling, J. S. Qiu, M. X. Yu, X. Y. Zhang, C. Yu and M. D. Zheng, *J. Power Sources*, 2013, **240**, 109-113.

208. P. Z. Guo, Q. Q. Ji, L. L. Zhang, S. Y. Zhao and X. S. Zhao, *Acta. Phys-Chim. Sin.*, 2011, **27**, 2836-2840.
209. G. T. K. Fey, Y. Y. Lin, K. P. Huang, Y. C. Lin, T. P. Kumar, Y. D. Cho and H. M. Kao, *Adv. Mater. Res.*, 2012, **415-417**, 1572-1585
210. I. Watanabe, T. Doi, J. I. Yamaki, Y. Y. Lin and G. T. K. Fey, *J. Power Sources*, 2008, **176**, 347-352.
211. M. Ahmad, S. S. Lee, X. Dou, D. Mohan, J. K. Sung, J. E. Yang and Y. S. Ok, *Bioresour Technol.*, 2012, **118**, 536-544.
212. Z. Y. Zhong, Q. Yang, X. M. Li, K. Luo, Y. Liu and G. M. Zeng, *Ind. Crop. Prod.*, 2012, **37**, 178-185.
213. X. D. Zhang, M. Xu, R. F. Sun and L. Sun, *J. Eng. Gas Turb. Power*, 2006, **128**, 493-496.
214. Y. H. Liu, J. S. Xue, T. Zheng and J. R. Dahn, *Carbon*, 1996, **34**, 193-200.
215. C. Vidal-Abarca, P. Lavela, J. L. Tirado, A. V. Chadwick, M. Alfredsson and E. Kelder, *J. Power Sources*, 2012, **197**, 314-318.
216. A. Bhide, J. Hofmann, A. K. Durr, J. Janek and P. Adelhelm, *Phys. Chem. Chem. Phys.*, 2014, **16**, 1987-1998.
217. H. Kim, Y. U. Park, K. Y. Park, H. D. Lim, J. Hong and K. Kang, *Nano Energy*, 2014, **4**, 97-104.
218. S. Y. Kim, J. Hong, R. Kaviani, S. W. Lee, M. N. Hyder, Y. Shao-Horn and P. T. Hammond, *Energy Environ. Sci.*, 2013, **6**, 888-897.
219. S. H. Ha, Y. S. Jeong and Y. J. Lee, *ACS Appl. Mater. Inter.*, 2013, **5**, 12295-12303.
220. H. Kim, H. D. Lim, S. W. Kim, J. Hong, D. H. Seo, D. C. Kim, S. Jeon, S. Park and K. Kang, *Sci. Rep.*, 2013, **3**, 1506.
221. M. N. Hyder, S. W. Lee, F. C. Cebeci, D. J. Schmidt, Y. Shao-Horn and P. T. Hammond, *ACS Nano*, 2011, **5**, 8552-8561.
222. S. W. Lee, N. Yabuuchi, B. M. Gallant, S. Chen, B. S. Kim, P. T. Hammond and Y. Shao-Horn, *Nat. Nanotechnol.*, 2010, **5**, 531-537.

223. W. T. Gu, N. Peters and G. Yushin, *Carbon*, 2013, **53**, 292-301.
224. F. Y. Tu, S. Q. Liu, T. H. Wu, G. H. Jin and C. Y. Pan, *Powder Technol.*, 2014, **253**, 580-583.
225. H. R. Byon, B. M. Gallant, S. W. Lee and Y. Shao-Horn, *Adv. Funct. Mater.*, 2013, **23**, 1037-1045.
226. S. W. Lee, B. M. Gallant, Y. Lee, N. Yoshida, D. Y. Kim, Y. Yamada, S. Noda, A. Yamada and Y. Shao-Horn, *Energy Environ. Sci.*, 2012, **5**, 5437-5444.
227. R. Mukherjee, A. V. Thomas, D. Datta, E. Singh, J. W. Li, O. Eksik, V. B. Shenoy and N. Koratkar, *Nat. Commun.*, 2014, **5**, 3710.
228. X. Zhou, Y. G. Guo, *ChemElectroChem*, 2014, **1**, 83-86.
229. A. Ponrouch, A. R. Goni and M. R. Palacin, *Electrochem. Commun.*, 2013, **27**, 85-88.
230. http://www.jmenergy.co.jp/en/products_cell_can.html
231. Y. Gogotsi, P. Simon, *Science*, 2011, **334**, 917-918.
232. <http://www.jsrmicro.com/index.php/EnergyAndEnvironment>
233. H. Wang, C. M. Holt, Z. Li, X. Tan, B. S. Amirkhiz, Z. Xu, B. Olsen, T. Stephenson, D. Mitlin, *Nano Res.*, 2012, **5**, 605-617.
234. W. Wei, X. Cui, W. Chen, D. Ivey, *Chem. Soc. Rev.*, 2011, **40**, 1697-1721.
235. D. Cericola, R. Kotz, *Electrochim. Acta*, 2012, **72**, 1-17.
236. G. Wang, L. Zhang, J. Zhang, *Chem. Soc. Rev.*, 2012, **41**, 797-828.
237. J. Yan, Z. J. Fan, W. Sun, G. Q. Ning, T. Wei, Q. Zhang, R. F. Zhang, L. J. Zhi and F. Wei, *Adv. Funct. Mater.*, 2012, **22**, 2632-2641.
238. S. Shi, C. J. Xu, C. Yang, Y. Y. Chen, J. J. Liu and F. Y. Kang, *Sci. Rep.*, 2013, **3**, 2598.
239. C. G. Liu, Z. N. Yu, D. Neff, A. Zhamu and B. Z. Jang, *Nano Lett.*, 2010, **10**, 4863-4868.
240. Z. Chen, V. Augustyn, J. Wen, Y. W. Zhang, M. Q. Shen, B. Dunn and Y. F. Lu, *Adv. Mater.*, 2011, **23**, 791-795.
241. J. H. Pikul, H. G. Zhang, J. Cho, P. V. Braun, W. P. King, *Nat. Commun.*, 2013,

- 4, 1732.
242. M. S. Whittingham, *Chem. Rev.*, 2014, **114**, 11414-11443.
243. N. Yabuuchi, K. Kubota, M. Dahbi, S. Komaba, *Chem. Rev.*, 2014, **114**, 11636-11682.
244. V. Palomares, M. Casas-Cabanas, E. Castillo-Martinez, M. H. Han, T. Rojo, *Energy Environ. Sci.*, 2013, **6**, 2312-2337.
245. S. W. Kim, D. H. Seo, X. H. Ma, G. Ceder, K. Kang, *Adv. Energy Mater.*, 2012, **2**, 710-721.
246. L. Wang, Y. H. Lu, J. Liu, M. W. Xu, J. G. Cheng, D. W. Zhang, J. B. Goodenough, *Angew. Chem. Int. Edit.*, 2013, **52**, 1964-1967.
247. B. Koo, S. Chattopadhyay, T. Shibata, V. B. Prakapenka, C. S. Johnson, T. Rajh, E. V. Shevchenko, *Chem. Mater.*, 2013, **25**, 245-252.
248. M. Han, E. Gonzalo, G. Singh, T. Rojo, *Energy Environ. Sci.*, 2015, **8**, 81-102.
249. Y. Jung, C. Lim, D. Kim, *J. Mater. Chem. A*, 2013, **1**, 11350-11354.
250. S. Li, Y. Dong, L. Xu, X. Xu, L. He, L. Mai, *Adv. Mater.*, 2014, **26**, 3545-3553.
251. W. Song, X. Cao, Z. Wu, J. Chen, K. Huangfu, X. Wang, Y. Huang, X. Ji, *Phys. Chem. Chem. Phys.*, 2014, **16**, 17681-17687.
252. J. Ding, H. Wang, Z. Li, K. Cui, D. Karpuzov, X. Tan, A. Kohandehghan, D. Mitlin, *Energy Environ. Sci.*, 2015, **8**, 941-955.
253. H. Cha, H. Jeong, J. Kang, *J. Mater. Chem. A*, 2014, **2**, 5182-5186.
254. Y. Xu, E. M. Lotfabad, H. L. Wang,; B. Farbod, Z. W. Xu,; A. Kohandehghan, D. Mitlin, *Chem. Commun.*, 2013, **49**, 8973-8975.
255. H. L. Pan, X. Lu, X. Q. Yu, Y. S. Hu, H. Li, X. Q. Yang, L. Q. Chen, *Adv. Energy Mater.*, 2013, **3**, 1186-1194.
256. Y. Zhu, P. Nie, L. Shen, S. Dong, Q. Sheng, H. Li, H. Luo, X. Zhang, *Nanoscale*, 2015, **7**, 3309-3315.
257. L. F. Xiao, Y. L. Cao, J. Xiao, W. Wang, L. Kovarik, Z. M. Nie, J. Liu, *Chem. Commun.*, 2012, **48**, 3321-3323.
258. B. Farbod, K. Cui, W. P. Kalisvaart, M. Kupsta, B. Zahiri, A. Kohandehghan, E.

- M. Lotfabad, Z. Li, E. J. Lubber, D. Mitlin, *ACS Nano*, 2014, **8**, 4415-4429.
259. L. Baggetto, K. J. Carroll, H. Y. Hah, C. E. Johnson, D. R. Mullins, R. R. Unocic, J. A. Johnson, Y. S. Meng, G. M. Veith, *J. Phys. Chem. C.*, 2014, **118**, 7856-7864.
260. V. Kulish, O. Malyi, M. Ng, Z. Chen, S. Manzhos, P. Wu, *Phys. Chem. Chem. Phys.*, 2014, **16**, 4260-4267.
261. Y. H. Xu, Q. Liu, Y. J. Zhu, Y. H. Liu, A. Langrock, M. R. Zachariah, C. S. Wang, *Nano Lett.*, 2013, **13**, 470-474.
262. D. Bresser, F. Mueller, D. Buchholz, E. Paillard, S. Passerini, *Electrochim. Acta*, 2014, **128**, 163-171.
263. C. K. Chan, H. L. Peng, G. Liu, K. McIlwrath, X. F. Zhang, R. A. Huggins, Y. Cui, *Nat. Nanotechnol.*, 2008, **3**, 31-35.
264. X. Zhu, H. Chen, Y. Wang, L. Xia, Q. Tan, H. Li, Z. Zhong, F. Su, X.S. Zhao, *J. Mater. Chem. A*, 2013, **14**, 4483-4489.
265. Y. Yao, N. Liu, M. T. McDowell, M. Pasta, Y. Cui, *Energy Environ. Sci.*, 2012, **5**, 7927-7930.
266. M. H. Seo, M. Park, K. T. Lee, K. Kim, J. Kim, J. Cho, *Energy Environ. Sci.*, 2011, **4**, 425-428.
267. T. Ramireddy, M. Rahman, T. Xing, Y. Chen, A. M. Glushenkov, *J. Mater. Chem. A*, 2014, **2**, 4282-4291.
268. Y. Wang, F. Su, JY. Lee, X.S. Zhao, *Chem. Mater.*, 2006, **18**, 1347-1353.
269. X. Wang, X. Q. Cao, L. Bourgeois, H. Guan, S. M. Chen, Y. T. Zhong, D. M. Tang, H. Q. Li, T. Y. Zhai, L. Li, Y. Bando, D. Golberg, *Adv. Funct. Mater.*, 2012, **22**, 2682-2690.
270. H. W. Song, N. Li, H. Cui, C. X. Wang, *J. Mater. Chem. A*, 2013, **1**, 7558-7562.
271. J. Liu, H. G. Zhang, J. Wang, J. Cho, J. H. Pikul, E. S. Epstein, X. Huang, J. Liu, W. P. King, P. V. Braun, *Adv. Mater.*, 2014, **26**, 7096-7101.
272. N. Yesibolati, M. Shahid, W. Chen, M. N. Hedhili; M. C. Reuter, F. M. Ross, H. N. Alshareef, *Small*, 2014, **10**, 2849-2858.

273. M. Shahid, N. Yesibolati, M. C. Reuter, F. M. Ross, Whittingham, *J. Power Sources*, 2014, **263**, 239-245.
274. H. Bryngelsson, J. Eskhult, L. Nyholm, M. Herranen, O. Alm, K. Edstrom, *Chem. Mater.*, 2007, **19**, 1170-1180.
275. V. Aravindan, P. Vickraman, *Solid State Sci.*, 2007, **9**, 1069-1073.
276. L. Zhang, H. Wu, B. Liu, X. Lou, *Energy Environ. Sci.*, 2014, **7**, 1013-1017.
277. S. Li, Y. Wang, J. Qiu, M. Ling, H. Wang, W. Martens, S. Zhang, *RSC Adv.*, 2014, **4**, 50148-50152.
278. X. Xie, D. Su, J. Zhang, S. Chen, A. Mondal, G. Wang, *Nanoscale*, 2015, **7**, 3164-3172.
279. A. M. Nie, L. Y. Gan, Y. C. Chong, H. Asayesh-Ardakani, Q. Q. Li, C. Z. Dong, R. Z. Tao, F. Mashayek, H. T. Wang, U. Schwingenschlogl, R. F. Klie, R. S. Yassar, *ACS Nano*, 2013, **7**, 6203-6211.
280. G. M. Zhou, D. W. Wang, L. Li, N. Li, F. Li, H. M. Cheng, *Nanoscale*, 2013, **5**, 1576-1582.
281. L. D. Ellis, T. D. Hatchard, M. N. Obrovac, *J. Electrochem. Soc.*, 2012, **159**, A1801-A1805.
282. D. W. Su, C. Y. Wang, H. Ahn, G. X. Wang, *Phys. Chem. Chem. Phys.*, 2013, **15**, 12543-12550.
283. J. Park, J. W. Park, J. H. Han, S. W. Lee, K. Y. Lee, H. S. Ryu, K. W. Kim, G. X. Wang, J. H. Ahn, H. J. Ahn, *Mater. Res. Bull.*, 2014, **58**, 186-189.
284. H. X. Zhang, C. Feng, Y. C. Zhai, K. L. Jiang, Q. Q. Li, S. S. Fan, *Adv. Mater.*, 2009, **21**, 2299-2304.
285. Y. Wang, H. C. Zeng, J. Y. Lee, *Adv. Mater.*, 2006, **18**, 645-649.
286. S. M. Paek, E. Yoo, I. Honma, *Nano Lett.*, 2009, **9**, 72-75.
287. X. D. Huang, X. F. Zhou, L. Zhou, K. Qian, Y. H. Wang, Z. P. Liu, C. Z. Yu, *ChemphysChem*, 2011, **12**, 278-281.
288. C. A. Bonino, L. W. Ji, Z. Lin, O. Toprakci, X. W. Zhang, S. A. Khan, *ACS Appl. Mater. Inter.*, 2011, **3**, 2534-2542.

289. X. Zhang, J. Liang, G. X. Gao, S. J. Ding, Z. L. Yang, W. Yu, B. Q. Li, *Electrochim. Acta*, 2013, **98**, 263-267.
290. L. Zhang, G. Q. Zhang, H. B. Wu, L. Yu, X. W. Lou, *Adv. Mater.*, 2013, **25**, 2589-2593.
291. M. He, L. X. Yuan, X. L. Hu, W. X. Zhang, J. Shu, Y. H. Huang, *Nanoscale*, 2013, **5**, 3298-3305.
292. Y. Zhang, J. Xie, S. Zhang, P. Zhu, G. Cao, X. Zhao, *Electrochim. Acta*, 2015, **151**, 8-15.
293. X. W. Lou, C. Yuan, L. A. Archer, *Small*, 2007, **3**, 262-265.
294. W. S. Kim, Y. Hwa, H. C. Kim, J. H. Choi, H. J. Sohn, S. H. Hong, *Nano Res.*, 2014, **7**, 1128-1136.
295. A. Z. Adamyan, Z. N. Adamian, V. M. Aroutiounian, *Sensors*, 2003, **3**, 438-442.
296. X. W. Lou, Y. Wang, C. Yuan, J. Lee, L. A. Archer, *Adv. Mater.*, 2006, **18**, 2325-2329.
297. S. Ikeda, K. Tachi, Y. H. Ng, Y. Ikoma, T. Sakata, H. Mori, T. Harada, M. Matsumura, *Chem. Mater.*, 2007, **19**, 4335-4340.
298. X. W. Lou, J. S. Chen, P. Chen, L. A. Archer, *Chem. Mater.*, 2009, **21**, 2868-2874.
299. C. Wang, Y. Zhou, M. Y. Ge, X. B. Xu, Z. L. Zhang, J. Z. Jiang, *J. Am. Chem. Soc.*, 2010, **132**, 46-47
300. T. Egami, S. J. L. Billinge, *Underneath the Bragg Peaks: Structural analysis of Complex Materials*, Elsevier Ltd., 2003.
301. A. Ponrouch, P. L. Taberna, P. Simon, M. R. Palacin, *Electrochim. Acta*, 2012, **61**, 13-18.
302. S. Grugeon, S. Laruelle, L. Dupont, J.-M. Tarascon, *Solid State Sciences*, 2003, **5**, 895-940.
303. S. Laruelle, S. Grugeon, P. Poizot, M. Dolle, L. Dupont, J.-M. Tarascon, *J. Electrochem. Soc.*, 2002, **149**, 627-634.
304. Z. W. Xu, H. L. Wang, Z. Li, A. Kohandehghan, J. Ding, J. Chen, K. Cui, D.

- Mitlin, *J. Phys. Chem. C*, 2014, **118**, 18387-18396.
305. Y. Chen, B. Song, R. Chen, L. Lu, J. Xue, *J. Mater. Chem. A*, 2014, **2**, 5688-5695.
306. F. Han, W. Li, M. Li, A. Lu, *J. Mater. Chem.*, 2012, **22**, 9645-9651.
307. Y. H. Xu, J. C. Guo, C. S. Wang, *J. Mater. Chem.*, 2012, **22**, 9562-9567.
308. X. W. Lou, C. M. Li, L. A. Archer, *Adv. Mater.*, 2009, **21**, 2536-2539.
309. K. Dai, H. Zhao, Z. Wang, X. Song, V. Battaglia, G. Liu, *J. Power Sources*, 2014, **263**, 276-279.
310. S. A. Webb, L. Baggetto, C. A. Bridges, G. M. Veith, *J. Power Sources*, 2014, **248**, 1105-1117.